UNIVERZITET U NOVOM SADU

PRIRODNO-MATEMATIČKI FAKULTET

NOVEL WAVE PHENOMENA BASED ON PLASMONIC METAMATERIALS AND THEIR APPLICATION IN SENSORS AND COMPONENTS

---DOCTORAL DISSERTATION---

NOVI TALASNI FENOMENI BAZIRANI NA PLAZMONIČNIM METAMATERIJALIMA I NjIHOVA PRIMENA U SENZORIMA I KOMPONENTAMA

---DOKTORSKA DISERTACIJA---

Mentori:

Prof. dr Zoran Mijatović

dr Nikolina Janković

Kandidat:

Žarko Šakotić

Novi Sad, 2021

КЉУЧНА ДОКУМЕНТАЦИЈСКА ИНФОРМАЦИЈА[1]

Врста рада:	Докторска дисертација
Име и презиме аутора:	Жарко Шакотић
Ментор (титула, име, презиме, звање, институција)	Проф. др Зоран Мијатовић, редовни професор, природно-математички факултет, Универзитет у Новом Саду др Николина Јанковић, виши научни сарадник, Институт БиоСенс – истраживачко-развојни институт за информационе технологије биосистема, Универзитет у Новом Саду
Наслов рада:	Нови таласни феномени базирани на плазмоничним метаматеријалима и њихова примена у сензорима и комппонентама
Језик публикације (писмо):	Енглески језик
Физички опис рада:	Страница 161 Поглавља 8 Референци 232 Табела 2 Слика 73 Графикона 0 Прилога 0
Научна област:	Физика
Ужа научна област (научна дисциплина):	Плазмоника и метаматеријали
Кључне речи / предметна одредница:	Метаматеријали, плазмоника, оптика, фотоника, везана стања у континууму, сензори
Резиме на језику рада:	Generating, detecting, and controlling the frequency, amplitude, phase, and polarization of electromagnetic waves is at the center of a broad range of important applications today. The functionality of devices and technologies such as antennas, lasers, solar cells, optical fibers, imaging systems, optical computers, and biosensors relies on precise control over electromagnetic wave

properties. In order to obtain these properties and meet the demands of modern wave-based technologies, a fundamental understanding and discovery of novel wave phenomena is necessary.

In this dissertation, our goal is to expand the possibilities of wave control and enhance light-matter interaction based on novel phenomena in metamaterials and plasmonics. Specifically, we focus on surface plasmon-polariton modes enabled by substrate integrated waveguides at microwave frequencies. Furthermore, embedded eigenstates and their topological aspects in optical ENZ structures are studied. Exploiting the functionalities of these phenomena, we discuss the consequences on wave propagation and scattering, and explore various structures to achieve control of frequency, amplitude, phase, and polarization of electromagnetic waves. We provide new theoretical insights on the underlying physics and demonstrate the utility of the discussed phenomena by proposing several applications including two microwave dual-band filters, a microwave sensor for liquid analyte detection, a narrowband and directive thermal emitter, an infrared polarization control and switching scheme, an improved phase sensor, and an unusual laser-absorber structure. The generality of the presented theoretical insights indicates new possibilities in the fields of thermal emission engineering, topological photonics and lasers.

Датум прихватања теме од стране надлежног већа:	28.05.2020.
Датум одбране: (Попуњава одговарајућа служба)	
Чланови комисије: (титула, име, презиме, звање, институција)	Председник: Весна Бенгин, редовни професор, природно-математички факултет, Универзитет у Новом Саду; научни саветник, Институт БиоСенс – истраживачко-развојни институт за информационе технологије биосистема, Универзитет у Новом Саду Члан: Љупчо Хаџиевски, научни саветник, Институт за нуклеарне науке „Винча", Универзитет у Београду Члан: Андреа Алу, редовни професор, City University of New York - CUNY, Њујорк, САД
Напомена:	

UNIVERSITY OF NOVI SAD

FACULTY OF SCIENCES

KEY WORD DOCUMENTATION[2]

Document type:	Doctoral dissertation
Author:	Žarko Šakotić
Supervisor (title, first name, last name, position, institution)	Prof dr Zoran Mijatović, full professor, Faculty of Sciences, University of Novi Sad Dr Nikolina Janković, senior research associate, BioSense Institute - Research Institute for Information Technologies in Biosystems, University of Novi Sad
Thesis title:	Novel wave phenomena based on plasmonic metamaterials and their application in sensors and components
Language of text (script):	English language
Physical description:	Pages 161 Chapters 8 References 232 Tables 2 Illustrations 73 Graphs 0 Appendices 0
Scientific field:	Physics
Scientific subfield (scientific discipline):	Plasmonics and metamaterials
Subject, Key words:	Metamaterials, plasmonics, optics, photonics, bound states in the continuum, sensors
Abstract in English language:	Generating, detecting, and controlling the frequency, amplitude, phase, and polarization of electromagnetic waves is at the center of a broad range of important applications today. The functionality of devices and technologies such as antennas, lasers, solar cells, optical fibers, imaging systems, optical computers, and biosensors relies on precise control over electromagnetic wave properties. In order to obtain these properties and meet the demands of modern

	wave-based technologies, a fundamental understanding and discovery of novel wave phenomena is necessary. In this dissertation, our goal is to expand the possibilities of wave control and enhance light-matter interaction based on novel phenomena in metamaterials and plasmonics. Specifically, we focus on surface plasmon-polariton modes enabled by substrate integrated waveguides at microwave frequencies. Furthermore, embedded eigenstates and their topological aspects in optical ENZ structures are studied. Exploiting the functionalities of these phenomena, we discuss the consequences on wave propagation and scattering, and explore various structures to achieve control of frequency, amplitude, phase, and polarization of electromagnetic waves. We provide new theoretical insights on the underlying physics and demonstrate the utility of the discussed phenomena by proposing several applications including two microwave dual-band filters, a microwave sensor for liquid analyte detection, a narrowband and directive thermal emitter, an infrared polarization control and switching scheme, an improved phase sensor, and an unusual laser-absorber structure. The generality of the presented theoretical insights indicates new possibilities in the fields of thermal emission engineering, topological photonics and lasers.
Accepted on Scientific Board on:	28.05.2020.
Defended: (Filled by the faculty service)	
Thesis Defense Board: (title, first name, last name, position, institution)	President: Vesna Bengin, full professor, Faculty of Sciences, University of Novi Sad; scientific advisor, BioSense Institute - Research Institute for Information Technologies in Biosystems, University of Novi Sad Member: Ljupčo Hadžievski, scientific advisor, Vinča Institute of Nuclear Science, University of Belgrade Member: Andrea Alu, Einstein Professor, City University of New York, New York, USA
Note:	

Acknowledgements

First, I would like to thank my supervisors Dr. Nikolina Janković and Prof. Zoran Mijatović for their excellent guidance and support during the making of this dissertation. I want to especially thank Dr. Nikolina Janković for her continuous support and trust which dates back to my undergraduate studies, without which this dissertation would not be possible.

I want to thank my colleagues and friends at the BioSense Institute for providing an enjoyable work enviroment and for being supportive since the very beginning. I especially thank my friend and former colleague Dr. Norbert Čeljuska for his advice and expert help, which helped me significantly in the early stages of my research career.

A significant part of this dissertation originates from my visits to the University of Texas at Austin and the Advanced Science Research Center CUNY, New York in the groups led by Prof. Andrea Alù, whom I thank for the scientific inspiration, illuminating discussions, and unreserved support in all stages of our collaboration. I want to thank all the group members at UT Austin and CUNY who made me feel welcome, and for their help both at work and privately. I want to especially thank Prof. Alex Krasnok who made a signifcant impact on my research through countless insightful discussions, and whose expertise and guidance helped make our collaborations successful. Doing exciting research and having the necessary support system to do so is a privilege, so I want to extend my thanks to all my supervisors, colleagues, and collaborators not mentioned by name who made that possible.

On a personal note, I would like thank my family for their patience and unwavering support throughout this whole journey. I want to thank all my friends for being there along the way and for regularly asking me to explain what exactly my research is about – an unwitting gut check that was always welcome. Lastly, I want to thank Milena for checking my English, and more imporantly, for supporting me and making it all make sense.

Table of contents

List of figures

Chapter 1: Introduction and motivation

Electromagnetic (EM) waves are undoubtably an important part of the everyday human experience. Whether considering how we visualize and experience the world (visible light), how bodies absorb and radiate heat (infrared light), or how we communicate remotely in the modern world (radio frequency waves) - EM waves underpin many facets of life, science and technology. The theoretical foundations of electromagnetics were set in the period of time leading up to the mid-19th century, in a series of experiments by Carl Friedrich Gauss, Michael Faraday, André-Marie Ampere, and others. Their results were ultimately unified in a compact set of equations in 1865 by James Maxwell [1], and since then wave-based science and technology have seen tremendous advancement.

Generating, detecting, and controlling the frequency, amplitude, phase, and polarization of EM waves is at the center of a broad range of important applications today. The functionality of devices and technologies like antennas, lasers, solar cells, optical fibers, imaging systems, optical computers, and biosensors relies on precise control over EM wave properties. Meeting the demands of modern wave-based technologies requires a multidisciplinary approach – engineering novel materials with improved electric and magnetic properties, using nanotechnology to engineer nanoscale structures which interact with visible/IR light, and most of all, a fundamental knowledge and discovery of novel wave phenomena to overcome the technological and physical limitations of wave-based devices. One example of a physical limitation considered impossible to overcome for many years is the diffraction limit, stating that light cannot be localized to dimensions smaller than half of its wavelength [2]. This limit stands in the way of achieving strong light-matter interaction, since the size mismatch between atomic scales and, for example, visible light wavelengths is extremely large. This shortcoming was first addressed by Rufus Ritchie in 1957 who showed that the coupling of light to collective excitations of electrons at metallic surfaces is possible [3], a phenomenon later termed surface-plasmon polariton [4]. In the following decades, the unusual dispersion of these surface waves was used to confine light at a deeply subwavelength scale, breaking the diffraction limit [5]. The field of plasmonics thus provided the ability to control wave dynamics and enhance light-matter interaction at a subwavelength scale, opening new avenues in biosensing and spectroscopy technologies [6,7].

However, conventional plasmonics has limitations. Only a small set of materials can provide the necessary electric response for the formation of plasmon-polaritons and such a response is available only in narrow regions of the EM spectrum. Furthermore, the unavoidable absorption loss in plasmonic materials significantly hinders the larger propagation lengths and field enhancements, properties which are important in communication, sensing, and quantum technologies. The plasmonics example is an illustration of a larger challenge in modern electromagnetics; the degree of wave control and the strength of light-matter interaction with naturally available materials is limited, as they provide only a limited set of electric and magnetic responses. This puts many opportunities for wave-based technology out of reach with conventional materials.

In order to bring these opportunities to reality, a concept called metamaterials has been employed [8]. Metamaterials represent a research area which aims to overcome the limits of conventional materials by tailoring the electric and magnetic responses with artificially designed structures, or by exploiting the extreme wave regimes in ordinary materials. By harnessing the potential of metamaterials, the realization of novel wave phenomena is possible, and the gaps in understanding the physics and the possibilities of their application are being filled. Although there has been a great progress in the last 20 years, metamaterials and plasmonics are yet to reach their full potential, leaving unexplored avenues for scientific discovery and real-world application.

In this thesis, our goal is to expand the possibilities of wave control and enhance light-matter interaction based on novel phenomena in metamaterials and plasmonics. Exploiting the functionalities of different phenomena, we discuss the theoretical consequences on wave propagation and scattering, and explore various structures to achieve control of frequency, amplitude, phase, and polarization of EM waves.

Surface-plasmon-polaritons (SPP) have advantageous properties for waveguiding and are excellent at enhancing light-matter interaction. In order to exploit these properties at microwave frequencies, a metamaterial approach to induce effective SPP-modes will be explored. The large control over the effective SPP band's characteristics provides an excellent base for designing multiband microwave filters and sensors. To demonstrate the utility of the concept, two high-performance microwave dual-band filters and a microwave sensor are designed, fabricated and characterized.

Another wave phenomenon enabling enhanced light-matter interaction and versatile scattering properties which will be thoroughly explored is the epsilon-near-zero (ENZ) phenomenon [9]. In order to exploit the properties of ENZ, multilayer planar structures with singular permittivity response will be analyzed in detail. Specifically, the emergence of non-radiating resonances called embedded eigenstates (EEs) in such structures will be thoroughly explored. By probing these systems with non-Hermitian perturbations in the form of loss and gain, a series of novel, unusual scattering scenarios with a range of possible applications will be uncovered. Based on these phenomena, several applications will be discussed including a narrowband directive thermal emitter, a sensitive phase-sensing scheme, a polarization control system, and an unconventional lasing and absorbing scenario.

Outline of the thesis

Chapter 2 gives a brief overview of the wave phenomena related to the research in this thesis, with the theoretical insights into the basic physics of metamaterials, plasmonics, surface-plasmon polaritons (SPP) and bulk-plasmon polaritons (BPP), surface-integrated waveguides (SIW), epsilon-near-zero materials, embedded eigenstates, and parity-time-symmetry (PT-symmetry).

Chapter 3 deals with SPP-like phenomena in SIW configuration, a concept which proposes the structural dispersion in SIWs as a basis to create a tunable plasmonic environment. As it will be shown, such a structure is a promising candidate for designing filters and sensors in the microwave regime. We will provide a theoretical analysis and explore their plasmonic response in detail, and finally demonstrate two novel components based on this principle – a dual-band microwave filter and a microwave sensor for detection of liquid analytes.

In Chapter 4 we move on from guided to scattering scenarios, and discuss various scattering processes within the framework of the scattering matrix formalism. Expanding the analysis to the complex frequency plane, we focus on the emerging singularities of the scattering matrix, and how they can be used to describe a range of unusual scattering phenomena. This chapter represents a theoretical basis for the research results shown in chapters 5, 6, and 7.

Chapter 5 focuses on embedded eigenstates in planar ENZ multilayers. We discuss the symmetry-protected and accidental EEs supported in such structures and analyze the associated scattering properties in detail. We then implement a realistic model and show how a highly

directive and spectrally selective absorber/thermal-emitter can be designed based on the supported EE.

Chapter 6 addresses reflective multilayers supporting EEs. We show that emerging scattering singularities originate from the underlying EEs and they are topologically protected. We discuss the creation and annihilation of topological charges, and consider applications based on the introduced concept. We propose a versatile polarization control scheme, as well as aphase-sensing mechanism based on the manipulation of topological charges.

In chapter 7, we consider active and PT-symmetric ENZ systems. We explore the effects PT-symmetry has on EEs supported in ENZ systems, and analyze the scattering anomalies appearing in such multilayers. The topological nature of the emerging singularities is addressed, expanding the concept of topological scattering singularities to two-port systems. We also consider a coherent, two-port excitation of a suitably designed active system, where an EE-like scattering response is induced even if the structure itself does not support an EE. In addition, it is also shown how simple phase tuning can switch the system between extreme scattering states – from unidirectional absorbing to unidirectional lasing, and further to EE-like scattering, all in a simple multilayer configuration.

Finally, in chapter 8 we draw conclusions and give an outlook on further research directions.

Chapter 2: Wave phenomena in metamaterials and plasmonics

2.1 Introduction

In this chapter, we will give an overview of wave phenomena in metamaterials and plasmonics which relate to the research results presented in this thesis. As mentioned in the first chapter, metamaterials and plasmonics have shown exceptional capabilities in controlling the frequency, phase, amplitude, and polarization of electromagnetic waves, thus opening many opportunities for scientific and technological advancement. To provide insight into the physics behind wave dynamics in such environments, we will start from basic wave propagation properties, and subsequently introduce recent advancements in metamaterials and plasmonics. In the following chapters, we will expand the discussion and explore novel phenomena in different structures with various applications.

2.2 Wave propagation

The propagation of electromagnetic waves has been intensively studied in the last 150 years. Although properties of light were studied since the times of Ancient Greece [10], the wave nature of light was not understood until Maxwell's equations were established. Electromagnetic field and its interaction with the medium are fully described by Maxwell's equations:

$$\nabla \times E = \frac{\partial B}{\partial t} \tag{2.1}$$

$$\nabla \times H = J + \frac{\partial D}{\partial t} \tag{2.2}$$

$$\nabla \cdot E = \rho \tag{2.3}$$

$$\nabla \cdot H = 0 \tag{2.4}$$

These equations represent Faraday's law of induction, Ampere-Maxwell's law, and Gauss' laws for the electric and magnetic fields, respectively. The quantities E and H are the electric and magnetic field intensities and are measured in units of [V/m] and [A/m], respectively. D is known as the electric displacement vector, and B, the magnetic induction. The quantities ρ and J are the volume charge density and electric current density (charge flux)

of any external charges barring induced polarization charges and currents. They are measured in units of [C/m^3] and [A/m^2]. The right-hand side of the fourth equation is zero because there are no magnetic monopole charges.

The electric and magnetic flux densities D, B are related to the field intensities E, H via the so-called constitutive relations, whose precise form depends on the material in which the fields exist. In a linear, isotropic medium they are:

$$D = \varepsilon E = \varepsilon_r \varepsilon_0 E \qquad (2.5)$$

$$B = \mu H = \mu_r \mu_0 H \qquad (2.6)$$

where ε_r, μ_r are the relative permittivity and permeability of the medium, and ε_0, μ_0 are the permittivity and permeability of vacuum. By considering a source free region of space, combining (2.1), (2.2) and the constitutive relations, the Helmholtz equation is obtained as:

$$\nabla^2 E = \mu\varepsilon \frac{\partial^2 E}{\partial t^2}. \qquad (2.7)$$

By further considering electric field with only an x-component and uniform in the x and y directions, the Helmholtz equation states:

$$\frac{\partial^2 E_x}{\partial z^2} = \omega^2 \mu\varepsilon E_x, \qquad (2.8)$$

which further leads to the plane wave solution:

$$E_x(z) = E^+ e^{-jkz} + E^- e^{jkz}, \qquad (2.9)$$

where $k = \omega\sqrt{\mu\varepsilon}$ is the wave number in the medium, and E^+ and E^- are amplitudes of forward and backward propagating solutions. Solving the wave equation is usually the starting point in the analysis of a scattering or waveguiding problem. The relationship between the wavenumber and the frequency, called the dispersion, is extremely important for light-matter interaction and waveguiding. The dispersion of waves in homogeneous dielectric media is usually small and cannot be significantly controlled, while in metamaterials and plasmonics it possible to engineer the dispersion through the control of permittivity and permeability, which is discussed in the following.

2.3 Metamaterials

The propagation of electromagnetic waves within a medium, as well as its interaction with the material through which it propagates, is mostly dependent on two parameters – the

dielectric permittivity ε, and the magnetic permeability μ of the material. As described in the constitutive relations above, they dictate a materials response induced by electric and magnetic fields. Naturally appearing materials come with different values of permittivity and permeability, thus it is useful to separate materials in classes with different values according to the nature of their response to the driving field. In Figure 2.1, a representative distinction of different classes of material is shown, based on the values of real parts of relative permittivity and permeability.

Most common solid materials in nature are dielectrics, which have a relative permittivity larger than 1. This value reflects on their ability to store electric energy, since they do not conduct electricity and have little or no free charges. On the other hand, negative permittivity values are associated with materials which have free charges, i.e., conductive materials and mediums such as metals and plasmas. Additionally, polar dielectrics have optical phonon vibrations, which provide a negative permittivity region of the dielectric function, i.e., the Reststrahlen band. Furthermore, transparent conductive oxides (TCOs) and doped semiconductors can have negative value permittivities in certain frequency regions as well.

In terms of magnetic properties, most materials have a weak magnetic response with relative permeability $\mu_r \approx 1$. The exceptions are paramagnetic and ferromagnetic materials, which can display various values of $\mu_r > 1$, and diamagnetic materials which can have relative permeability slightly less than 1. However, magnetic materials lose their response in the optical domain of EM spectrum, which significantly limits their use at higher frequencies. Negative permeability values are also absent in natural materials, as magnetic monopole charges do not exist in nature.
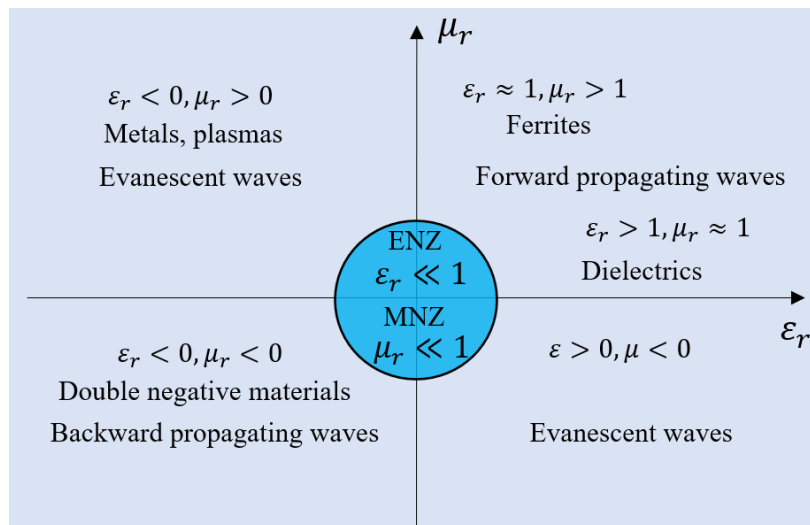
Figure 2.1. Classification of materials according to the relative permittivity and permeability.

The full control of wave dynamics in a medium would require having arbitrary values of ε and μ available in a desired range of frequencies. As discussed above, natural materials cannot provide such flexibility. To go beyond these limitations, there has been a great effort to artificially induce arbitrary electric and magnetic responses to control wave propagation properties. One of the first efforts to induce a desired electric response using artificially engineered materials was done by Winston Kock [11]. Kock introduced the concept of the artificial dielectrics with the aim to realize microwave lenses. Namely, a traditional optics approach would result in very bulky structures due to the long wavelength, however the artificial dielectrics he proposed could reduce this footprint. They consisted of inclusions much smaller than the wavelength, which gave a unique electric and magnetic response of the whole composite. These repeated inclusions, now often referred to as meta-atoms, each provide electric and magnetic moments, which in total give an effective response different than the material of the inclusions itself. In this way, it is possible to induce EM responses otherwise unavailable with ordinary materials. These artificial materials are now commonly referred to as metamaterials, although at the time the concept was not yet fully developed and named.

Arguably, Viktor Veselago posed the question that marks the initial spark of metamaterials research. In his paper from 1969 [12], he presented a thought experiment on the possibility of achieving double-negative behavior and its consequences on wave propagation – although it is worth mentioning the works of D.V. Sivukhin [13] and V.E Pafomov [14] who also researched double negative behavior. Such behavior would exist in materials with simultaneously negative ε and μ, which are also known as left-handed materials since in these materials, the wave-vector, electric and magnetic field vectors obey the left-hand rule, as opposed to right-hand rule present in conventional materials. As a consequence, the wave in such medium travels "backwards", i.e. the phase velocity and group velocity have opposite directions. In his work, Veselago also suggested the possibility of negative refraction at the interface of regular and left-handed materials. This idea remained dormant due to the absence of left-handed materials in nature, until Pendry suggested in 1999 that arbitrary effective permeability can be induced by structuring materials on a subwavelength scale [15]. This led to the ideas of the perfect lens using negative refraction [16], and later the first experimental realizations of negative refraction [17]. In the coming years, many different ideas based on metamaterials came to reality, i.e., cloaking devices [18-20], absorbers [21-23], and directive emitters [24-26], to name a few.

The most famous example of an artificial atom, i.e., unit cell used for metamaterial design is the split-ring resonator (SRR) which induces negative permeability values through a

8
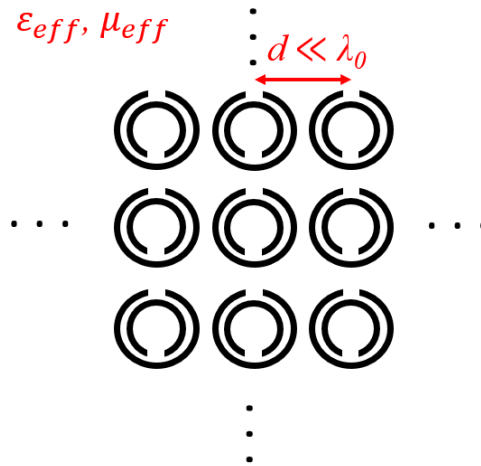
Figure 2.2. Typical metamaterial outline, consisting of metallic subwavelength inclusions (SRRs), whose response can be homogenized using effective medium theory.

magnetic resonance at a desired frequency, Figure 2.2. However, metamaterials are a wide term and there have been many different realizations over the years. In recent years, two-dimensional version of metamaterials – metasurfaces, have been attracting much attention, as they preserve the properties of metamaterials while being much easier to fabricate. Their ability to tailor the phase, amplitude, and polarization of waves at subwavelength thickness makes them advantageous over their 3-dimensional counterpart [27-28]. This area has now evolved into its own direction, and it is termed flat optics [29], aiming to replace traditional, bulky optical devices.

The power of metamaterials lies in providing a response that is not available in natural materials at a desired frequency. As mentioned above, most of the efforts in this area were first dedicated to realizing double-negative response using periodic structures consisting of subwavelength inclusions like the SRR. However, a separate class of metamaterials were investigated for epsilon-near-zero response and mu-near-zero response (MNZ), which will be a large focus point in this thesis. These are mutually called zero-index materials and have been attracting a lot of attention in the last decade [9,30-32], which is described in detail in the following section.

2.4 Epsilon-near-zero materials and consequences on wave propagation

Although the first efforts in metamaterials research were focused on achieving the double-negative behavior due to its exotic effects like negative refraction, there has been a separate effort to explore and realize near-zero index (NZI) metamaterials [30-36]. Since it is defined as $n = \sqrt{\mu_r \varepsilon_r}$, zero-refractive index can be achieved either by ε or μ, or both, going to zero.

However, since most materials found in nature are non-magnetic, achieving ENZ behavior is much more practical than MNZ, thus the former has been a dominant direction of research in the last decade [9]. ENZ studies focus on wave dynamics in materials where the true or effective permittivity of the materials goes to zero. Materials with singular permittivities have demonstrated exceptional capabilities in terms of control of the amplitude, phase and polarization of reflected/transmitted EM waves, however they are still under research and have a great potential for a number of applications.

One of the immediate consequences of permittivity going to zero can be observed by inspecting the source free Maxwell's equations:

$$\nabla \times E = i\omega\mu H \tag{2.10}$$

$$\nabla \times H = -i\omega\varepsilon E = 0 \tag{2.11}$$

This result implies the decoupling of electric and magnetic fields. These equations further lead to $\nabla^2 E = 0$, implying a spatially uniform, DC-like electric field distribution. The phase velocity in such a medium diverges, as it is defined by $v_p = c/\sqrt{\mu_r \varepsilon_r}$. In these conditions, the phenomenon of wavelength stretching happens [30], and phase distribution is near-constant in the ENZ medium. The wavelength in such a medium theoretically goes to infinity as epsilon ideally reaches zero, $\lambda = \lambda_0/\sqrt{\mu_r \varepsilon_r}$.

This feature has many interesting consequences, one of which are impedance-matching states allowing the perfect transmission and tunneling of EM waves. More interestingly, due to the uniform phase distribution, connecting channels with different characteristic impedances using an ENZ medium is possible [31]. This effect of tunneling energy through distorted channels has been termed "supercoupling", as the phase distribution inside the ENZ channels "couples" the phase at the input and output perfectly, regardless of the geometry. As shown in
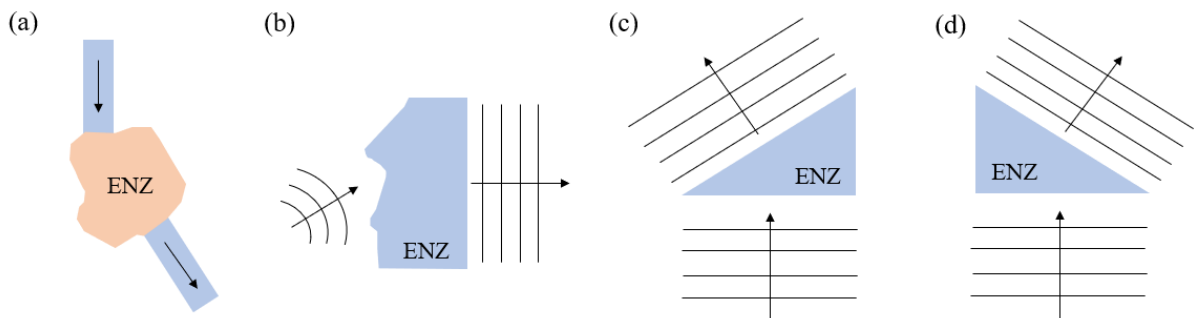
Figure 2.3. Illustration of ENZ effects: (a) tunneling through distorted channels, (b-d) manipulation of wavefronts and direction of propagation.

an example in Figure 2.3 (a), a waveguide turn would usually result in an unwanted reflection but using ENZ as the connecting channel removes the impedance mismatch.

Another interesting aspect of the phase-distribution in an ENZ slab is its wave-front shaping, enabled by geometrically shaping the exit boundary of the slab. This can be used to transform any arbitrary wavefront to a plane-wave, or to direct the transmitted waves in arbitrary directions, which is shown in three illustrative examples in Figure 2.3 (b-d).

Another important consequence for zero permittivity can be understood by analyzing the boundary problem between a dielectric medium and an ENZ medium. Namely, the normal displacement vector is continuous along the boundary with no additional charges, which implies anomalous field enhancement in the ENZ medium:

$$D_{1n} = D_{ENZn} \tag{2.12}$$

$$E_{ENZn} = E_{1n}\frac{\varepsilon_1}{\varepsilon_{ENZ}} \tag{2.13}$$

This fact has been used to enhance light-matter interaction, mostly for boosting the Purcell factor enhancement for emission [35,37], as well as enhancing non-linear effects in such a medium [34,38]. Enhancement of non-linear phenomena in ENZ media has been a particularly intense research area in the past few years due to unique opportunities ENZ phenomenon offers [39], and due to readily available natural ENZ media like indium tin-oxide (ITO) which does not require patterning or additional nanofabrication.

Epsilon near zero behavior can be found in natural materials such as transparent conductive oxides (TCOs) like ITO, Al-doped zinc-oxide (AZO), Ga-doped zinc-oxide (GZO), and polar dielectrics like SiC or AlN [40]. Namely, the commonly used Drude and Drude-Lorentz permittivity models necessarily contain an ENZ region, and any material which can be accurately described with these models will feature a zero-crossing in the permittivity dispersion. Natural materials such as Al also have a transition from optical opaqueness to transparency which marks the ENZ regime.

On the other hand, ENZ behavior can also be induced artificially [9]. One of the first demonstrations of an artificial ENZ response was based on using a rectangular waveguide cavity operating at the cutoff [41] where the effective permittivity of the mode goes to zero, achieving the near-constant phase distribution. Another approach which demonstrated the same effect was based on the use of the wire-medium [42].

A metamaterials approach to achieving ENZ behavior was based on stacking subwavelength layers of interchanging positive and negative permittivity, providing zero effective permittivity [33]. These stackings of positive and negative layers provide not only ENZ response, but the dispersion of the modes in such layer can become hyperbolic, offering interesting waveguiding properties [43]. Namely, hyperbolic metamaterials can offer extreme asymmetry in propagation characteristics, and enhance light matter interaction [44]. Another interesting proposition using photonic crystals was also made, where the Dirac point of photonic crystal serves as an effective zero-index medium [45].

Apart from all the mentioned opportunities, ENZ structures can also provide perfect light-trapping and geometry-independent resonances [46,47]. This feature will be explained more later in the chapter when discussing non-radiating eigenmodes, and it represents a major focus point of the chapters 5, 6 and 7.

2.5 Surface plasmon polaritons and bulk plasmon polaritons

2.5.1. The dielectric function of the free electron gas and plasma frequency

The most common classification of materials in solid state physics is done according to the energy separation between the valence and conduction bands of electrons. According to the nature of the energy gap, materials can be regarded as isolators (large gap), semiconductors (small gap) or metals (overlap of valence and conduction bands) [48]. The free charges in metals can thus freely move and respond to external electric fields acting upon them.

Since the plasmonic response will be thoroughly explored in the thesis, a brief introduction to the electrical response of metals and medias with free electrons is provided. A common way to model the optical properties of metals is to use the free electron gas model, i.e., the model which describes plasmas. To describe the electrical response of a free electron gas to EM excitation, we can start with the equation of motion of charges in a plasma due to external electric field E [49]:

$$m\frac{d^2x}{dt^2} + m\gamma\frac{dx}{dt} = -eE,$$

(2.14)

where x is the position of the charge, m is the electron mass, and γ is damping or collision frequency. By assuming a harmonic time dependence $E(t) = E_0 e^{-j\omega t}$ of the driving field, a particular solution of this equation describing the oscillation of the electron is $x(t) = x_0 e^{-j\omega t}$. The complex amplitude x_0 incorporates any phase shifts between driving field and response via

$$x(t) = \frac{e}{m(\omega^2 + j\gamma\omega)} E(t).$$

(2.15)

The electron displacement is described by the macroscopic polarization $P = -nex$, which gives:

$$P = -\frac{ne^2}{m(\omega^2 + j\gamma\omega)} E.$$

(2.16)

Inserting this in $D = \varepsilon_0 E + P$ further leads to:

$$D = \varepsilon_0 \left(1 - \frac{\omega_p^2}{\omega^2 + j\gamma\omega} \right) E,$$

(2.17)

where $\omega_p^2 = \frac{ne^2}{\varepsilon_0 m}$ is the plasma frequency of the free electron gas. Thus, the dielectric function of the free electron gas reads:

$$\varepsilon(\omega) = 1 - \frac{\omega_p^2}{\omega^2 + j\gamma\omega}.$$

(2.18)

This is known as the Drude model of permittivity. If the damping is negligible, then the lossless Drude dispersion states:

$$\varepsilon(\omega) = 1 - \frac{\omega_p^2}{\omega^2}.$$

(2.19)

The plasma frequency represents the zero-crossing point of the dispersion and the ENZ phenomenon, which is discussed throughout the thesis, is specifically tied to it. In that sense, ENZ effect can be achieved in natural and artificial materials around their plasma frequency.

2.5.2. Bulk plasmon-polaritons

Plasmonic materials support modes in their bulk or the so-called bulk-plasmon-polaritons. These modes are facilitated through the excitation of volume plasmons and are not tied to the surface. Such modes are characterized with low lifetimes and can be coupled directly with free-space radiation. They exist only above plasma frequency, and they represent propagating solutions.

Such modes were first studied in the context of absorption peaks in thin films by Ferrel [50] and Berreman [51] and are thus referred to as Ferrel-Berreman modes. It was found that

excitation of these bulk plasma modes was responsible for previously unexplained absorption peaks appearing in thin film configurations. The fact that this bulk mode is radiative has been used for absorption application, such as near-perfect absorption/thermal emission [52] and polarization switching [53]. These modes will be discussed in detail in Chapters 5 and 6.

2.5.3. Surface plasmon-polaritons

Surface plasmon-polaritons (SPP) are electromagnetic waves that occur at an interface between a dielectric and a conductor due to the coupling of light to collective electron oscillations [49]. A plasmon-polariton represents a quasi-particle, and it propagates as a hybrid surface mode which entails a continuous exchange of energy between photons and electrons oscillating in metals due to the driving EM field of photons.

The electric response of a metal in the visible and infrared fields is dominated by the free-electron plasma. Therefore, electromagnetic waves in a metal are called plasmon-polaritons. When an EM wave is incident upon a metal film it is possible to excite a plasma mode which propagates along the metal/dielectric interface. These hybrid surface modes are characterized by an evanescently decaying field perpendicular to the surface, existing on either side of the interface. By imposing boundary conditions at such an interface, the transverse magnetic wave solutions can provide a real transverse wavenumber, thus leading to the SPP dispersion relation [49]

$$k_x = k_0 \sqrt{\frac{\varepsilon_1 \varepsilon_2}{\varepsilon_1 + \varepsilon_2}}. \tag{2.20}$$

A propagating solution for TE waves does not exist, thus the SPP phenomenon is exclusive to the TM-polarization. This makes sense, as the component of electric field perpendicular to the interface has to exist in order to engage the plasma oscillations and the polariton formation. Illustration of the field profile is shown in Figure 2.4 (a). Since the wavevector component in the z-direction is imaginary, and the wave is evanescently decaying away from the surface, it is not possible to excite them with them freely propagating waves: they instead require prism or grating coupling schemes to excite such modes [49]. Another way to engage SPP modes, as well as to control their dispersion, is through their realization with metamaterials, which is explored in the following section. The dispersions of both BPP and SPP at an interface between dielectric and a metal are shown in Figure 2.4 (b).
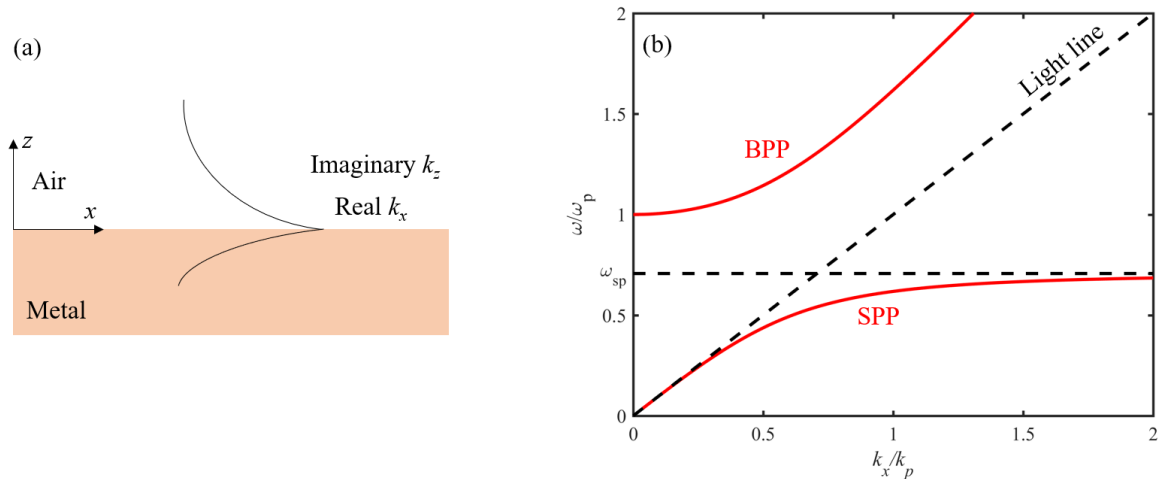
Figure 2.4. (a) Sketch of the SPP field profile at a metal-dielectric interface. (b) SPP and BPP dispersion for the interface.

2.5.4. Surface plasmon-polaritons using metamaterials

Due to the extreme confinement of SPPs to the interface, they have been a subject of research aiming to control propagation and enhance the light-matter interaction at the nanoscale [5,6, 54-56]. However, the specific nature of these modes requires a negative permittivity which is limited mostly to metals, which further implies that the frequency range where such excitations are possible is limited to optical regime. Since their confined character can be useful for many different applications, there has been an effort to use metamaterials to induce a plasmonic response at different frequency ranges. Specifically, terahertz and microwave plasmonics have been a particularly active research area in the past decades [57-71].

Namely, the so-called spoof SPPs, first proposed by Pendry [59], are based on a simple periodically perforated metal, Figure 2.5. By making square hole arrays in metal such that the size and distance between them is much smaller than the operating wavelength, an effective plasma-like response is achieved. Each square hole acts like a waveguide with an exact cutoff frequency depending on the size of the hole. This cutoff frequency acts as an effective plasma frequency, under which the structure supports propagating surface modes. This opens opportunities to transfer the plasmonic physics to different domains in the EM spectrum.

More concretely, this development led to the birth of designer plasmons, taking advantage of the confinement and propagation characteristics of spoof SPPs to realize filters [60-61], slow-light waveguides [62-63], antennas [64-66], absorbers [67-68] and sensors [69-71].

Furthermore, a conceptually different approach has been proposed recently to achieve effective SPP propagation without using negative permittivity materials [72]. This approach is
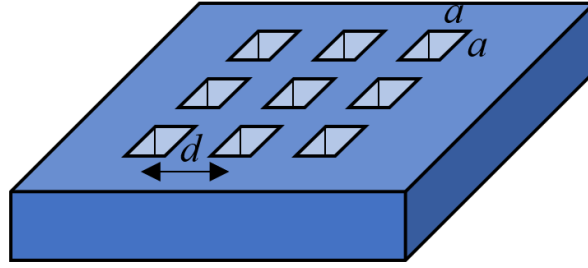
Figure 2.5. Perforated metal proposed by Pendry [52] that has a plasma-like effective permittivity.

based on the structural dispersion in waveguides, where the effective permittivity seen by the waves is controlled by the geometrical attributes of the waveguide, Figure 2.6.

Namely, each mode supported in such a waveguide has a cutoff frequency at which the propagation constant switches from imaginary to real character, enabling propagation of waves above the said cutoff frequency. This behavior can be approximated with an effective permittivity the wave experiences, which is given by the relation [72]:

$$\varepsilon_{eff} = \varepsilon_b - \frac{\lambda_0^2}{4a^2}. \tag{2.21}$$

where ε_b is the permittivity of the waveguide filling material, λ_0 is the cutoff wavelength, and a is the waveguide height, Figure 2.6 (a).
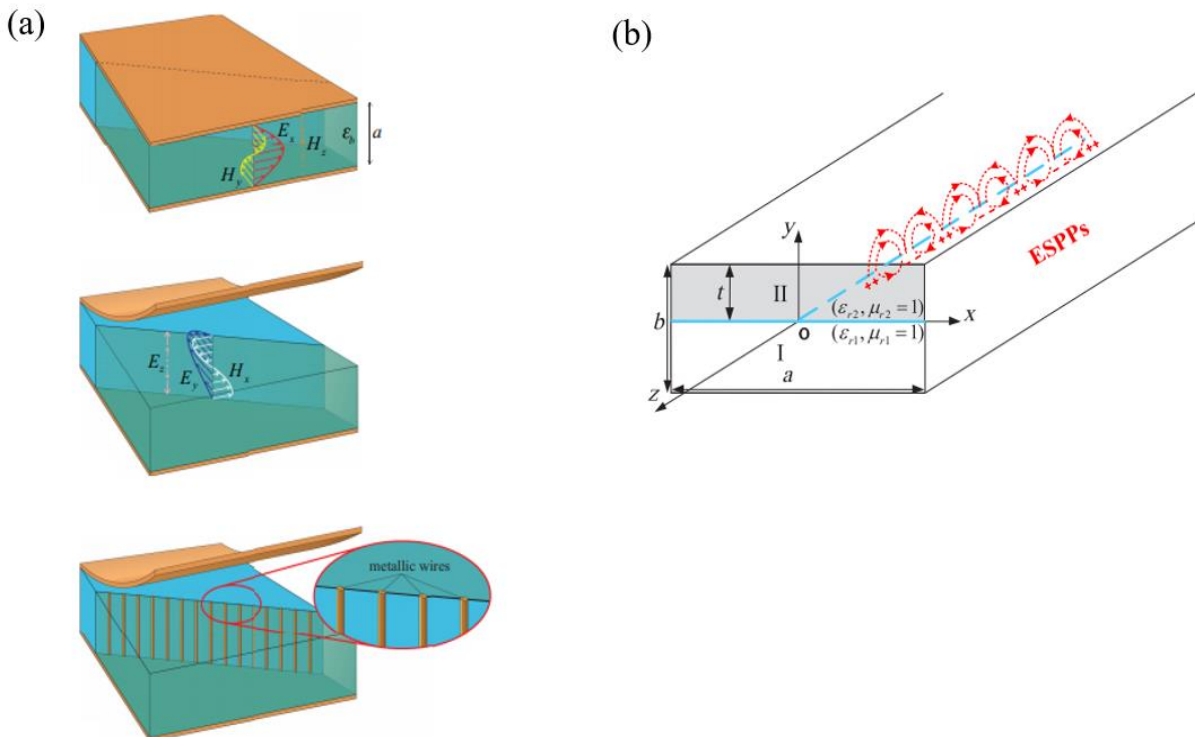
Figure 2.6. (a) Natural SPP-like propagation in coupled PPW [72]. (b) SIW plasmonic modes [73].

This permittivity resembles a lossless Drude dispersion which can take negative, zero, and positive values. By coupling two waveguides with effective permittivities of opposite signs, the condition for formation of SPPs can be satisfied. In addition, a mechanism for coupling of these two separated regions is necessary, and this can be done using metallic wires. The wires provide the proper mode coupling, allowing for excitation of effective SPPs. This concept can be realized in a parallel-plate waveguide (PPW) [72] or substrate integrated waveguide (SIW) [73]. The latter version is the basis of Chapter 3, where we describe in detail the basics of "SIW plasmonics" concept and demonstrate two high-performance microwave components based on it.

2.6 Embedded eigenstates

Resonances play an essential role in wave-based devices, as they represent a ubiquitous wave phenomenon. Assuming $e^{-j\omega t}$ time dependence and no sources, the solution to Maxwells equations with outgoing solutions represent system eigenmodes or resonances [74]. Resonances usually refer to the states excitable by incoming free-space waves, which are characterized by their eigenfrequency (resonant frequency). The common knowledge about resonances states that they are located in the continuum of radiating modes, i.e., above the light line – they can receive energy from the outside and radiate the energy back into the surrounding medium. That means that their eigenfrequency is complex $\omega = \omega_r + j\omega_i$, where the imaginary part of the eigenfrequency is related to resonance lifetime. Resonance lifetime is usually defined through its Q-factor, the quality-factor of the oscillations:

$$Q = -\frac{\omega_r}{2\omega_i}. \tag{2.22}$$

The Q-factor of a resonance is a very important characteristic, as it defines the temporal response to an excitation, and has major consequences on light-matter interaction. High-Q resonances have been a commodity in every region of the EM spectrum, e.g., narrowband filters, lasers, and sensors all benefit from having high-Q resonators as their basis of operation. Thus, demand for extremely high-Q factor resonators is high for devices in modern technology.

Embedded eigenstates (EE), also known as bound states in the continuum (BIC), are a particular sort of resonances. Although they are located in the continuum of radiating states, they are non-radiating. Their lifetime, and consequently their Q-factor, is infinite – waves are perfectly trapped in the resonant structure. This counterintuitive phenomenon was first discussed in quantum mechanics by Wigner and Von Neumann in 1929, who mathematically
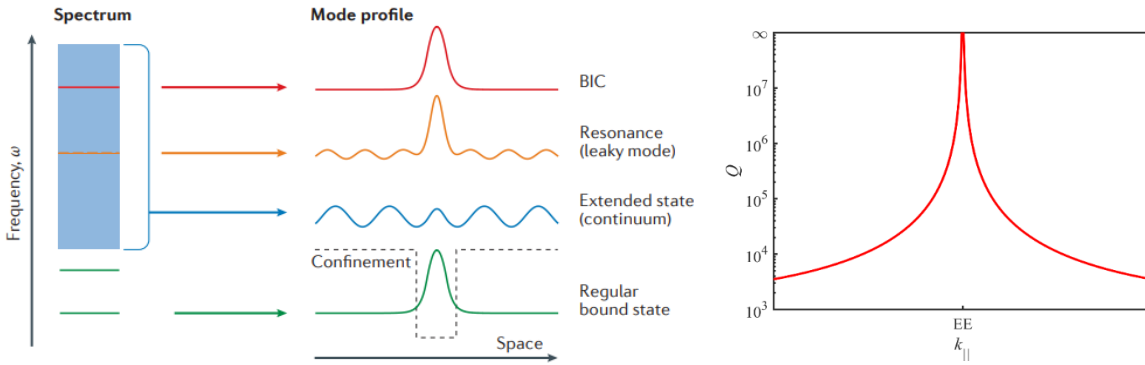
Figure 2.7. Different types of states, with EE (BIC) [77], and the typical Q-factor divergence at a specific transverse wave number.

tailored a potential distribution that "bounded" an electron residing above a potential well, without decaying to the continuum [75]. While this idea was purely theoretical and remained dormant for a good part of the 20th century, it has since resurfaced in different aspects of wave physics. While there were important works appearing by theorists like Friedrich and Wintgen about interacting resonances [76], the true ubiquity of EEs was only realized in the last decade [77-93]. As a pure wave phenomenon, EEs have been explored in different wave systems including mechanics [78], acoustics [79], and electromagnetics [80]. Electromagnetic EEs have become a particularly intense research direction in the last few years, since the maturity of nanofabrication technologies has allowed experimental realizations of such structures in microwave, terahertz, visible, and infrared ranges [81-84].

Trivial EEs can arise due to symmetry-forbidden radiative decay [77], usually appearing at the band edge of a periodic open structure. More recently, nonsymmetry-protected EEs have been engineered based on the Friedrich and Wintgen model, where two or more nonorthogonal modes are strongly coupled and all radiate towards the excitation channel. An EE state arises when the interference of partial waves of the modes becomes purely destructive [77]. An intuitive illustration of the different types of states of EM waves, as well as a typical Q-factor divergence of an EE are shown in Figure 2.7.

2.6.1. Embedded eigenstates in metamaterials and ENZ media

Soon after the discovery of EEs in photonic crystals, there were many efforts to find non-radiating states in different EM systems. For example, they can be realized with dielectric or metallic metasurfaces in cylindrical, cubical, and symmetry-broken structures [85,86]. Although dielectric nanoresonators typically suffer from low Q-factors, the EEs were found to enhance the Q-factors significantly, providing an alternative to the usually superior plasmonic metasurfaces [87].

18
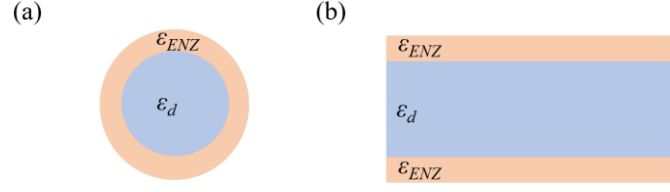
Figure 2.8. ENZ based light-trapping schemes in (a) plasmonic shells and (b) waveguides.

ENZ media on the other hand offer a conceptually different approach to trap light. When permittivity of a medium goes to zero, its intrinsic impedance goes to infinity $Z = Z_0 / \sqrt{\varepsilon} \to \infty$. This means that ENZ effectively acts like a perfect magnetic conductor (PMC) for TM waves [88].

Given that the TM waves experience a perfectly reflecting boundary when impinging on ENZ media, designing a resonant cavity surrounded by ENZ media can lead to perfectly trapped modes, as illustrated in Figure 2.8 (a). The first examples of perfect light-trapping with plasmonic shells were proposed in [88],[89]. Namely, the eigenmodes of the spherical core become perfectly trapped when their resonant frequency coincides with the ENZ condition, forming a non-radiating eigenmode in an open 3D structure, i.e., an EE. The paper [89] provides an analysis of scattering singularities, i.e., scattering coefficient poles and zeros and showed that EE represents the peculiar case when the scattering coefficient simultaneously admits a pole and zero, essentially providing a "0/0" uncertainty. This outlook is a part of a broader picture on scattering anomalies, which can be fully captured by the analysis of the singularities of the scattering matrix eigenvalues [90]. The scattering matrix and its singularities in the complex frequency plane will be explored in more detail in Chapter 4, as this analysis represents a major analytical tool used in this thesis.

Another approach to trap waves in a 2D-waveguiding using ENZ materials was proposed in [91], Figure 2.8 (b). Namely, a dielectric slab covered by ENZ layers from both sides exhibits a non-symmetry protected EE. The embedded eigenstates in planar ENZ multilayers will be the main focus of Chapters 5, 6 and 7.

Following the argument that ENZ media provides PMC response for TM waves, we can conclude that, in general, a singular permittivity response of either zero or infinity can offer light trapping capabilities [77]. This can be understood by noticing that perfect electric conductor (PEC) in fact has negative infinity permittivity, providing a hard wall boundary. In that sense, a lossless Lorentzian resonance in a material's permittivity function can provide

perfect light trapping. This will be explored in detail in Chapter 6, where different reflective systems supporting EEs will be analyzed.

2.6.2. Topological features of embedded eigenstates

An interesting caveat to the EEs discovered in photonic crystals is that they do not disappear upon continuous changing of geometrical parameters, i.e., the perfect destructive interference condition that is the origin of their existence simply moves in the parameter space. It was quickly realized that EE solutions could not be destroyed by simply changing any parameter, and that they can be joined with a conserved quantity – i.e., they represent a topological charge in the wavevector space [92,93].

Topology is a branch of mathematics that deals with conserved quantities [94]. The translation of the concepts of topology to physics led to the discovery of topological insulators [95] - electronic systems which display propagating solutions in a forbidden band, protected against small perturbations. Soon after the success of topological physics in condensed matter systems, the analogies that can be drawn between electron wave functions and EM wave equations lead to the advent of topological electromagnetics or topological photonics [96,97]. Recently, it gained tremendous interest of researchers because realizing EM systems is easier and there are many different ways to induce topological behavior for EM waves [98], leveraging the analogies between EM and condensed matter systems. Furthermore, photons have distinct features comparing to electrons, opening new avenues for topological effects in EM systems [99]. Specifically, scattering anomalies such as EEs have been shown to have a topological nature [92]. Using their topological features, novel phenomena were recently realized – e.g., unidirectional guided resonances [100], enhanced Q-factors due to merging of several charges [101], and polarization control [102-105].

However, EEs in singular permittivity structures have not been analyzed from the topological perspective, which could further boost their potential for thermal emission, polarization control, filtering and sensing applications. This will be the focus of Chapters 6 and 7, where we will extend the notion of topological scattering to planar systems supporting EEs.

2.7 PT-symmetry

One aspect of metamaterials and plasmonics not considered in previous discussion is loss. Namely, it represents a major obstacle in achieving desirable performance in plasmonics and metamaterials [106]. Anomalous dispersion regimes which are interesting for metamaterials design are necessarily accompanied with large losses due to the Kramers-Kronig relations

[107-108]. While intrinsic material loss can be utilized in practical ways, for example to enhance absorption, it mostly stands in the way of unlocking the full potential of EM systems.

The loss in EM structures can be separated in absorption and radiation losses. The concept of EEs described in the previous section deals with minimizing radiation loss – with the careful design of resonant structures it is possible to completely suppress the radiation loss, and in this way minimize the total loss. However, the absorption loss is intrinsic to the materials used, and thus cannot be suppressed. For this reason, there is a good motivation to compensate absorption losses by incorporating materials with gain into the design of EM structures. The use of active materials for loss compensation and performance enhancement has been attracting attention in recent years [109-111], as material science can provide structures displaying optical gain in the form of dye molecules, quantum-wells, and quantum-dots [112], and negative resistance circuits in the microwave regime [113]. This approach has been successfully implemented for loss compensation in nanoparticles, plasmonic waveguides, and metamaterials [114-116]. Furthermore, new functionalities like lasing and signal amplification have also been demonstrated pushing the concept of coherent stimulated emission down to the diffraction limit and beyond [117].

However, beyond using gain only for compensation of loss, there exists peculiar physics in structures that have spatially balanced loss and gain regions, i.e., the structures that conform to PT-symmetry requirements [118].

The idea of PT-symmetry originates from the study of non-Hermitian quantum systems. Namely, in quantum mechanics it has been long thought that eigenspectrum of non-Hermitian (non-conserving) Hamiltonians must be complex, while only the Hermitian (conserving) systems can have real energy eigenspectrum. However, it was shown that a special set of non-Hermitian Hamiltonians that commute with parity-time symmetry operator can also display purely real eigenvalues [119], which marked the start of PT-symmetry physics.

Using the similarities between the Schrodinger equation and the Helmholtz equation, PT-symmetry has been successfully translated to EM systems [120-122]. A particular advantage of EM systems is that obtaining gain and loss in EM environments is easier in practice when compared to quantum systems. Furthermore, open EM systems are inherently non-Hermitian, even without materials loss/gain by virtue of radiative losses, thus they open possibilities for new and interesting results observable in basic scattering experiments. For

example, unidirectional invisibility [123-125], anisotropic transmission resonances [126], and CPA-laser [127-128] have been demonstrated.

An important characteristic for PT-symmetric systems is the exceptional point (EP). EPs represent special points where two or more eigenvalues and corresponding eigenvectors coalesce and become degenerate. The exceptional point marks the transition from PT-symmetric to broken phase regime [122], leading to accentuated splitting of the eigenfrequencies which is especially interesting to sensing technology [129,130].

Although there are many ongoing efforts to use PT-symmetry in different applications, there has not been many studies addressing EEs in PT-symmetric systems. In chapter 7 we will focus on active and PT-symmetric multilayers which in the Hermitian case support EEs, and we will discuss unusual scattering scenario which arise in such structures.

2.8 Conclusion

To conclude, this Chapter provided an overview of EM wave phenomena which are related to the results to be presented in the following chapters of the thesis. Recent advances regarding their physics and applications were discussed, which represent a necessary introduction for the discussion in the rest of the dissertation.

Chapter 3: Surface-plasmon-polaritons using substrate-integrated waveguides[3]

3.1 Introduction

In this chapter we explore in detail the idea of using structural dispersion of SIWs for creating plasmonic response at microwave frequencies. As mentioned briefly in Chapter 2, structural dispersion in substrate-integrated waveguides is a powerful tool for creating a plasmonic environment in the microwave regime. This makes SIW a very promising candidate of leveraging the plasmonic properties for wave-propagation and enhanced light-matter interaction in an integrated circuit, which is readily fabricated in standard printed circuit-board (PCB) or Low-Temperature Co-Fired Ceramic (LTCC) technology. We will provide the theoretical basis of plasmonic modes in SIWs based on which we propose, design, and experimentally validate two dual-band microwave filters and microwave sensor.

3.2 SIW plasmonics

One of the main drawbacks of traditional rectangular waveguides is their bulky structure and inability to be integrated with other planar circuits. On the other hand, integrated planar microwave electronics have revolutionized the communications technology, as antennas, filters, and couplers are indispensable in modern devices. However, certain characteristics of waveguides like power-handling are hard to replicate in a planar device. To address these issues, SIWs have been proposed, as they represent an integrable circuit with propagation characteristics of a waveguide [130].
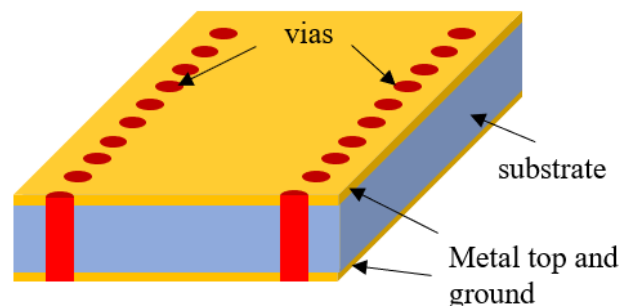
Figure 3.1. Outline of a SIW

SIWs are dielectric filled cavities where bottom and top metals provide the PEC boundary, while arrays of vias connecting the top and bottom boundaries represent side walls, Figure 3.1. The vias that are imitating side walls prohibit the existence of TM modes, and only TE-modes are propagating [131]. The TE-modes are characterized by a cutoff-frequency, and each mode can be characterized by an effective permittivity which is dependent on the geometry of the SIW. This gives rise to structural dispersion – a frequency-dependent effective permittivity the waves experience while propagating in the SIW:

$$\varepsilon_{eff} = \varepsilon_r - \left(\frac{c}{2af}\right)^2 \tag{3.1}$$

where ε_r is the dielectric filling permittivity, c is the speed of light in vacuum, f is the frequency, and a is the SIW width. In Chapter 2 the idea of using structural dispersion of SIWs for plasmonic purposes was briefly introduced. To expand on that idea, here it is shown in more detail how plasmonic environment arises in such a setting.

Figure 3.2 (a) shows a basic building block which enables propagation of effective SPPs. We start by analyzing idealized SIW cavities, treating them as rectangular waveguides allowing TE modes. The structure consists of two SIW cavities stacked on top of each other, with each cavity having its own dielectric filling ε_r and cavity width a. According to the eq.
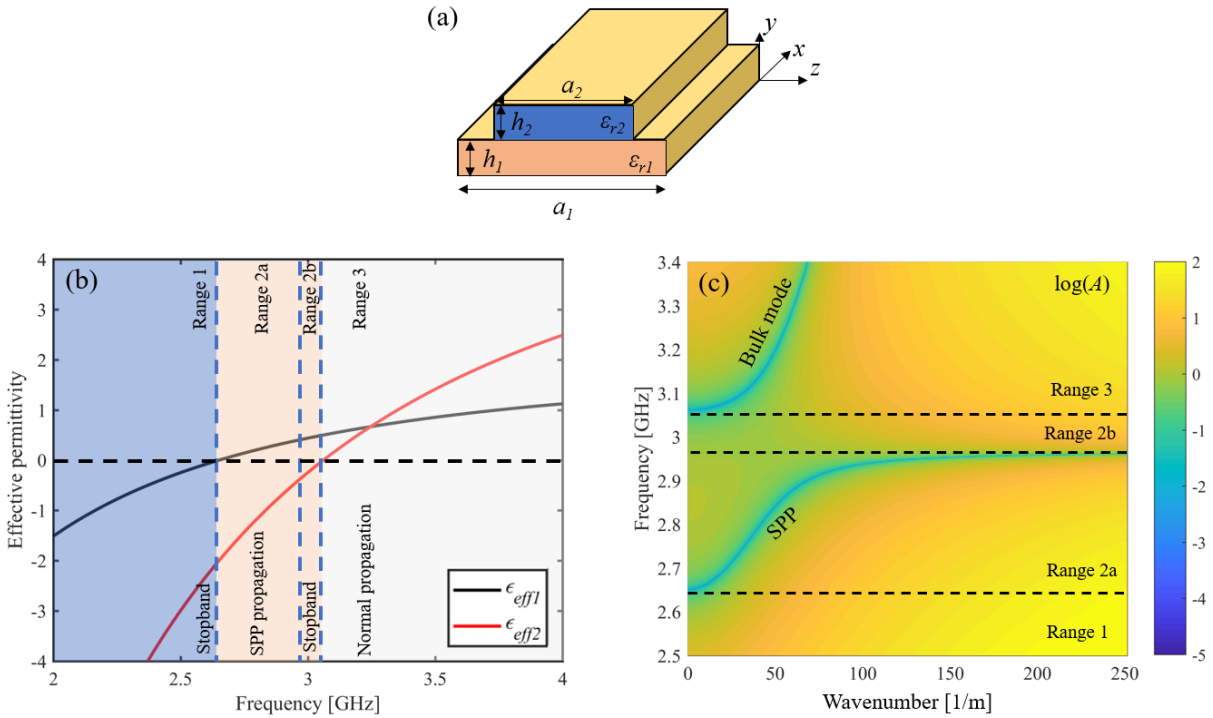
Figure 3.2. SIW plasmonics principles: (a) idealized coupled SIW system. (b) Effective permittivities of each sub-SIW. (c) SPP dispersion relation (rearranged condition from eq. (3.2) such that zero value represents the mode solution).

(3.1), these are the two degrees of freedom with which the effective permittivity of the waveguide mode is controlled, namely ε_r and a, and thus each sub-SIW has its own independent two degrees of freedom.

To better understand the opportunities that such a building block offers, we plot effective permittivities as a function of the frequency. The effective permittivities of TE$_{10}$ modes in each sub-SIW pass through the zero point at different frequencies, thus opening a range where SPP-like propagation can be realized at the boundary between the upper and the lower sub-SIW. It is of interest to separate the frequency spectrum intro three ranges, as shown in Figure 3.2 (b). Namely, range 1 delineates the frequency band where both permittivities have negative values, i.e., both have "metal" behavior. In the second frequency range, the permittivities have opposite signs, basically providing the metal-dielectric interface and allowing for formation of SPPs. Specifically, to obtain a propagating SPP wavevector, the negative effective permittivity is required to have a higher absolute value than the positive effective permittivity [49]. Thus, the second range is further separated into regions 2a and 2b, where SPP propagation is allowed and forbidden, respectively. In the third range both permittivities are positive, enabling normal propagation of transverse modes.

To understand the propagation of SPPs better, we analyze the dispersion relation of the system shown in Figure 3.2 (a) [73]:

$$\frac{k_{y2}}{\varepsilon_{e2}}\tanh(k_{y2}h_2) = -\frac{k_{y1}}{\varepsilon_{e1}}\tanh(k_{y1}h_1), \tag{3.2}$$
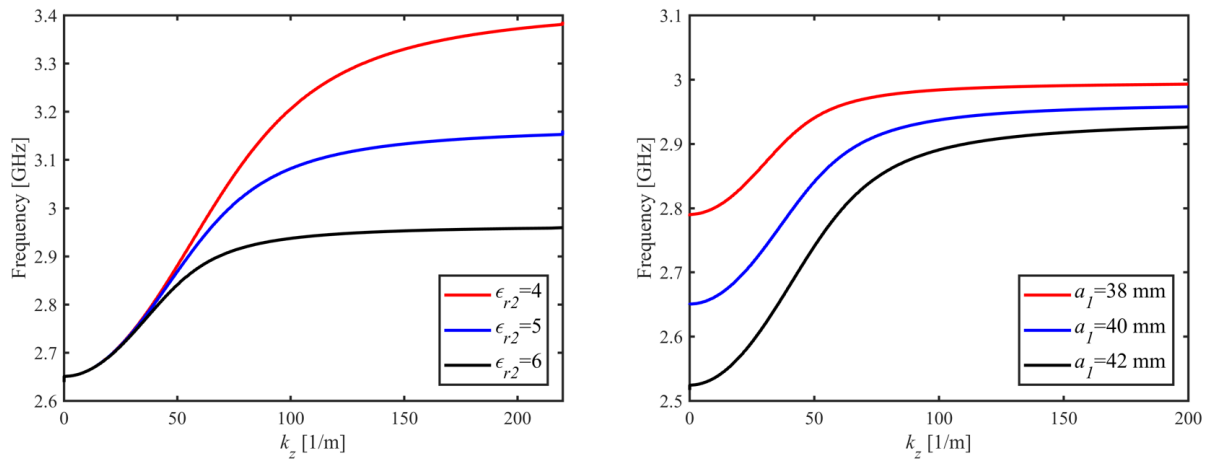
Figure 3.3. Parametric analysis of SPP dispersion: (a) SPP dispersion control with permittivity. (b) SPP dispersion control by SIW width.

$$\varepsilon_{e1} = \varepsilon_{r1} - \left(\frac{c}{2a_1 f}\right)^2,$$ (3.3)

$$\varepsilon_{e2} = \varepsilon_{r2} - \left(\frac{c}{2a_2 f}\right)^2.$$ (3.4)

The remarkable property of the proposed setup is the tunability of the SPP range – namely, using the four degrees of freedom one can arbitrarily position the start and the end of the SPP region, and tune the dispersion characteristics. To demonstrate this feature in an example, we plot the SPP dispersion relation as a function of relative permittivity and SIW width. Figure 3.3(a) shows that permittivity of the top layer controls the stopband position, i.e., we can extend or shrink the SPP range (range 2a) without changing the starting point. On the other hand, changing the width of the bottom layer can shift the starting frequency of the SPP range, with smaller effect on the stopband frequency. By combining these effects and using all four degrees of freedom, the SPP range can be finely tuned, which has a great potential for filtering applications.

This brief analysis shows how a stack of SIWs can act as a plasmonic system with controllable SPP band, and consequently a controllable stopband, which has potential uses in communication and sensor technology. However, we note that in a realistic system, the modes of sub-SIW need to be coupled to support a surface mode. This is done using subwavelength metal wires, which provide proper coupling as well as the free carriers necessary for plasmonic
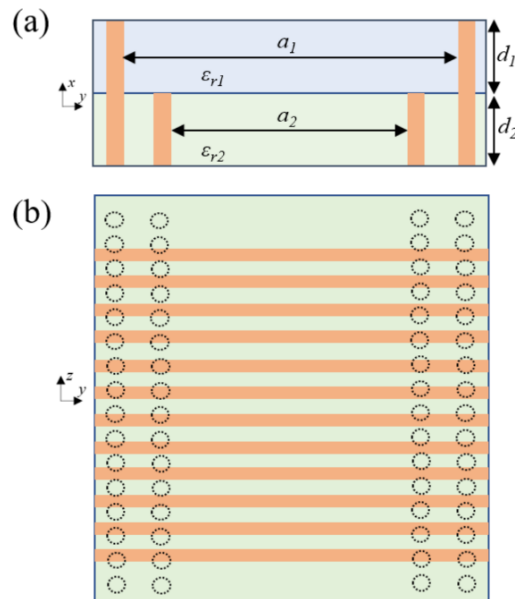
Figure 3.4. Parametric analysis of SPP dispersion (a) SPP dispersion control with permittivity. (b) SPP dispersion control by SIW width.

mode formation [73]. A cross-section of a realistic SIW stack is shown in Figure 3.4, where four rows of vias and cross-connecting wires are shown. This represents the realistic building block for SIW plasmonics, based on which we propose, design, fabricate, and measure two microwave components as described in the following.

3.3 Dual-band Band-Pass filter based on structural dispersion of SIW

It is well-known that the rapid growth of communication systems imposes the requirements for high-performance, low-cost, low-profile components that operate at two or more non-harmonically related frequencies. Taking into consideration those demands and the potential of the introduced concept of SIW plasmonics, here we propose two novel dual-band filters that employ SPP-like phenomenon to achieve operation at two non-harmonically related microwave frequencies. Besides slow-wave behavior and field confinement, SPP-like propagation also provides a transmission zero in spectral response, capable to clearly separate a passband in the spectrum, which is the underlying idea of filtering operation based on SPP-like propagation.

The proposed filters are realized as a microstrip-fed three-layer SIW where each layer represents a sub-SIW structure with intrinsic structural dispersion depending on its geometry and dielectric material. One filter comprises sub-SIW structures of the same width but with different dielectric materials, whilst the other one is comprised of three sub-SIWs which are filled with the same dielectric material but have different widths. Since the layers are designed to have effective permittivities of opposite signs in certain frequency ranges, two distinct SPP-like modes occur at the interfaces between the top and middle sub-SIWs and the middle and bottom sub-SIWs, which ultimately provides two passbands in the filters' response.

The independent choice of geometrical parameters of sub-SIWs and/or the corresponding dielectric materials provide a great freedom to arbitrarily position the passbands in the spectrum, which is a significant advantage of the proposed configurations. At the same time, they meet the requirements for excellent in-band characteristics and selectivity as well as the requirements for low-cost low-profile configuration since they are realized as SIW structures.
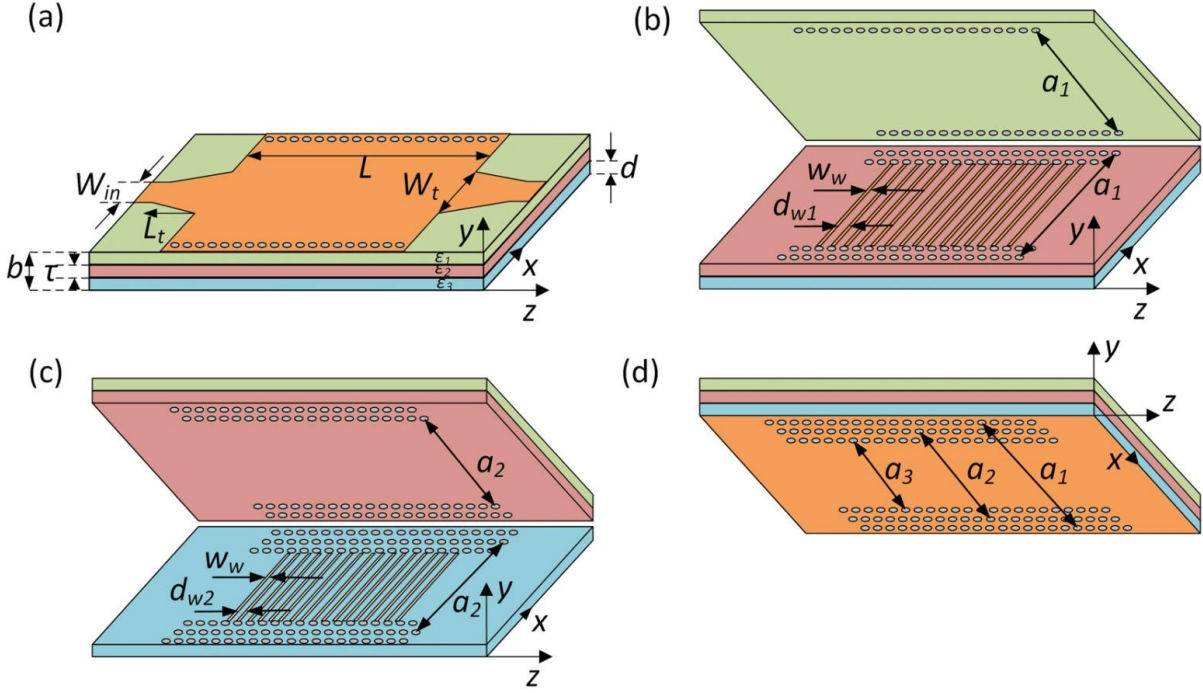
Figure 3.5. The layout of the proposed filters. (a) Overall structure. (b) Interface between the top and the middle sub-SIWs. (c) Interface between the bottom and the middle sub-SIWs. (d) Bottom side of the bottom sub-SIW.

To achieve SPP-like propagation in the proposed configuration, the SIW is divided into three layers, i.e., there are three sub-SIWs in the proposed structure, Figure 3.5. In general case, the three sub-SIWs have different widths a_1, a_2, and a_3 and they are filled with different dielectric materials whose dielectric constants are ε_1, ε_2, and ε_3, respectively. Since effective dielectric constant of a sub-SIW depends on its width and the filling dielectric material, by the proper choice of those parameters we can tailor the frequency ranges in which the three sub-SIWs have desirable sign of the effective dielectric constant.

If we consider that the top sub-SIW has the lowest, and the bottom sub-SIW the highest cut-off frequency, then Figure 3.6 summarizes the four frequency ranges according to the signs of the effective dielectric constants of the dominant TE_{10} mode in the three sub-SIWs. Whilst the first frequency range entirely forbids propagation, and the fourth allows conventional propagation typical for a SIW, the second and the third ranges are of a particular interest for the filters' design. Namely, in the second range the top and the middle sub-SIWs exhibit effective dielectric constants of opposite signs, thus allowing for SPP-like propagation at their interface. By the same token, in the third frequency range SPP-like propagation occur at the interface between the middle and the bottom sub-SIWs.
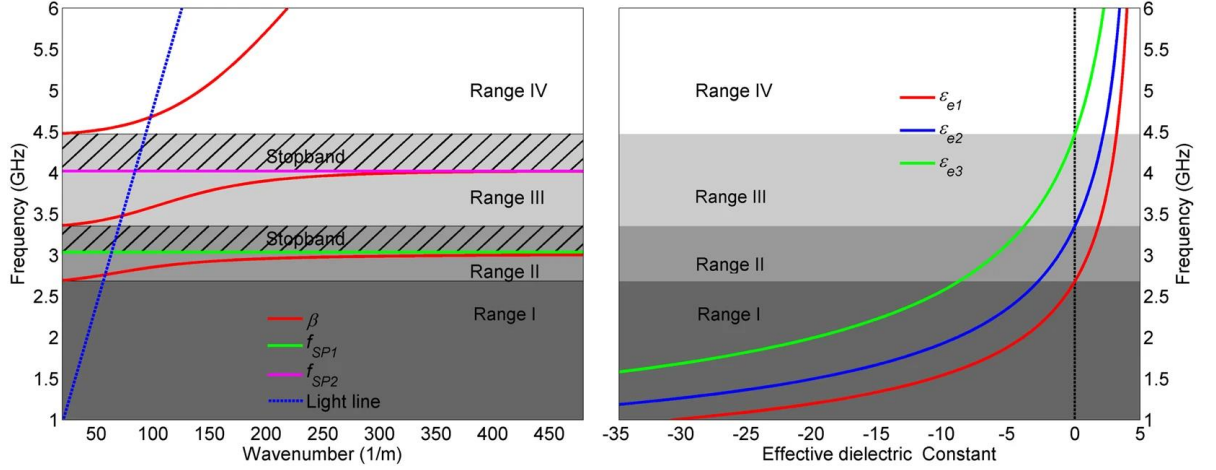
Figure 3.6. Frequency ranges according to the signs of the effective dielectric constants of TE$_{10}$ mode in the three sub-SIWs and the corresponding dispersion curve. The geometrical parameters of the structure are the following: $a_1 = 25$ mm, $a_2 = 20$ mm, $a_3 = 15$ mm, $\varepsilon_1 = \varepsilon_2 = \varepsilon_3 = 5$, $d = \tau = 1$ mm and $b = 3$ mm.

Since the proposed structure can support SPP-like propagation in two different frequency ranges, this opens up possibility to design dual-band filtering operation. To further explain how the passbands are actually formed, the dispersion relation of the structure should be considered. The whole SIW can be considered as a partially filled waveguide. The wavenumber in the three sub-SIWs can be defined as [132,133]:

$$k_{y1} = \sqrt{\beta^2 - k_0^2 \varepsilon_{ei}}, \tag{3.5}$$

where β is the propagation constant in the z direction, k_0 is the wavenumber in vacuum, k_{yi} is the wavenumber in the y direction, ε_{ei} effective dielectric constant, whilst i takes the values 1, 2, and 3, denoting the top, middle, and bottom layer, respectively. The dispersion relation of total structure is given by [134]:

$$\frac{k_{y3}}{\varepsilon_{e3}} \tanh(k_{y3}d) = \frac{k_{y2}}{\varepsilon_{e2}} \coth(k_{y2} \frac{\tau}{2} + \psi), \tag{3.6}$$

$$\frac{k_{y1}}{\varepsilon_{e1}} \tanh(k_{y1}(b-d-\tau)) = \frac{k_{y2}}{\varepsilon_{e2}} \coth(k_{y2} \frac{\tau}{2} - \psi), \tag{3.7}$$

where d, τ, and b are the geometrical parameters of the structure as shown in Figure 3.5 (a), and k_{yi} are the wave-vector components along y direction in each layer. The dispersion curves are shown in Figure 3.6 (a).

29

Similar to the discussion earlier in the chapter, one can distinguish the four frequency ranges– in the first range all sub-SIWs have negative effective permittivity and thus there is no propagation, whilst in the fourth frequency range conventional propagation occurs which is indicated by the propagation constant curve positioned on the right side of the light line. In the second and the third frequency ranges, the dispersion curve displays the same behavior as genuine SPPs, being positioned below the light line and going to infinity at surface-plasmon frequencies f_{SP1} and f_{SP2}. We note the region marked with lines in the second range, in which the effective dielectric constant of the middle layer is still negative, however its absolute value is smaller than that of the top layer, thus it represents a stopband region. The same explanation can be applied to the region marked with lines in the third frequency range.

In other words, once an SPP-like propagation is established at the interface between the top and middle layers, propagation exists in the second frequency range, which is interrupted at f_{SP1} and forbidden in the region marked with lines. Propagation is established again once an SPP-like occurs at the interface between the bottom and middle layers, which is interrupted at f_{SP2} and forbidden in the corresponding region marked with lines. These transmission zeros together with the described stopband regions are capable to clearly separate passbands in the spectrum, and this is the main principle of the filters' design.

3.3.1. Filter design

To demonstrate the potential of the SPP-like propagation and the three-layer SIW structure for dual-band filtering operation, two dual-band filters have been designed. Since the sub-SIWs' width and dielectric constants are mechanisms for independent control of the passbands, theoretically there are six degrees of freedom in filter design. However, it should be noted that the top sub-SIW should have the lowest cut-off frequency and the bottom one the highest cut-off frequency or vice versa, to achieve dual-band operation. Otherwise, the two SPP-like propagation would overlap and only one passband would be formed. Also, to further simplify the procedure and simultaneously keep the design freedom it is judicious to use either the same width or the same dielectric constant for the three sub-SIWs.

Therefore, the first filter comprises three sub-SIWs of the same width filled with different dielectric materials. The dielectric constant of the middle layer and its width have been chosen to position its cut-off frequency in the range 2.7–3.2 GHz to be able to position the passbands around 2.4 and 3.5 GHz. We note that these frequencies correspond to the IEEE standards, but in general they are arbitrarily chosen. Afterwards, the dielectric constants of the top and bottom sub-SIWs have been chosen to obtain the passbands at the desired frequencies.

Since the three layers have different dielectric materials, they are realized using the following dielectric substrates: Rogers TMM10i with relative permittivity $\varepsilon_{r1} = 9.8$, dielectric loss $\tan\delta_1 = 0.002$, and thickness $t_1 = b\text{-}d\text{-}\tau = 1.27$ mm, Neltec NH9450 with relative permittivity $\varepsilon_{r2} = 4.5$, dielectric loss $\tan\delta_2 = 0.0027$, and thickness $\tau = 0.768$ mm, and Rogers RT5880 with relative permittivity $\varepsilon_r = 2.2$, dielectric loss $\tan\delta = 0.0009$, and thickness $d = 0.51$ mm. Also, it should be noted that using of the commercially available substrates somewhat limit the range of the available dielectric constants, and consequently the design freedom. However, this does not affect the overall idea and this limitation can be overcome by variation of the widths.

After the three sub-SIWs are designed based on theoretical analysis, numerical simulations are used to finely tune the structure's response. Although the theory can very precisely determine the positions and bandwidths of the passbands, the filter needs to be numerically optimized since the theoretical model cannot predict minute mutual couplings between the layers that affect the filter response. Also, good impedance matching in the whole range of interest is very important for filter performance and thus the microstrip-to-SIW transition has to be optimized.

We note here that the sub-SIWs are mutually coupled through arrays of wires as indicated in Figure 3.5 and explained earlier in the chapter.

The final geometrical parameters of the filter are the following: $a = 22$ mm, $L = 40$ mm, $L_T = 12.5$ mm, $W_{in} = 4.5$ mm, $W_t = 5$ mm, $w_w = 0.2$ mm, $d_{w1} = 1$ mm, $n_{w1} = 33$, $d_{w2} = 0.4$ mm, $n_{w2} = 65$, $d_{via} = 0.8$ mm, $p_{via} = 1.1$ mm, where d via represents the diameter of the via, p_{via} the spacing between the vias, whilst n_{w1} and n_{w2} represent the number of wires at the interface between neighboring materials.

Figure 3.7 (a) shows the response of the filter. The central frequencies of the two passbands are positioned at 2.4 and 3.5 GHz, and their 3-dB bandwidths are 10.3% and 15.8%, respectively. The insertion losses are 1.1 and 1.2 dB, whereas the return losses are below 13 and 11 dB, respectively. The passbands are characterized by the excellent selectivity which is primarily due to transmission zeros that occur at surface-plasmon frequencies. Analytically and numerically obtained dispersion diagrams of the structure are compared in Figure 3.7 (b). The analytically obtained dispersion diagram confirms the validity of the theoretical model since the passbands, stopbands, and transmission zeros in the response excellently agree with the model. This is further supported by the numerically obtained dispersion diagram, which shows a very good agreement with the theoretical one.
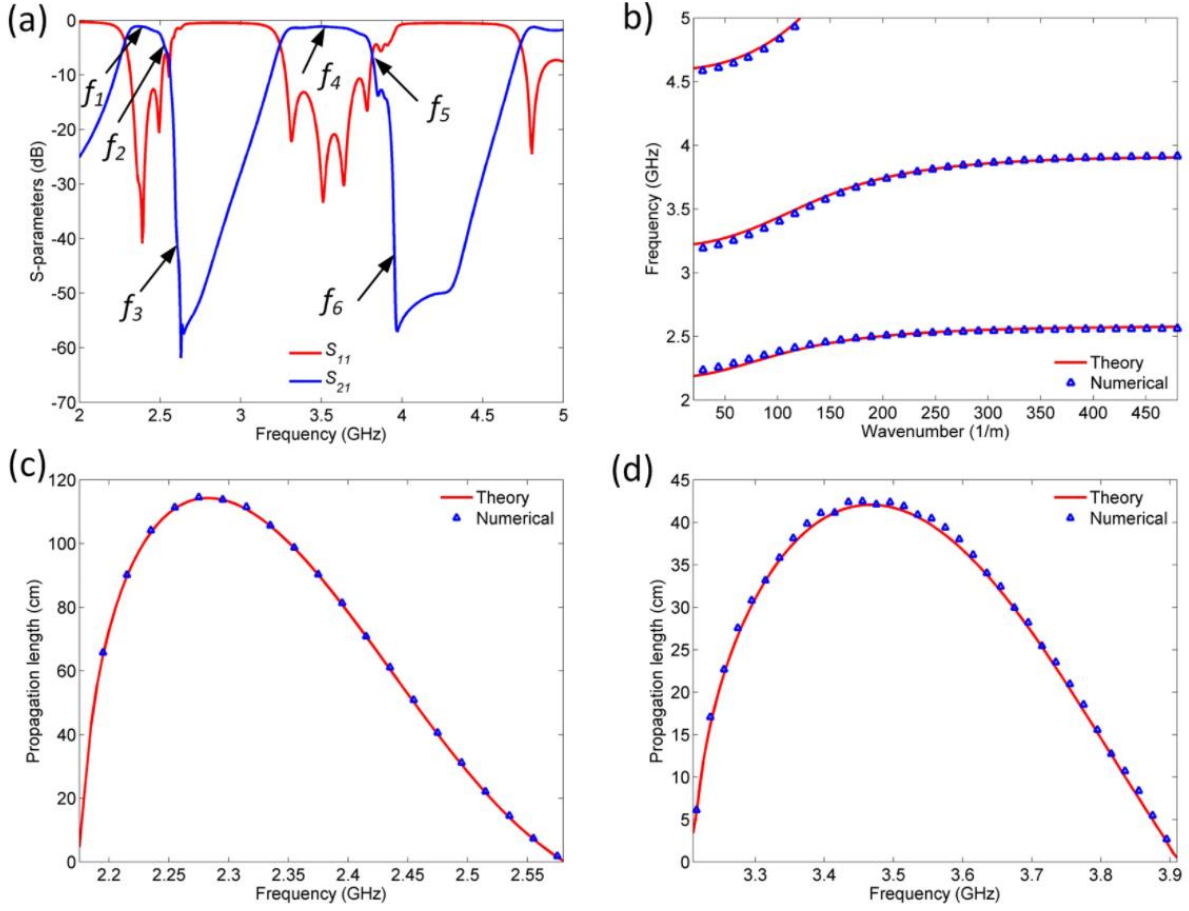
Figure 3.7. (a) Simulation response of first proposed filter. (b) Analytically and numerically obtained dispersion relations of the first proposed filter. (c) Analytically and numerically calculated propagation length of the first SPP-like mode. (d) Analytically and numerically calculated propagation length of the second SPP-like mode.

In addition, Figure 3.7 shows the analytically and numerically obtained propagation length of the SPP-like modes around the central frequencies of the two passbands, both of which have been calculated using the expression [134]:

$$L = Q \frac{v_g}{\text{Re}(\omega)} = \frac{1}{2\,\text{Im}(\beta)} \,. \tag{3.8}$$

The parameter v_g is the group velocity obtained as derivative of the dispersion relation, ω is the complex eigenfrequency, β propagation constant, and Q is the quality factor of SPP-like mode calculated as $Q = Re(\omega)/2Im(\omega)$. Theoretical and numerical results show an excellent agreement. Also, both SPP-like modes exhibit relatively long propagation lengths, with the greatest values equal to 117.1 and 43.2 cm, respectively.
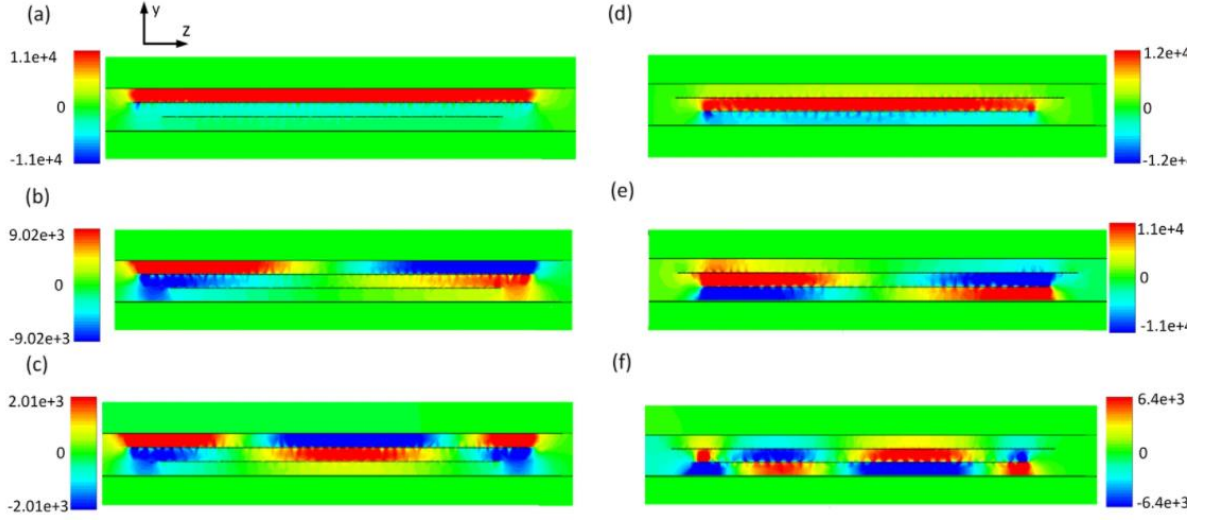
Figure 3.8. Electric field distribution in second proposed filter at y-z cross section along the line of symmetry at: (a) f_1. (b) f_2. (c) f_3. (d) f_4. (e) f_5. (f) f_6. The unit of the shown electric field is V/m.

The SPP-like behavior is also confirmed in Figure 3.8 that shows the electric field distribution at the interfaces at the frequencies denoted in Figure 3.7 (a). Whilst E-field distribution at f_1 and f_4 is very similar to that of the conventional SIW, at f_2, f_3, f_5, and f_6 the wavelength is significantly smaller implying increase of β and its approaching to the infinity. At f_1 and f_4 the absolute values of dielectric constants in the corresponding layers are still sufficiently different, whilst at f_2 and f_5, and particularly at f_3 and f_6 they have practically the same absolute values causing β to abruptly increase.

The second filter that we propose comprises three sub-SIWs with different widths and same dielectric constants. To that end, the dielectric substrate Neltec NH9450 with relative permittivity $\varepsilon_{r2} = 4.5$, dielectric loss $\tan\delta_2 = 0.0027$, and thickness $\tau = 0.768$ mm, has been used. The widths a_1, a_2, and a_3 have been determined to achieve the passbands around the frequencies 4.7 and 5.5 GHz. Following the analytical model, numerical simulations have been performed to optimize the filter response in terms of impedance matching and suppressing non-desirable coupling. To that end, the microstrip-to-SIW transmission has been optimized and strips between the arrays of vias in different layers added. As in the previous case, the sub-SIWs are mutually coupled through the array of wires to achieve the SPP-like propagation. The final geometrical parameters of the filter are the following: $a_1 = 16$ mm, $a_2 = 13.8$ mm, $a_3 = 12.4$ mm, $L = 25$ mm, $L_T = 5$ mm, $W_{in} = 4.5$ mm, $W_t = 9$ mm, $w_w = 0.25$ mm, $d_{w1} = 0.25$ mm, $n_{w1} = 45$, $d_{w2} = 0.375$ mm, $n_{w2} = 30$, $d_{via} = 0.5$ mm, $p_{via} = 0.8$ mm.
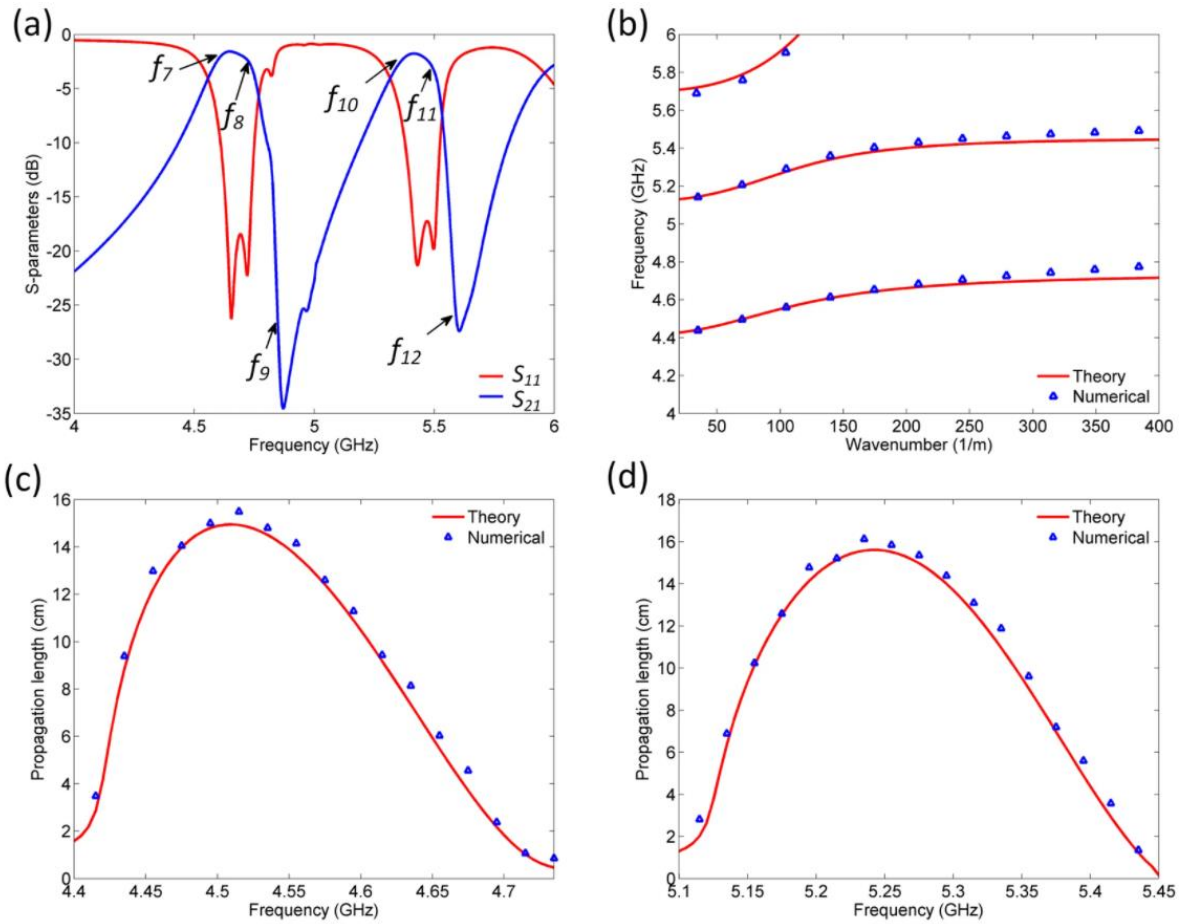
Figure 3.9. (a) Simulation response of second proposed filter. (b) Analytically and numerically obtained dispersion relations of the second proposed filter. (c) Analytically and numerically calculated propagation length of the first SPP-like mode. (d) Analytically and numerically calculated propagation length of the second SPP-like mode.

Figure 3.9 shows the response of the filter together with the analytically and numerically obtained dispersion diagram of the structure and propagation lengths of the SPP-like modes. The central frequencies of the two passbands are positioned at 4.7 and 5.5 GHz, and the 3-dB bandwidths are 4.5% and 4.1%, respectively. The insertion losses are equal to 1.58 and 1.77 dB, whereas the return losses are below 18 and 17 dB, respectively. The passbands are also characterized by the excellent selectivity. The analytical dispersion diagram confirms the validity of the theoretical model, which is further confirmed by the numerical dispersion diagram. Besides an excellent agreement between the analytically and numerically obtained propagation lengths, one can note that the propagation lengths of SPP-like modes are somewhat shorter than those in the previous filter, which is due to the higher dielectric losses in the second filter. Figure 3.10 shows the electric field distribution at the interfaces at the frequencies denoted in Figure 3.9, which clearly confirms SPP-like behavior of the proposed structure.
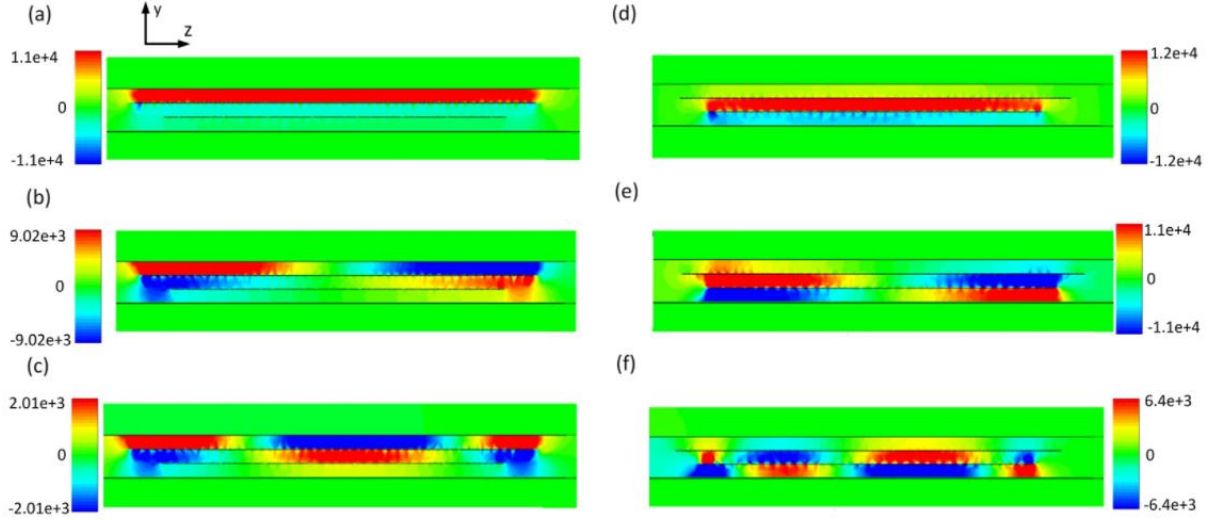
Figure 3.10. Electric field distribution in second proposed filter at y-z cross section along the line of symmetry at: (a) f_7. (b) f_8. (c) f_9. (d) f_{10}. (e) f_{11}. (f) f_{12}. The unit of the shown electric field is V/m.

3.3.2. Fabrication and measurement results

To validate the designed filters, they have been fabricated using standard printed circuit board (PCB) technology. For the first filter, the three layers have been realized using the commercially available substrates Rogers TMM10i with relative permittivity $\varepsilon_{r1} = 9.8$, dielectric loss $tan\delta_1 = 0.002$, and thickness $t_1 = b - d - \tau = 1.27$ mm, Neltec NH9450 with relative permittivity $\varepsilon_{r2} = 4.5$, dielectric loss $tan\delta_2 = 0.0027$, and thickness $\tau = 0.762$ mm, and Rogers RT5880 with relative permittivity $\varepsilon_{r3} = 2.2$, dielectric loss $tan\delta_3 = 0.0009$, and thickness $b = 0.51$ mm. Metallic parts of each layer were etched according to the design and the three layers have been assembled using six nylon screws. In the final step, SMA connectors have been mounted on the structure.

The second filter has been fabricated using the same technology. Three layers of the substrate Neltec NH9450 with relative permittivity $\varepsilon_{r2} = 4.5$, dielectric loss $tan\delta_2 = 0.0027$ have been used to realize the filter. Metallic parts of each layer were etched according to the design and the three layers have been assembled using four nylon screws. In the final step, SMA connectors have been mounted on the structure. Photographs of the fabricated circuits are shown in Figure 3.11. The three layers of each filter are fabricated separately and afterwards assembled into the final structure using screws, which causes small air gaps between the layers. Since SPP-like propagation is confined to the interface between the layers, it is very sensitive to the existence of small disturbances around the interface. Therefore, the air gaps, although very thin, can influence the spectral positions of the passbands. Although their thickness cannot be precisely determined, the air gaps have been approximated by the thickness of the copper layer, i.e. 0.035 mm, which might be taken as the limit by which the layers can be screwed. In
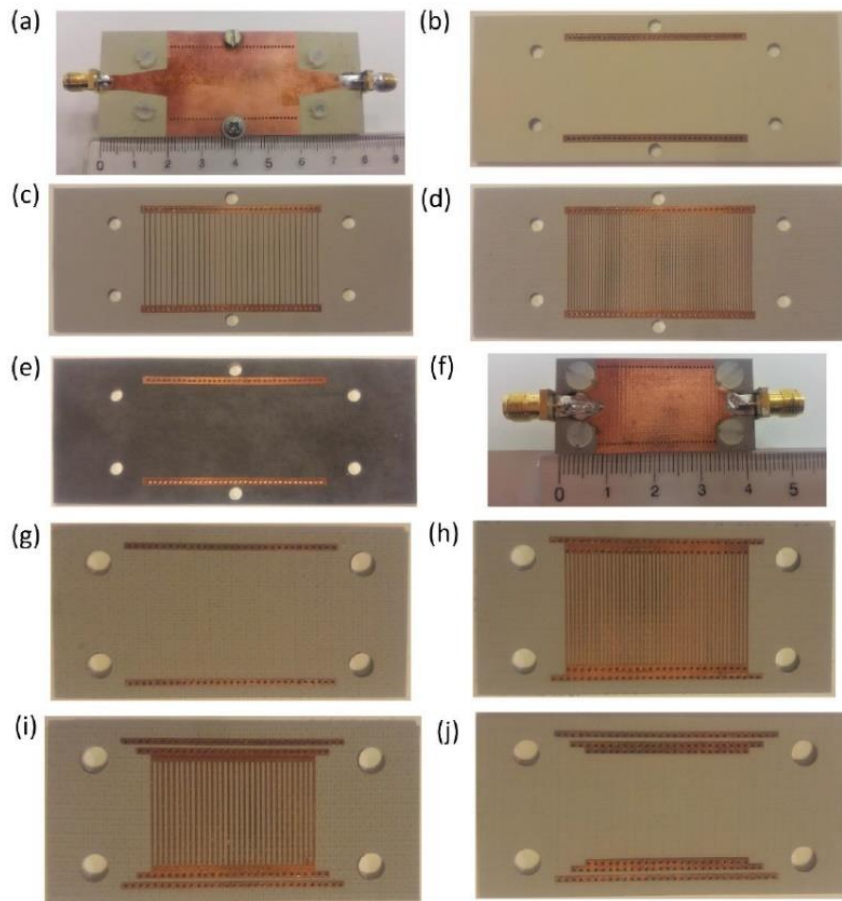
Figure 3.11. Fabricated filters. (a) First proposed filter - top side of the top sub-SIW. (b) First proposed filter - bottom side of the top sub-SIW. (c) First proposed filter - top side of the middle sub-SIW. (d) First proposed filter - bottom side of the middle sub-SIW. (e) First proposed filter - top side of the bottom sub-SIW. (f) First proposed filter – overall structure. (g) Second proposed filter - top side of the top sub-SIW. (h) Second proposed filter - bottom side of the top sub-SIW. (i) Second proposed filter - top side of the middle sub-SIW. (j) Second proposed filter - bottom side of the middle sub-SIW. (k) Second proposed filter - top side of the bottom sub-SIW. (l) Second proposed filter – overall structure.

accordance with the previous approximation, Figure 3.12 shows the simulation results that correspond to the designed structures in which the air gaps between the layers are taken into account.

If these simulation results are compared to those in Figures 3.7 and 3.9, the same trend of the curves can be noted, except for the spectral shifts of around 0.2 GHz. The comparison of the measurement and simulation results in Figure 3.12 reveals a good agreement except for slight differences in the bandwidths which can be attributed to the tolerance of the manufacturers related to the dielectric constant, as well as to a slight misalignment of the via arrays in fabrication process. The first filter exhibit two passbands at 2.65 and 3.75 GHz, with insertion loss of 1.47 and 1.69 dB, and the 3-dB bandwidths of 8.7% and 13.3%, respectively. The central frequencies of the second filter are 4.8 and 5.7 GHz, their insertion losses 2.22 and

(a)   (b)
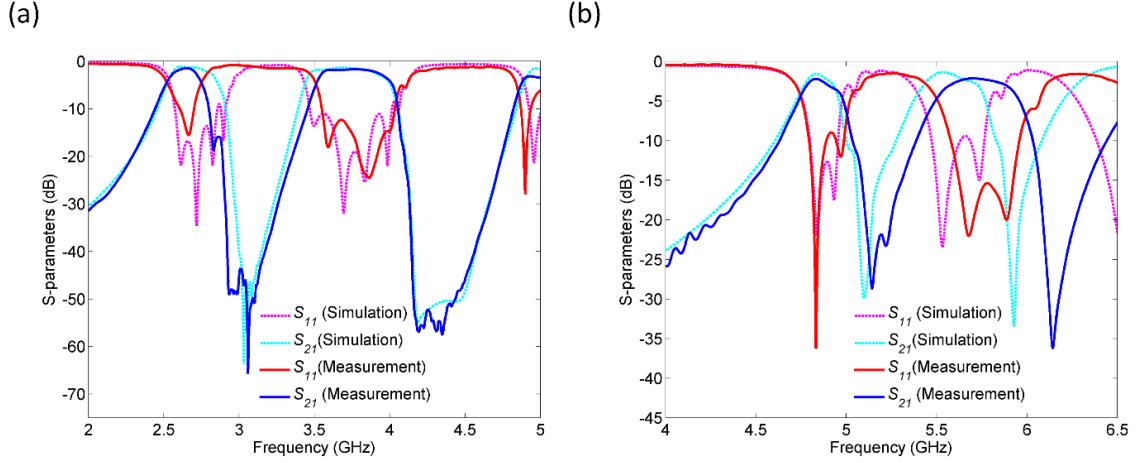
Figure 3.12. Comparison of the measurement and simulation results: (a) First proposed filter. (b) Second proposed filter.

2.17 dB, and the 3-dB bandwidths 5.2% and 8.2%, respectively. Both filters are characterized by good in-band and out-of-band performance as well as by excellent selectivity owing to the transmission zeros. The difference in the insertion losses between the first and the second filter can be attributed to the fact that the first filter comprises three different substrates whose dielectric losses are $\tan\delta_1 = 0.002$, $\tan\delta_2 = 0.0027$, and $\tan\delta_3 = 0.0009$, respectively, whilst in the second proposed filter only the substrate with $\tan\delta_2 = 0.0027$ has been used. Therefore, the losses in dielectric are more pronounced in the second proposed filter, which results in higher insertion losses.

The proposed filters are first dual-band filters based on the SIW plasmonics concept, and they are characterized by good overall performance and possibility for independent control of the passbands in terms of position and bandwidth. Moreover, they meet requirements for low-cost and low-profile configuration since they are realized as SIW structures. As such, they can be considered as very promising candidates for dual-band filtering operation at microwave frequencies.

3.4 Microwave sensor based on half-mode SIW plasmonics

In the last years, microwave sensors have attracted a considerable attention since they can provide non-invasive, label-free, as well as real-time detection due to their instant response to the change in the sensed analyte. Moreover, microwave circuitry can be readily fabricated in printed-circuit board (PCB) technology and easily integrated, which make them favourable when it comes to requirements for compactness and cost-effective fabrication. Thus, microwave sensors have been utilized in various applications including dielectric constant sensing [135-145], food quality control [146-147], gas sensing [148-150], glucose detection

[151-152], microwave imaging [153], and concentration measurements of liquid solutions [154]. Nevertheless, microwave sensors very often suffer from low resolution and sensitivity, e.g. even a significant change in the real part of the dielectric constant normally causes a very small relative resonant shift or *S*-parameter magnitude change. Such drawback limits the applicability of microwave sensors. As previously described, SPPs enable enhanced light-matter interaction at the subwavelength scale and are a great candidate for sensing devices due to their excellent sensitivity [155-158], thus applying the previously described concept of SIW plasmonics could enable high-performance microwave sensors.

In that sense, a microwave sensor based on half-mode substrate integrated waveguide (HM SIW) for very sensitive dielectric constant detection is proposed. The HM SIW is comprised of two parts filled with a dielectric substrate material, where the bottom part also features a reservoir that hosts the sensed liquid analyte. The two parts are coupled through an array of wires, enabling SPP-like propagation at their interface, as explained earlier in the chapter. This setup provides a sharp transmission zero in HM SIW response, which is very sensitive to small changes of the real part of the dielectric constant of the analyte.

3.4.1. Theoretical and numerical analysis

The layout and the corresponding geometrical parameters of the proposed sensor are shown in Figure 3.13. The core element of the sensor is a half-mode substrate integrated waveguide. The HM SIW is fed by the microstrip lines, and the proposed structure has been analyzed using Rogers TMM6 substrate with relative permittivity $\varepsilon_r = 6$, and dielectric loss $\tan\delta = 0.0023$. HM SIW practically has the same performance as substrate integrated waveguide (SIW), however with a half reduction in size compared to SIW. Its dominant propagating mode is TE$_{0.5,0}$ half mode whose effective dielectric constant can be defined as:

$$\varepsilon_e = \varepsilon_r - \left(\frac{c}{2af}\right)^2, \qquad (3.9)$$

where *f* is frequency, *a* is the width of the HM SIW, *c* is the speed of light, and ε_r dielectric constant of the material that fills the HM SIW. Below the cut-off frequency defined as $f_{cTE0.5,0} = c/(4a\sqrt{\varepsilon_r})$, the real part of the effective dielectric constant is negative, which means that the wave propagation is not allowed. In the frequency range above the cut-off frequency, the real part of the effective dielectric constant is positive allowing the signal to propagate in HM SIW.
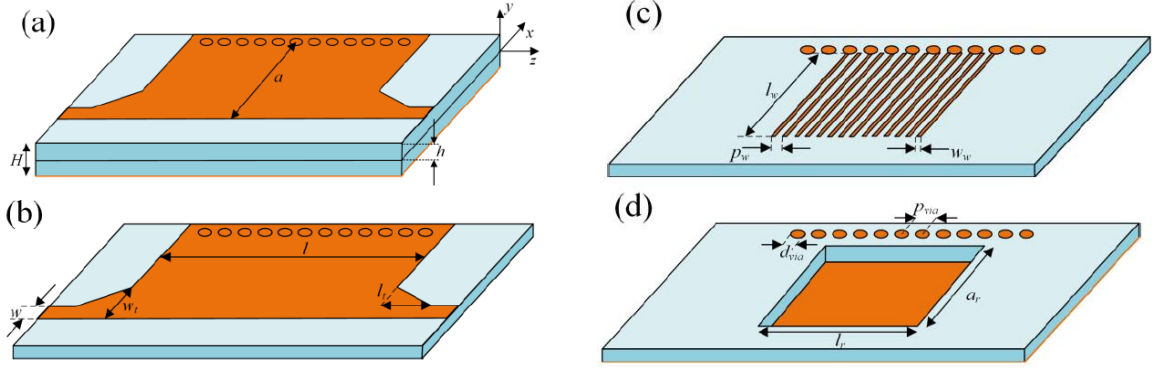
Figure 3.13. The layout of the proposed sensor: (a) overall structure, (b) top side of the top part, (c) bottom side of the top part, and (d) bottom part.

To achieve SPP-like propagation and exploit it for sensing, the proposed HM SIW is divided into top and bottom parts as shown in Figure 3.13 (b-d). Both parts are filled with the dielectric substrate material, whilst in the bottom part, a portion of dielectric substrate has been removed to realize a reservoir that hosts a liquid analyte. Following the theory presented earlier in the chapter, SPP-like propagation can be formed at the interface of the liquid analyte and the substrate.

To illustrate the idea of the dielectric constant detection, Figure 3.14 shows HM SIW transmission response for different materials in the reservoir, whose real part of the dielectric constant ranges from 2.4 to 3.8. To imitate a real scenario, the materials were assigned with losses in accordance with the experiments to be presented in the following section, and their imaginary parts of the dielectric constant ranged from 0.1 to 0.5. The responses have been obtained using finite element method in CST solver, and the geometrical parameters are chosen to provide the response of interest in the range from 2 to 3 GHz: $a = 15$ mm, $a_r = 12.1$ mm, $l = 40$ mm, $l_r = 20$ mm, $H = 1.27$ mm, $h = 0.635$ mm, $w = 1.9$ mm, $w_t = 5$ mm, $l_t = 30$ mm, $l_w = 12.7$ mm, $w_w = 0.1$ mm, $p_w = 0.5$ mm, $d_{via} = 0.8$ mm, $p_{via} = 1.1$ mm. Also, the width of the microstrip lines that feed HM SIW have been optimized to achieve good impedance matching and low-loss response. The range of the real part of the dielectric constants has been chosen in accordance with the eq. (3.1) and the dielectric constant of the substrate, to allow for SPP to propagate and to demonstrate the potential for small dielectric constant change detection.

One can notice that a cut-off frequency of the overall structure is the same for all responses – 2.2 GHz. However, the responses differ in the position of the sharp transmission zero. Namely, when β goes to the infinity, propagation is not allowed and a sharp transmission zero occurs in HM SIW response, which depends on εr2 as explained in Figure 3.3. Also, the depths of the transmission zeros differ due to different dielectric losses in the material.
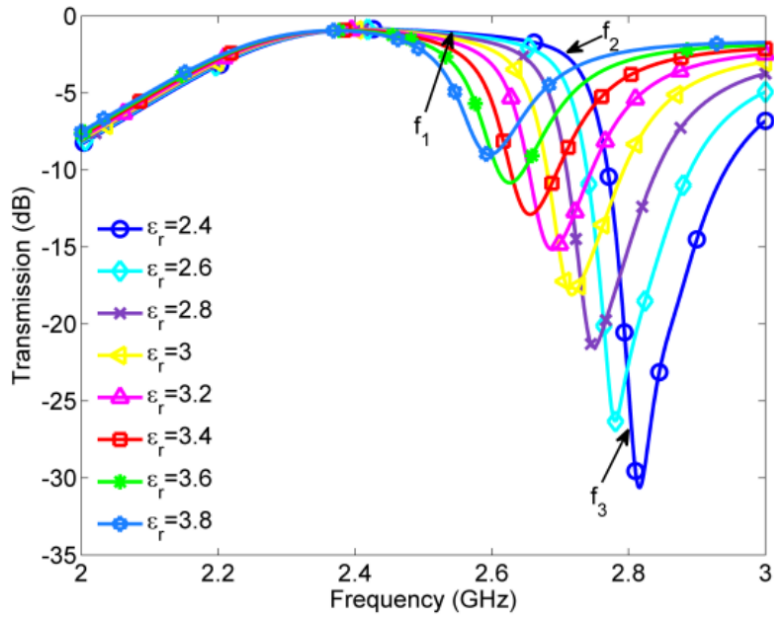
Figure 3.14. Simulated HM SIW transmission response for different materials in the reservoir.
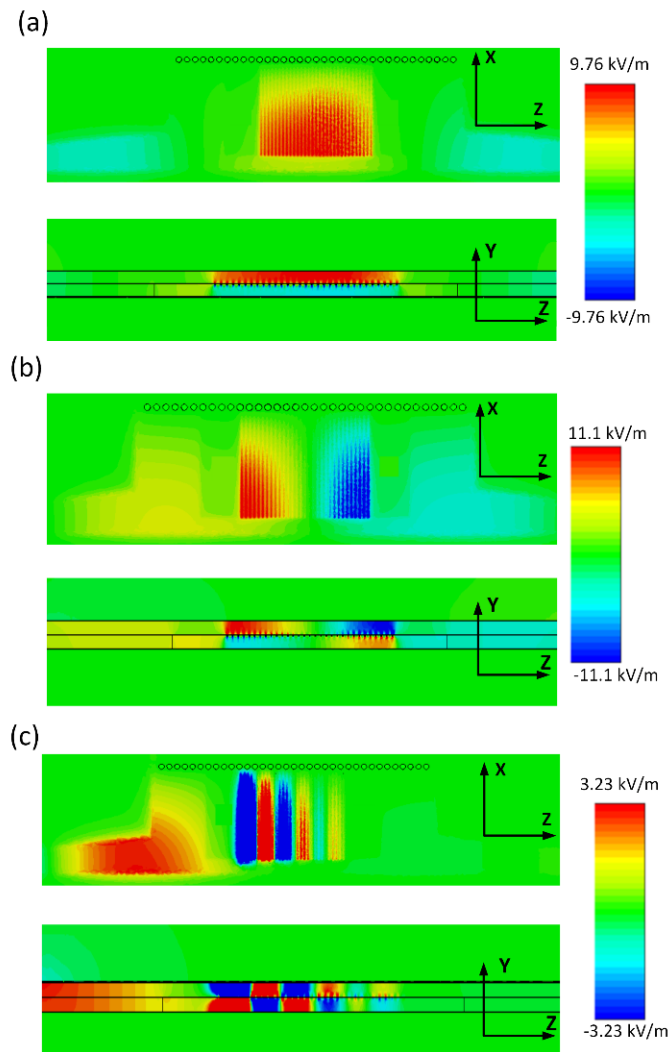
Figure 3.15. Electric field distribution at the interface at (a) f_1, (b) f_2, and (c) f_3.

The SPP-like behavior is also confirmed in Figure 3.15 that shows the electric field distribution at the interface at the frequencies denoted in Figure 3.14. The frequencies f_1, f_2, and f_3 are equal to 2.55 GHz, 2.70 GHz, and 2.81 GHz, respectively, and they correspond to the case when the reservoir is filled with the analyte whose $\varepsilon_{r2} = 2.4$-$j0.11$. The frequency f_1 has been chosen to illustrate the field distribution in the middle of the passband, whilst f_2 and f_3 have been chosen to illustrate the propagating and non-propagating field distribution once the β starts to abruptly increase. Whilst E-field distribution at f_1 is very similar to that of the conventional HM SIW in terms of the wavelength, at f_2 and f_3 the wavelength is significantly smaller implying increase of β, which is characteristic for surface plasmons.

Although the focus is on the high sensitivity detection of the real part of the dielectric constant, in the following the calculation method of both real and imaginary parts of the dielectric constant is presented. The analytes used are the mixtures of toluene and methanol, which are highly lossy.

The complex effective dielectric constant of the lossy substrate and the lossy analyte to be sensed can be defined as

$$\varepsilon_{e1} = \varepsilon_{e1}' - j\varepsilon_{e1}'' = \varepsilon_{r1}\left(1 - \frac{\omega_{p1}^2}{\omega(\omega + j\gamma_1)}\right), \tag{3.10}$$

$$\varepsilon_{e2} = \varepsilon_{e2}' - j\varepsilon_{e2}'' = \varepsilon_{r2}\left(1 - \frac{\omega_{p2}^2}{\omega(\omega + j\gamma_2)}\right), \tag{3.11}$$

where ω is the angular frequency, ε_{r1} and ε_{r2} are the real parts of the dielectric constants of the substrate and the sensed analyte, respectively, ω_{p1} and ω_{p2} are the cut-off frequencies for the HM SIW filled with the substrate material and sensed analyte. The latter parameters can be defined as

$$\omega_{p1} = \frac{\pi c}{2a_{eff}\sqrt{\varepsilon_{r1}}}, \tag{3.12}$$

$$\omega_{p2} = \frac{\pi c}{2a_{eff}\sqrt{\varepsilon_{r2}}}, \tag{3.13}$$

where a_{eff} is the effective width of HM SIW.

The parameters γ_1 and γ_2 are the damping coefficients for the substrate and the sensed analyte, thus representing the imaginary parts of the dielectric constants, and they can be

expressed as a function of loss tangent of the substrate and the sensed analyte, i.e. $\gamma_1 = \frac{1}{2}\omega \tan \delta_1$, $\gamma_2 = \frac{1}{2}\omega \tan \delta_2$.

To determine the dielectric constant of the sensed analyte, we first use the condition for surface plasmon polariton frequency. At the plasmon frequency, $\omega=\omega_{SP}$, the wavenumber goes to infinity $\beta\rightarrow\infty$, and consequently the real part of effective permittivities are related as follows: $Re(\varepsilon_{e2}) = -Re(\varepsilon_{e1})$. Using the eqs. (3.10) and (3.11), the condition can be rewritten as

$$Re\left(\varepsilon_{r1}\left(1 - \frac{\omega_{p1}^2}{\omega(\omega + j\gamma_1)}\right)\right) = -Re\left(\varepsilon_{r2}\left(1 - \frac{\omega_{p2}^2}{\omega(\omega + j\gamma_2)}\right)\right). \tag{3.14}$$

To determine the complex dielectric constant, we need to know, besides the plasmon frequency, the quality factor of the structure at the plasmon resonance that includes only the dielectric losses in the system, Q_d. As already known, the ratio of the resonant (plasmon) frequency and the 3-dB bandwidth from S_{21} response of the structure determines the quality factor that includes dielectric, ohmic, and radiation losses, Q_M. The factors Q_d and Q_M are related as follows [159]

$$Q_d = \left(\frac{1}{Q_M} - \frac{1}{Q_C} - \frac{1}{Q_{rad}}\right)^{-1}, \tag{3.15}$$

On the other hand, the quality factor that includes only the dielectric losses at the plasmon resonance can be defined using the expression from [159].

$$Q_d = \Upsilon\left(\frac{\varepsilon_{e2}''}{|\varepsilon_{e2}'|} - \frac{\varepsilon_{e1}''}{\varepsilon_{e1}'}\right)^{-1}, \tag{3.16}$$

where Υ is defined as:

$$\Upsilon = \frac{\omega\left[\frac{d\varepsilon_{e2}'}{d\omega} + \frac{|\varepsilon_{e2}'|}{\varepsilon_{e1}'}\frac{d\varepsilon_{e1}'}{d\omega}\right]}{2|\varepsilon_{e2}'|}. \tag{3.17}$$

The eq. (3.16) implies that the imaginary part of the effective dielectric constant of the sensed analyte can be expressed as

$$\varepsilon_{e2}'' = |\varepsilon_{e2}'|\left(\frac{\varepsilon_{e1}''}{\varepsilon_{e1}'} + \frac{\Upsilon}{Q_d}\right). \tag{3.18}$$

Using the previous equation and the equation (3.11) the following expression can be derived:

$$\varepsilon_{e2}'' = Im(\varepsilon_{e2}) = Im\left(\varepsilon_{r2}\left(1 - \frac{\omega_{p2}{}^2}{\omega(\omega + j\gamma_2)}\right)\right) = |\varepsilon_{e2}'|\left(\frac{\varepsilon_{e1}''}{\varepsilon_{e1}'} + \frac{\Upsilon}{Q}\right). \tag{3.19}$$

It should be noted that the Q_d factor in the eq. (3.19) includes only the dielectric losses in the system. On the other hand, the quality factor that is determined from the S_{21} response, Q_M, comprises dielectric, ohmic, and radiation losses. Therefore, the Q_d factor to be used in the eq. (3.19) is obtained using the eq. (3.17). To account for the parameters Q_c and Q_{rad} and determine the parameter Q_d, Q_c has been estimated by full wave simulations, as $Q_c \approx 250$, whilst Q_{rad} is neglected. Namely, the radiation can be considered as negligible in the sensor's operating frequency range, and thus Q_{rad} is neglected.

In eqs. (3.12) and (3.13) the width of the HM SIW a has been replaced by a_{eff} to compensate for the fact that, strictly speaking, the SPP phenomenon occurs along the width of the reservoir a_r, rather than along a. Furthermore, the coupling between the two parts is not perfectly bounded within the width of the reservoir, i.e., there is a slight field leakage causing deviations from the ideal case. Therefore, the sensing structure is firstly calibrated by the calculation of a_{eff} using the response for the case the reservoir is filled with the air, and afterwards the calculated a_{eff} is used for the detection of other unknown dielectric constants. The calculated value of a_{eff} is equal to 13 mm, which is actually very similar to the a_r, showing that a_{eff} serves for a fine compensation.

To demonstrate the validity of the method, Figure 3.16 shows the comparison of two sets of the real and imaginary parts of the dielectric constants of the analyte in the reservoir – the first one represents the values initially set in the simulator, according to which the responses in Figure 3.14 have been obtained, whilst the other represents the values calculated using the
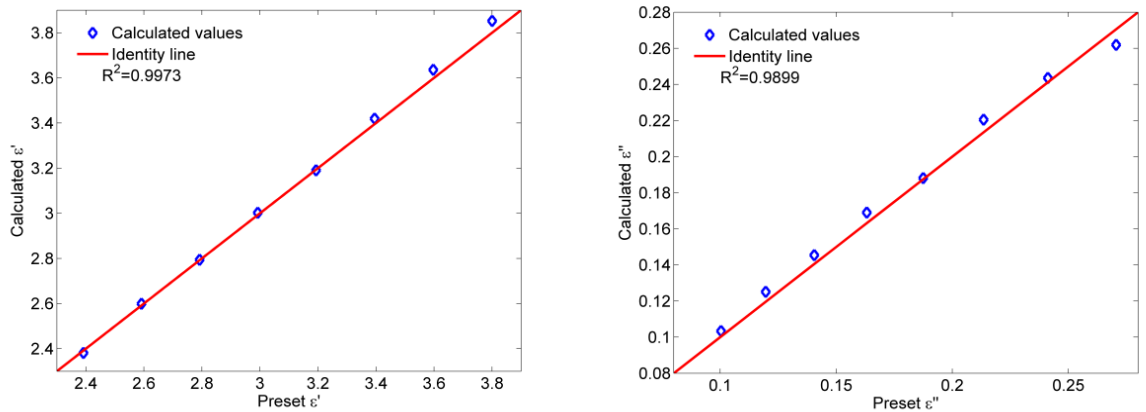
Figure 3.16. Comparison of the preset and calculated dielectric constant values: (a) real part, (b) imaginary part.

transmission responses and the previously explained method. An excellent agreement can be noted, with the highest relative error lower than 1.4% and 5% for real and imaginary parts, respectively. The calculated values were fitted by identity line and the coefficient of determination R^2 is equal to 0.9973 and 0.9899 for real and imaginary part, respectively, which indicates the excellent sensing potential of the proposed structure.

3.4.2. Fabrication and measurement results

The proposed sensor has been fabricated using standard PCB technology combined with Computer Numerical Control (CNC) milling process. The fabrication process started with the preparation of photomasks for the PCB using UV exposure on the photosensitive film and etching process. The top and bottom parts of the circuit have been fabricated on the dielectric substrate Rogers TMM6 with relative permittivity $\varepsilon_r = 6$, dielectric loss $tan\delta = 0.0023$, and thickness $t = 0.635$ mm, using PCB technology. Afterwards, Syil X5 Plus CNC machine with resolution of 0.01mm has been used to drill the microfluidic reservoir in the bottom part. Also, CNC milling process was used to drill the holes for the connectors, inlet and outlets, as well as the holes for the joining top and bottom parts.

Figure 3.17(a-c) shows the top and bottom parts of the sensor after etching and milling process, in which all sensor's elements can be observed. In the final step the top and bottom parts have been joined using four nylon screws and SMA connectors Southwest Microwave 292-04A-5, Figure 3.17(d).

The fluidic analytes to be sensed have been prepared as binary toluene/methanol mixtures. In the pure toluene whose dielectric constant is equal to 2.4-j0.11, different amounts of methanol were added using micropipette to achieve the real parts of the dielectric constant values in the range from 2.4. to 3.8. Consequently, due to the losses in methanol, the range of the imaginary part of the dielectric constant in the mixtures was from 0.1 to 0.5. The exact value of the dielectric constant of the mixtures have been determined using Kraszewski formula [161]:

$$\varepsilon_{rMIX} = \left(\sqrt{\varepsilon_{rM}} v_M + \sqrt{\varepsilon_{rT}} v_T \right)^2, \tag{3.20}$$

where ε_{rMIX} is the permittivity of the mixture, ε_{rM} is the permittivity of methanol, ε_{rT} is the permittivity of toluene, whilst v_M and v_T are the fractional volume of methanol and toluene respectively. Table 3.1 shows the concentrations of toluene and methanol used for preparation of 13 different analytes, together with their calculated dielectric constants.
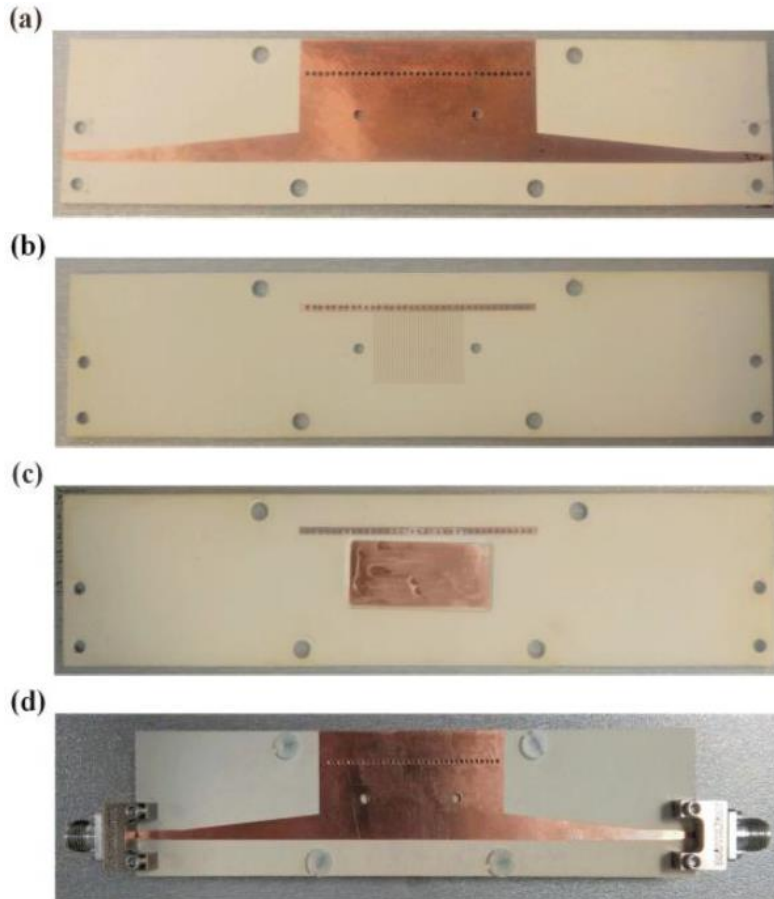
Figure 3.17. Fabricated sensor: (a) top side of the top part, (b) bottom side of the top part, (c) top side of the bottom part with drilled reservoir, and (d) sensor with mounted SMA connectors.

To maximally reduce the error of measurements which can be caused by the manufacturer's tolerance of the substrate parameters, we have also determined the dielectric constant of the substrate. To that end, we have fabricated a simple microstrip line on the same piece of the substrate as HM SIW, measured its phase delay in the range 1-5 GHz, and ultimately calculated the dielectric constant based on the electrical length of the line [132]. The calculated dielectric constant of the substrate is equal to 5.89, somewhat different than suggested by the manufacturer.

The measurement setup is shown in Figure 3.18. The fluidic analytes were injected through the additional tubules into the microfluidic reservoir using a syringe pump. The responses of the sensor have been measured using vector network analyzer Agilent N5230A in the frequency range from 2 and 3 GHz. Figure 3.19 shows the measured responses of the sensor for different analytes, and they exhibit the same trend as the simulated ones. Due to the losses introduced by the methanol, the S_{21} of the transmission zeros becomes lower as the concentration of the methanol in the analytes increases.

Table 3.1
CONCENTRATIONS OF TOLUENE AND METHANOL IN SENSED
ANALYTES, AND
CALCULATED DIELECTRIC CONSTANTS

Sample number	Toluene concentration [μl]	Methanol concentration [μl]	Calculated real part of dielectric constant	Calculated imaginary part of dielectric constant
1	1000	0	2.46	0.11
2	1000	6.6	2.52	0.128
3	1000	10	2.56	0.135
4	1000	12.2	2.58	0.14
5	1000	15	2.6	0.151
6	1000	22.2	2.68	0.169
7	1000	32.2	2.78	0.19
8	1000	42	2.87	0.217
9	1000	61.8	3.06	0.275
10	1000	81.2	3.25	0.334
11	1000	100.8	3.44	0.399
12	1000	120	3.63	0.462
13	1000	139.4	3.82	0.53
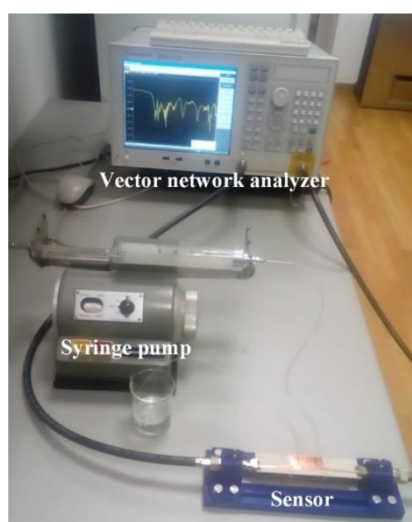
Figure 3.18. Measurement setup for the proposed sensor.
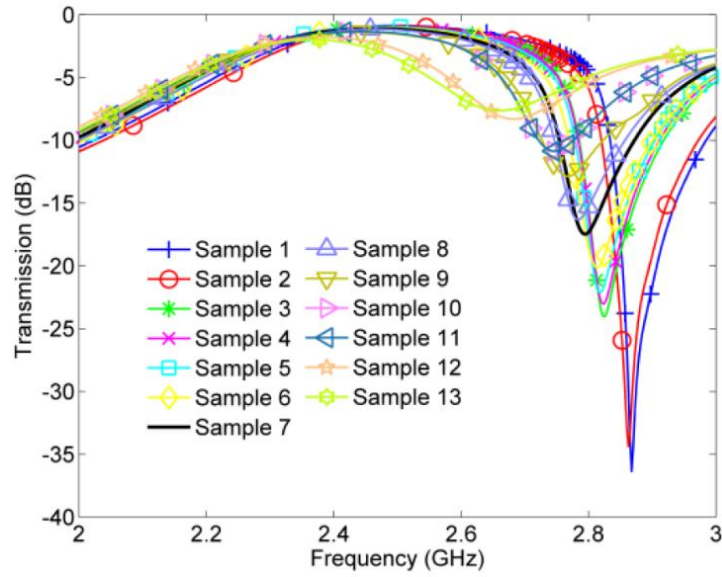
Figure 3.19. Measured responses of the sensor for different analytes.
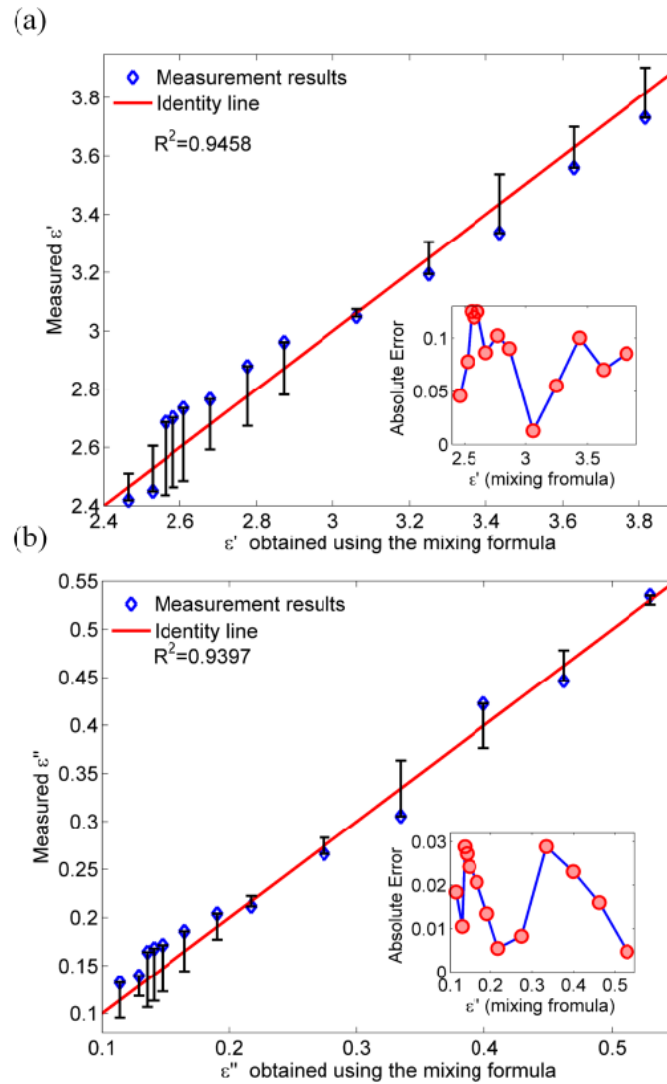
Figure 3.20. Comparison of dielectric constants obtained using the mixing formula and spectral positions of the transmission zeros in the measured responses: (a) real part, (b) imaginary part.

47

To determine the dielectric constants of the sensed analytes, firstly, the value of a_{eff} had been determined for the case when the reservoir is filled with the air, and it is equal to 12.6 mm. Afterwards, the dielectric constants of the analytes have been determined using the spectral positions of the transmission zeros in the measured responses and the method presented in Section II. The obtained values have been compared to those calculated using the eq. (3.20) and this is shown in Figure 3.20. One can note an excellent agreement between the two sets of the values for both real and imaginary part of the dielectric constant - the relative error is lower than 4% and 9%, respectively, for the whole set of measurement. The relative error was calculated as $\delta = 100*(|\varepsilon_{cr/ci}-\varepsilon_{mr/mi}|/\varepsilon_{mr/mi})$, where ε_c and ε_m are calculated and measured values, whilst r and i denote real and imaginary parts of the dielectric constants, respectively. The calculated values were fitted by identity line and the coefficient of determination R^2 is equal to 0.9458 and 0.9397 for real and imaginary part, respectively, which shows excellent sensing potential of the structure.

To further illustrate the excellent performance of the proposed sensor, Table 3.2 provides the comparison of the proposed sensor to other recently published sensors for dielectric constant detection whose operating principle is based on resonance shift. The sensitivity is defined as $(f_{max}-f_{min})/(\varepsilon_{max}-\varepsilon_{min})$, where the parameters f_{min} and f_{max} correspond to the resonance positions for the cases of the highest measured real part of the relative permittivity ε_{max} and lowest measured real part of the relative permittivity ε_{min}.

The proposed sensor exhibits excellent sensitivity, which compares favorably to the other high-sensitivity microwave sensors for dielectric constant detection. Although the structure in [141] is more sensitive, it should be noted that it operates at frequencies above 20 GHz. Therefore, its relative sensitivity, i.e. percentage ratio of f_{max} and f_{min} divided by (ε_{max}-ε_{min}), is lower than that of the proposed sensor, implying that the two sensors would have comparable sensitivity if operating in the same frequency range. However, the sensor in [141] is realized as a waveguide, thus having remarkably greater dimensions than the proposed sensor. Also, it should be noted that a particular strength of the proposed sensor is the detection of the real part of the dielectric constant in a very small range, whilst the majority of the published sensor are aimed at the detection of a wide range of the dielectric constant.

We note here that the range of the real part of the dielectric constant values detectable by the proposed sensor can be widened using substrate with higher dielectric constant of HM SIW. Taking into account the proposed calculation method and the expression for the cut-off frequency of HM SIW, as well as the fact that surface plasmon frequency has to be higher than

Table 3.2

COMPARISON OF THE PROPOSED SENSOR AND OTHER RECENTLY
PUBLISHED

SENSORS FOR DIELECTRIC CONSTANT DETECTION.

Ref	f_{min} [GHz]	f_{max} [GHz]	ε_{min}	ε_{max}	Senistivity*	Relative sensitivity**
[135]	2.1	2.195	1	10.4	10.4	0.49
[136]	14.05	17.08	1	80.1	38.35	0.27
[137]	1.8	2.016	2.45	22.52	54.8	0.60
[138]	2.02	3.51	3.1	32.6	50.5	2.50
[139]	8.8	9.9	1	80.1	13.92	0.16
[140]	5.6	5.62	2.8	80.1	0.26	0.00
[141]	21	23.4	1	3	1200	5.71
[142]	10	10.4	47	63	25	0.25
[143]	4.52	4.9	1	4.4	111.76	2.47
[144]	1.52	1.92	9	79.5	5.67	0.37
[145]	0.915	1	1	80.1	1.07	0.12
This work	**2.65**	**2.85**	**2.4**	**3.54**	**175.43**	**6.62**

*Expressed as $(f_{max}\text{-}f_{min})/(\varepsilon_{max}\text{-}\varepsilon_{min})$ in MHz/Relative Epsilon
** Expressed as $(f_{max}/f_{min}\text{-}1)*100/(\varepsilon_{max}\text{-}\varepsilon_{min})$ in [%]/Relative Epsilon

the cut-off frequency, one can come to the conclusion that the theoretical higher limit of the dielectric constant to be measured is the dielectric constant of the HM SIW substrate. In practice, this limit is lower since the cut-off frequency and the transmission zero that corresponds to surface-plasmon frequency, have to be separated in the spectrum, so the transmission zero is clearly observable, and the operation of the HM SIW is not significantly deteriorated. On the other hand, there is no lower limit to the measurable dielectric constant range.

These results confirm that the proposed sensor has a great potential for highly sensitive dielectric constant detection in liquid analytes in microwave regime, which can be applied in quality analysis of engine and edible oils. Moreover, the sensor represents a compact and low-cost solution since it is fabricated in low-profile configuration using PCB technology.

3.5 Conclusion

In this chapter, it was demonstrated how a metamaterial approach to achieve SPP-like propagation can benefit devices operating at microwave frequencies. In order to realize effective SPP propagation, the concept of SIW plasmonics was introduced and analyzed in detail. Based on this concept, two novel microwave dual-band filters, as well as a microwave sensor, were designed, fabricated, and measured.

The filters are realized as a stack of sub-SIW structures, tailored to exhibit effective permittivities of opposite signs in certain frequency ranges. It was shown how the choice of the geometrical parameters and dielectric constants of sub-SIWs can provide arbitrarily positioning of the passbands in the spectrum, which is the basic principle of the filter design. The filters are characterized by excellent in-band characteristics and selectivity. The designed filters have been fabricated using standard PCB technology, and the measurements results agree well with the simulated ones.

Furthermore, a novel, highly sensitive microwave SPP-like sensor was presented. The core element of the sensor is a HM SIW whose two comprising guiding parts, one of which contains the sensed analyte, enable SPP-like propagation to occur at their interface. As a consequence, a sharp transmission zero occurs in the HM SIW response, which is very sensitive to the change in the real part of the dielectric constant of the liquid analyte. This concept was exploited for dielectric constant detection of different toluene/methanol mixtures. Analytical and numerical analysis together with the measurement results confirmed the potential of the sensor for very sensitive measurements with low relative error. At the same time, the structure is characterized by the low-profile configuration and cost-effective fabrication, which makes it an excellent candidate for low-cost, high sensitivity microwave sensor for dielectric constant detection.

Chapter 4: Complex frequency analysis of scattering phenomena

4.1 Introduction

In the analysis of the interaction of light with macroscopic structures, linear scattering processes play a significant role. When impinging on a linear scattering object, EM waves can undergo several simple processes such as reflection, transmission, absorption, and diffraction. These processes have been under intense investigation in metamaterials research, where waves interact with more complex structures, and where exceptional control of the wave properties through the scattering processes can be obtained. A range of unusual scattering phenomena in metamaterials and nanophotonics has been recently reported, such as coherent perfect absorption (CPA) [162], parity-time symmetric phase transitions [163], superscattering [164], embedded eigenstates [89], virtual absorption [165], to name a few. Such scattering anomalies can be captured in an intuitive and meaningful way through the scattering matrix formalism [90,166], a useful tool in the analysis and design of wave-based devices with novel functionalities. Namely, by continuing the frequency to the complex plane, singularities of the scattering matrix and scattering coefficients in the forms of poles and zeros can be observed. As it turns out, the scattering process can be fully described by the position of the poles and zeros [90].

In this chapter we put forward a theoretical framework for the analysis of scattering anomalies based on the scattering matrix formalism in the complex frequency plane. We discuss the scattering of plane waves for extended planar, linear, non-magnetic, isotropic materials, and show a range of scattering anomalies which can arise in such simple systems. This provides the groundwork for the analysis and design of devices based on different scattering phenomena reported in chapters 5, 6 and 7.

4.2 Scattering matrix

The scattering matrix describes the relationship between the incoming and outgoing waves by connecting their amplitudes [167,168]. A scattering problem is usually formulated in a specific basis of scattering channels (e.g., plane waves, spherical or cylindrical harmonics) as $\mathbf{s}^- = \hat{S}(\omega)\mathbf{s}^+$, with corresponding amplitudes of incoming $\mathbf{s}^+ = \{s_1^+, s_2^+, ...\}$ and outgoing

$\mathbf{s}^- = \{s_1^-, s_2^-, ...\}$ waves[169,170]. Here, $\hat{S}$ is the frequency dependent scattering matrix of the system in the chosen basis:

$$\hat{S} = \begin{bmatrix} S_{11} & \cdots & S_{1n} \\ \vdots & \ddots & \vdots \\ S_{n1} & \cdots & S_{nn} \end{bmatrix}. \tag{4.1}$$

The amplitudes are normalized such that $|s_n^+|^2$ and $|s_n^-|^2$ correspond to the energy of incoming and outgoing waves in channel n. The output s represents a linear combination of incoming wave amplitudes. In this scenario, we separate the incident and scattering waves or channels, as shown in an example in Figure 4.1.

In a single port system, such as a dielectric slab backed with a reflector, the $\hat{S}$-matrix is the reflection coefficient. For a two-port system, such as a free-standing dielectric slab, the scattering matrix is of the form

$$\hat{S} = \begin{pmatrix} r_{11} & t_{12} \\ t_{21} & r_{22} \end{pmatrix}, \tag{4.2}$$

where r and t stand for reflection and transmission coefficients from both sides. For reciprocal systems, the transmission is equal from both sides $t_{12} = t_{21}$. Furthermore, if the system is also symmetric under mirror reflection, then both the reflection and transmission coefficients are equal from both sides, $r = r_{11} = r_{22}$ and $t = t_{12} = t_{21}$ [90]. When the frequency ω is analytically continued in the complex plane, $\omega = \omega_r + j\omega_i$ the scattering matrix eigenvalues can generally take any complex value. When their magnitude is ∞ or 0, they correspond to poles and zeros
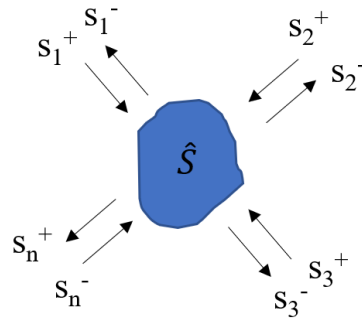
Figure 4.1. Scattering matrix description of a linear scatterer.

of the $\hat{S}$-matrix, respectively. Poles of $\hat{S}$ are related to self-sustained states (eigenmodes) of the system[171], whereas zeros of the $\hat{S}$-matrix are associated with ideally absorbing states, or solutions to Maxwell's equations consisting of purely incoming energy that satisfy all the boundary conditions[165].

4.3 Scattering anomalies and singularities of the S-matrix for two port systems

Here we analyze a simple two-port system – a free-standing dielectric slab with thickness d and permittivity ε, surrounded by air or vacuum. Such a structure can be described by a 2x2 scattering matrix shown in eq (4.2). Since the system is reciprocal and symmetric under mirror reflection, i.e. $t_{12}=t_{21}=t$ and $r_{11}=r_{22}=r$, the scattering matrix $\hat{S}$ has pair of eigenvalues $s_{1/2} = r \pm t$, and corresponding eigenvectors $\mathbf{s}^+ = \{1, \pm 1\}$, representing symmetric and antisymmetric inputs of equal intensity. Poles and zeros appearing in the complex frequency plane thus correspond to symmetric and antisymmetric field excitations. To visualize both the symmetric and antisymmetric poles and zeros, we plot the density plot of the $\hat{S}$-matrix determinant in the complex frequency plane, $\det(\hat{S}) = r^2 - t^2 = (r+t)(r-t) = s_1 s_2$, Figure 4.2.

4.3.1. Perfect absorption, coherent perfect absorption, and lasing

Absorption of light plays an important role in modern optical technologies like photovoltaics [172], polarizers [173], and sensors [174]. To achieve perfect absorption, one must eliminate scattering to all outgoing channels, i.e., eliminate transmission and reflection in two-port systems, or just reflection in one-port systems. Most perfect absorbers have a single
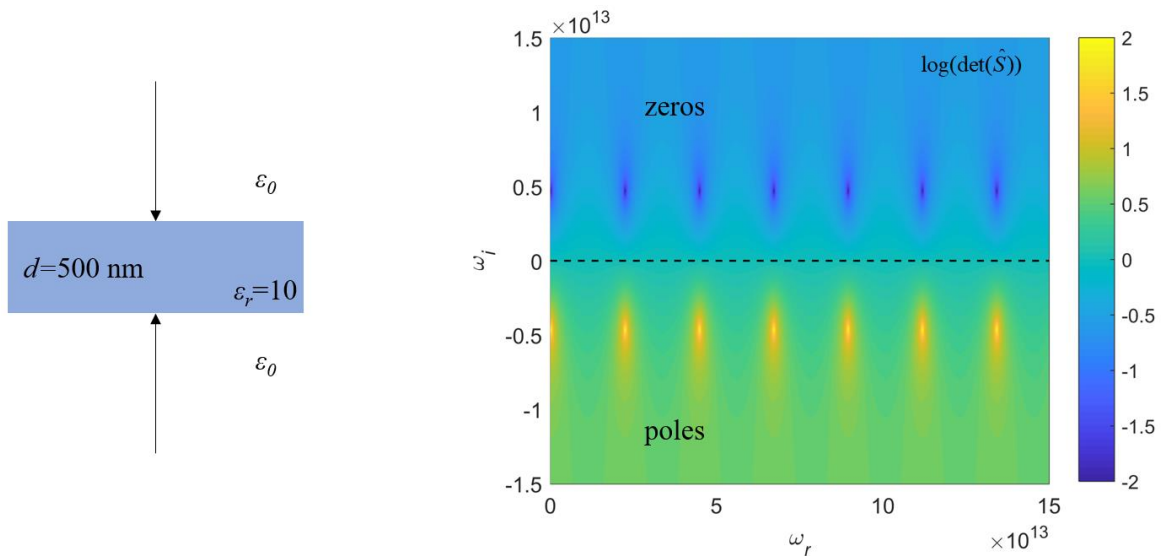
Figure 4.2. Dielectric slab symmetric under mirror reflection with two input signals. Determinant of the S-matrix is shown where poles and zeros are indicated.

scattering channel (reflection), like the Salisbury or Dallenbach screens [175,176], where absorption is attributed to destructive self-interference facilitated through the backing mirror.

The origin of this perfect absorption of waves can be intuitively understood through the scattering matrix formalism. As briefly mentioned above, zeros of the scattering matrix eigenvalue represent solutions to the Maxwell's equation for an open structure with purely incoming waves. This means that if only incoming waves in all the scattering channels are supposed, such that outgoing waves have zero amplitude $\mathbf{s}^+ \hat{S} = \mathbf{s}^- = 0$, the solutions of such a problem constitute coherent perfect absorption (CPA) [162]. These solutions coincide with the zeros of the scattering matrix eigenvalue shown in Figure 4.2. In lossless systems, these zeros are found in the upper complex half-plane under e^{-jwt} assumption. They are the exact complex conjugate of the system eigenmodes (poles), which are solutions to a purely outgoing problem, i.e. they represent the time-reversed versions of each other.

To achieve CPA for monochromatic excitation (real frequency), loss must be incorporated in the structure. In general, loss moves the poles and zeros down along the imaginary frequency axis [90]. When one of the zeros has a purely real frequency, it represents a CPA solution, Figure 4.3. As there are two ports, the specific state associated with CPA requires two input waves with a particular phase and amplitude, i.e., eigenvectors associated with the eigenvalues of this state [162]. CPA represents the generalization of perfect absorption (PA) to multiport structures. In a single port system, the perfect absorption condition is equal to a zero reflection coefficient. Since the *S*-matrix in that case is the reflection coefficient, the zeros of the *S*-matrix eigenvalue are equal to the zeros of the reflection coefficient.

Apart from using material loss to achieve perfectly absorbing states, one can engage the zeros even in the lossless case by temporally tailoring the excitation [165]. Namely, the zeros in the lossless case have a complex frequency, and if the excitation matches that complex frequency (exponentially rising amplitude of the incoming wave $\omega = \mathrm{Re}(\omega) + j\,\mathrm{Im}(\omega)$), one can achieve virtual perfect absorption. In this scenario, energy is being stored inside the material without being absorbed, as long as the input signal exactly matches the eigenvector associated with zero of eigenvalues. The concept of using complex frequency excitation is a powerful paradigm used to first demonstrate the concepts of enhanced wireless power transfer [177], virtual parity-time symmetry [178], virtual critical coupling [179], and virtual optical pulling force [180]. A useful way of interpreting the CPA solutions is to look at them as the time-reversed version of the laser. Namely, a lasing state constitutes a self-sustained oscillation,
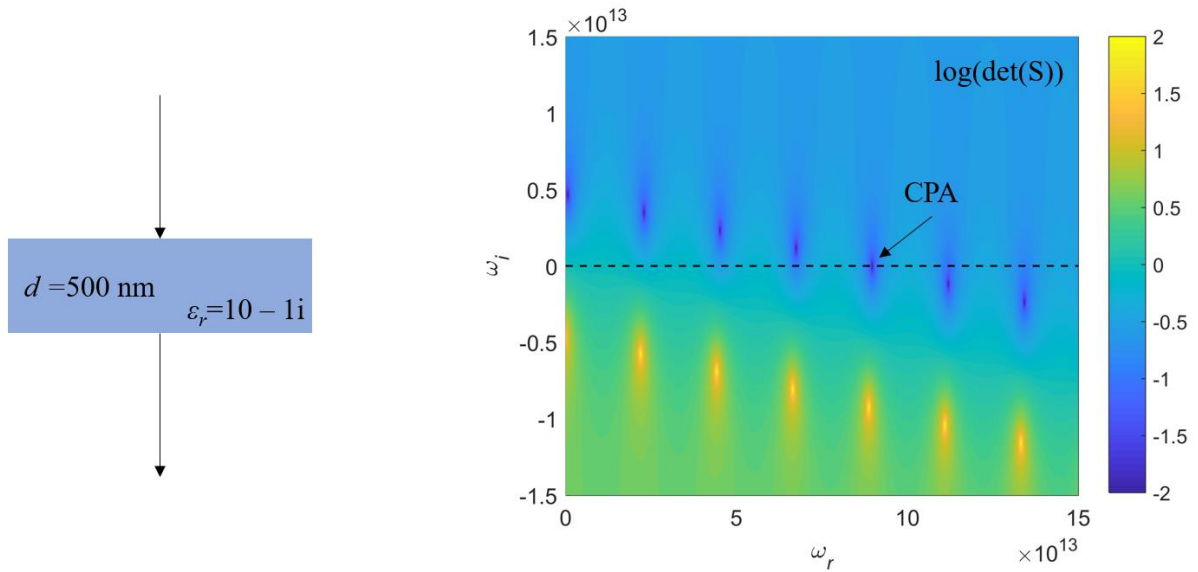
Figure 4.3. Lossy dielectric slab with two input signals. Determinant of the S-matrix shows that one of the zeros is positioned at the real frequency axis, constituting a CPA.

i.e., a pole (mode) at a real frequency. These poles are solutions for the boundary value problem with purely *outgoing* solutions, i.e., the system generates an output without any input. The population inversion providing the gain in lasers is excluded here, as it is simply incorporated in the complex permittivity of the material.

The onset of lasing can be analyzed through the poles of the scattering matrix – adding gain to the material moves up the poles and zeros of S-matrix along the imaginary frequency axis. When one of the poles hits the real frequency axis, it delineates the onset of a lasing state,
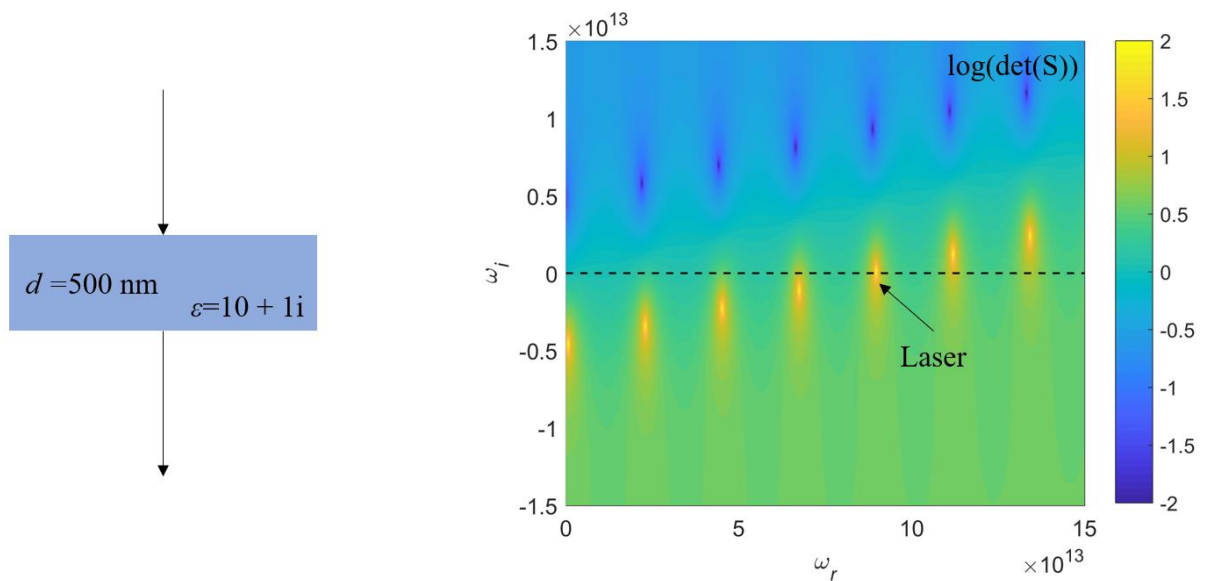
Figure 4.4. Gainy dielectric slab with two input signals. Determinant of the S-matrix shows that one of the poles is positioned at the real frequency axis, constituting a lasing state. Poles in the upper complex half-plane indicate instability.

Figure 4.4. This linear approach to the analysis of lasers can be applied until the lasing threshold is met – the moment one of the poles hits the real frequency axis. However, nonlinearities come into play and more complex optical models like the Maxwell-Bloch equations must be employed to accurately describe the laser operation when threshold is reached [181]. Furthermore, when the poles cross to the upper complex plane, they represent self-sustained solutions with an exponentially growing character, indicating instability of the system.

4.3.2. CPA-laser

A particularly interesting case arises when using both gain and loss in a spatially symmetric manner. For example, a PT-symmetric structure in an EM system can be achieved by spatially separating regions of gain and loss such that they comply with $\varepsilon(r, \omega) = \varepsilon^*(-r, \omega)$. As mentioned briefly in Chapter 2, PT-symmetric structures can undergo spontaneous symmetry breaking, where the eigenvalues of the scattering matrix become complex and non-unimodular after a certain non-Hermiticity threshold (loss/gain coefficient). This phase transition from PT-symmetric to broken phase regime happens at an exceptional point EP, around which scattering observables (resonant dips or peaks) dramatically change. This feature has been proposed as a basis for hyper-sensitive sensing mechanisms [129]. In the broken phase regime, it is possible that one eigenvalue acquires zero amplitude while the other diverges – a case which constitutes the CPA-laser [163]. In the complex frequency plane, this happens when a pole/zero pair have the same real frequency.

An example of a PT-symmetric system and the evolution of its eigenvalues is shown in Figure 4.5. In this example, the gain/loss level is kept constant, and the frequency is changed. In Figure 4.5 (b), we see that eigenvalues are unimodular until they split at the EP, and subsequently the CPA-Laser point is reached. Under these conditions the system operates as a
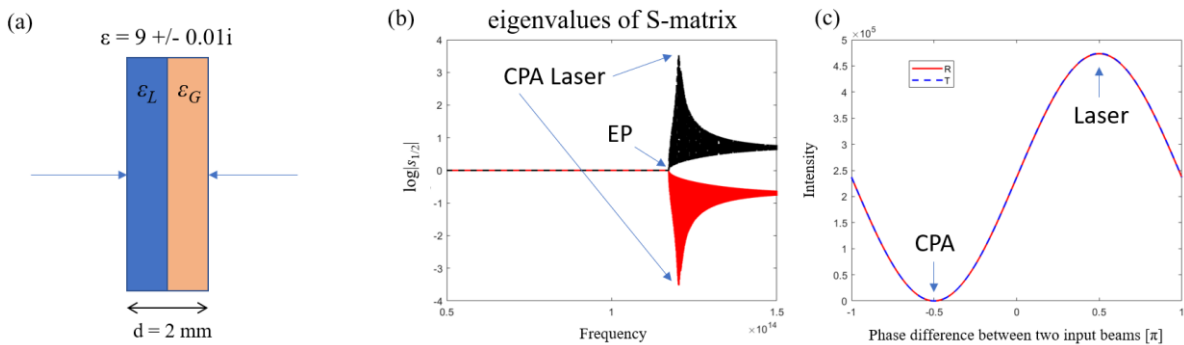
Figure 4.5. (a) Example of a PT-symmetric system (b) S-matrix eigenvalues with the characteristic EP and CPA-Laser points (c) Coherent control and switching between CPA and Laser by tuning the phase difference between input beams

laser without excitation, however with precise control of the excitation signals' phase, one can switch between lasing and perfect absorption, as shown in Figure 4.5 (c).

4.3.3. Embedded eigenstates

Embedded eigenstates are a particularly interesting scattering anomaly which can be handily described within the scattering-matrix formalism. As briefly explained in Chapter 2, they represent resonances (modes) with zero-linewidth, i.e., they are resonant states situated in the radiation continuum but do not radiate due to their infinite lifetime.

Resonances, i.e., modes, appear as poles of the scattering matrix eigenvalues [90]. As the imaginary part of their complex eigenfrequency is oppositely proportional to their lifetime, an infinite lifetime resonance has zero imaginary frequency -- it constitutes a pole at the real-frequency axis. One must not confuse the real-frequency pole associated with the onset of lasing in a gainy system with this scenario. Since EEs appear in Hermitian systems (no loss or gain), a pole on the real frequency axis would break the energy conservation law. However, due to hermiticity, the poles and zeros come in conjugate pairs, and consequently an *S*-matrix zero meets the pole at the real frequency axis where they cancel each other. This merging of a pole and zero of the *S*-matrix constitutes an EE in lossless scattering systems. To differentiate between these mentioned scenarios, an illustration of all the different scattering anomalies is shown in Figure 4.6.

4.3.4. Scattering (reflection) zeros

So far, we have discussed the poles and zeros of the scattering matrix eigenvalues, and shown several unusual scattering phenomena based on their analysis. Another important set of poles and zeros are those associated with the scattering coefficients. In planar systems, these represent singularities of the reflection/transmission coefficient. The poles of the reflection coefficient coincide with the poles of the scattering matrix discussed above, both of which can be attributed to the outgoing wave solutions or eigenmodes. Namely, finding the poles of reflection is a common procedure of determining the eigenmodes of the system [182].

However, the zeros of the scattering coefficient have a different meaning than the zeros of the *S*-matrix – they are not associated with purely incoming wave solutions but rather designate zero scattering power to a given outgoing channel. They have recently been generalized to an *n*-port scattering system, and termed *reflectionless scattering modes* [183]. These solutions can appear anywhere in the complex frequency plane. When they appear on the real frequency axis, they are usually associated with impedance-matched states. Well-
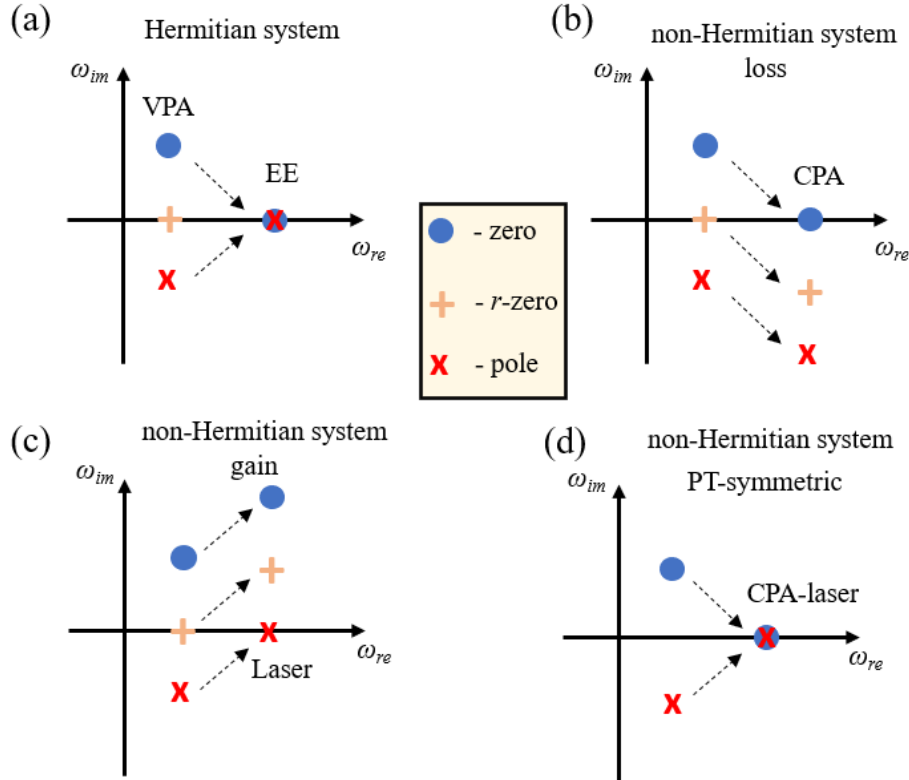
Figure 4.6. Different scattering scenarios described by the position poles and zeros of the scattering matrix and scattering coefficient. (a) Through resonator design in a Hermitian system, it is possible to merge a pole and zero at the real frequency axis for an exact incidence angle (transverse wavevector) (b) Loss can push one of the S-matrix zeros on the real frequency axis which constitutes a CPA state (c) Gain can do the same with a pole and provide a lasing state (d) In PT-symmetric systems, it is possible to push a pole and zero together at the same real frequency, making a CPA-Laser state.

known examples are Fabry-Perot resonances, where the reflection is eliminated by virtue of destructive interference, and Brewster's effect where the reflected and refracted waves are at a right angle. However, as pointed out in [183], these impedance-matched zeros just represent a subset of all the available reflectionless scattering states.

An interesting feature of one-port systems is that their scattering matrix is the reflection coefficient. This makes the observable features directly related to the general discussion above, since the reflection coefficient singularities exactly coincide with the S-matrix singularities. Since the zeros and poles of the S-matrix are complex conjugates in Hermitian systems, an interesting scenario arises when such a one-port system also supports an EE, Figure 4.7. Specifically, in this setting the reflection zeros correspond to perfect absorption states, which follow the same dispersion as the poles (modes). Any non-Hermitian perturbation (loss or gain) will break the EE into a pair of singularities (lasing or perfect absorption), which can be
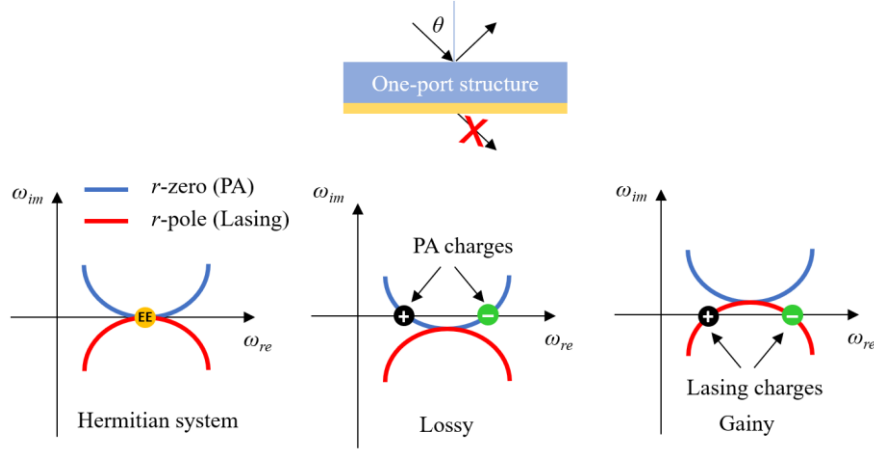
Figure 4.7. One-port structure supporting an EE and emerging topological scattering singularities: sketches of dispersions of poles and zeros of reflection for different incident angles θ for lossless, lossy and gainy structures. Charges of opposite polarity emerge from EEs at the real frequency axis.

associated to a topological charge. These topological scattering singularities emerging from EEs have many potential applications and will be further discussed in Chapter 6.

4.4 Conclusion

We have introduced the basic properties of the scattering matrix in the complex frequency plane for planar resonant systems. We have shown how the singularities of the scattering matrix eigenvalues determine the scattering properties of the system, and we have discussed various scattering anomalies appearing in such systems. The presented analysis can be used as a tool in the design of optical devices, since the scattering responses of the structures depend on the position of scattering matrix singularities. Furthermore, it enables new understanding of the topological nature of embedded eigenstates and related scattering singularities, as shown in the following chapters. To demonstrate this claim, we will further expand the presented analysis to different structures and show various scattering scenarios with applications in thermal emission, polarization control, sensing, and unconventional coherent control of scattering.

Chapter 5: Embedded eigenstates based on ENZ materials and their applications[4]

5.1   Introduction

Scattering of waves is a ubiquitous process across science and technology. For a scattering process to occur, electromagnetic waves need to interact with matter. This interaction lies at the center of today's experimental physics and technology, both in classical and quantum regimes. A property intimately tied to light-matter interaction is wave confinement in the form of the system eigenmodes. The quest for confining large amounts of electromagnetic energy into small volumes has been at the forefront of technological advances in recent decades, where high Q-factors and low mode volumes have been sought-after with various approaches [90,184,185].

A recent approach to this problem holds the promise for extreme light confinement in the form of embedded eigenstates (EE) or bound states in the continuum (BIC) [77-89]. Most of the approaches to eliminate radiation leakage are based on symmetry-forbidden decay and destructive interference of partial modes in photonic crystals and other period structures [77]. A conceptually different approach to realize light-trapping structures that support EEs is based on using epsilon-near-zero (ENZ) materials [88,89,91], as mentioned briefly in Chapter 2.

In this chapter, we discuss a class of EEs stemming from Berreman modes in epsilon-near-zero materials comprising dielectric layers. We show that these modes manifest themselves as zero reflection contours in the reflection spectra, associated with the complete transmission of energy for plane-wave excitation. It is also shown that a uniform ENZ slab supports a trivial embedded eigenstate at normal incidence, in analogy to symmetry-protected EEs found in periodic structures. Furthermore, it is shown that a three-layer system consisting of ENZ-dielectric-ENZ layers supports different orders of Berreman modes, which can support both trivial and *accidental* EEs. We apply these ideas to design of an extremely narrowband perfect absorber/thermal emitter based on SiC, which may provide temporally and spatially narrowband thermal emission based on embedded eigenstates [186].

5.2 Planar ENZ slab – Brewster's effect and symmetry-protected EE

We start by analyzing a simple structure – a slab of ENZ material – infinitely extended in two spatial directions, having a finite thickness, as shown in Figure 5.1(a). We study reflection of TM waves obliquely incident on the slab from air. Namely, by using a transmission-line equivalent circuit model, Figure 5.1 (b), and the ABCD matrix approach we can derive the expressions reflection and transmission coefficients. Since there is only one layer of propagation connecting the input and the output (both assumed air), the ABCD matrix of such a slab is given by:

$$
\begin{bmatrix} A & B \\ C & D \end{bmatrix} = \begin{bmatrix} \cos(k_{1z}t) & jZ_1 \sin(k_{1z}t) \\ \dfrac{j}{Z_1}\sin(k_{1z}t) & \cos(k_{1z}t) \end{bmatrix},
\tag{5.1}
$$

$$
k_{1z} = \sqrt{k_0^2 \varepsilon_1 - k_x^2},
\tag{5.2}
$$

where k_{1z} represents the wavenumber along the z-axis in the ENZ material, t is the slab thickness and $Z_1 = k_{1z}/\omega\varepsilon_0\varepsilon_1$ is the TM wave impedance in the slab. The reflection and transmission coefficients are then calculated as:

$$
r_1 = \frac{A + \dfrac{B}{Z_0} - CZ_0 - D}{A + \dfrac{B}{Z_0} + CZ_0 + D},
\tag{5.3}
$$

$$
t_1 = \frac{2}{A + \dfrac{B}{Z_0} + CZ_0 + D},
\tag{5.4}
$$

$$
r_1 = \frac{j\dfrac{Z_1^2 - Z_0^2}{2Z_1Z_0}\sin(k_{1z}t)}{\cos(k_{1z}t) + j\dfrac{Z_1^2 + Z_0^2}{2Z_1Z_0}\sin(k_{1z}t)},
\tag{5.5}
$$

$$
t_1 = \frac{2}{\cos(k_{1z}t) + j\dfrac{Z_1^2 + Z_0^2}{2Z_1Z_0}\sin(k_{1z}t)},
\tag{5.6}
$$

where $Z_0 = k_{0z}/\omega\varepsilon_0$ is the TM wave impedance of air.
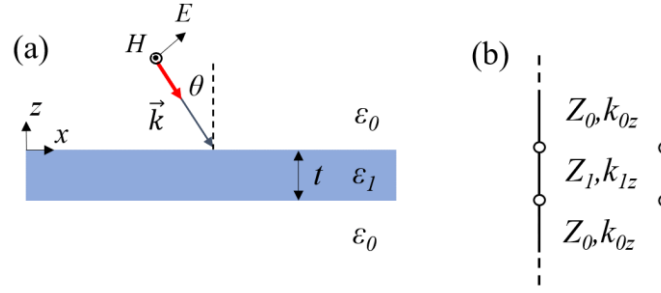
Figure 5.1. (a) Slab reflection problem. (b) Transmission line equivalent circuit.

We assume the permittivity of the ENZ slab follows a lossless Drude dispersion, with $\omega_p = 2\pi \cdot 50$ THz, and we take subwavelength thickness $t = 500$ nm ($t \ll \lambda_p$). We analyze the problem in the frequency-incident angle space, where several things become apparent. Figure 5.2 (a) shows the reflection coefficient amplitude, while 5.2 (b) the transmission coefficient amplitude.

An interesting feature in this plot is the reflection zero, which follows a parabolic dispersion around the plasma frequency. As we show next, this reflection zero happens due to non-resonant impedance matching, corresponding exactly to Brewster's effect.

It is well known that Fabry-Perot resonances in a slab problem allow zero-reflection and full transmission when there is a π phase shift between incoming waves and waves reflected after traversing the slab, making the exact conditions for perfect destructive interference in reflection. This event happens when $\sin(k_{1z}t) = 0$, or $k_{1z}t = n\pi$ which results in zero reflection, eq (5.5). However, near plasma frequency the phase advance through the slab is negligible as the ENZ effect takes place, and thus there are no Fabry-Perot modes available, i.e., $\sin(k_{1z}t)$ term cannot be zero. This is expected since the wavelength in the slab is stretched as one approaches the plasma frequency, making the slab thickness seen by the waves as extremely
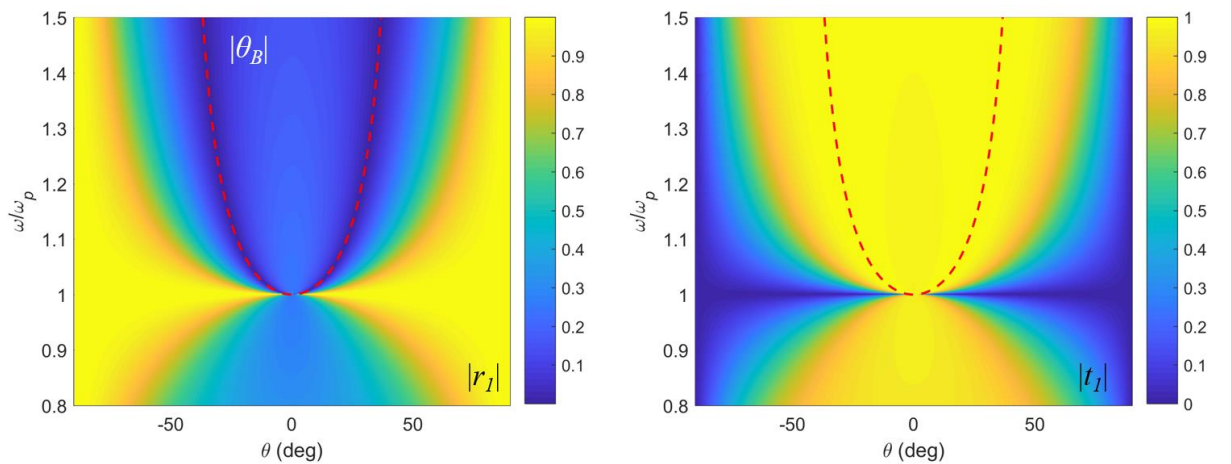
Figure 5.2. (a) TM reflection coefficient amplitude with the Brewster's condition (red stripped line) (b) TM transmission coefficient amplitude

subwavelength, never allowing the phase to advance and reach the resonant condition. Below plasma frequency, the slab behaves like a metal thus the propagation is evanescent, and no resonance effect is expected to be seen in the reflection spectrum.

This leaves the effect of non-resonant impedance matching as the only possible way to achieve zero-reflection according to eq. (5.5), i.e. the transverse wave impedances of air and the slab are matched $Z_0 = Z_1$. By equating the TM wave impedances, we can write:

$$Z_0 = \eta_0 \cos \theta_0 = Z_1 = \frac{\eta_0 \cos \theta_1}{\sqrt{\varepsilon_1}}, \eta_0 = \sqrt{\frac{\mu_0}{\varepsilon_0}}, \tag{5.7}$$

$$\cos \theta_1 = \sqrt{\varepsilon_1} \cos \theta_0, \tag{5.8}$$

where θ_0 and θ_1 are angles of propagation in air and the slab, respectively. If we apply Snell's law of refraction, we obtain

$$\sin \theta_1 = \frac{1}{\sqrt{\varepsilon_1}} \sin \theta_0. \tag{5.9}$$

By squaring and adding together last two equations, we obtain the following:

$$\sin^2 \theta_1 + \cos^2 \theta_1 = 1 = \sin^2 \theta_0 + \cos^2 \theta_0 = \frac{1}{\sqrt{\varepsilon_1}} \sin^2 \theta_0 + \sqrt{\varepsilon_1} \cos^2 \theta_0, \tag{5.10}$$

$$\frac{\sqrt{\varepsilon_1} - 1}{\sqrt{\varepsilon_1}} \sin^2 \theta_0 = (\sqrt{\varepsilon_1} - 1) \cos^2 \theta_0, \tag{5.11}$$

$$\tan \theta_0 = \tan \theta_B = \sqrt{\varepsilon_1}. \tag{5.12}$$

This corresponds to the Brewster's condition, which can be obtained from standard Fresnel coefficients in a similar way. Since the slab has a Drude permittivity dispersion, the Brewster's angle is frequency dependent, and exists for positive values of permittivity, i.e., above plasma frequency:

$$|\theta_B| = \tan^{-1} \sqrt{\varepsilon_1} = \tan^{-1} \left(\sqrt{1 - \frac{\omega_p^2}{\omega^2}} \right), \omega > \omega_p. \tag{5.13}$$

Alternatively, it can be said that for a specific incident angle, the full transmission occurs at the Brewster's frequency:

$$\omega_B = \frac{\omega_p}{\sqrt{1 - \tan^2 \theta_0}}, \; -\frac{\pi}{4} < \theta_0 < \frac{\pi}{4}. \tag{5.14}$$

Although this result is not surprising, it provides necessary context to the reflection spectrum. The analyzed problem becomes more interesting when closely inspecting the reflection coefficient near the plasma frequency for small incident angles. Figure 5.3 shows the reflection coefficient as a function of frequency for different incident angles, which eventually reduces to zero. The shape of the feature closely resembles a classic Fano resonance, whose linewidth narrows as the angle is reduced to zero, where the feature completely disappears. The disappearance of the resonant feature marks the presence of an embedded eigenstate. As we will show later, the Brewster reflection zero disappears as it meets the reflection pole associated with the underlying mode.

To understand the origin of the EE, we now extend our analysis by continuing the frequency to the complex plane. As described in Chapter 4, poles of the reflection coefficient and consequently the poles of the *S*-matrix eigenvalues represent source-free solutions with outgoing boundary conditions or system eigenmodes. Since we are analyzing the structure within the radiation continuum, where we will search for EEs, we are constraining our analysis to the bulk-plasmon-polariton mode, as it is the only leaky-mode available, i.e., the only mode within the radiation continuum. The bounded surface-plasmon modes are omitted from the discussion as they are irrelevant for EE-related phenomena in this structure.

To find the eigenfrequencies of the resonances we employ the transverse resonance (TR) method [187-188], as described in the Chapter 2. In this approach, a 1D waveguiding
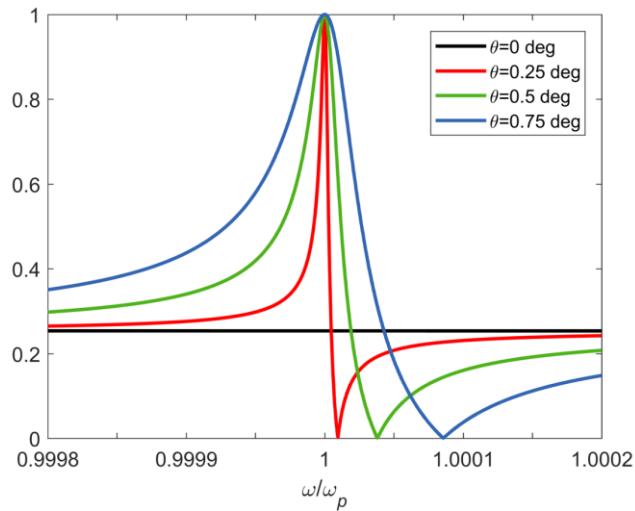
Figure 5.3. Reflection coefficient amplitude for small incident angles, as the resonant feature disappears at 0 deg.

structure is represented by an equivalent transverse transmission line network, and the supported modes can be found through the resonance condition

$$Z_{up} + Z_{down} = 0, \tag{5.15}$$

where Z_{up} and Z_{down} represent impedances looking up and down towards the end of the waveguiding structure from an arbitrary point in the transverse network, Figure 5.4 (a,b). This can be expressed as:

$$\frac{2Z_1 \left[Z_0 + jZ_1 \tan\left(\frac{k_{1z}t}{2}\right) \right]}{Z_1 + jZ_0 \tan\left(\frac{k_{1z}t}{2}\right)} = 0. \tag{5.16}$$

From this expression the even mode dispersion is derived as:

$$\tan\left(\frac{k_{1z}t}{2}\right) = j\frac{Z_1}{Z_0} = j\frac{k_{0z}\varepsilon_1}{k_{1z}}, \tag{5.17}$$

while the odd mode dispersion is obtained by placing an open circuit in the center of the transverse network model and yields:
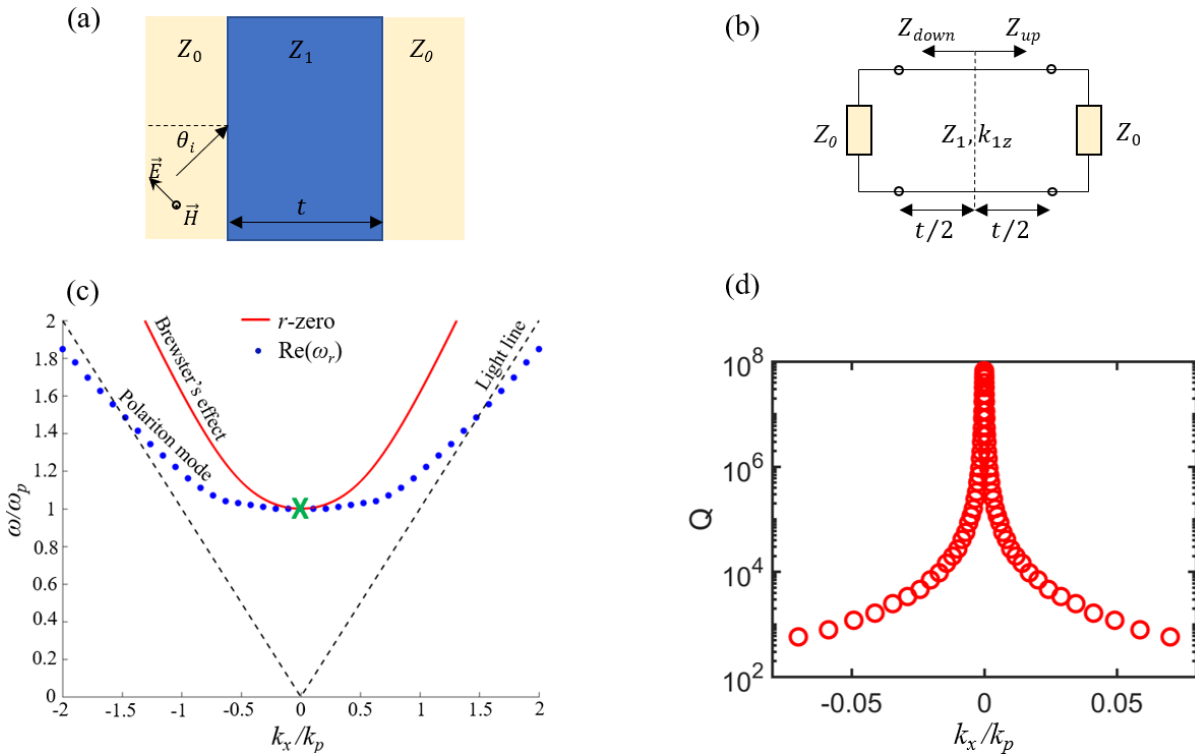
Figure 5.4. (a) Slab under consideration (b) TR model of the slab (c) Mode dispersion, *r*-zero dispersion (d) the Q-factor of the mode .
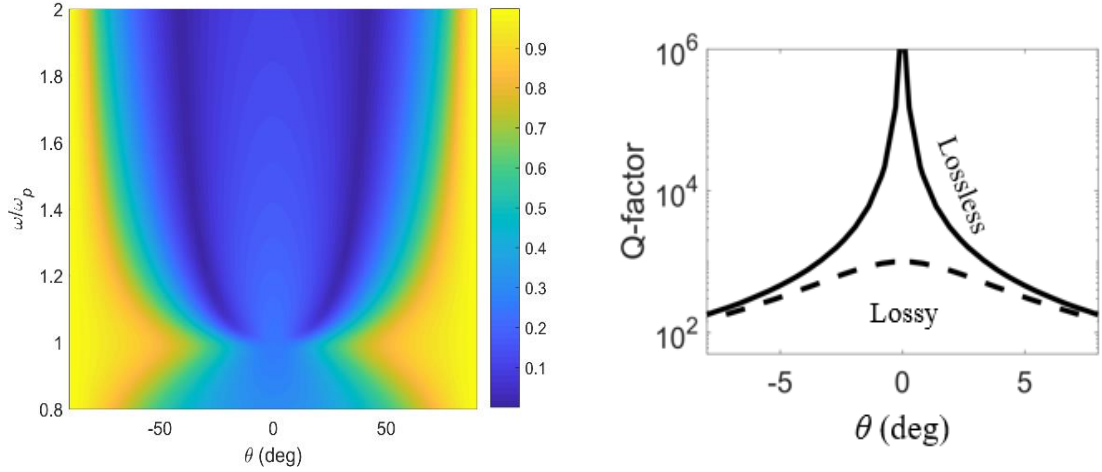
Figure 5.5. Reflection coefficient amplitude for a lossy Drude model and Q-factor comparison between lossless and lossy cases.

$$\cot\left(\frac{k_{1z}t}{2}\right) = j\frac{Z_1}{Z_0} = j\frac{k_{0z}\varepsilon_1}{k_{1z}}. \tag{5.18}$$

We plot the dispersion relation of the odd mode dispersion, which corresponds to the leaky polariton mode. As it enters the light cone, its eigenfrequency becomes complex, delineating the radiative nature of this mode. Namely, even if the materials considered are lossless, the imaginary part of the eigenfrequency is non-zero due to radiation loss, and it allows for calculation of the Q-factor of the mode. As shown in the Figure 5.4 (d), the Q-factor diverges at normal incidence, marking the presence of an embedded eigenstate.

The charges in this self-sustained mode of the slab oscillate along the z-direction in the entire volume ($E_{x,y}=0$, $E_z\neq0$). Consequently, an incoming wave impinging at normal incidence ($E_z^{inc}=0$) cannot excite this dark mode, in accordance with reciprocity, since the mode is not coupled to the radiation continuum.

It is interesting to comment on the effects of losses in the Drude material on the embedded eigenstate and the reflection coefficient. Figure 5.5 (a) shows the reflection coefficient amplitude with a lossy Drude model considered ($\gamma = 0.05\omega_p$), where it can be seen that zero associated with the Brewster effect is now absent close to normal incidence, and the sharp linewidth is not present. Figure 5.5(b) shows the comparison between the Q-factors of the lossless and lossy cases, indicating a major drop in the Q-factor when even small losses are considered.

5.3 Planar multilayer ENZ – Berreman EEs

To expand the discussion, we now consider a three-layer structure, such that a subwavelength dielectric gap opens in the middle of the ENZ layer, keeping the total thickness of ENZ constant, as shown in the Figure 5.6(a). We again analyze the reflection coefficient for this multilayerusing the ABCD matrix method, Figure 5.6 (b),. Interestingly, the Brewster effect reflection zeros just above the plasma frequency remain almost unchanged, indicating that the non-resonant impedance matching remains possible even if the overall effective permittivity of the multilayer is changed.

However, just below plasma frequency, a new zero of reflection appears. This zero represents the 0th order resonance of the multilayer, which guarantees impedance matching and full transmission of the waves. Although the single slab of ENZ did not allow full transmission bellow plasma frequency, the insertion of the dielectric gap changes the character of the overall
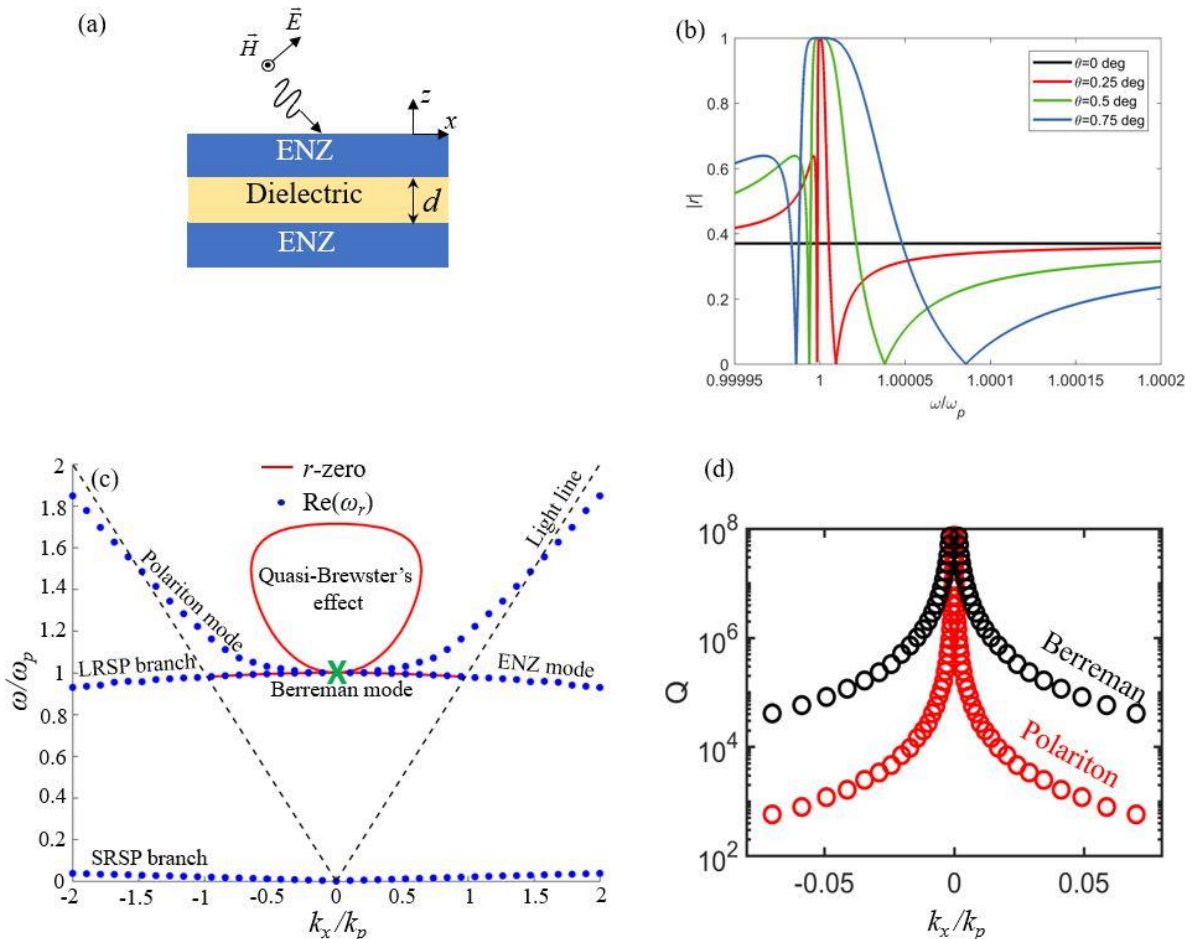
Figure 5.6. (a) Reflection problem sketch for a 3-layer structure. (b) Reflectance for TM excitation at small angles for t=400 nm, d=20 nm ($d \ll \lambda_{diel}$), ε_d =10. (c) Mode dispersion for the ENZ-dielectric-ENZ structure, LRSP corresponds to the long-range surface plasmon; SRSP corresponds to short-range surface plasmon. (d)Q factor of the polariton and Berreman modes. Plasma frequency is $f_p = \omega_p /2\pi$ =50 THz. Frequency axis is normalized to ω_p, while wave number axis is normalized to $k_p = \omega_p /c$.

structure. There is now a pair of reflection zeros on either side of plasma frequency for each incident angle, and both resonant features become narrower for smaller angles until they eventually disappear at zero incidence. This marks a presence of two EEs, both situated at the same point in the dispersion diagram.

To properly asses these EEs, we caluclate the dispersion relation for the three-layer structure. Using the TR method, we can obtain the even and odd mode dispersion relations – the TR condition for the multilayer states:

$$Z_{\text{up}} + Z_{\text{down}} = 2Z_2 \frac{Z_1\left(Z_0 + jZ_1 \tan\left(k_{1z}t\right)\right) + jZ_2 \tan\left(k_{2z}\frac{d}{2}\right)\left(Z_1 + jZ_0 \tan\left(k_{1z}t\right)\right)}{Z_2\left(Z_1 + jZ_0 \tan\left(k_{1z}t\right)\right) + jZ_1 \tan\left(k_{2z}\frac{d}{2}\right)\left(Z_0 + jZ_1 \tan\left(k_{1z}t\right)\right)} = 0. \quad (5.19)$$

Setting the numerator to zero leads to the even mode dispersion:

$$\tan\left(\frac{k_{2z}d}{2}\right) = j\frac{k_{1z}\varepsilon_d}{k_{2z}\varepsilon_{enz}} \frac{\left(k_{0z} + j\frac{k_{1z}}{\varepsilon_{enz}} \tan\left(k_{1z}t\right)\right)}{\left(\frac{k_{1z}}{\varepsilon_{enz}} + jk_{0z} \tan\left(k_{1z}t\right)\right)} \quad (5.20)$$

$$\cot\left(\frac{k_{2z}d}{2}\right) = j\frac{k_{1z}\varepsilon_d}{k_{2z}\varepsilon_{enz}} \frac{\left(k_{0z} + j\frac{k_{1z}}{\varepsilon_{enz}} \tan\left(k_{1z}t\right)\right)}{\left(\frac{k_{1z}}{\varepsilon_{enz}} + jk_{0z} \tan\left(k_{1z}t\right)\right)} \quad (5.21)$$

Figure 5.6 (c) shows the dispersion diagram for the TM modes of interest (blue dots), as well as the reflection zeros (red line). The peculiarity of this dispersion diagram comparing to the single ENZ slab is the new mode emerging just below plasma frequency. This is the so-called Berreman mode or Ferrel-Berreman mode, whose extension bellow the lightline is often referred to as the ENZ mode. It was first discussed by analyzing narrow absorption peaks appearing in thin-film multilayers [51].

Figure 5.6 (d) shows the Q-factor of the modes around plasma frequency, where both the polariton and Berreman modes' Q-factor diverges at zero transverse wavevector, indicating the presence of a doubly-degenerate EE.

To further confirm the existence of the two co-located EEs, we search for poles and zeros of the scattering matrix eigenvalues in the complex frequency plane for small incident
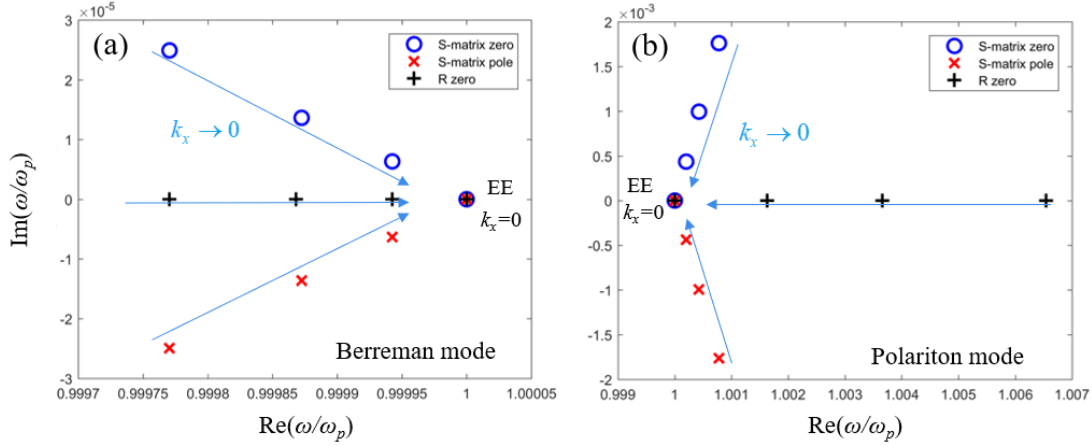
Figure 5.7. Singularities of the *S*-matrix eigenvalue-reflection spectrum in the complex frequency plane near normal incidence for four different values of k_x/k_p =[0.1, 0.075, 0.05, 0]. (a) Single slab of ENZ of thickness *t*=800 nm. (b) Polariton mode singularities for ENZ-dielectric-ENZ, *t*=400 nm, and dielectric thickness *d*=20 nm. (c) Berreman mode for (b).

angles (small transverse wavevector). Additionally, we plot the reflection zeros to complete the picture in the complex plane. Namely, the scattering matrix eigenvalues for reciprocal two-port network can be derived in general form as:

$$\sigma_1 = \frac{1}{2}\left(r_l + r_r + \sqrt{r_l^2 + r_r^2 - 2r_l r_r + 4t^2}\right),$$ (5.22)

$$\sigma_2 = \frac{1}{2}\left(r_l + r_r - \sqrt{r_l^2 + r_r^2 - 2r_l r_r + 4t^2}\right).$$ (5.23)

One consequence of Hermiticity (losslessness) is that the poles and zeros are complex conjugates, as they mirror each other in opposite complex half-planes. As shown in Figure 5.7, poles and zeros associated with both Berreman and polariton modes converge towards the real eigenfrequency $\omega = \omega_p$ from opposite sides, forming a doubly-degenerate EE. Additionally, the reflection zeros in both cases have purely real frequencies due to perfect impedance matching, indicating that perfect transmission occurs for real-frequency excitations in the lossless case.

To further understand the peculiarity of the Berreman mode arising in this three-layer structure, we next propose an analogy with lumped element circuits, which completely unveils the origin of the Berreman mode transmission, and gives it an intuitive physical explanation, Figure 5.8.

Due to purely evanescent behavior of waves in the ENZ layer below plasma frequency, the slab can be replaced by an inductor, as its wave impedance is purely inductive allowing no phase advance. In this first approximation, we will model the dielectric gap as a transmission

line with length d and characteristic impedance Z_2 which depends on the polarization and angle of propagation, Figure 5.8 (b). We choose a fixed frequency at which we will model our structure, $\omega = 0.98\,\omega_p$, i.e., we choose a fixed permittivity value which is around -0.04 at this frequency. Next we choose an arbitrary incidence angle, e.g. $\theta = 50\,deg$. To accurately portray the ENZ slab in these conditions, we choose the appropriate reactance value which we found to be $X = \omega L = 2270\,\Omega$. To validate this analogy, we plot reflectance, and real and imaginary parts of the input impedances as a function of dielectric thickness, and compare the original structure with the lumped element one. As it can be seen from the Figure 5.8 (c-e), the results nearly perfectly match, and the reflection zero associated with the Berreman mode happens at small values of d. This first reflection zero can be associated 0th order Berreman mode, as we designate it as such to differentiate it with higher-order r-zeros appearing at larger d. Namely, when d is slightly larger than half wavelength, another reflection zero happens,
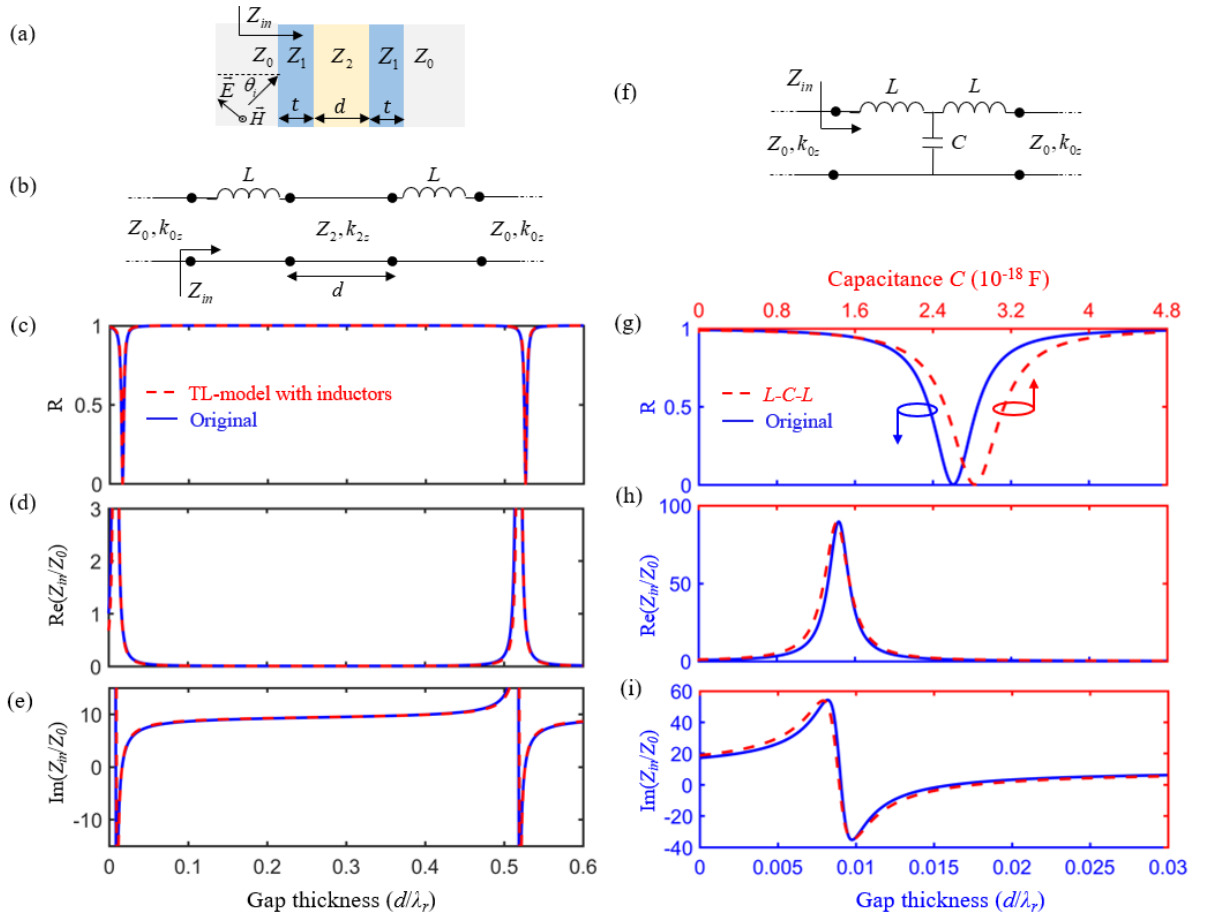
Figure 5.8. (a) Three layer structure under analysis. (b) Transmission line model of the structure, ENZ replaced by an inductor (c) Reflection coefficient of (a) and (b). (d) Real part of the input impedance of (a) and (b). (e) Imaginary part of the input impedance of (a) and (b), (f) Transmission line model of the L-C-L circuit, (g) Reflection coefficient of (a) and (f), as a function of d and C, respectively. (h) Real part of the input impedance of (a) and (f), (i) Imaginary part of the input impedance of (a) and (f).

indicating a higher order mode of the same resonant phenomena. These higher order modes will be discussed later in the chapter.

To get the full physical picture of the 0th order Berreman mode, we can next replace the dielectric gap in our structure with a capacitor. Namely, the impedance of the subwavelength dielectric layer is capacitive in nature, and although the waves are propagating in it, the phase advance through it is negligible, i.e., $k_{2z}d \approx 0$. Thus, the resonant behavior of such a multilayer can be accurately captured by a lumpled element lossless *L-C-L* circuit, Figure 5.8 (f).

To confirm this, we replace the dielectric with a capacitor. By changing the capacitance *C*, and consequently the reactance X_c, we can mimic the change of dielectric thickness. Thus, we simultaneously change the thickness *d* in the original structure and the capacitance *C* in the lumped-element circuit model – notice there are two x-axes, with each curve corresponding to its own x-axis. As it can be seen from Figure 5.8 (g-i), both models behave in the similar fashion, as the impedance and reflection coefficient follow the same trends. The nature of the response is completely analogous to the LCL circuit, however as thickness *d* grows, propagation effects start to contribute to the response and there is a noticeable difference for larger *d*. Nevertheless, it is clear that the nature of the 0th order Berreman mode can be entirely attributed to a classical LC resonance, where reactance contributions of the ENZ and dielectric layers cancel out, balancing the magnetic and electric energy of the resonator and allowing full transmission with negligible phase advance.

5.4 Higher-order EEs

To further investigate the potential of the 3-layer structure, we increase the gap size such that its thickness is equal to half of the longitudinal wavelength in the material at an angle of 50°. The corresponding dispersion diagram is shown in Figure 5.9 (a). In this case the 0th order Berreman mode shifts to lower frequencies, and its flat dispersion indicates its slow light nature, which can be used for enhanced light-matter interactions [189-191]. The angular bandwidth of this slow-light regime is exceptionally large, spanning across most of the light cone. Below the light line, the LRSP and SRSP modes occur, with the well-known asymptote $\omega = \omega_p / \sqrt{1 + \varepsilon_d}$.

Since the dielectric is half-wavelength thick, it also supports a Fabry-Perot mode. The precise resonant thickness for which a non-zero longitudinal wavenumber k_x supports such a resonance (corresponding to an incidence angle $\sin(\theta_i) = |k_x/k_o|$) is given by:

$$d = \frac{\lambda_r}{2} = \frac{c}{2f_r\sqrt{\varepsilon_d - \left(\frac{k_x}{k_0}\right)^2}} = \frac{c}{2f_r\sqrt{\varepsilon_d - \sin^2\theta_i}} \tag{5.24}$$

where λ_r is the resonant wavelength, f_r is the resonant frequency, c is the speed of light in vacuum. If the dispersion of this mode crosses the plasma frequency for some angle, i.e., if $f_r = f_p$, an off-normal (accidental) EE forms, for which the mode is perfectly confined without radiation leakage [91]. This Fabry-Perot mode, which represents a 1st order Berreman mode, supports full energy tunneling. The described system now supports two embedded eigenstates: the symmetry-protected one at normal incidence and an accidental one. Figure 5.9 (c) shows the dispersion zoomed in around the plasma frequency, and Figure 5.9 (d) shows the Q-factors of Fabry-Perot and polariton modes.
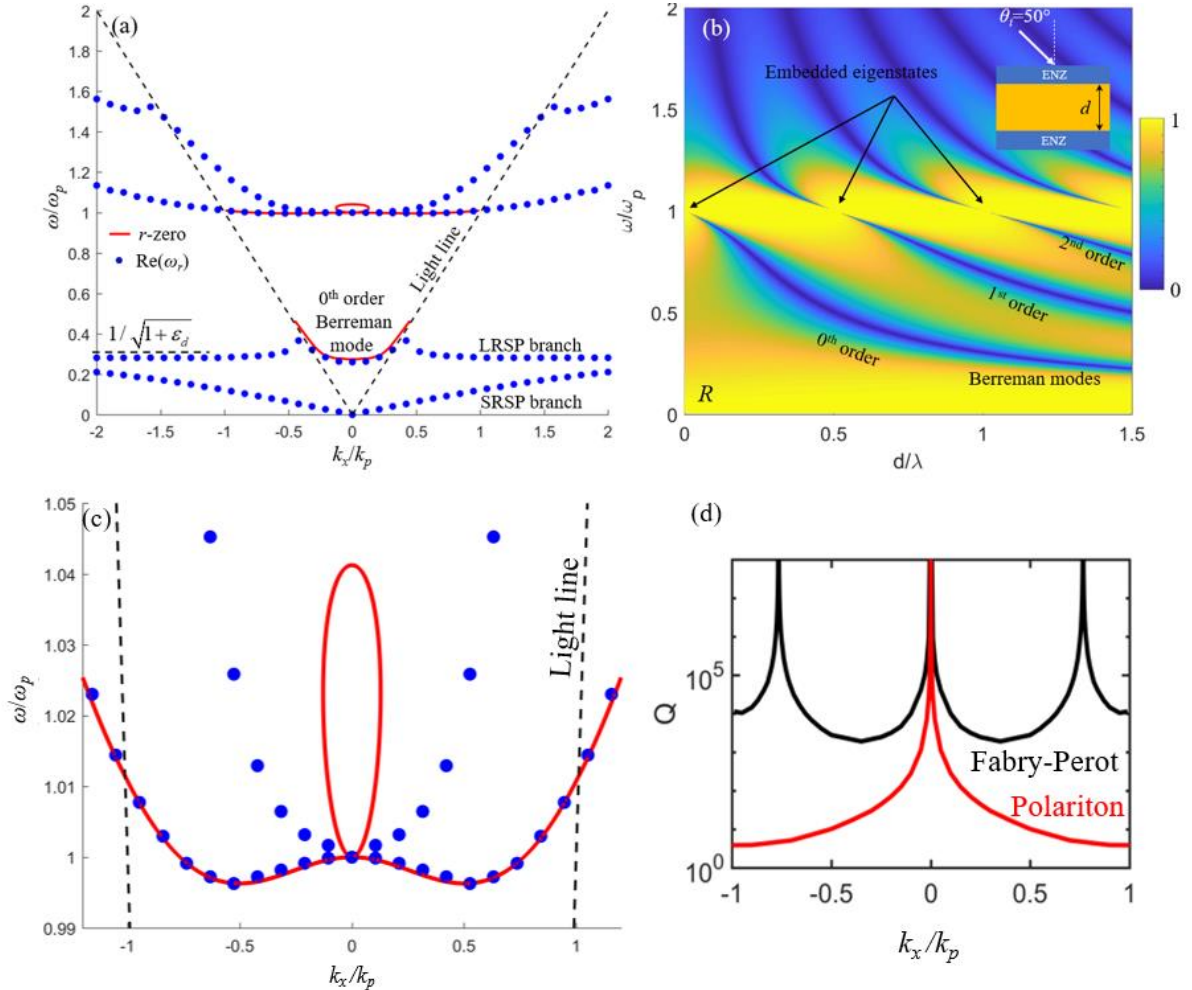
Figure 5.9. Higher-order Berreman modes and accidental EEs. (a) Mode dispersion for a half-wavelength thick dielectric gap, supporting both normal and off-normal incidence (θ_i =50°) embedded eigenstates, d=980 nm, ε_d =10.). (b) Reflectance for TMpolarized wave at θ_i =50° for different dielectric thicknesses, where different orders of Berreman modes and accidental EEs are visible.(c) magnification of the dispersion relation around the plasma frequency. (d) Q factor of the modes.

In order to better describe the effect of the dielectric thickness on the modal evolution, we plot the reflectance for TM polarized waves at an incidence angle of 50 deg for different dielectric thicknesses d, Figure 5.9 (b). The vanishing linewidth can be observed at the plasma frequency for $d = n\lambda_r/2$, corresponding to an embedded eigenstate of the nth order Berreman mode. It is worth noting that for $n = 0$ the system corresponds to a single ENZ slab, which makes this EE a trivial one.

5.5 Loss in ENZ

The role of loss in ENZ-based devices cannot be understated, as they are unavoidable in realistic materials and represent a limiting factor in many applications. Any material carries intrinsic loss, and when they are paired with the low group velocity of ENZ materials, even small loss can become critical. To study the effect of losses, we plot the Q-factor of the localized Fabry-Perot mode as a function of the loss factor g, Figure 5.10 (a). The loss of the ENZ material has been incorporated in the Drude model using $\varepsilon_{enz} = 1 - \omega_p^2/(\omega^2 + j\gamma\omega)$, where $\gamma = g\omega_p$ ($g = \text{Im}[\varepsilon_{enz}(\omega_p)]$) (. We fix the incidence angle again to 50 deg and the frequency to ω_p, at which the system supports an embedded eigenstate, and calculate the reflection coefficient in the complex frequency space as a function of g. The reflection poles correspond to the eigenmodes of the system with complex frequency $\omega_r = \omega_{re} + j\omega_{im}$, and therefore the Q-factors can be readily calculated as $-\omega_{re}/2\omega_{im}$. It can be seen that there is a linear relation between g and Q-factor, with $Q \sim 1/g$, putting a rather restrictive limit on the achievable Q-factors.

Another critical effect associated with the material loss can be highlighted by analyzing the poles and zeros of reflection. The Fabry-Perot resonance in this system is a 1st order
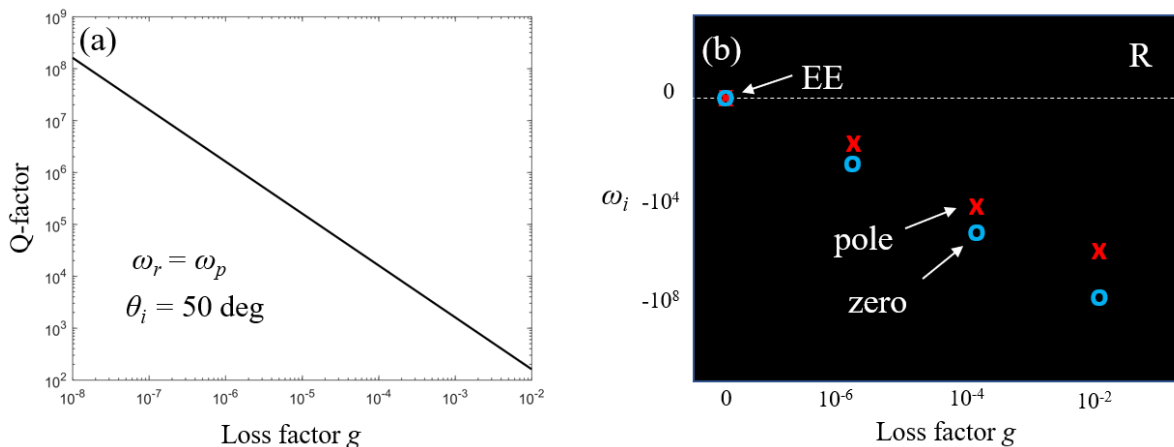
Figure 5.10. Effect of loss on the accidental embedded eigenstate. (a) Q factor as a function of loss factor g. (b) Sketch of the position of complex poles and zeros of reflection as a function of g.

Berreman mode, supporting complete tunneling of energy in the lossless limit, with all of the zeros of reflection pinned to the real frequency axis (zero imaginary part). This tunneling persists along the whole Fabry-Perot dispersion line, except at the EE where the reflection has both a pole and a zero at the same real frequency, i.e., the reflection coefficient is undefined in the lossless limit. By adding loss, the pole and zero split and move down in the complex plane, making this state a quasi-EE (qEE). Interestingly, the pole stays *closer* to the real frequency axis than the zero, as shown in Figure 5.10 (b). This peculiarity has important implications: in the lossy case, the tunneling of the Berreman mode vanishes at the angle corresponding to the quasi-EE. In parallel, the reflection coefficient becomes larger than zero and approaches unity at the qEE. Indeed, the transition from metal to dielectric at the plasma frequency necessarily results in strong reflection of the ENZ layers and significant impedance mismatch with free space, which persist against added losses. As a consequence, the resonant line vanishing in the realistic lossy system happens not only due to the Q-factor enhancement but also due to inevitable reflection at the qEE.

5.6   Realistic structure comprising SiC

Although the discussed effects of loss may fundamentally limit the Q-factor of quasi-embedded eigenstates in the proposed geometry, low-loss ENZ materials can be used to achieve very high-Q quasi-EE resonances, which are of interest for selective transmission and sensing. Here, we explore a realistic structure with silicon carbide as the ENZ material that supports high-Q quasi-EE at 50 deg incidence, Figure 5.11. SiC is an excellent candidate for this purpose since it exhibits very low loss at the longitudinal phonon frequency where the real
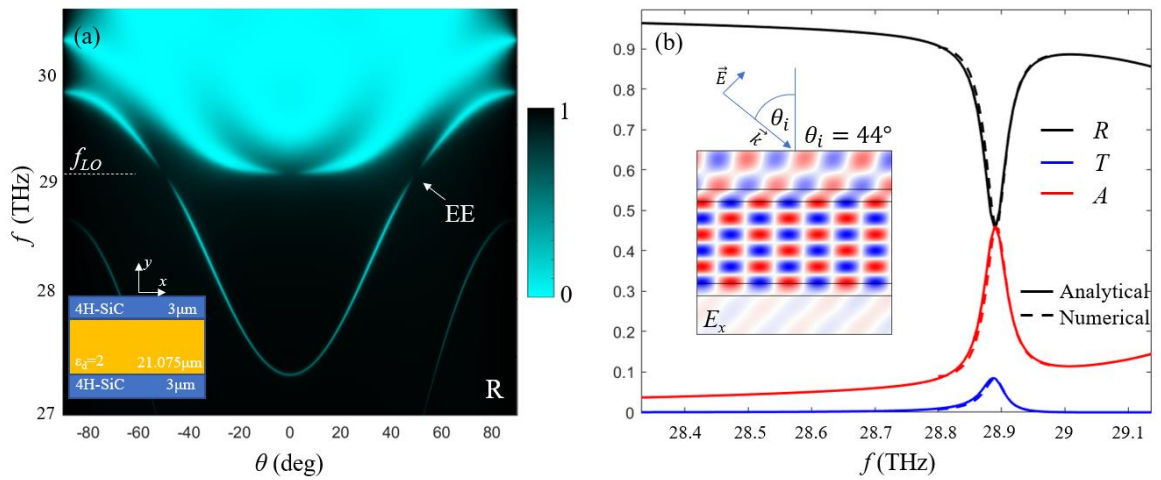
Figure 5.11. Demonstration of quasi-EE in SiC. (a) Reflection spectrum for TM polarized light; inset shows a sketch of the geometry.(b) Reflectance, transmittance, and absorptance of a higher-order Berreman mode at 44° incidence. Inset: E-field distribution inside the structure.

part of permittivity crosses zero [40, 192,193]. The permittivity of 4H-SiC can be approximated as [40]:

$$\varepsilon_{\text{SiC}} = \varepsilon_\infty \left(1 + \frac{(\omega_{LO}^2 - \omega_{TO}^2)}{\omega_{TO}^2 - \omega^2 + j\gamma\omega} \right),$$

(5.25)

where ω_{LO}=29.08 THz and ω_{TO}=23.89 THz are longitudinal and transverse optical phonon frequencies, γ=0.04 THz is damping, ε_∞=6.6. The material in the dielectric layer has permittivity of 2 and thichkness $d = 21.075\ \mu$m.

Figure 5.11(a) shows the reflection spectrum of a SiC-dielectric-SiC cavity, displaying a q-EE that occurs at the angle of incidence of 50 deg. The high-Q Berreman mode supported by this structure has a dispersion crossing with the ω_{LO} frequency of SiC where the ENZ regime arises. This is corroborated by vanishing of the resonant line in the reflection spectrum. A numerical demonstration of a resonance close to the EE point is shown in Figure 5.11 (b), with Q $\sim 10^3$.

5.7 Quasi-EE for narrowband perfect absorption and thermal emission

The ENZ regime implies strong light-matter interactions with ultranarrow scattering lines. In the case of a realistic lossy ENZ, this property results in enhanced absorption near the ENZ point, as shown in Figure 5.11 (b), and this property can be used to engineer narrow-band absorbers based on quasiembedded eigenstates [186]. Following the conventional approach to obtain perfect absorption [194], we reduce transmission through the structure by increasing the thickness of the lower SiC layer and consider the asymmetric structure geometry in Figure 5.12(a). As discussed above, incorporation of loss ensures reflection maxima exactly at the qEE, which results in weak absorption. However, the resonances around the qEE can display absorption peaks with extremely narrow angular and frequency bandwidths. To exploit the potential of the proposed multilayer structure to its full extent, we first analyze the absorption of the single-slab and asymmetric three-layer structures (Figures 5.12(a) and 5.12(d), respectively). Both the polariton mode in a thin free-standing ENZ layer (Figure 5.12(d)) and the higher-order Berreman (Fabry-Perot) mode in the three-layer structure (Figure 5.12(a)) have absorption features that are strongly related to the spectral position of the ENZ point. However, the polariton mode does not allow efficient dispersion control, has poor angular selectivity, and does not support engineering of perfect absorption). Although the dispersion of the Fabry-Perot mode in the 3-layer structure can be controlled with the resonator itself, thus potentially improving the angular and frequency bandwidth of the absorption peaks, the structure in Figure 5.12 (a) has poor angular selectivity, since the dispersion of the Fabry-Perot

mode follows the ENZ frequency ω_{LO} closely for all incident angles where the absorption is enhanced.

To change the dispersion of the mode and further improve selectivity, we incorporate a distributed Bragg reflector (DBR) between the resonator and each SiC layer, Figure 5.12 (b,c). While the proposed structure can get quite bulky, the spectral and angular bandwidths become exceptionally narrow for the long-wavelength IR region. The introduction of a DBR expectedly narrows the spectral width of the resonance, yet it introduces a steep angular dispersion of the Fabry-Perot mode as well, moving it further away from the ENZ frequency. This, in turn, enables a narrower angular width of near-perfect absorption regions around the quasi-EE.
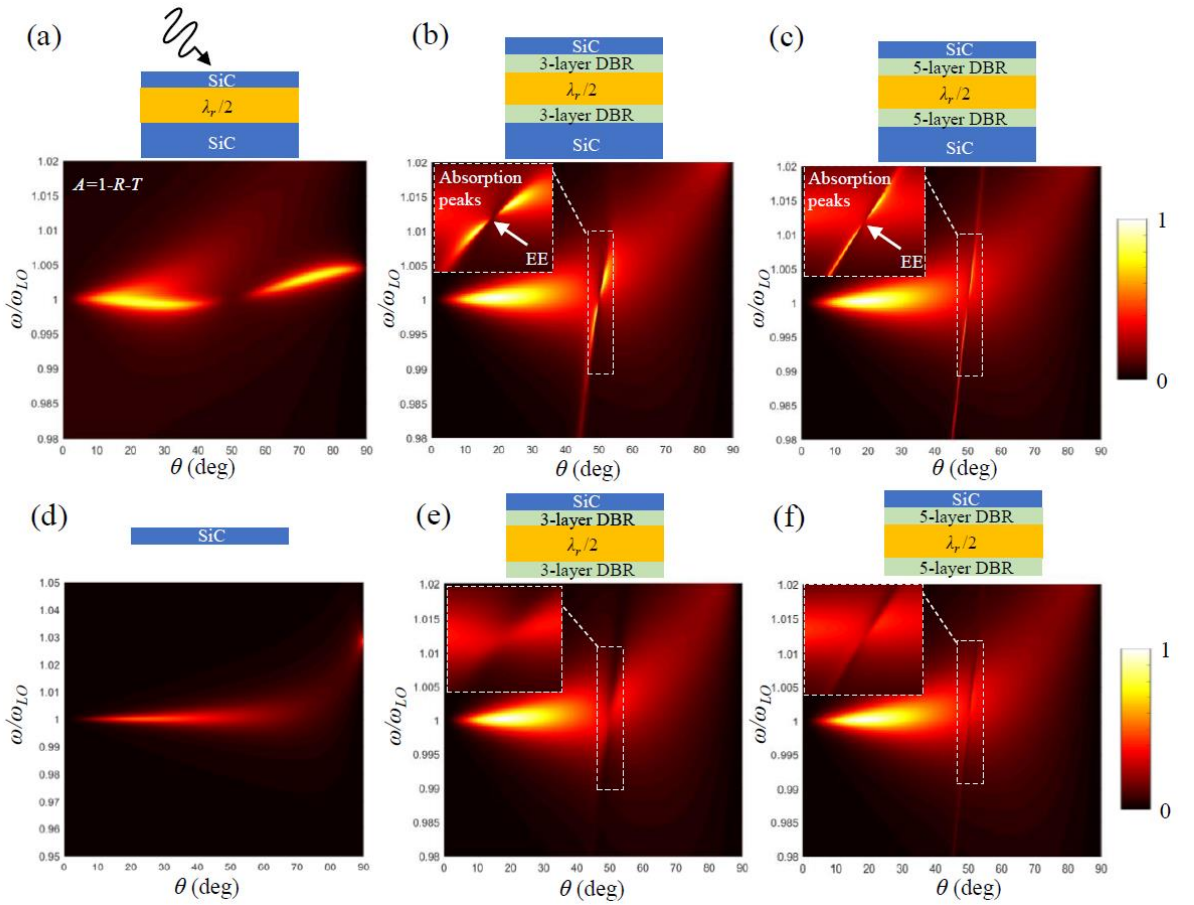
Figure 5.12. Absorption for TM illumination from the top with schematics of the multilayer structures under investigation (a) Asymmetric SiC-Dielectric-SiC structure supporting near-perfect absorption of the Fabry-Perot mode. (b) Absorption spectrum for a multilayer structure with 3-layer DBR, and close-up view around q-EE. (c) Absorption spectrum for a multilayer structure with 5-layer DBR, and close-up view around q-EE, (d) Single SiC slab, (e) same as (b) with removed bottom SiC layer, (f) same as (c) with removed bottom SiC layer. Top SiC layer thickness is $t_T = 500$ nm, bottom is $t_B = 1500$ nm. High and low permittivity quarter-wave thickness' are $d_H = 656$ nm and $d_L = 2.168$ μm, while the resonator thickness is $d_R = 4.33$ μm. Resonator and the low permittivity slab of the DBR are made of a low-loss low permittivity material, modeled after BaF$_2$ with $\varepsilon_r \approx 2$ around 10μm. The high permittivity slab for DBR used here is made of Ge which has $\varepsilon_r \approx 16$ and negligible losses around 10μm.
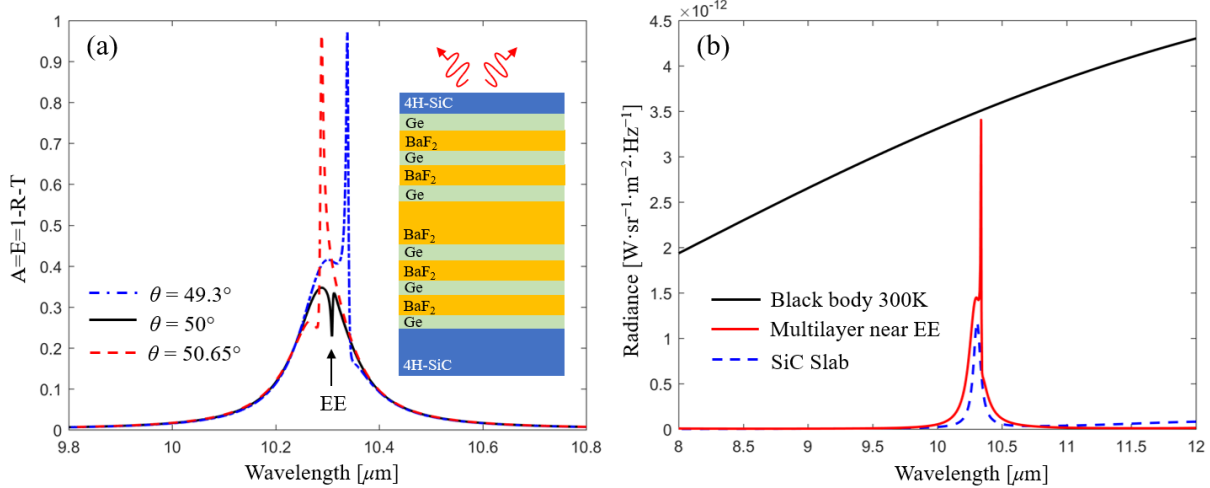
Figure 5.13. Multilayer structure, with same parameters as in figure 5 except for optimized t_i=400 nm and t_B=2 μm, with 19.35μm thickness in total. (a) Absorption/thermal emission around EE (b) TM spectral radiance of the proposed structure at 49.3° compared to a single SiC slab and black body radiance at 300K

These features abruptly disappear when one of the SiC is removed, as shown in Figures 5.12 (e,f), which demonstrates the importance of the ENZ-resonator-ENZ configuration to yield this exotic absorption and thermal emission features. Figure 5.12 (b) shows near-perfect absorption at two points near the q-EE, which are both spectrally and spatially narrowband. Both the absorption peak and the large Q-factor are a direct result of the q-EE in the ENZ regime, indicating its pivotal role in engineering extreme light-matter interactions and absorption with extremely narrow spectral and angular features.

Given the extreme spectral and spatial selectivity of the proposed absorbing structure, and the fact that operation frequency falls within the thermal long-wave infrared window (8-12μm), it represents an ideal candidate for the design of quasi-coherent thermal emitters, given Kirchhoff's law that directly relates optical absorption and thermal emission [195].

In that sense, we study a multilayer structure with 5-layer DBR, as shown in the inset of Figure 5.13 (a). The absorption (emission) lines for angles around the embedded eigenstate display a very narrow band, with minimum absorption exactly at the q-EE as discussed previously. To compare the thermal performance of the structure with a single slab of SiC, we plot spectral radiance in the region 8-12 μm for the same structure, Figure 5.13 (b). Emission peak near the qEE demonstrates extreme spectral selectivity, with a linewidth of less than 10 nm at half-maximum, and consequently superiority in comparison to the single-layer SiC structure.

5.8   Conclusion

In this chapter, an in-depth investigation of modes supported by planar structures comprising ENZ materials was presented, and several key features of these modes were identified. Specifically, we explain the origin and nature of leaky Berreman modes and how they relate to embedded eigenstates using a simple model based on the transverse resonance technique. We identify two types of EEs in such structures: symmetry-protected EEs at normal incidence and accidental EEs at a desired angle of incidence. For practical considerations, we propose a realizable SiC based structure that supports quasi-EEs with high Q factors and field enhancements. Based on these concepts, we demonstrate extremely narrow-band absorber-thermal emitters near the qEE.

Chapter 6: Topological scattering singularities and EEs for polarization control and sensing[5]

6.1 Introduction

As discussed briefly in Chapter 2, electromagnetic EEs supported by periodic systems have been shown to possess a topological feature in the form of a polarization singularity in the transverse wavevector space. Their robustness has been explicitly attributed to their topological nature [92,93], rooted in the fact that these singularities comply with topological charge conservation [196,197]. The topological nature of EEs has spun-off several research efforts, exploring the merging of EE charges to produce even more confined resonances in realistic systems [101] and unidirectional guided modes within the continuum [100]. The topological properties of EEs have been especially useful for polarization control, as it was shown that topologically protected polarization conversion is possible [102], and circularly polarized states can arise from BICs by breaking spatial symmetries [103-105]. Recently, the generation of vortex beams through EEs [198] and efficient topological vortex laser generation [199] were demonstrated, showing the potential of topological phenomena in radiative and scattering processes. Further connection between novel topological phenomena in the form of higher-order corner states and EEs has also recently been established in [200], indicating the far-reaching topological consequences that non-radiating states may have on the topological states of electromagnetic structures. Besides using the standard Hamiltonian formalism, the topological features of these systems can be studied through the scattering matrix formalism, and specifically by analyzing the complex reflection coefficient, where phase vortices arise [102, 201,202]. This approach is very valuable because the features of the scattering matrix correspond to actual observables that can be looked for experimentally.

In this chapter we will extend the concept of topological photonics to planar reflective systems that support EEs. Using the scattering matrix formalism and complex frequency analysis, we will unveil their topological nature and the emergence of topologically-protected scattering singularities. The proposed system supports symmetry-protected and accidental EEs, which are shown to be the origin of scattering singularities emerging upon insertion of loss/gain in the constituent materials. We focus on the lossy case and show that perfect-absorption

---

singularities are intrinsically connected to the underlying EEs. Methods of formation, annihilation and control of these topological charges are discussed, providing a versatile tool to manipulate amplitude, phase, and polarization of reflected waves. Using these concepts, we demonstrate several applications of these phenomena for polarization control and sensing.

6.2 EEs and topological charges in planar reflective multilayers

We constrain the discussion to reflective structures; such structures can be described by a scattering matrix with only one element – the reflection coefficient. As discussed in Chapter 4, the singularities of the scattering matrix eigenvalues now exactly coincide with reflection coefficient singularities which has interesting consequences when considering one-port structures that support embedded eigenstates.

We will consider planar reflective structures as shown in Figure 6.1. (a) and (b), infinitely extended in two directions. Namely, we will analyze the reflection coefficient of a resonant top layer that is backed by PEC, both with and without a dielectric spacer between them. To start, we first develop a reflection coefficient formalism employing complex frequency, which will provide a simple and intuitive picture of the underlying phenomena. We can represent such a reflective system with a transmission line model shown in Figure 6.1 (c,d), where derived input impedance for both cases are:

$$Z_{in1} = Z_1 \tanh(jk_{1z}t), \tag{6.1}$$

$$Z_{in2} = Z_1 \frac{Z_2\tanh(jk_{2z}d) + Z_1\tanh(jk_{1z}t)}{Z_1 + Z_2\tanh(jk_{2z}d)\tanh(jk_{1z}t)} \tag{6.2}$$
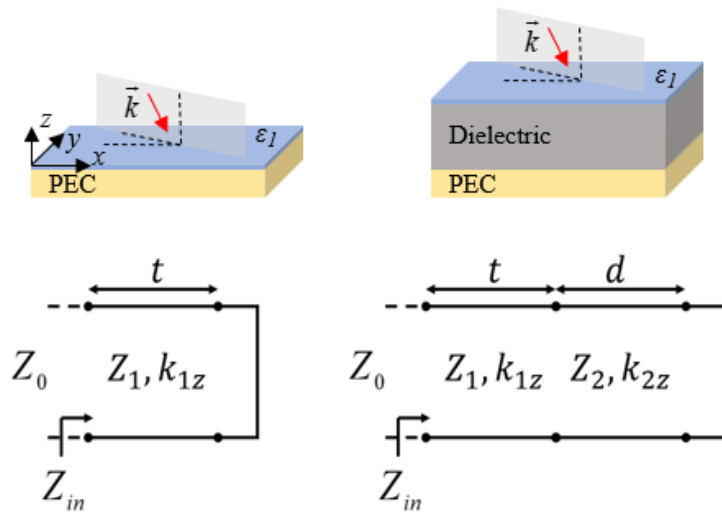
Figure 6.1. Reflective structures under consideration, and their equivalent transmission line network.

where k_{1z}, k_{2z} represent the wavenumbers along the z-axis in the layers, t is the top layer thickness, d is spacer thickness, $Z_1 = k_{1z}/\omega\varepsilon_0\varepsilon_1$ and $Z_2 = k_{2z}/\omega\varepsilon_0\varepsilon_2$ are the TM wave impedances of the two materials. The reflection coefficient for both cases can be calculated as:

$$r = \frac{Z_{in} - Z_0}{Z_{in} + Z_0},$$ (6.3)

from which the condition for singularities can be derived as:

$$\tanh(jk_{1_z}t) = \pm\frac{Z_0}{Z_1},$$ (6.4)

$$\tanh(jk_{2_z}d) = \pm\frac{Z_0}{Z_1}\left(\frac{Z_1\tanh(jk_{1_z}t) - Z_0}{Z_0\tanh(jk_{1_z}t) - Z_1}\right).$$ (6.5)

By searching for reflection coefficient singularities in the complex frequency plane i.e., poles and zeros of reflection coefficient, we also determine the S-matrix singularities associated with eigenmodes and perfectly absorbing states. We start our analysis by considering the structure in Figure 6.2 (a), where the top layer material follows a Drude dispersion
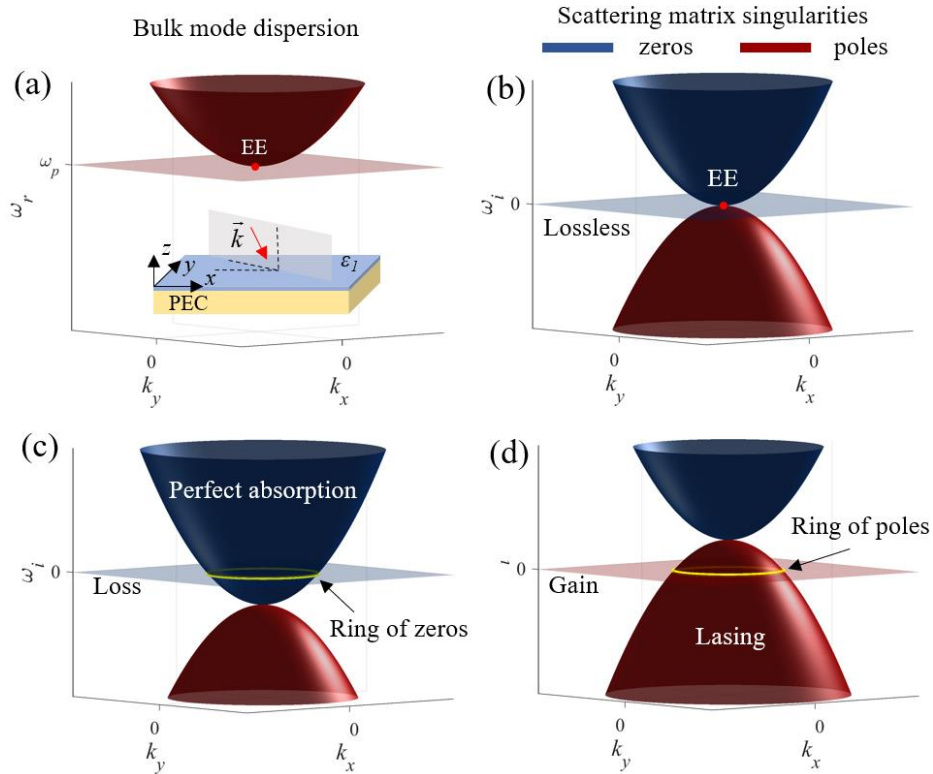
Figure 6.2. (a) TM-bulk mode dispersion. Pole and zero dispersion in the imaginary frequency space for: (b) lossless case, (c) lossy case, (d) gainy case.

$\varepsilon_1 = \varepsilon_0\left[1 - \omega_p^2/(\omega^2 + j\gamma\omega)\right]$. We analyze the leaky mode dispersion in the proximity of the plasma frequency ω_p, Figure 6.2 (a), which is obtained by searching for poles of the reflection coefficient, eq (6.4). Transverse magnetic (TM) bulk modes in a plasma slab have been discussed in the previous chapter, and the underlying symmetry-protected embedded eigenstate has been analyzed in detail. When compared to the free-standing ENZ slab analyzed in the previous chapter, the PEC-backed ENZ slab has the same modal dispersion, Figure 6.2(a). This time, we plot the dispersion in the whole transverse wavevector space. The mode gets less radiative as it approaches the zero transverse wavevector and it eventually turns into an EE as it touches the plasma frequency at $k_\parallel = 0$.

The main difference between the PEC-backed and freestanding ENZ is the reflection zero dispersion. Namely, due to having a single port, the zeros and poles of the reflection coefficient are identical to the *S*-matrix singularities, meaning that in a Hermitian system they come in complex conjugate pairs. Thus, the *r*-zero (perfect absorption) dispersion is a mirror copy of the pole (mode) dispersion in the imaginary frequency space, Figure 6.2 (b). Furthermore, *r*-zero in a single port system implies perfect absorption, $A = 1 - |r|^2$, which is in contrast to the 2-port lossless case where reflection zero implies full transmission.

Due to the existence of EE, the zero and pole dispersion coincide at zero-imaginary frequency, i.e., exactly at plasma frequency. By introducing loss (gain) in the slab, the dispersion surfaces translate down (up) along the imaginary frequency axis, creating a ring of real-frequency zeros (poles), Figure 6.2 (c,d). The intersection of scattering singularities with the real frequency axis represents a topological object – a charge with non-zero winding number of a physical parameter in given parameter space.

The topological signature of these states can be observed in the wavenumber-frequency plane by plotting the vector flow of r, Figure 6.3. In the ω_r-$k_\parallel$ two-dimensional space, taking into account a single incidence plane, it is easily observable that, upon adding loss, the EE
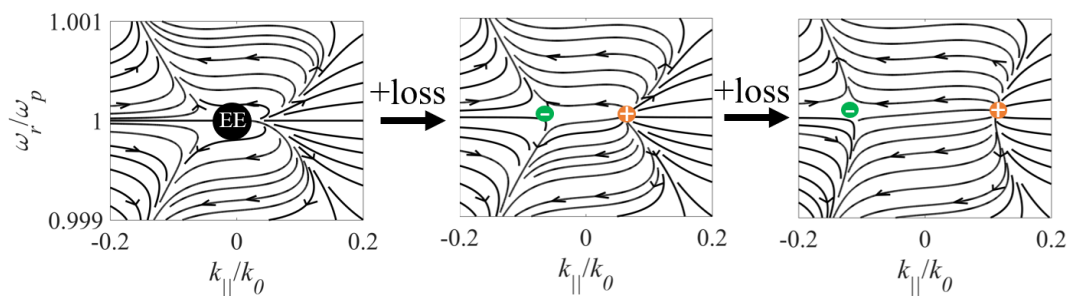
Figure 6.3. Vector flow of the reflection coefficient in a single incidence plane for lossless and lossy cases. Splitting of two degenerate charges (reflection zeros) as loss is incorporated.

splits into two vortices, a saddle-type (green) and a source type (orange). We only use loss in the following discussion to control the non-Hermiticity of the system, since loss is unavoidable while gain cannot be as readily obtained in most practical scenarios, but similar considerations may be applied to gain as well. As it is visible in Figure 6.4, the non-zero winding number associated with these vortices arises in the phase of the reflection coefficient in the real-frequency space, as phase acquires a $\pm 2\pi$ increment when encircling them in the frequency-incident angle space. The charge and polarity is defined by the amount of phase accumulation when encircling them counter-clockwise in the plane:

$$q = \frac{1}{2\pi} \oint d\phi. \tag{6.6}$$

These types of vortices have been studied extensively in the context of singular optics [203,204]. The splitting of EE into a pair of charges, in this case a pair of perfectly absorbing points, sheds a new outlook to previous reports on pairs of perfect absorption occurring in reflective systems [201, 205-206]. As we show later, each one of the analyzed EEs produces exactly two charges on the $k_{//}$ axis (incidence angle $\theta = \sin^{-1}|k_{//}/k_0|$), due to the parabolic dispersion of the scattering singularity around the EE. These perfectly absorbing states can only be destroyed by charges of opposite polarity if they are available. In the case studied here, there are no additional charges available, thus there is no mechanism to annihilate charges except going back to an EE in the lossless limit ($\gamma=0$), which represents a special case of merging charges. This merging is, in fact, necessary due to energy conservation, as no energy can be absorbed in a lossless system. Another way to interpret this result is to notice that perfect absorption (reflection-zero) corresponds to the condition of critical coupling, where absorption and radiation losses are perfectly matched. If absorption losses γ turns to zero, radiation losses must also turn to zero to yield a singularity, and the eigenstate is decoupled from the
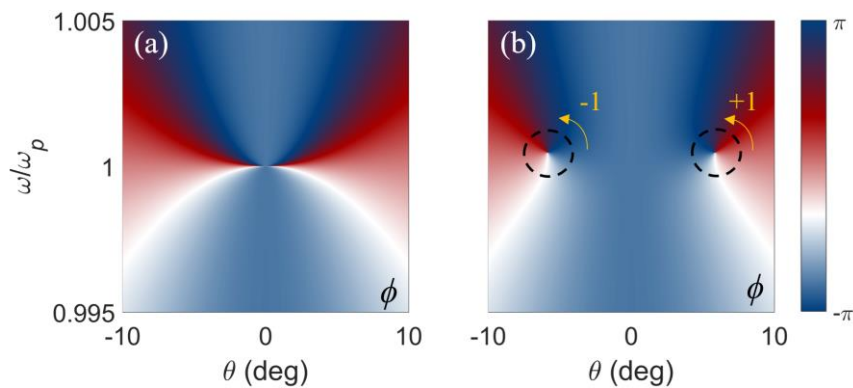
Figure 6.4. Phase of the reflection coefficient for different incidence angles for: (a) lossless and (b) lossy cases. Two oppositely charged phase vortices emerge upon insertion of losses.

environment, thus showing the close correlation between critical coupling and EEs in one port systems.

To further enrich the discussion, we move to a more general scenario and analyze the spacer shown in Figure 6.5 (a), consisting of a dielectric spacer sandwiched between a PEC and a resonant top layer. We model the top layer with a Lorentz type of permittivity response, as shown in Figure 6.5 (b):

$$\varepsilon_1 = \varepsilon_0 \left(1 + \frac{\omega_p^2}{\omega_0^2 - \omega^2 - j\gamma\omega} \right), \tag{6.7}$$

where ε_0 is the vacuum permittivity, ω_p is the plasma frequency, ω_0 is the Lorentz resonance frequency, and γ is the damping or absorption loss. This type of permittivity describes the electric response of different naturally occurring materials, including metals, semiconductors and polar dielectrics like SiC or AlN [207]. Moreover, such a response can be induced by resonant metasurfaces, either with metallic or dielectric realizations [201, 208]. Thus, our theoretical discussion can be applied to various scenarios, whether using isotropic bulk materials, 2D materials or metasurfaces.
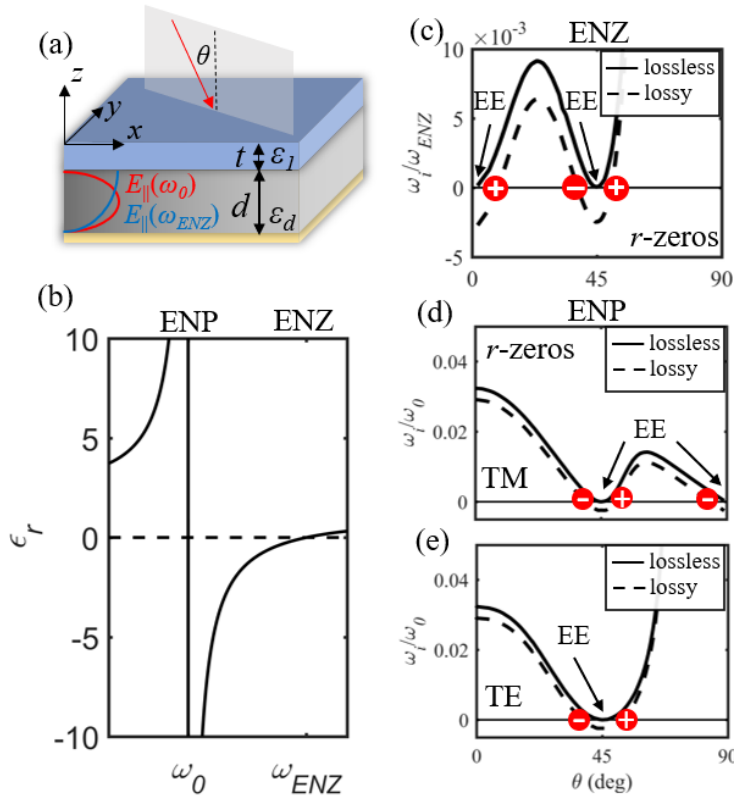
Figure 6.5. (a) Spacer structure under analysis with sketched non-radiative mode profiles. (b) Drude-Lorentz permittivity dispersion with designated ENP and ENZ frequencies (c). TM reflection-zero dispersion in the ω_i-θ plane for the ENZ case. (d) TM reflection-zero dispersion in the ω_i-θ plane for the ENP case. (e) TE reflection-zero dispersion in the ω_i-θ plane for the ENP case.

The spectral points of particular interest are the Lorentz resonance frequency ω_0 and zero-crossing ω_{ENZ} frequency. In the lossless case (γ=0), the permittivity attains singular values at these frequencies, $|\varepsilon|=\infty$ and ε=0, respectively. We refer to these regions as ENP (epsilon near-pole) and ENZ [209]. Under these conditions, such a layer imposes a hard boundary condition [88] – at ω_0 it effectively acts like an electric wall or PEC (for both transverse-electric TE and transverse-magnetic TM polarizations), while at ω_{ENZ} it acts like a magnetic wall or PMC (for TM polarization only). This can be attributed to the surface impedance of the layer going to 0 (PEC at ω_0) or infinity (PMC at ω_{ENZ}). With the bottom PEC, such a theoretical structure can provide perfect light trapping at the frequencies of singular permittivity, since the top and bottom layers act like perfect mirrors.

The dielectric spacer supports a continuum of modes above the lightline, which can couple to free-space radiation, as this structure is electromagnetically open from the top. However, if a mode of the spacer, i.e., a Fabry-Perot mode, overlaps with one of the top layer material resonances, a leaky mode with zero radiation decay (EE) is supported [91]. At $\omega_0=2\pi f_0$, the spacer thickness required to support such a mode is

$$d = \frac{n\lambda_r}{2} = \frac{nc}{2f_0\sqrt{\varepsilon_d - \sin^2\theta}}, n = 0, 1, 2..., \tag{6.8}$$

where c is the speed of the light in vacuum, f_0 is the Lorentz resonance frequency, ε_d is the dielectric layer permittivity, and θ is the incidence angle. The tangential component of the electric field is required to be zero at both top and bottom boundaries, as sketched in the inset of Figure 6.5 (a). On the other hand, at $\omega_{ENZ}=2\pi f_{ENZ}$ the magnetic field has a null at the boundary with the top layer, thus the resonant thickness is

$$d = \frac{(2n+1)\lambda_r}{4} = \frac{(2n+1)c}{4f_{ENZ}\sqrt{\varepsilon_d - \sin^2\theta}}, n = 0, 1, 2.... \tag{6.9}$$

We first focus on the ENZ case – Figure 6.5 (c) shows the dispersion of the reflection-zeros in ω_i-θ plane, calculated with eq. (6.5) in ω_r-ω_i-θ plane. We note here that the reflection-zero condition is identical to the condition of perfect absorption, perfect impedance matching, and critical coupling, as all of these describe the same phenomenon in one-port systems. At the plasma frequency, this structure supports a symmetry-protected EE at 0 deg and an accidental EE at a designed angle of 45 deg. Namely, the dispersion of the resonant mode is "pinned" to the point of normal-incidence and ENZ frequency for any dielectric thickness, thus this symmetry-protected EE is intrinsic to this configuration and cannot be controlled or moved.

On the other hand, the accidental EE can freely move along the incident angle axis at ω_p, and the angle of EE can be chosen according to eq. (6.9).

Although the magnitude of the reflection coefficient is unity for any frequency and angle in the lossless case, the EEs are visible in the reflection coefficient phase. In real-frequency space, they manifest themselves as phase resonances with diverging linewidth, as visible in Figure 6.6 (a) (left). These features are only available for TM excitation due to the plasmonic nature of the underlying modes. A similar result with diverging phase-resonances was reported in [210], although the origin of EE here is quite different.

The utility of phase analysis becomes apparent when losses are introduced, Figure 6.5 (c) and Figure 6.6 (a). Namely, the dispersion of reflection-zeros shown in Figure 6.5 (c) shifts down along the imaginary frequency axis, creating intersections with the θ-axis and thereby creating topological charges.

As shown in the amplitude plot in Figure 6.6 (a, right), pairs of reflection-zeros and consequently perfect absorption points emerge from EE, where the charge emerging from the
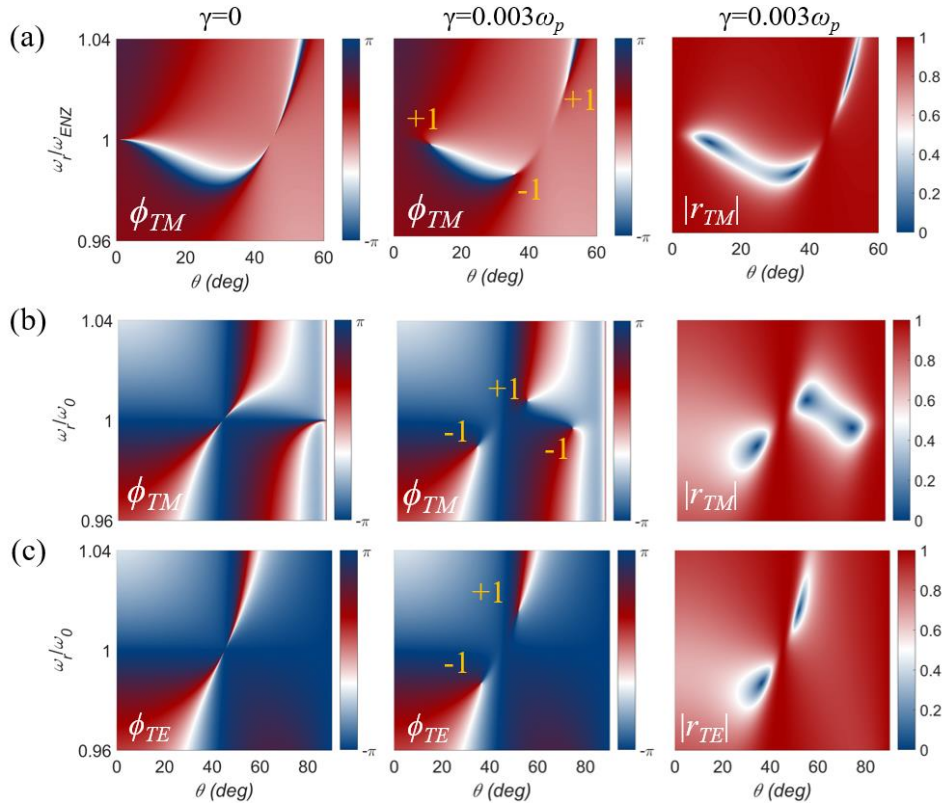
Figure 6.6. (a) ENZ TM reflection coefficient phase and amplitude for lossless (left) and lossy cases (center and right). (b ENP TM reflection coefficient phase and amplitude for lossless (left) and lossy cases (center and right). (c). ENP TE reflection coefficient phase and amplitude for lossless (left) and lossy cases (center and right).

symmetry-protected EE has a mirror copy in the negative θ-axis and thus is not visible in the plot.

A similar scenario arises for the ENP case – an accidental EE appears at a designed angle of 45 deg. More interestingly, however, both TM and TE modes have real-eigenfrequencies at the same point in the dispersion diagram, Figure 6.6 (b, left) and (c, left). This happens because at ω_0 the impedance of the top layer goes to zero, essentially acting as a perfect mirror regardless of polarization. Additionally, for TM polarization a symmetry-protected EE appears at the light line (90 deg incidence) and, analogously to the ENZ case, it is "pinned" to the same point regardless of the spacer thickness. We again introduce loss and notice topological charges emerging. Symmetry protected EE produces one charge with the oppositely charged mirror copy in the negative θ space (due to symmetry), while the accidental EEs split into two charges. It should be noted that the ENP layer used as a mirror here has a finite thickness, and thus hosts an infinite number of FP modes in the lossless case as the permittivity approaches $+\infty$, for $\omega \rightarrow \omega_{0-}$. However, for structures and materials considered here, these modes are suppressed, and their effect on the scattering properties can be disregarded as the response is dominated by the spacer mode (see Figure). Another remarkable difference between the ENP and ENZ cases is that the former can produce perfect absorption points at normal incidence, Figure 6.7, whereas ENZ requires a non-zero incident angle to engage plasmons and absorb waves.

Another important aspect of ENP-based structures is that, at ω_0, the permittivity changes from one extreme to another, drastically changing the nature of the top layer in the spacer structures considered throughout the chapter. Namely, in the lossless case, by approaching the Lorentz resonance from the right $\omega \rightarrow \omega_0^+$, the permittivity of the top layer goes
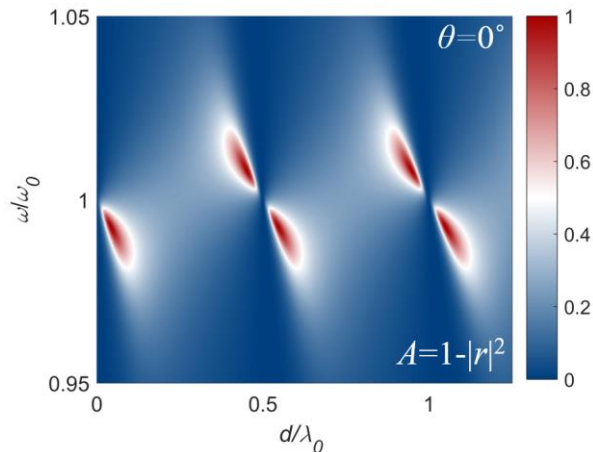
Figure 6.7. ENP reflection coefficient at normal incidence.
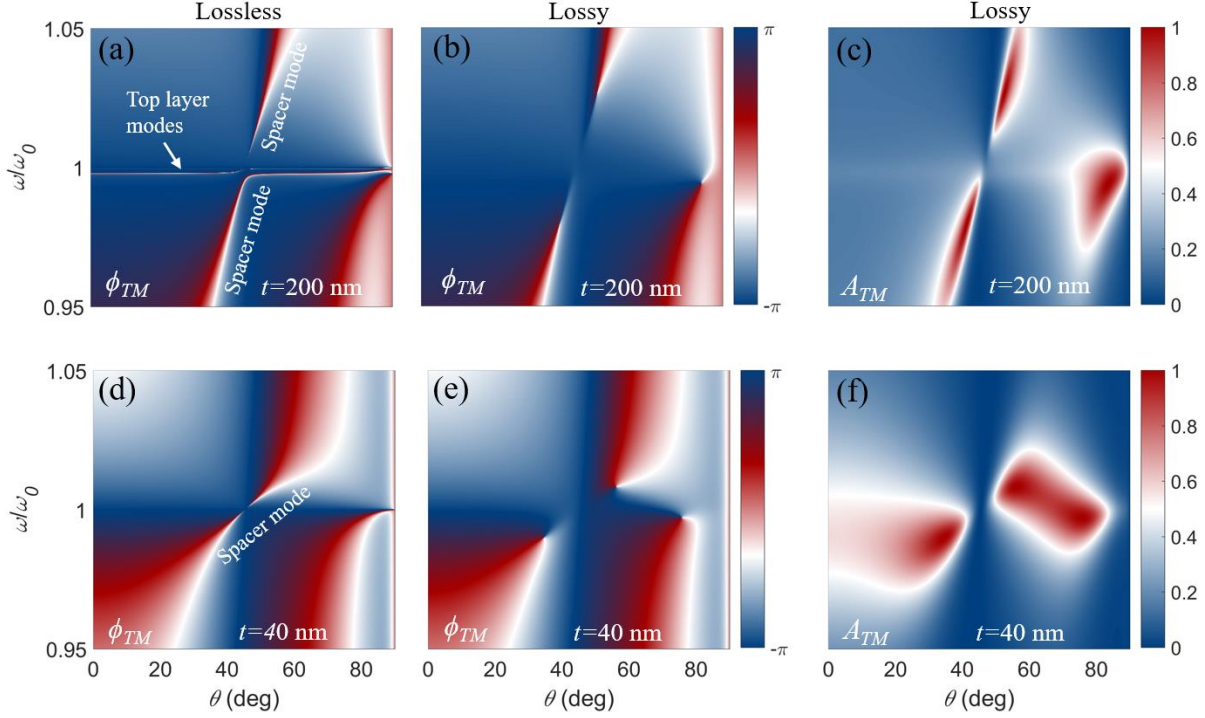
Figure 6.8. ENP scattering features. (a) For t=200 nm, propagating modes in the top layer are visible in the lossless case, along with the spacer mode. (b) Phase vortices appear in lossy case, top layer modes are strongly suppressed and not visible. (c) Perfect absorption points appear in the lossy case. (d)-(f) Same as (a)-(c) for t=40 nm.

to -∞, providing metallic, and ultimately PEC character to the layer and in this way enabling perfect light trapping of the Fabry-Perot mode existing in the spacer. However, by approaching the resonant frequency from the left side $\omega \rightarrow \omega_0^-$, permittivity of the top layer goes to +∞, allowing for an infinite number of propagating solutions in the top layer which complicates the picture in terms of scattering, Figure 6.8 (a). By reducing the thickness of the top layer, these modes are confined very close to the resonant frequency ω_0, and thus are not visible in the graphs in Figure 6.8 (d) and Figure 6.6 (b, c). However, as shown in Figure 6.8 (b,c,e,f), applying losses considered in main text leads to strong suppression of the modes propagating in the top layer, both for thicker and thinner top layers. The emergence of three charges remains apparent in both cases, and there is little difference in terms singularities associated with the spacer mode. Nevertheless, certain material permittivities and thicknesses might yield a more complicated scattering picture around the resonance frequency, and require a more careful analysis of the topological scattering features.

6.3 Charge annihilation

To verify the conservation of topological charge, we introduce a mechanism to annihilate charges. As evident from the reflection-zero dispersion diagrams in Figure 6.5, non-zero loss γ creates and pushes closer together charges originating from neighboring EEs. It is

then reasonable to assume that a further increase of loss can eventually bring these charges together, causing their mutual annihilation. This would be equivalent to moving the reflection-zero dispersion in the lower complex half-plane, thus removing the intersection with the θ-axis, Figure 6.5 (c)-(e). However, instead of changing the absorption loss in the material, we can induce more radiation loss by lowering the Q-factor of the underlying eigenmode. This can be done by reducing the top layer thickness, which essentially reduces its reflectivity (weaker "light-trapping") and consequently moves charges closer to each other until they eventually annihilate.

Figure 6.9 shows the ENZ and ENP cases for TM polarized light with reduced top-layer thickness. Comparing these results to the lossy cases in Figure 6.6, the neighboring charges have been annihilated and consequently the reflection-zeros associated with them have vanished. A useful rule-of-thumb can be inferred here – the angles at which EEs arise represent vertical walls impenetrable to these charges, and charges can move and annihilate only with the ones originating from neighboring EEs. For example, the remaining charge in the ENZ case in Figure 6.9 (a) and (b) cannot be destroyed for any level of material loss and thickness. Although there is a mirror copy of this charge in the negative θ half-plane due to the symmetry, these charges cannot merge since they are separated by "impenetrable" EE-walls. The only
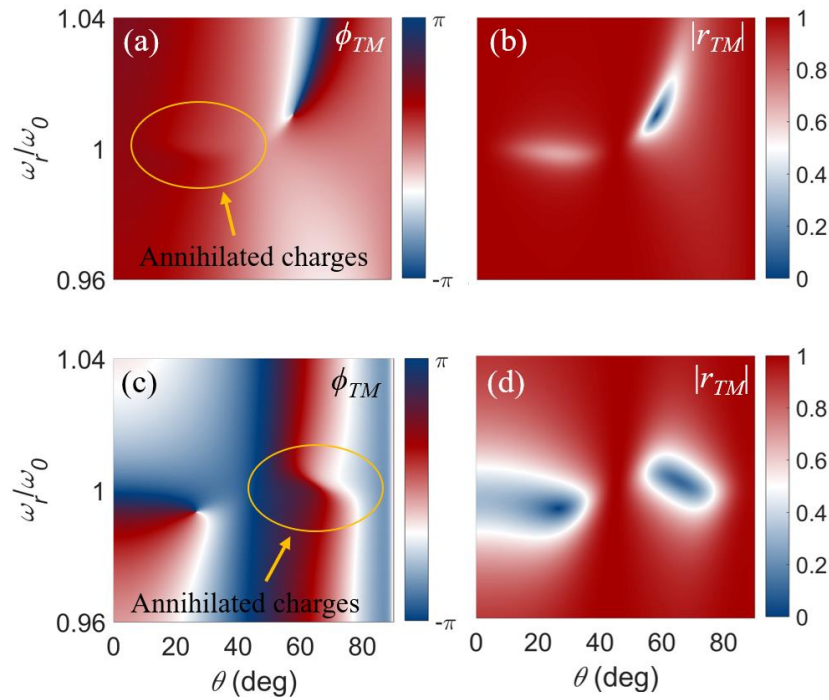
Figure 6.9. Charge annihilation for the lossy structures ($\gamma=0.003\omega_p$) considered in Figure 6.6. (a) Phase of reflection for the ENZ case. Two charges annihilated and one remaining. (b) The reflection zeros associated with these charges have vanished. (c) Same as (a) for ENP case. (d) Same as (b) for ENP case.
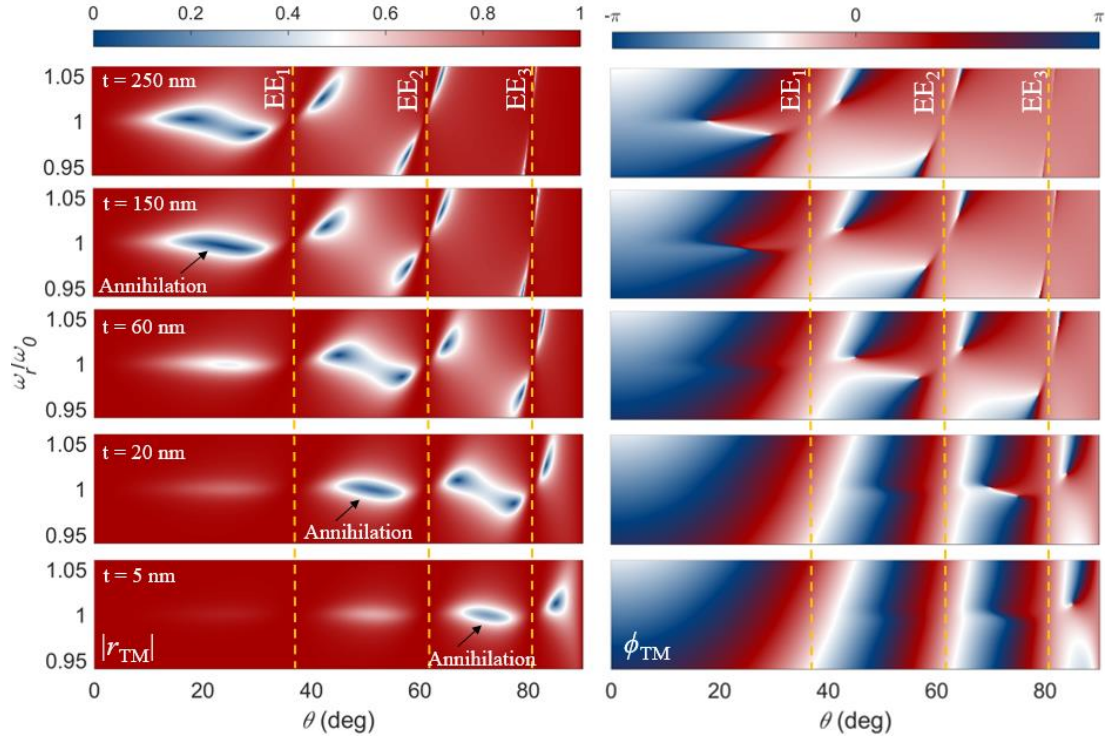
Figure 6.10. Annihilation of charges in a system with multiple embedded eigenstates. Reflection coefficient amplitude (left) and phase (right).

way to annihilate this charge is to increase the resonator length such that second-order Fabry-Perot mode EE appears, and its associated charge is brought into contact with the other charge. In the ENP case in Figure 6 (c) and (d), however, the remaining charge and its mirror copy in the θ-plane do not have an EE between them, and they are free to annihilate for a proper amount of radiation (or absorption) loss.

To better grasp the annihilation of charges, we show here in more detail how charges behave and what role embedded eigenstates have. As charges emerge in pairs around the angle at which embedded eigenstate occurs, it is evident that these cannot annihilate each other (except for precisely EE with zero losses). Figure 6.10 shows how neighboring charges for the ENZ case annihilate in a system with several EEs. Starting from a system with $d=\lambda_0$ and $t= 250$ nm, we reduce the top layer thickness t and lower the Q-factor of the modes. This system supports 3 orders of the Fabry-Perot resonances and consequently supports 3 non-symmetry protected EEs.

Charges associated with symmetry-protected EE and the first accidental one at a small angle (EE_1) are of lower Q-factors, thus annihilate first. As thickness is further reduced, charges between EE_1 and EE_2, and finally, the pair between EE_2 and EE_3 annihilates. Thus the resonant angle of EE behaves as an impenetrable wall for these charges. The last unpaired charge of EE_3 remains in the spectrum and cannot be annihilated unless a 4th order EE is made available.

These results open the question of material loss – indeed, some of the naturally occurring materials have high absorption loss and consequently some features discussed here are not available, i.e., charges may already be destroyed due to large loss. However, if we constrain the discussion to low-loss or moderately lossy materials, e.g., polar dielectrics like SiC, all of the previously described aspects hold. Furthermore, artificial materials as well as 2D materials, can provide ENZ or ENP response, thus expanding the validity of the presented analysis to a wide range of realistic geometries. For example, a Lorentzian (ENP) response can be induced as an electric dipole resonance in metasurfaces [201,205] or graphene strips [211], where similar features have been observed.

It is worth noting that the accidental EE at the designed angle θ, and its mirror copy at $-\theta$, are part of a ring of EEs in k-space, as they represent intersection points of a chosen incidence plane and the EE-condition in the whole $k_\parallel$ plane. This condition, which can be derived from Eqs. (6.8) and (6.9), is described by a circle, whose radius is defined by the spacer thickness:

$$\left(\frac{k_x}{k_0}\right)^2 + \left(\frac{k_y}{k_0}\right)^2 = \sin^2\theta = \begin{cases} \varepsilon_d - \left(\frac{n\lambda_0}{2d}\right)^2, k_0 = \frac{2\pi}{\lambda_0} \ for \ the \ ENP \ case. \\ \varepsilon_d - \left(\frac{n\lambda_{ENZ}}{4d}\right)^2, k_0 = \frac{2\pi}{\lambda_{ENZ}} \ for \ the \ ENZ \ case. \end{cases} \tag{6.10}$$

This is in contrast to EEs in photonic crystals, where accidental EEs arise at isolated k-points. This property implies that EEs here do not represent singularities in k-space, and thus have different features than EEs in periodic systems.

6.4 Polarization control based on the EE and emerging charges

So far, our discussion has been constrained to the analysis of phase and amplitude of the reflection coefficient around EEs. However, an important aspect intrinsically connected to these features is polarization. Traditionally, manipulation of the polarization state of light has been based on waveplates [212]. When light propagates through birefringent crystals, orthogonal linear polarizations (LP) experience different absorption coefficients and phase accumulation, enabling the generation of purely horizontal, vertical or circular polarization (CP) at the output.

As we have shown in the previous discussion, the system of Figure 6.5 displays co-located EEs with TE and TM polarization in the ENP case, and after accounting for loss, reflection-zeros of both polarizations emerge in the vicinity of each other. This property has interesting consequences for polarization control, as the two orthogonal polarization states

experience dramatically different absorption coefficients and phase accumulation in the region containing these charges, allowing for different linear transformations of the polarization state upon reflection. To test the potential of this property, we use isotropic SiC to model the top layer permittivity. We choose t=300 nm for the SiC layer, and the dielectric layer thickness is calculated according to eq. (6.8) at the transverse optical phonon frequency $\omega_{TO} = 2\pi\ 23.89$ THz for the angle of 50 deg. Namely, the ENZ and ENP regions are available at the longitudinal and transverse optical phonon frequencies of SiC.

Figure 6.11 shows the sketch of the system under consideration and the reflection coefficient dispersion for two different incident angles and polarization; zeros of TE and TM reflection coefficient are clearly achieved for the shown angles.

To assess the polarization properties of the structure, we define the transverse electric field in the plane normal to the incident k-vector, as sketched in Figure 6.11:

$$E^i = E_V + E_H = \begin{bmatrix} a \\ b e^{j\delta_i} \end{bmatrix} e^{-j(k_{0x}x + k_{0z}z)}, \tag{6.11}$$

where the incident electric field consists of vertically and horizontally polarized components with amplitudes a and b with the phase difference δ_i. The compact way to describe the polarization is the Jones vector:

$$J^i = \begin{bmatrix} a \\ b e^{j\delta_i} \end{bmatrix}. \tag{6.12}$$

The reflected field now has:
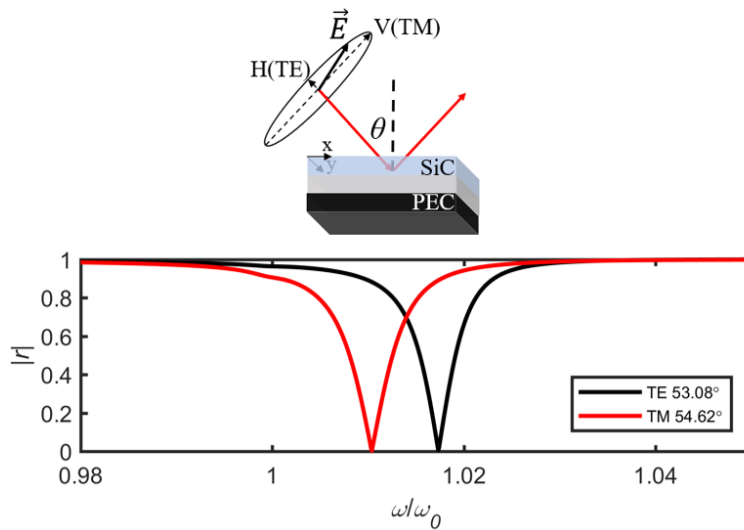
Figure 6.11. Sketch of the structure under analysis with the reflection zeros of orthogonal polarizations emerging near the ENP EE.

$$E^r = \begin{bmatrix} r_{TE} & r_{TE-TM} \\ r_{TM-TE} & r_{TM} \end{bmatrix} \begin{bmatrix} a \\ be^{j\delta_i} \end{bmatrix} e^{-j(k_{0x}x - k_{0z}z)}, \tag{6.13}$$

where the reflection matrix describes the connection between the incident and the reflected field. As there is no cross-coupling mechanism between orthogonal polarizations, the terms $r_{TE\text{-}TM}$ and $r_{TM\text{-}TE}$ are equal to zero. The output Jones vector can then compactly be written as:

$$J^o = \begin{bmatrix} r_{TE}a \\ r_{TM}be^{j\delta_i} \end{bmatrix} = \begin{bmatrix} |r_{TE}|a \\ |r_{TM}|e^{j\delta_r}be^{j\delta_i} \end{bmatrix} = \begin{bmatrix} A \\ Be^{j\delta_o} \end{bmatrix}, \tag{6.14}$$

with A, B, and δ_o being the output amplitudes and phase difference of orthogonal polarizations, and $\delta_r = \delta_o - \delta_i$ being the phase retardation between H- and V-polarizations that the structure introduces.

To better visualize the whole parameter space and capture the discussed charges we next plot the ellipsometric parameter $\tan^{-1}(r_{TM}/r_{TE})$, Figure 6.12 (a), where the maximum value in the density plot represents the TE-zero, while the minimum represents the TM-zero. It is clear that these two points in the parameter space can work as polarization filters or polarizers – for a mixed polarization input, only TM or TE polarized light exits the structure. This is in contrast to the ENZ case, where only the TM-zero is available - we note that this was the basis
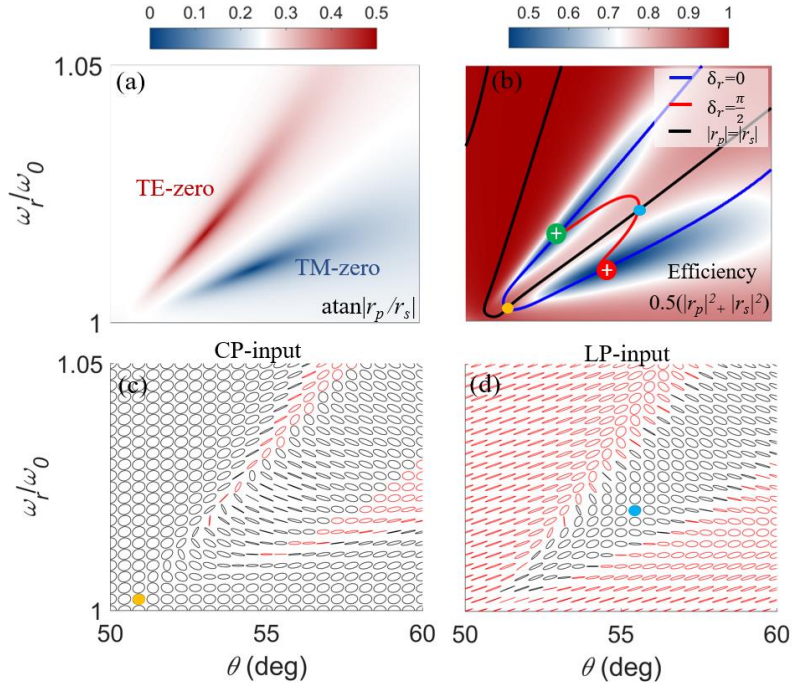
Figure 6.12. Polarization manipulation. (a) Ellipsometric parameter $\psi = \tan^{-1}\left(r_{TM}/r_{TE}\right)$ normalized to π. (b) Total reflectance as an efficiency indicator. (c) Polarization ellipses in the output for CP-input. Red and black colors indicate handedness (red for RCP, black for LCP). (d) Polarization ellipses in the output for 45 deg LP-input.

for the polarization switching scheme studied in [53]. Beyond admitting zeros of both polarizations, the phase difference between orthogonal polarizations induced by the structure also dramatically changes around the charges, as they represent phase vortices. This property opens up possibilities for generation of various polarization states in the output for a mixed input – for example, converting LP to CP light. To illustrate the opportunities for polarization control, we also plot the total reflectance and the contour lines with specific δ_r values. In this way, we can find conversion points from LP to CP and vice versa, Figure 6.12 (b). Namely for $a=b$, and $|r_{TE}|=|r_{TM}|$ the output amplitudes are equal, $A=B$. Thus by finding the intersection of $|r_{TE}|=|r_{TM}|$ and $\delta_r=\pi/2$, we have a LP to CP conversion point and vice versa. This is represented by the blue dot in the Figure 6.12 (b). The orange dot represents the point that preserves polarization, as $|r_{TE}|=|r_{TM}|$ and $\delta_r=0$, and the green and red circles represent phase vortices. Thus, the proposed system has polarization conservation, filtering, and LP$\leftrightarrow$CP conversion capabilities, all in the EE proximity.

In order to better visualize this effect, we plot the output polarization ellipses for both CP and 45 deg LP inputs, Figure 6.12 (c,d). Singular phase points produce purely vertical or horizontal polarization states in the output. This can be done efficiently since most of the desired polarization is reflected, while the other is fully absorbed. However, extracting horizontal or vertical polarization from a 45 deg LP or CP input is limited to 50% in efficiency, as no conversion from one to the other happens, $|r_{TE\text{-}TM}|=|r_{TM\text{-}TE}|=0$. CP to LP and LP to CP conversion is also possible (blue dot), preserving around 80% of incident power.

Due to the vicinity of the different polarization features, the output polarization state is sensitive to small changes in the system, and specifically to the permittivity (loss) of the SiC layer. This could lead to a versatile polarization switching platform based on active control of material permittivity - for example, a moderate change in permittivity of InAs in the Reststrahlen region was recently demonstrated using laser-induced nonlinear processes [213]. Polarization control in the long-wave infrared range is especially important, as birefringent materials are scarce in this range of the electromagnetic spectrum [214], and the presented topological features using SiC and other IR materials may help circumvent this challenge. Thus there is a possibility of external control and switching of polarization by changing the permittivity (loss) of the top layer, where small changes would significantly change the output polarization.
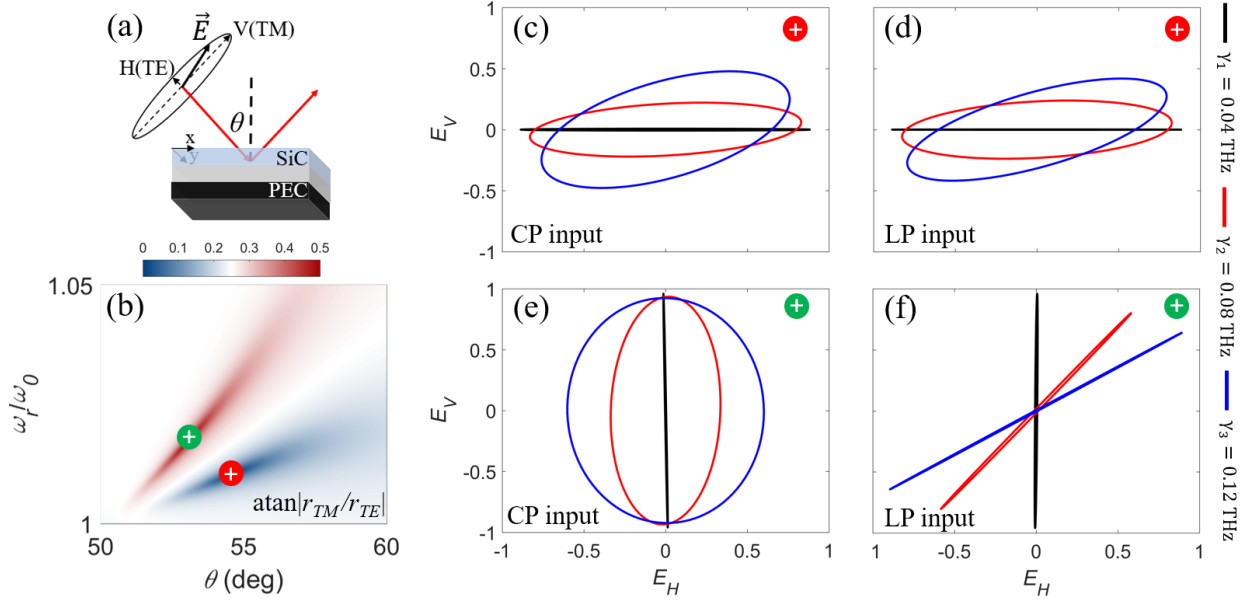
Figure 6.13. (a) Sketch of the polarization plane and the reflection problem under analysis. (b) Ellipsometric parameter $\psi = tan^{-1}(r_{TM}/r_{TE})$ where zeros of different polarizations are highlighted. (c) Output polarization dependence on the material loss parameter γ for CP input at TM zero. (d) 45 deg LP input at TM zero. (e) CP input at TE zero. (f) 45 deg LP input at TE zero.

To demonstrate the sensitivity of the output polarization to material losses and its potential for polarization switching implementation, we plot the output polarization in two spectral points for different values of the SiC loss parameter γ, Figure 6.13. We excite the system at the singular points of vertical (TE) and horizontal (TM) polarization at starting loss value γ_1=0.04 THz. By increasing loss to γ_2=0.08 THz and γ_3=0.012 THz, output polarization changes notably for the same frequency and angle of excitation, indicating switching capabilities.

6.5 Singular phase and near-annihilation point sensing

Phase vortices are characterized by an undefined phase point in their center, around which the phase changes dramatically. This feature, most commonly observable around reflection-zeros, has been used as a basis for interferometric phase sensing schemes [215-220]. Namely, even small changes in the environment can result in giant phase changes, thus creating one of the most sensitive schemes. Various systems exhibit these types of singular points, including metasurfaces [215], 1-D photonic crystals [216], hyperbolic [217] and 2D materials [218]. Instead of using a traditional interferometric setup, most of these schemes use ellipsometric measurements, which measure phase and amplitude differences between orthogonal linear polarization components.

The caveat of this sensing method is the following: by approaching the singular point of the vortex, phase changes more dramatically, thus increasing the sensitivity of the system.

However, the amplitude of the reflection coefficient drops at the same time. The sensitivity diverges as the singular point is reached, but there is no reflection to be measured at the detector. This inverse relationship between sensitivity and $|r|$ plays an essential role in such devices.

There are indeed qualitative differences between different realizations. Engineering structures with lower possible values of $|r|$ lead to higher sensitivity. Furthermore, higher Q-factors of the underlying mode can improve the sensitivity, as these modes produce stronger fields and interactions with the environment. A critical issue to reconcile in such devices is the need for a highly precise angle of incidence to engage abrupt phase jumps – e.g., extremely high sensitivity was reported in [218]. However, the angle required for such performance requires precision on the order of 10^4 degrees, and any deviation from the exact angle reduces the sensitivity. Thus, the sensitivity of such devices is hard to predict and maintain stable.

To address these issues, we exploit the unusual physics around the EE and the related topological charges discussed in this paper. First, we show that using EEs in SiC provides high-Q factors and enables remarkably high sensitivities around the reflection-zeros associated with EEs. Secondly, we introduce the concept of near-annihilation point sensing and show that we can alleviate the requirement for an extremely precise angle of incidence by manipulating charges, thus creating an extended angular range with stable sensitivity.

To achieve these goals, we envision a gold-backed air gap (spacer) covered by a SiC layer to be used as a trace gas sensor, operating at long-wave infrared wavelengths, Figure 6.14 (a). Gold is highly reflective at longwave IR wavelengths, thus it can work as an efficient reflective bottom layer. For the chosen gap size $d=32$ μm, several higher-order FP modes are engaged. However, the spectrum is not overcrowded, due to the long operating wavelength of 10.3 μm. Furthermore, having a gap this size is advantageous because a nanofluidic channel can also be integrated to function as a spacer, therefore expanding the possible applications of the proposed structure.

As shown in the previous discussion, the SiC-capped resonator can support an EE around 10.3 μm (ENZ region) and the accompanying reflection-zeros. To demonstrate the phase jump, we plot the reflection coefficient near EE and its phase as it passes near the vortex at 52.3 deg, Figure 6.14 (b). Based on this phase jump, we can detect tiny changes in the sensing layer – as indicated in the bottom left inset in Figure 6.14 (b). At a constant frequency and angle, the phase of reflected waves changes dramatically for permittivity changes on the order
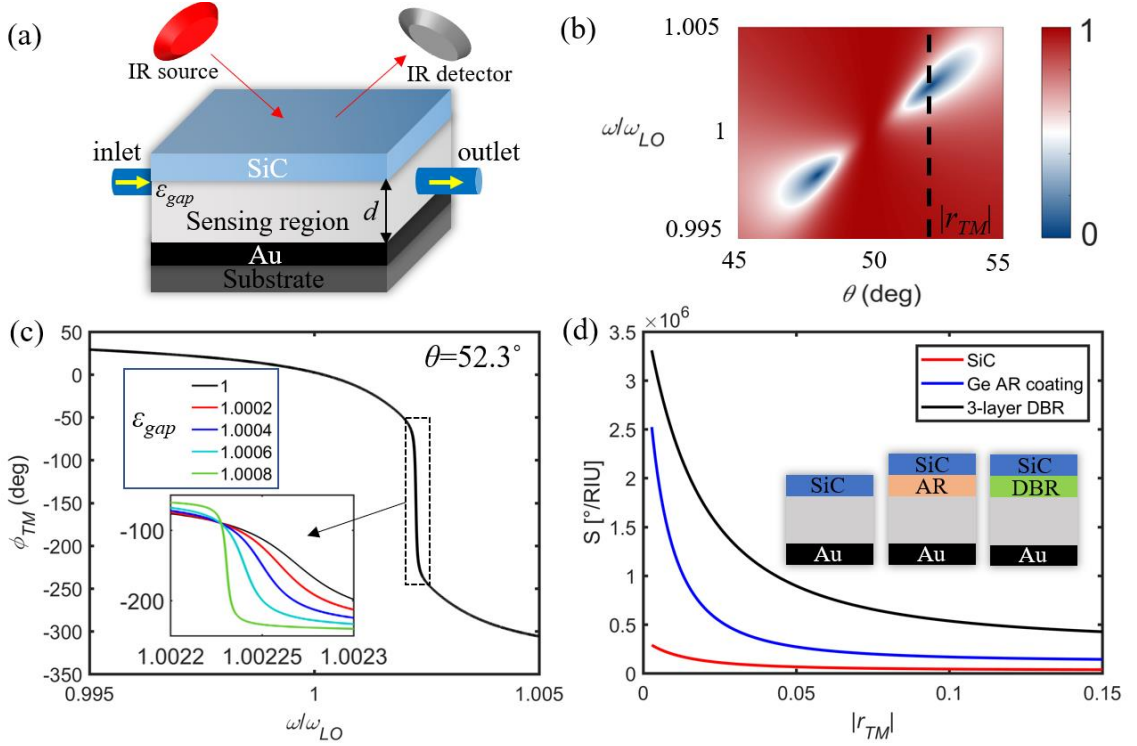
Figure 6.14. (a) Sensing scheme based on phase singularities. (b) Reflection coefficient amplitude near the EE at 50 deg (c) Phase of the reflection coefficient as the frequency is changed and passes near the vortex. Inset: Phase sensitivity to small changes of the gap permittivity. (d) Sensitivity for three different configurations – improvement due to enhanced Q-factor with antireflection coating and DBR.

of 10^{-4}, producing very high sensitivity, of the order of 10^5 deg/RIU. However, as mentioned before, the sensitivity is highly dependent on the amplitude of the reflection coefficient, i.e., the proximity of the measurement to the singular point. To better grasp this correlation, we plot the sensitivity calculated at different values of $|r|$, red curve in Figure 6.14 (d). As expected, we see an increase in sensitivity as $|r|$ approaches zero. However, instead of relying on extremely small values of $|r|$ to get higher sensitivity, which could make the signal at the detector indistinguishable from noise, we can improve the sensitivity by increasing the Q-factor of the mode instead. This can be done by placing a high-index anti-reflection coating or a distributed Bragg reflector (DBR) between the spacer and SiC, improving the reflectivity of the top layer. To this end, we can use low-loss longwave IR materials, for example, Ge and BaF_2, as high and low index materials, respectively. As shown in Figure 6.14 (d), this results in an increase by order of magnitude at constant $|r|$, making the scheme comparable or better than the most sensitive available schemes [215-219].

However, the displayed increase in sensitivity requires resolving the incidence angle in the order of 0.01 deg. For the DBR structure displayed in Figure 6.14 (c), the sensitivity drops by an order of magnitude with angle changing by just 0.02 deg, Figure 6.15 (a). Although the
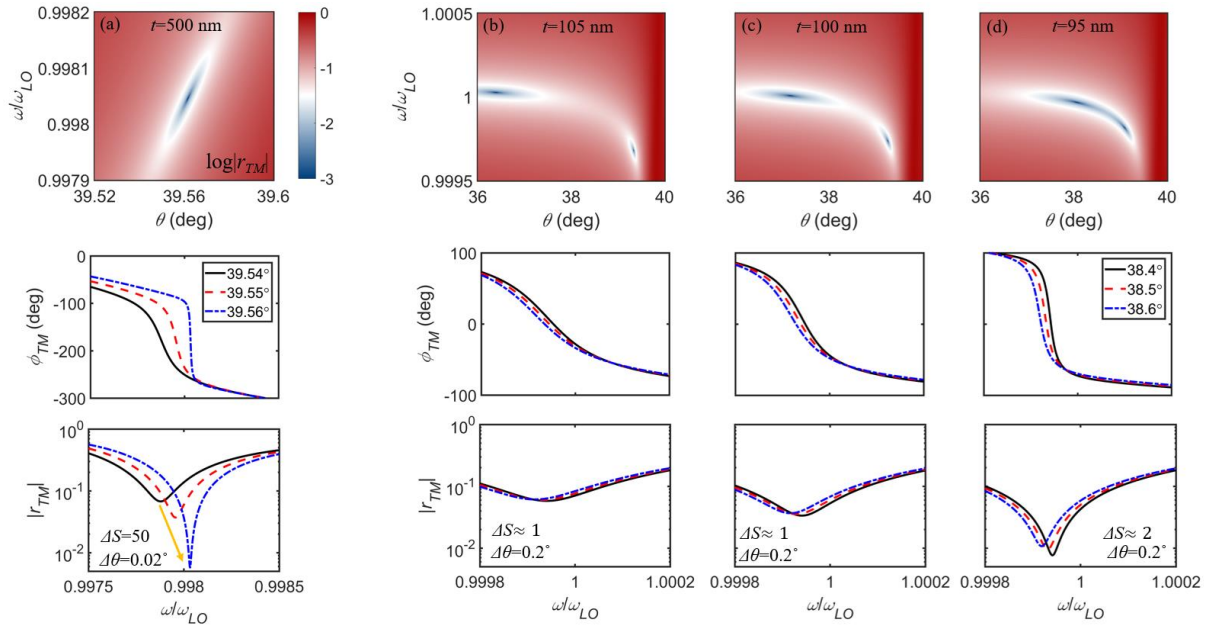
Figure 6.15. Sensitivity of the reflection coefficient and sensitivity for different incidence angles. (a) The reflection coefficient of the DBR structure in Fig. 5(c) is extremely sensitive to small changes in incidence angle, resulting in one order of magnitude change in sensitivity for extremely small angle changes. (b)-(d) Near annihilation point sensing with stabilized sensitivity. The amplitude of the reflection coefficient is more robust to incidence angle variations, with the sensitivity not changing substantially for 1 deg changes in angle for (b) and (c), and 0.2 deg for (d).

presented system has superior sensitivity, it suffers from the same drawback as [218], as sensitivity is exceptionally dependent on the chosen incidence angle. This may result in unreliable sensitivity values, as most instruments cannot resolve at that level of precision.

To alleviate this stringent requirement, we exploit the phenomenon of merging charges introduced above. Interestingly, we show that by bringing two neighboring charges in close proximity, the reflection coefficient between them displays almost constant magnitude while keeping the strong phase jump, Figure 6.15 (b)-(d). Furthermore, by fine-tuning the SiC thickness, we show that $|r|$ can be steadily controlled and kept constant over an extended angular range, thus eliminating the stringent requirement on incidence angle and providing stable sensitivity. However, this comes at the cost of lower absolute sensitivity, because bringing two charges together requires lowering the overall Q-factor. A trade-off emerges between sensitivity of the system and robustness to incidence angle variations. For example, the structure in Figure 6.15 (a) has 3 times larger absolute sensitivity than the structure in Figure 6.15 (d) (calculated for the same value of $|r|$). However, in most practical scenarios, it would be much easier to access the required angles of the latter structure and get the predicted sensitivity. Nevertheless, these results demonstrate that the topological features of EEs offer a versatile tool for sensing and can address different challenges of advanced sensing systems.

6.6 Discussion

The theoretical results discussed in this chapter extend the notion of topological scattering effects to planar structures and show that topological quantities can find their use in various scenarios of interest. Although the presented theory builds upon the topological features of EE-related phenomena, it is worth stressing the differences between the homogeneous planar systems analyzed here and EEs emerging due to the periodicity in photonic crystals (PCs). EEs in PCs come as isolated points in k-space, whereas in the homogeneous planar systems studied here, EEs generally emerge in rings in k-space and isolated points in real space. Thus, a topological charge cannot be defined by integrating in k-space like in PCs, but in real space (either in ω-d or ω-θ space). Somewhat analogous to breaking spatial symmetries in PCs, which splits the EE into two half-integer charges [103], dissipation in our system lifts the degeneracy of two singularities of opposite integer charge, destroying the EE. Since all real systems have losses, this degeneracy is always lifted, whereas EEs in PCs remain topologically protected as long as spatial symmetries are not broken. Although PCs have more degrees of freedom to control the topological properties of EE scattering, we have shown that planar structures offer a versatile tool for intensity, phase and polarization control based on the topological nature of the reflection coefficient. Moreover, our proposed structures do not require complicated lithography fabrication process, as in the case of periodic structures.

The scattering matrix approach used here has also been utilized in a different area of topological photonics - Weyl physics [221], where topologically non-trivial states have been shown to have a non-zero winding number of the phase of scattering matrix eigenvalues [222]. This approach is especially valuable because the scattering matrix features can be observed experimentally, differently from the standard Hamiltonian approach. Furthermore, recent studies show that accounting for dissipation turns Weyl points into rings [223], somewhat analogous to what happens to EEs in our structures. A comprehensive study addressing Weyl physics in structures supporting both symmetry-protected and accidental EEs, and its effects on scattering/reflection, is yet to be done. As discussed in the previous paragraph, breaking spatial symmetries in PCs leads to splitting of EEs into half-integer, CP states. Similarly, breaking time-reversal symmetry by applying a magnetic field in plasma was shown to split Dirac points into Weyl points associated with CP and helical states [224]. Thus, applying a symmetry-breaking mechanism to our system may provide rich topological phenomena and establish a deeper connection between different branches of topological photonics.

6.7 Conclusion

In this chapter we have introduced a topological perspective on scattering singularities in planar systems supporting EEs, connecting several research areas. We have unveiled that the singularities of the scattering matrix necessarily emerge from EEs and carry topological charges observable as phase vortices. Charge conservation was demonstrated by proposing a method of charge annihilation, where tuning the underlying radiation losses provides control over the features and motion of charges. It was shown that perfect absorption and phase vortices associated with these charges enable extreme control of the intensity, phase and polarization of the reflected waves. Based on these concepts, we have proposed applications for versatile polarization control and switching, as well as for phase sensing schemes that may be implemented using silicon carbide.

Chapter 7: PT-symmetric and active ENZ structures

7.1 Introduction

In Chapters 5 and 6, we considered embedded eigenstates in structures based on singular permittivity (ENZ and ENP) and shown how realistic material loss affects their behavior. Motivated by the recent advances of PT-symmetric scattering systems [121,122], we expand the analysis of singular permittivity embedded eigenstates by considering PT-symmetric perturbations. So far, EE have seldomly been analyzed in PT-symmetric systems [225-228], leaving room for further deepening the understanding and association between different scattering phenomena, which has potential for a broad range of applications.

In this chapter we uncover a fundamental connection between EEs and singularities of the scattering matrix usually associated with non-Hermitian PT-symmetric systems. We analyze an ENZ multilayer system and probe the system with non-Hermitian perturbations, showing how the EE is destroyed for any non-Hermiticity. We then analyze the problem in the complex-frequency plane, considering loss and gain separately, and show that topologically protected CPA and laser solutions necessarily emerge from EEs. These spectral points are characterized by a winding number, appearing as a vortex in the phase of the scattering-matrix eigenvalue. We then consider PT-symmetric perturbations and show how pairs of CPA-Laser charges necessarily emerge from EEs, uncovering novel properties of the EEs and their fundamental connection to various coherent phenomena.

Finally, we propose a novel, unusual scattering scenario based on the analytic properties of complex scattering coefficients and coherent excitation. With careful choice of excitation signals' relative phase, complex zeros and poles of scattering coefficients can be tailored so that they converge towards a degenerate real frequency and cancel each other, realizing an EE resonance. This process yields an exceptional point in the scattering spectrum with vanishing linewidth, ideally suited for sensing and filtering applications. Its coherent nature also enables all-optical tunability of the system from EE-like scattering to unidirectional lasing features.

7.2 PT-symmetry in ENZ bi-layers

Following the discussion around the Brewster's effect in a single ENZ slab presented in Chapter 5, here we start our considerations from the same point. Figure 7.1 shows the reflection

coefficient for TM waves in the frequency-incidence angle parameter space for three different cases. Namely, we start from a lossless Drude model in Figure 7.1 (a), where the previously described non-resonant impedance matching due to Brewster's effect is visible as the reflection zero line. The Drude permittivity is defined by $\varepsilon_1 = \varepsilon_0 \left[1 - \omega_p^2 / (\omega^2 + j\gamma\omega) \right]$. The trivial symmetry protected EE is visible at zero-incidence, where the reflection zero disappears as it meets pole of the underlying polariton mode.

In the case in Figure 7.1 (b), we introduce losses in the Drude model $\gamma = 0.01\omega_p$. The losses have negligible effects away from the plasma frequency, and strong suppression of reflection is still visible – this near-impedance matching can be attributed to the quasi-Brewster's effect, accounting for the imaginary part of the permittivity. However, as plasma frequency is approached for smaller incident angles, the reflection is not small anymore. This is due to the unavoidable strong reflection at EE, where the reflection zero drops below the reflection pole in the complex plane, as explained in section 5 of Chapter 5. The EE is destroyed for any amount of loss, however one can still argue that this represents a quasi-EE as the reflection feature disappears symmetrically around it.

In the third case in Figure 7.1 (c), we now split the ENZ layer into two equal parts with opposite signs of imaginary permittivity, with permittivities $\varepsilon_{1/2} = \varepsilon_0 \left[1 - \omega_p^2 / (\omega^2 \pm j\gamma\omega) \right]$, where $\gamma = 0.01\omega_p$. Now, the structure has lossy and gainy parts such that PT-symmetry is achieved. Interestingly, the reflection coefficient now displays new features around plasma frequency. Away from the plasma frequency, the reflection coefficient is very similar to the lossless case, and the Brewster's effect is clearly visible. However, as plasma frequency is approached the reflection zero bends away from normal incidence and asymptotically approaches plasma frequency for maximum incidence angle.
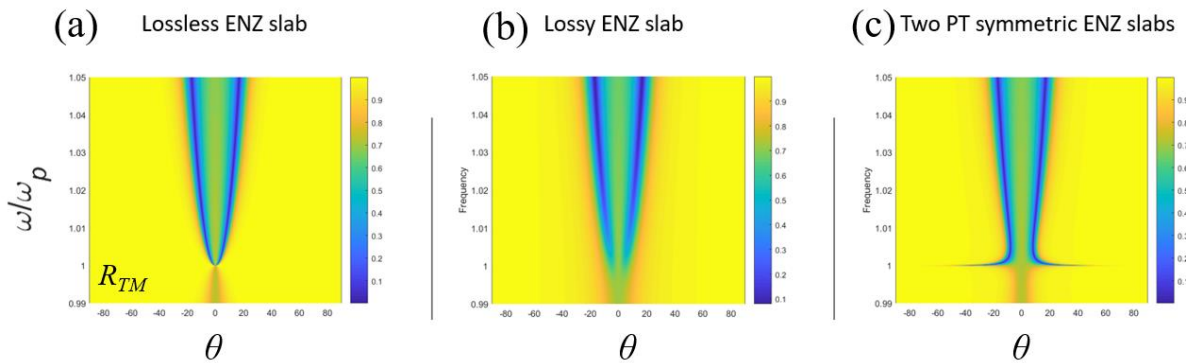
Figure 7.1. TM reflectance in the frequency-incident angle parameter space for: (a) Lossless ENZ slab. (b) Lossy ENZ slab. (c) PT-symmetric ENZ slabs.
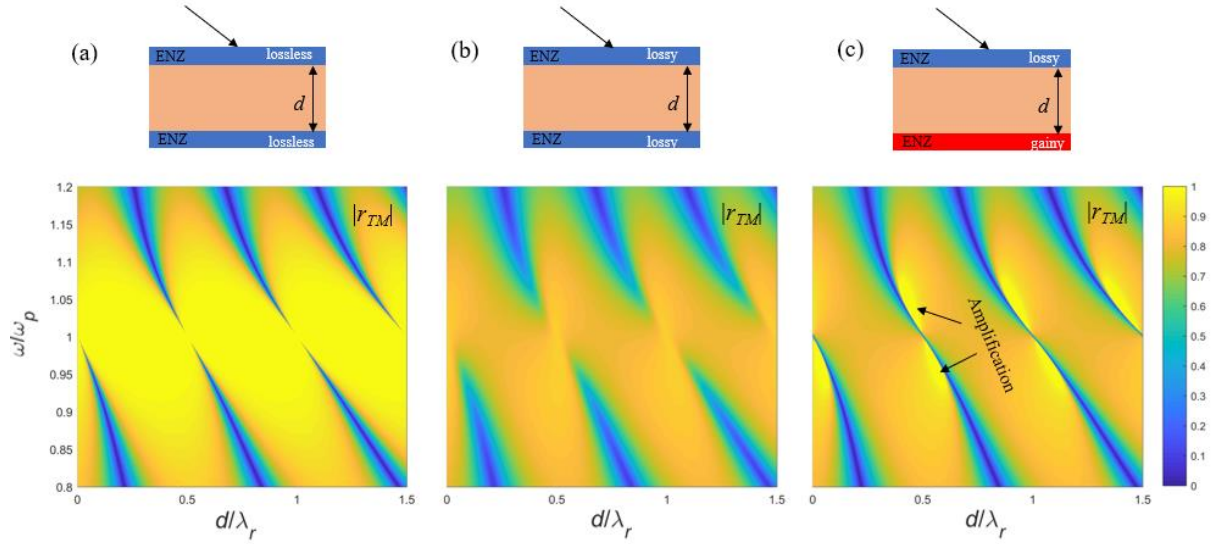
Figure 7.2. Reflection coefficient for an oblique incident angle: (a) Lossless ENZ. (b) Lossy ENZ. (c) PT-symmetric ENZ.

7.3 PT-symmetry ENZ layers and EEs

Next we consider a three-layer structure, such that a dielectric layer is inserted in between two ENZ layers, Figure 7.2. We use the same analysis as before, where we compare the lossless, lossy and PT-symmetric cases. This time, we plot reflection coefficient for different dielectric thicknesses considering an obliquely incident TM wave.

As thoroughly discussed in chapter 5, ENZ-dielectric-ENZ supports symmetry-protected and accidental EEs. Figure 7.2 (a) shows several orders of Fabry-Perot modes which are completely localized at the plasma frequency and represent non-symmetry protected EEs. When losses are introduced, the reflection zero around the EE is not available anymore.

In the PT-symmetric case, the reflection zero line is fully restored, as the impedance matching condition is guaranteed by PT-symmetry. Although the PT-symmetry restores the impedance matching and zero-reflection line, the system in Figure 7.2 (c) has two poles (lasing states) around each EE, making the system unstable between them. As we show next, these features can be explained through the topological aspects of the *S*-matrix singularities.

7.4 Topologically-protected coherent scattering singularities and embedded eigenstates

Previous results show that considering a PT-symmetric ENZ-multilayer structure can restore the sharp resonant feature (*r*-zero) that is lost in the lossy case. However, the true EE is not recovered, and new features arise around the EE - two poles appear in the reflection
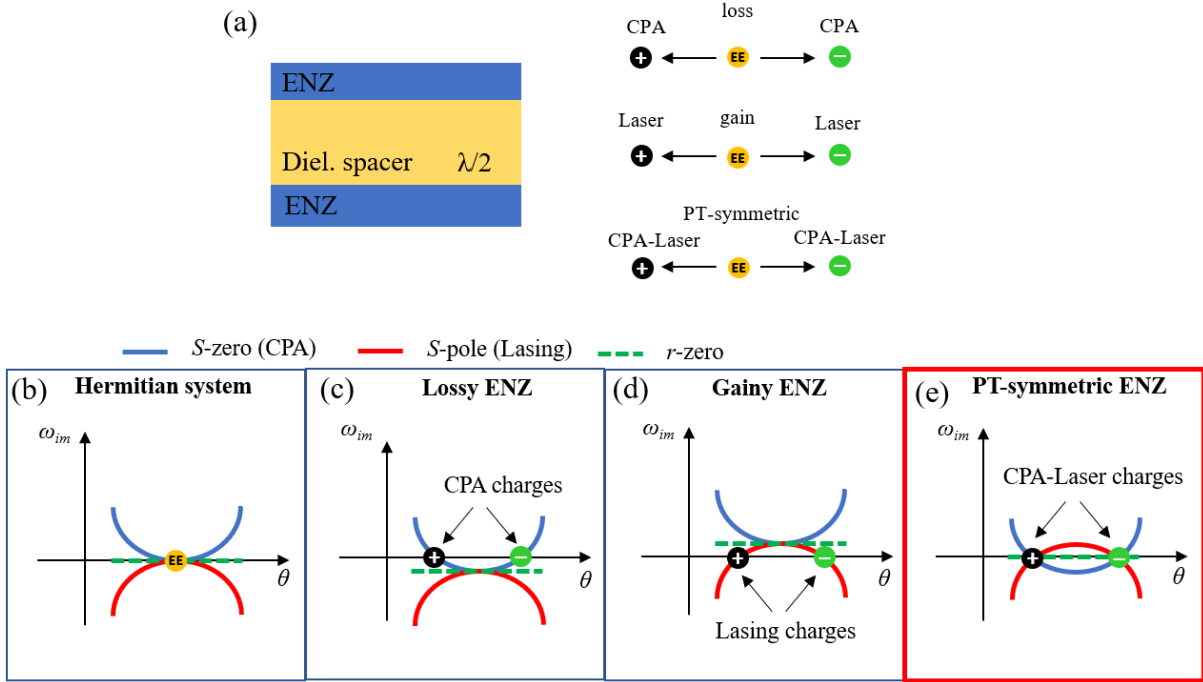
Figure 7.3. (a) Splitting of EE into oppositely charged singularities of the S-matrix with mirror-symmetric and PT-symmetric non-Hermitian perturbations. (b) In the lossless case, the dispersion of poles and zeros touch at $\omega_{im}=0$. (c) Losses push down the poles and zeros with two CPA solutions emerging around EE. (d) Gain pushes up the singularities creating two lasing states. (e) PT-symmetric perturbation simultaneously pushes zeros down and poles up, creating two CPA-Laser solutions at a real frequency.

spectrum. As we show next, the emergence of two singularities is a necessary consequence of non-Hermitian perturbations of the considered multilayer.

To uncover this fundamental property of EEs in two port systems, we revert to the analysis used in Chapter 6 – we consider the singularities of the S-matrix eigenvalues in the complex frequency plane. Figure 7.3 shows the sketch of the multilayer considered and a graphic explanation of emerging singularities, as well as the sketch of the S-matrix singularities in the ω_{im}-d plane.

We consider three cases, all starting from a lossless ENZ-dielectric-ENZ multilayer supporting an EE, same as in Figure 7.2 (a). As discussed thoroughly in Chapters 4-6, embedded eigenstate represents a degeneracy of the S-matrix pole and zero of Hermitian systems. Around the EE, the dispersion of S-matrix poles and zeros have a parabolic shape, Figure 7.3 (b). Introducing losses shifts down the singularity dispersion, creating two intersections with the d-axis ($\omega_{im}=0$, i.e. real frequency). These singularities represent two CPA solutions, as they are real-frequency solutions to the purely-incoming wave problem. This is different than the result discussed in Chapter 6, where two singularities were also reflection zeros – in the present case the reflection coefficient does not display any singular behavior

around EE, as shown in Figure 7.2 (b). Instead, to achieve the CPA state it is required to use precise eigenvector excitation corresponding to the zero eigenvalue, i.e., two-port excitation and proper phase tuning. Figure 7.3 (d) shows the time reversed case, as singularities move upward the imaginary frequency axis when gain is introduced symmetrically. This results in two lasing states, symmetrically placed around the EE. Finally, when the non-Hermitian perturbation is introduced in a PT-symmetrical manner, zeros move down and poles move up, creating the intersection of their dispersion lines exactly at the real-frequency axis, Figure 7.3 (e). This degeneracy of the *S*-matrix pole and zero represents CPA-Laser solution. As indicated in the figure, the poles (red line) cross over to the upper half of the complex plane which constitutes instability of the system. To better understand these effects, we will expand the analysis for the lossy and PT-symmetric case.

Figure 7.4 shows the coherent setup for the lossy ENZ structure, where we use two-port excitation at an incident angle. The input and output signals are connected via the S-matrix:

$$\begin{bmatrix} b_1 \\ b_2 \end{bmatrix} = \hat{S} \begin{bmatrix} a_1 \\ a_2 \end{bmatrix} \tag{7.1}$$

$$\begin{bmatrix} b_1 \\ b_2 \end{bmatrix} = \begin{bmatrix} r_1 & t \\ t & r_2 \end{bmatrix} \begin{bmatrix} a_1 \\ a_2 \end{bmatrix} \tag{7.2}$$

$$a_1 = A_1 \cos(\omega t) \tag{7.3}$$

$$a_2 = A_2 \cos(\omega t + \psi) \tag{7.4}$$

$$b_1 = a_1 r_1 + a_1 t \tag{7.5}$$

$$b_2 = a_2 r_2 + a_1 t \tag{7.6}$$

where a_1 and a_2 are input signals, A_1 and A_2 are their amplitudes, ψ is the phase difference between input signals, while b_1 and b_2 are output signals. A useful quantity to define when discussing coherent perfect absorption is the joint absorptivity [229, 230]:

$$A_T = 1 - \frac{|b_1|^2 + |b_2|^2}{|a_1|^2 + |a_2|^2} \tag{7.7}$$
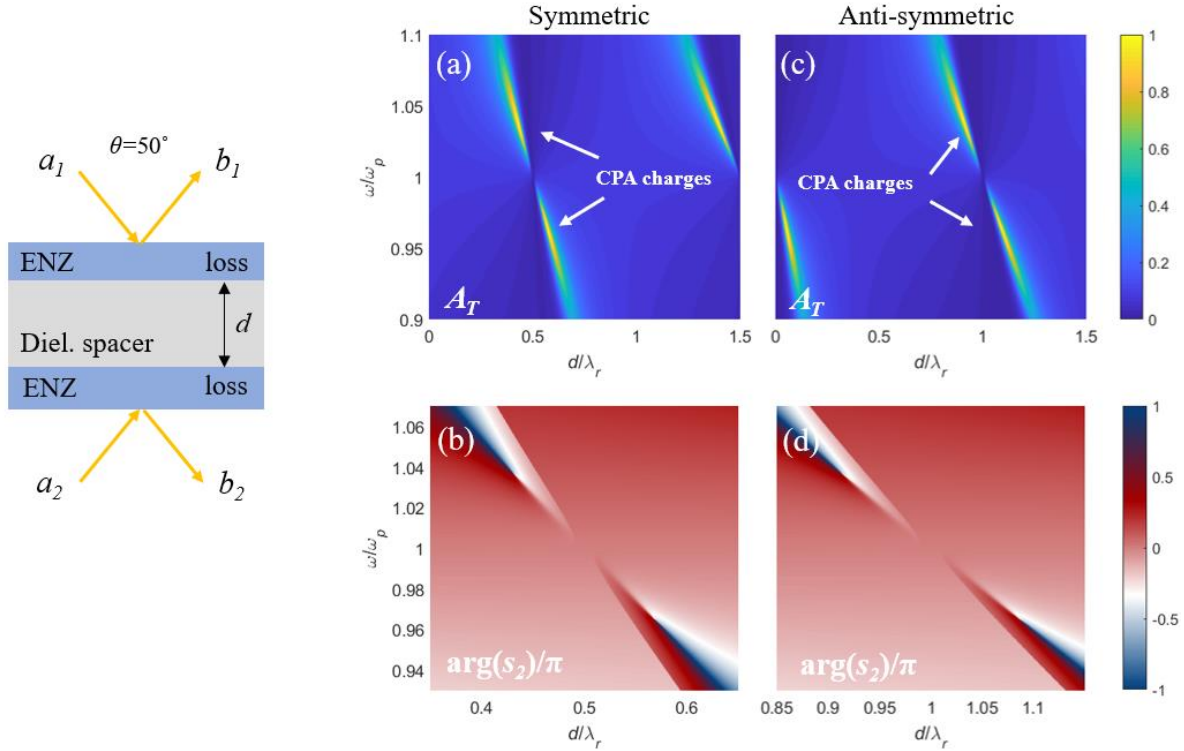
Figure 7.4. Coherent setup for lossy ENZ case. (a) Density plot of joint absorption A_T which shows two CPA solutions emerging around EE for the symmetric (in-phase) excitation. (b) Phase of the S-matrix eigenvalue where two vortices of opposite polarity are visible (symmetric case) (c) Two CPA solutions emerging around EE for the anti-symmetric (out-of-phase) excitation. (d) Phase of the S-matrix eigenvalue where two vortices of opposite polarity are visible (anti-symmetric case).

which accounts for total absorption in the coherent excitation scheme. When the output signals are equal to zero, total scattered power is zero and all energy is perfectly absorbed in the structure (A_T=1). Figure 7.4 (a, c) show the joint absorptivity for symmetric and anti-symmetric excitation. In the symmetric case, the input signals are in phase (ψ=0), while in the anti-symmetric case the signals are 180 degrees out of phase (ψ=π). The plots clearly show two CPA-points emerging around the EE, as discussed earlier. The winding number of these topological charges can be found in the phase of the *S*-matrix eigenvalue as vortices with an undefined phase point at their center, Figures 7.4 (b, d). The eigenvalues s_1 and s_2 are calculated according to eqs. (5.22, 5.23).

When loss is added to the structure, the EE splits into two vortices of opposite polarity. We note that this is the generalization of topological scattering singularities discussed in chapter 6 to two port systems. In one-port system the vortices are directly visible in the reflection coefficient. An important aspect to these features is that they are topologically protected, and can only be destroyed by charges of opposite polarity, as discussed in Chapter 6.

We next analyze the PT-symmetric case, Figure 7.5 (a). We start from the same lossless system and add loss/gain symmetrically, destroying the embedded eigenstate. Now, the EE splits into two degenerate pole-zero pairs, i.e. CPA-Laser solutions, Figure 7.5 (b). To demonstrate these are actually CPA-Laser points, we next plot the eigenvalues amplitudes near the frequency of the charges, Figure 7.5 (c, d). It is shown that at two different frequencies one eigenvalue diverges, while other drops to zero, indicating CPA-Laser state. Interestingly, one can visually conclude from Figure 7.5 (c, d) that reducing the non-Hermiticity parameter γ
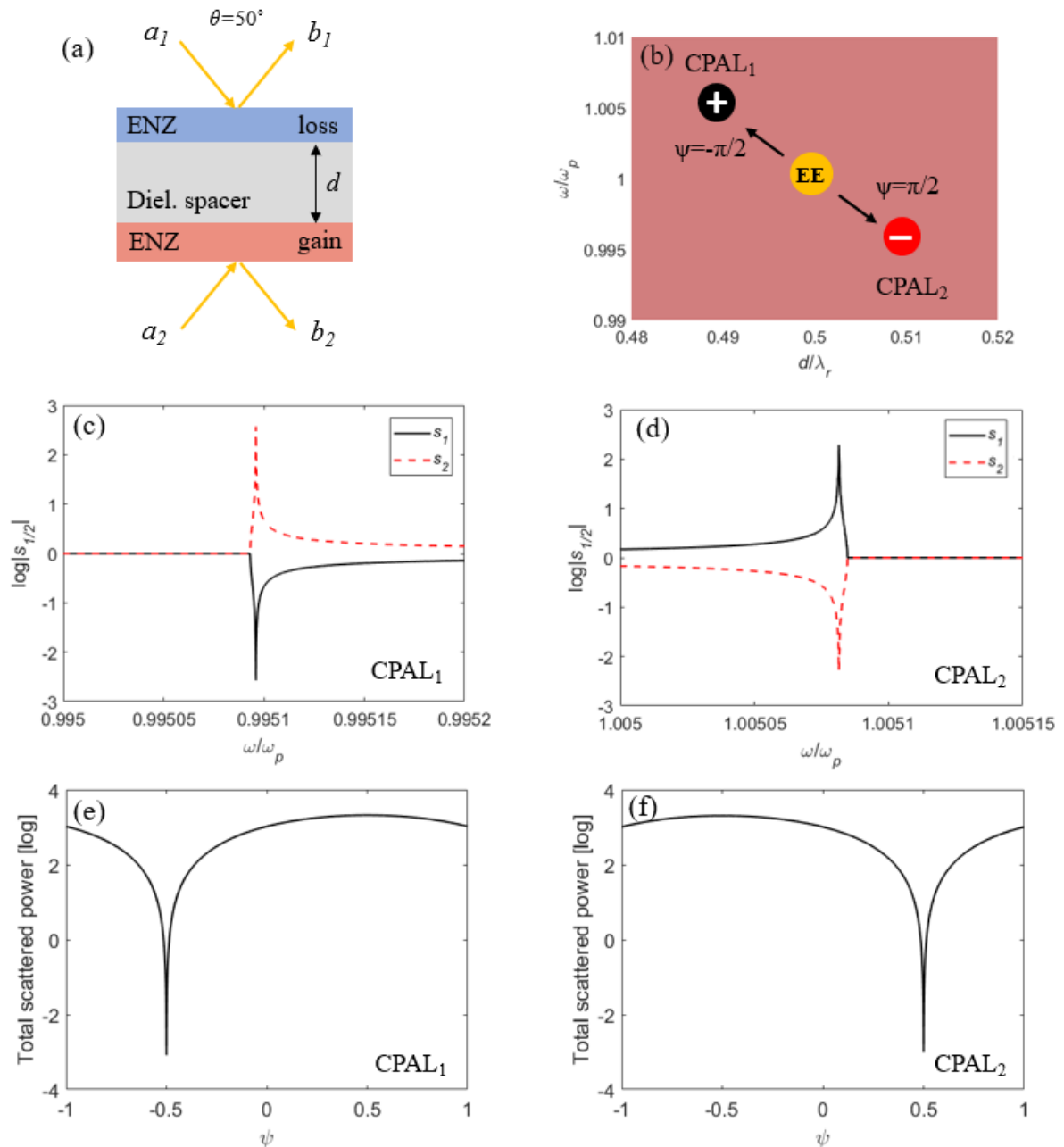
Figure 7.5. (a) Coherent setup of the PT-symmetric system. (b) Splitting of EE into two CPAL states in the parameter space. (c) Amplitude of the eigenvalues for $\psi = -\pi/2$ at CPAL$_1$ point. (d) Amplitude of the eigenvalues for $\psi = \pi/2$ at CPAL$_2$ point. (e) Output power as a function of the phase ψ at CPAL$_1$. (f) Output power as a function of the phase ψ at CPAL$_2$

would push the two CPAL points together, and ultimately bring them to plasma frequency where they destroy each other forming the EE and the eigenvalues become completely unimodular. In that sense, EE represents an exceptional point since any non-zero loss/gain coefficient results in a broken PT-symmetric phase and splitting of the eigenvalues. Additionally, we plot the total scattering power (total output power) at the CPA-Laser points as a function of the phase difference between input signals ψ, Figure 7.5 (e, f). As phase changes, output power is decreased until it vanishes at $\psi=+/- \pi/2$ for states CPAL$_{2/1}$.

7.5 Embedded Scattering Eigenstates in Open Non-Hermitian Systems with coherent excitation

As previously discussed, many different scattering phenomena can be fully described considering the analytic properties of the scattering matrix in the complex frequency plane, as reiterated in Figure 7.6 (a). We next show how EE-like scattering states can be tailored in non-Hermitian structures based on the analytic properties of complex scattering coefficients and coherent excitation. In order to achieve this effect, instead of considering the singularities S-matrix, we work in the framework of the scattering coefficients, for which a zero does not imply full absorption of the wave, but instead zero scattered power to a given channel. In the following we show that the scattering coefficient zeros can be manipulated by using multiple
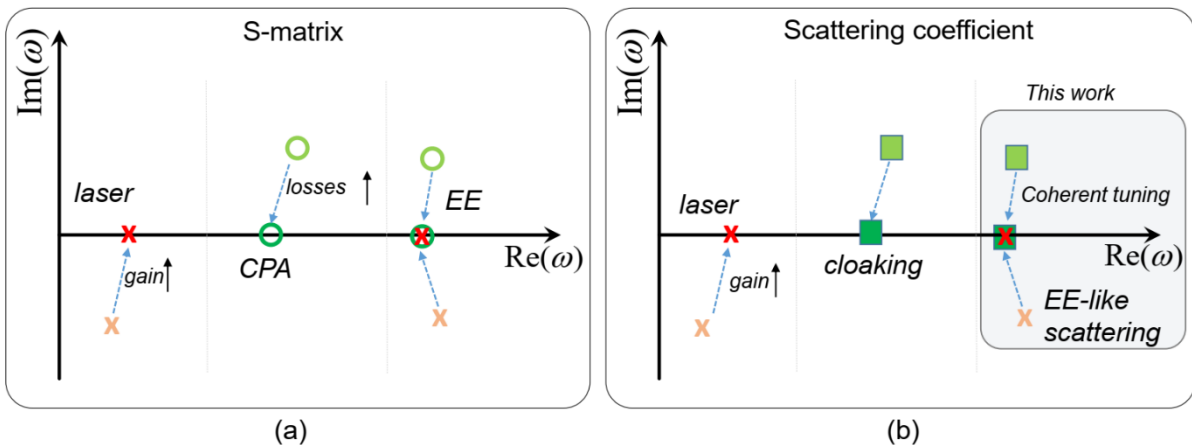
Figure 7.6. (a) Scattering scenarios in terms of the S-matrix in the complex frequency plane. Adding gain can push a pole (red cross) towards the real axis, giving rise to lasing. The time-reversed scenario of a zero approaching the real frequency axis leads to coherent perfect absorption (CPA). Embedded eigenstates (EE) correspond to the case in which a zero and pole of a Hermitian system coalesce on the real axis. (b) A description using the scattering coefficient. Scattering coefficient zeros imply no scattered waves, hence they are different from scattering matrix zeros, which imply no outgoing waves, while the two share the same poles. The position of a scattering coefficient zero can be coherently controlled through multiple excitation signals, and brought towards a pole, inducing EE-like scattering with vanishing linewidth.

coherent excitations in such a way that they may converge to the location of a pole on the real axis and realize a scattering EE with vanishing linewidth, Figure 7.6 (b).

To make the PT-symmetric structure from Figure 7.5(a) stable, we reduce the gain, pushing the poles down towards the lower complex half plane, Figure 7.7 (a). We select the value of gain to bring the pole with largest $\text{Im}(\omega)$ to the real axis, causing a very narrow resonant peak in scattering, transmission and reflection, Figure 7.7 (b), as the system is at the threshold of lasing. The $\hat{s}$-matrix eigenvalue amplitudes for the PT-symmetric case and the reduced gain (stabilized) case, are shown in Figure 7.8. As expected, one of the eigenvalues diverges in
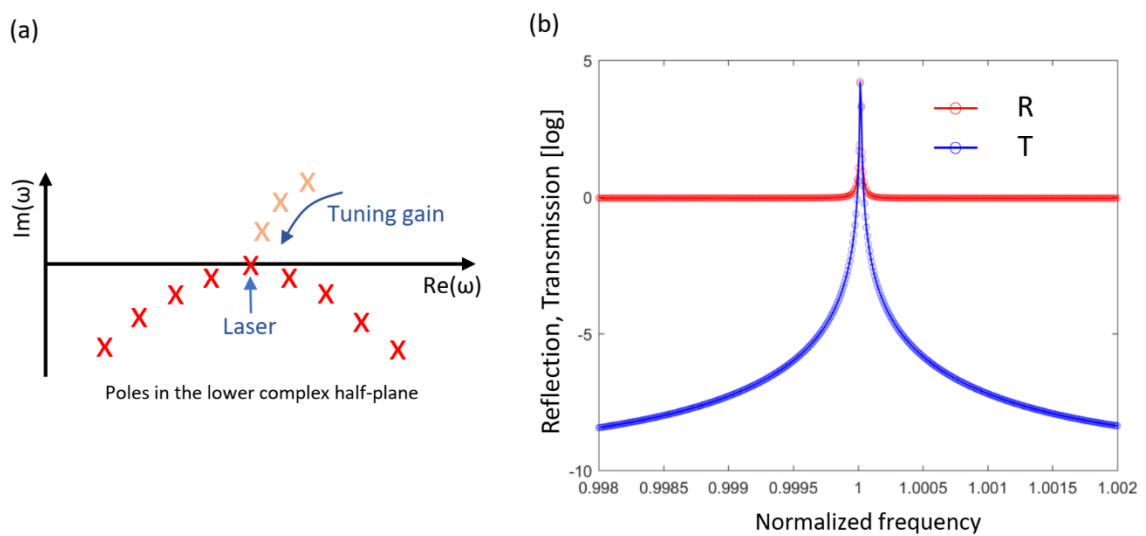
Figure 7.7. (a) Reducing the gain brings the system back to stability, with a pole lying on the real frequency axis (lasing threshold). (b) Transmission and reflection coefficients for fixed incidence angle, at the quasi-EE condition.
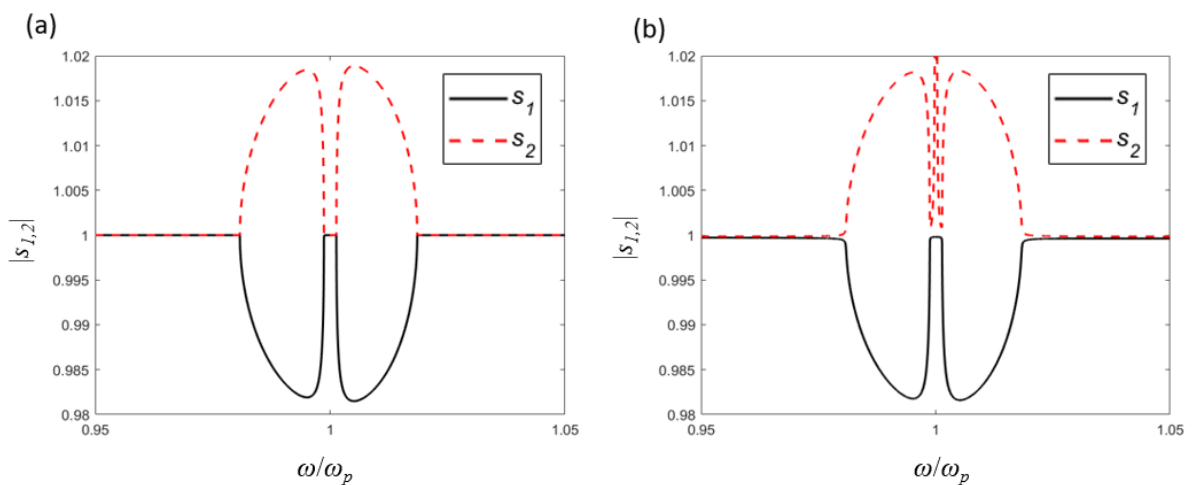
Figure 7.8. Eigenvalues amplitudes for (a) PT-symmetric case and (b) reduced gain (stabilized) case with a lasing mode.

amplitude representing the lasing mode. The other eigenvalue remains steady at amplitude equal to 1.

It is instructive to recall the situation of the CPA-Laser regime, where the eigenvalue spectrum contains a point for which one eigenvalue diverges and other goes to zero. In that regime, by choosing a proper set of eigenvectors, one can switch between CPA and lasing. However, in this case one can switch between lasing and "no scattering" regime by tuning the eigenvectors, where the regime of "no scattering" implies conservation of input energy (eigenvalue modulus equal to 1).

To manipulate and tailor the scattering zeros of the system, ideally to align it with a scattering pole, we can now resort to coherent excitations, as recently proposed in the context of CPA systems, in which by tuning of the amplitude or phase of one of the coherent waves allows pushing a scattering zero towards the real axis and achieve perfect absorption. Detuning the excitation allows switching on/off the CPA regime coherently [230]. Here, we consider a different scenario and start from the lasing regime, Figure 7.7 (a). We search for a specific coherent excitation that would push a scattering zero (not an $\hat{s}$-matrix zero, which would be independent of the excitation) towards the pole and cancel it out, enabling the EE operation. Similar to the CPA regime, we also would be able to coherently switch on/off the lasing operation by controlling the excitation scheme.

We adopt the previous coherent setup, and designate the input channels as ports 1 and 2, and output channels as ports 3 and 4. We define the amplitude of scattering to port 3 as $R_3(\omega, \theta_i) = |b_1 / (a_1 + a_2)|$. The analysis of poles and zeros of $R_3(\omega, \theta_i)$ demonstrates that indeed a scattering zero can be continuously tuned to converge to the same location as the pole lying on the real frequency axis, whereas the coherent excitation does not affect the position of the pole. Interestingly, when the zero meets the pole, they cancel out, inducing an EE-like response with vanishing linewidths, and lasing disappears, Figure 7.9 (b). The scattering spectrum around this point shows an EE-like response, Figure 7.9 (a). Thus, coherent excitation of a non-Hermitian system allows tailoring the position of poles and zeros, enabling extreme scattering control up to inducing an EE-like point in scattering spectrum.

This setup also allows us to coherently tune our system. In contrast to CPA, where the energy is inevitably dissipated into heat, in our structure dissipation is balanced by gain at the EE-like state. At the specific excitation supporting the EE-like state, the reflectivity is unitary on both sides, Figure 7.9 (b), and the system acts as a reflecting mirror. This is confirmed by
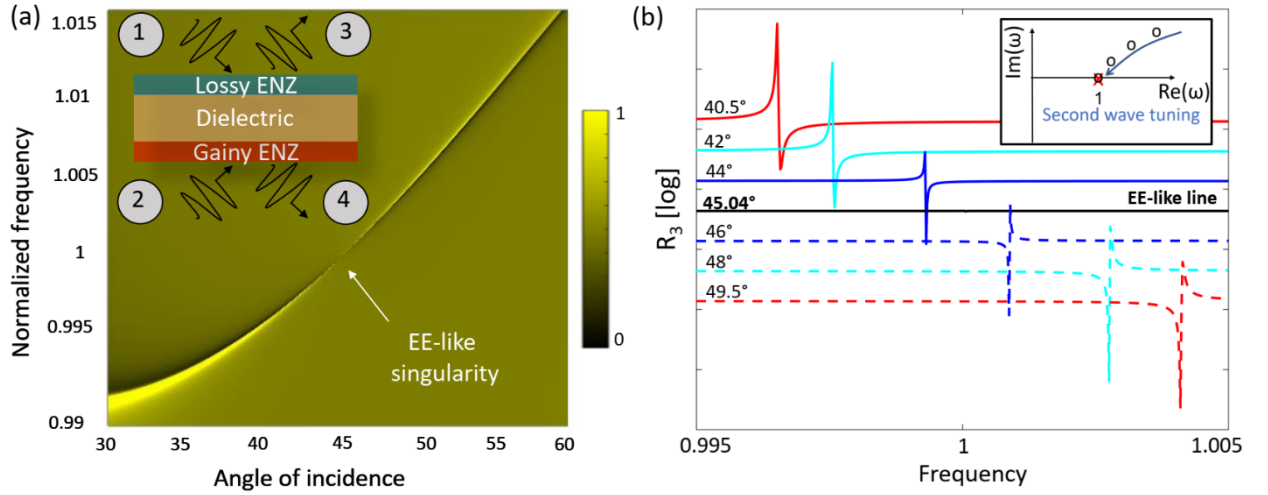
Figure 7.7. (a) Scattering spectrum $R_3(\omega, \theta_i) = |b_1 / (a_1 + a_2)|$ for coherent excitation. Inset: two-port excitation configuration for coherent excitation of the non-Hermitian structure with unbalanced gain and loss. The structure is stable, since it has no poles in the upper complex frequency half-plane and the lasing threshold pole lays on the real frequency plane. Coherent excitation from ports 1 and 2 allows continuous moving of a scattering zero to the same real frequency [inset in (b)], resulting in their cancelation and formation of an EE-like state in the scattering spectrum (a). (b) Port 3 scattering spectrum, demonstrating a vanishing linewidth at the EE-like scattering state.

the electric and magnetic field distributions of the structure, showing zero fields inside the dielectric layer, Figure 7.10 (a), which implies that the resonant EE-like mode at the lasing threshold supported by the structure cannot be excited by the outside. If we now detune the excitation from this EE state, the scattering zero is shifted away, and an asymmetric lasing regime can be observed, Figure 7.10 (b). For example, if the excitation amplitude at port 2 is
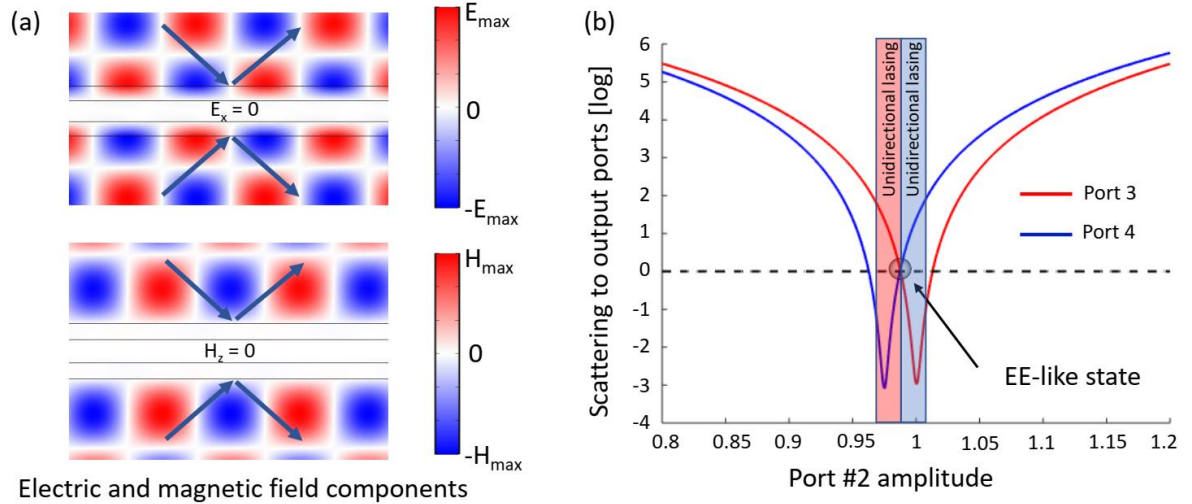
Figure 7.8. Coherent tuning of the non-Hermitian structure with unbalanced gain and loss. (a) Electric and magnetic field distribution profiles in the structure at the EE-like scattering state. (b) Reflection coefficients to ports 3 and 4 as a function of the port. When the excitation is balanced, the joint reflection to ports 3 and 4 is unitary, and the scattering spectrum shows an EE-like behavior (Figure 7.9 (a)) with vanishing fields inside the structure. As the amplitude of port 2 is detuned from this state, unidirectional lasing arises. This is achieved through coherent manipulation of the scattering zero position.

113

lower than the required value to achieve EE-like state, scattering to port 3 is significantly amplified, whereas scattering to port 4 vanishes. Vice versa, if the amplitude of the excitation at port 2 is larger than the EE value, we have the opposite scenario, with lasing towards port 4 and no signal at port 3.

7.6 Conclusion

In this chapter we have established a fundamental connection between EE, CPA and CPAL states in planar systems. Under mirror-symmetric and PT-symmetric perturbations, EE splits into topological charges (CPA and CPAL, respectively) which have a winding number in the phase of the *S*-matrix eigenvalues. This result deepens the connection between the different topological phenomena in scattering systems, and opens new avenues of research at the intersection of embedded eigenstates, topological photonics, and PT-symmetry.

To use the unusual properties of the scattering offered in such systems, we propose a novel scattering scenario based on the analytic properties of complex scattering coefficients and coherent excitation. An EE-like state is induced, characterized by a diverging scattering feature, ideally suited for sensing and filtering applications. The coherent nature of the setup also enables all-optical tunability of the system, where the system can be tuned from EE-like scattering to unidirectional lasing. The presented ideas could also be useful for realization of low-threshold, switchable lasers.

Chapter 8: Conclusion and future work

In this thesis, we have explored novel wave phenomena in plasmonics and metamaterials. By studying unusual propagation and scattering scenarios, we have shown versatile and precise control of amplitude, phase and polarization of waves, with a broad range of demonstrated applications including microwave filters, microwave and optical sensors, polarizers, thermal emitters, and coherent control of extreme scattering events.

In Chapter 3, the fundamentals of the SIW-based SPP concept were analyzed and based on this analysis high-performance microwave components have been designed. Namely, the advantageous properties of SPP modes have been fully leveraged at microwave frequencies using stacked SIW structures. The fundamental building block was shown to be a promising candidate for communications and sensing technologies, as the unusual physics behind effective SPP waves provided new opportunities in waveguiding and enabled strong light-matter interaction due to confinement. Different than conventional plasmonics, the low-cost nature and ease of fabrication at microwave frequencies makes this concept particularly attractive. Two novel microwave filters and a sensor with good performance have been experimentally demonstrated, which represent the first realizations of such components based on SIW-based SPPs. Filters were characterized with good in-band characteristics, excellent out-of-band rejection, and overall small size, while the design guidelines were precisely given and explained. In addition, the confined nature of effective SPPs was utilized to realize a very sensitive liquid analyte sensor, which can detect very small changes in dielectric constant of the sensed analyte and has comparable or better sensitivity than other sensors of this type, as documented in Table 2. These experimental findings confirm the potential of effective SPPs in SIW structures for realizations of high-performance, low-cost, low-profile microwave components.

Starting from Chapter 4, we focused on a variety of scattering problems in planar structures. By using a scattering matrix formalism and complex frequency notation, we were able to classify different scattering processes and anomalies according to the presence and interplay of singularities of the scattering matrix eigenvalues and scattering coefficients. As demonstrated further in the Chapters 5, 6, and 7, the knowledge and control of positions of the singularities presents an excellent design method for various optical devices. Furthermore, this

method revealed new, fundamental properties of the scattering anomalies which had not been established beforehand.

A scattering anomaly we specifically focused on is the embedded eigenstate, a non-radiating eigenmode with exotic scattering properties. In Chapter 5, a class of symmetry-protected and non-symmetry-protected EEs in multilayer ENZ structures were systematically and comprehensively presented, which complements and unifies the current body of knowledge about their existence in such structures. Based on this analysis and using a low-loss infrared ENZ effect provided by SiC, a very narrowband and directive thermal absorber/emitter was demonstrated, expanding the possibilities of application of EEs in thermal emission control. The discussion was further expanded in Chapter 6 by analyzing the topological aspects of EEs in ENZ and ENP reflective planar structures. Using the scattering matrix framework, it was revealed that the topologically protected perfect absorption singularities necessarily emerge from EEs, and methods and rules for their creation and annihilation were established. Using their topological nature, we have exploited the singularities to design a versatile polarization control scheme in the long-wave infrared regime. Lack of naturally birefringent materials in this part of the EM spectrum makes the proposed concept particularly useful, as versatile polarization control can be obtained with available materials such as silicon carbide. Furthermore, a potential polarization switching method was proposed, based on modulating the permittivity of the resonant material.

Furthermore, the discussed topological charges associated with phase singularities have been used to propose a concept for improved phase sensing method which we termed near-annihilation point sensing. Namely, by bringing two charges in vicinity in the parameter space without annihilating them, a wide angular region with an abrupt phase jump is created. In this way a practical problem inherent to phase-singularity sensing schemes is eliminated, where usually a high resolution of incident angles is required for achieving high sensitivities. Apart from this practical consequence, it was shown that sensitivity can be further increased by using multilayer structures, making this concept a promising candidate for trace gas sensing and other highly sensitive schemes.

Finally, in Chapter 7 we expanded the scattering anomaly discussion by considering PT-symmetric ENZ structures. Using the same analysis as in previous chapter, it was revealed that lossy and PT-symmetric perturbations to the multilayer system cause EEs to split into pairs of CPA and CPA-laser charges, respectively. This confirms the topological nature of these effects, which has not been previously discussed, and provides a useful tool for creation and

control of these exotic states in optical structures. As an example of an unusual effect due to the manipulation of the singularities of the scattering coefficient, a method for obtaining an effective embedded eigenstate was shown, even though the system is non-Hermitian and does not support a true EE. This interplay of poles and zeros in the scattering spectrum with coherent excitation enables unusual scattering control. It was shown how tuning of the secondary wave amplitude can switch the system between extreme scattering states – from unidirectional absorbing to unidirectional lasing, and to EE-like scattering. These theoretical findings add new insights to the area of research at the intersection of embedded eigenstates, topological photonics, and PT-symmetryand they are well suited for sensing, filtering, and low-threshold lasing applications.

It should be noted that the results presented in Chapters 5, 6 and 7 represent a promising basis for future research. Although several new results are shown, the presented theoretical framework and the established topological nature of the analyzed effects, as well as the generality of the presented results leave room for new research directions.

8.1. Future Work

Although many different aspects of the topological scattering singularities were discussed, unexplored directions remain that could contribute to further understanding of the underlying physics and the development of new applications. Listed below are some considerations for future work:

- Experimental verification of the proposed ideas including thermal emission, polarization control and sensing in the infrared spectral region.

- Incorporating advanced models that account for nonlocal effects in the permittivity function, which are important for extremely thin ENZ layers. This can yield better theoretical predictions; however, nonlocality can also serve as another degree of freedom in the design of EM devices.

- In this thesis, only non-Hermitian perturbations to the planar systems were considered. However, breaking spatial and/or time-reversal symmetries would further enrich the topological picture. For example, a magnetized plasma model will be considered, where time-reversal symmetry is broken and Weyl points appear. Relying on the theory established in this thesis, a more comprehensive picture of the topological scattering effects can be obtained, bridging the gap between different areas of topological

photonics with practical implications for non-reciprocal thermal emission and chiral light.

References

[1]   Maxwell, J. C. A dynamical Theory of the Electromagnetic Field. *Phil. Trans. Royal Soc. London*. **155** (1865).

[2]   Abbe, E. Beiträge zur Theorie des Mikroskops und der mikroskopischen Wahrnehmung: I. Die Construction von Mikroskopen auf Grund der Theorie. *Arch. für mikroskopische Anat.* **9**, 413–418 (1873).

[3]   Ritchie, R. H. Plasma Losses by Fast Electrons in Thin Films. *Phys. Rev.* **106 N.5**, 8 (1956).

[4]   Ritchie, R. H. & Marusak, A. L. The surface plasmon dispersion relation for an electron gas. *Surf. Sci.* **4**, 234–240 (1966).

[5]   Barnes, W. L., Dereux, A. & Ebbesen, T. W. Surface plasmon subwavelength optics. *Nature* **424**, 824–830 (2003).

[6]   Homola, J., Yee, S. S. & Gauglitz, G. Surface plasmon resonance sensors: review. *Sensors Actuators, B Chem.* **54**, 3–15 (1999).

[7]   Willets, K. A. & Van Duyne, R. P. Localized surface plasmon resonance spectroscopy and sensing. *Annu. Rev. Phys. Chem.* **58**, 267–297 (2007).

[8]   Engheta, N. & Ziolkowski, R. *Electromagnetic Metamaterials: Physics and Engineering Explorations*. *Wiley–IEEE Press* (2006).

[9]   Liberal, I. & Engheta, N. Near-zero refractive index photonics. *Nat. Photonics* **11**, 149–158 (2017).

[10]   H. E. Burton. The Optics of Euclid. *J. Opt. Soc. Am.*, **35**(5), 357– 372 (1945)

[11]   Kock, W. E. Metal-Lens Antennas. *Proc. IRE* **34**, 828–836 (1946).

[12]   Veselago, V. G. The Electrodynamics of Substances with Simultaneously Negative Values of ε and μ. *Soviet Physics Uspekhi* **10**, 509–514 (1968).

[13]   Sivukhin, D.V. *Opt. Spectrosc*. **3** (1957)

[14]   Pafomov. V.E. ZHETF 36 1853 (1959), *Sov. Phys. JETP* **9** (1959)

[15]   Pendry, J. B., Holden, A. J., Robbins, D. J. & Stewart, W. J. Magnetism from conductors and enhanced nonlinear phenomena. *IEEE Trans. Microw. Theory Tech.* **47**, 2075–2084 (1999).

[16]   Pendry, J. B. Negative refraction makes a perfect lens. *Phys. Rev. Lett.* **85**, 3966–3969 (2000).

[17]   Shelby, R. A., Smith, D. R. & Schultz, S. Experimental verification of a negative index of refraction. *Science (80-.)*. **292**, 77–79 (2001).

[18]   Schurig, D. *et al.* Metamaterial electromagnetic cloak at microwave frequencies. *Science.* **314**, 977–980 (2006).

[19]   Pendry, J. B., Schurig, D. & Smith, D. R. Controlling electromagnetic fields. *Science.* **312**, 1780–1782 (2006).

[20]   Alù, A. & Engheta, N. Achieving transparency with plasmonic and metamaterial coatings. *Phys. Rev. E - Stat. Nonlinear, Soft Matter Phys.* **72**, 1–9 (2005).

[21]   Landy, N. I., Sajuyigbe, S., Mock, J. J., Smith, D. R. & Padilla, W. J. Perfect metamaterial absorber. *Phys. Rev. Lett.* **100**, 1–4 (2008).

[22]   Shen, X., Cui, T., Zhao, J., Ma, H., Jiang, W. and Li, H.. Polarization-independent wide-angle triple-band metamaterial absorber. *Opt. Express*, **19**(10), (2011).

[23]   Kang, S. *et al.* Ultra-Narrowband Metamaterial Absorbers for High Spectral Resolution Infrared Spectroscopy. *Adv. Opt. Mater.* **7**, 1–8 (2019).

[24]   Enoch, S., Tayeb, G., Sabouroux, P., Guérin, N. & Vincent, P. A Metamaterial for Directive Emission. *Phys. Rev. Lett.* **89**, 1–4 (2002).

[25]   Liu, X. *et al.* Taming the blackbody with infrared metamaterials as selective thermal emitters. *Phys. Rev. Lett.* **107**, 4–7 (2011).

[26]   Hossain, M. M., Jia, B. & Gu, M. A Metamaterial Emitter for Highly Efficient Radiative Cooling. *Adv. Opt. Mater.* **3**, 1047–1051 (2015).

[27]   Yu, N. *et al.* Light propagation with phase discontinuities: Generalized laws of reflection and refraction. *Science (80-.).* **334**, 333–337 (2011).

[28]   Ra'Di, Y., Sounas, D. L. & Alù, A. Metagratings: Beyond the Limits of Graded Metasurfaces for Wave Front Control. *Phys. Rev. Lett.* **119**, 1–6 (2017).

[29]   Yu, N. & Capasso, F. Flat optics with designer metasurfaces. *Nat. Mater.* **13**, 139–150 (2014).

[30]   Alù, A., Silveirinha, M. G., Salandrino, A. & Engheta, N. Epsilon-near-zero metamaterials and electromagnetic sources: Tailoring the radiation phase pattern. *Phys. Rev. B - Condens. Matter Mater. Phys.* **75**, 155410 (2007).

[31]   Edwards, B., Alù, A., Young, M. E., Silveirinha, M. & Engheta, N. Experimental verification of epsilon-near-zero metamaterial coupling and energy squeezing using a microwave waveguide. *Phys. Rev. Lett.* **100**, 1–4 (2008).

[32]   Silveirinha, M. & Engheta, N. Tunneling of electromagnetic energy through subwavelength channels and bends using ε-near-zero materials. *Phys. Rev. Lett.* **97**, (2006).

[33]   Maas, R., Parsons, J., Engheta, N. & Polman, A. Experimental realization of an epsilon-near-zero metamaterial at visible wavelengths. *Nat. Photonics* **7**, 907–912 (2013).

[34]   Alam, M. Z., De Leon, I. & Boyd, R. W. Large optical nonlinearity of indium tin oxide in its epsilon-near-zero region. *Science (80-.).* **352**, 795–797 (2016).

[35]   Fleury, R. & Alù, A. Enhanced superradiance in epsilon-near-zero plasmonic channels. *Phys. Rev. B - Condens. Matter Mater. Phys.* **87**, 201101 (2013).

[36]   Moitra, P. *et al.* Realization of an all-dielectric zero-index optical metamaterial. *Nat. Photonics* **7**, 791–795 (2013).

[37]   Chebykin, A. V., Orlov, A. A., Shalin, A. S., Poddubny, A. N. & Belov, P. A. Strong Purcell effect in anisotropic ε-near-zero metamaterials. *Phys. Rev. B - Condens. Matter Mater. Phys.* **91**, 1–6 (2015).

[38]   Caspani, L. *et al.* Enhanced Nonlinear Refractive Index in ϵ -Near-Zero Materials. *Phys. Rev. Lett.* **116**, 1–5 (2016).

[39]   Reshef, O., De Leon, I., Alam, M. Z. & Boyd, R. W. Nonlinear optical effects in epsilon-near-zero media. *Nat. Rev. Mater.* **4**, 535–551 (2019).

[40]   Kim, J. *et al.* Role of epsilon-near-zero substrates in the optical response of plasmonic antennas. *Optica* **3**, 339 (2016).

[41]   Vesseur, E. J. R., Coenen, T., Caglayan, H., Engheta, N. & Polman, A. Experimental verification of n=0 structures for visible light. *Phys. Rev. Lett.* **110**, 1–5 (2013).

[42]   Pollard, R. J. *et al.* Optical nonlocalities and additional waves in epsilon-near-zero metamaterials. *Phys. Rev. Lett.* **102**, 1–4 (2009).

[43]   Poddubny, A., Iorsh, I., Belov, P. & Kivshar, Y. Hyperbolic metamaterials. *Nat. Photonics* **7**, 958–967 (2013).

[44]   Argyropoulos, C., Estakhri, N. M., Monticone, F. & Alù, A. Negative refraction, gain and nonlinear effects in hyperbolic metamaterials. *Opt. Express* **21**, 15037 (2013).

[45]   Huang, X., Lai, Y., Hang, Z. H., Zheng, H. & Chan, C. T. Dirac cones induced by accidental degeneracy in photonic crystals and zero-refractive-index materials. *Nat. Mater.* **10**, 582–586 (2011).

[46]   Liberal, I. & Engheta, N. Nonradiating and radiating modes excited by quantum emitters in open epsilon-near-zero cavities. *Sci. Adv.* **2**, e1600987 (2016).

[47]   Liberal, I., Mahmoud, A. M. & Engheta, N. Geometry-invariant resonant cavities. *Nat. Commun.* **7**, 1–7 (2016).

[48]   Kittel, C. "Introduction to Solid State Physics," Wiley (1986).

[49]   Maier, S. "Plasmonics: Fundamentals and Applications," Springer (2007).

[50] Ferrell, R. A. Predicted Radiation of Plasma Oscillations. *Phys. Rev.* **111**, 1214 (1958).

[51] Berreman, D. W. Optic Fretluency. *Phys. Revie* **130**, 2193–2198 (1963).

[52] Nordin, L. *et al.* Mid-infrared epsilon-near-zero modes in ultra-thin phononic films. *Appl. Phys. Lett.* **111**, (2017).

[53] Yang, Y. *et al.* Femtosecond optical polarization switching using a cadmium oxide-based perfect absorber. *Nat. Photonics* **11**, 390–395 (2017).

[54] Ebbesen, T. W., Genet, C. & Bozhevolnyi, S. I. Surface-plasmon circuitry. (2008).

[55] Mayer, K. and Hafner, J., 2011. Localized Surface Plasmon Resonance Sensors. *Chemical Reviews*, **111**(6), pp.3828-3857.

[56] Ozbay. E. Plasmonics : Merging Photonics and. *Science (80-.).* **189**, 189–194 (2012).

[57] Ng, B. *et al.* Spoof Plasmon Surfaces: A Novel Platform for THz Sensing. *Adv. Opt. Mater.* **1**, 543–548 (2013).

[58] Shen, X. & Cui, T. J. Ultrathin plasmonic metamaterial for spoof localized surface plasmons. *Laser Photonics Rev.* **8**, 137–145 (2014).

[59] Pendry, J. B., Martín-Moreno, L. & Garcia-Vidal, F. J. Mimicking surface plasmons with structured surfaces. *Science (80-.).* **305**, 847–848 (2004).

[60] Zhao, L. *et al.* A novel broadband band-pass filter based on spoof surface plasmon polaritons. *Sci. Rep.* **6**, 1–8 (2016).

[61] Guan, D. F., You, P., Zhang, Q., Xiao, K. & Yong, S. W. Hybrid spoof surface plasmon polariton and substrate integrated waveguide transmission line and its application in filter. *IEEE Trans. Microw. Theory Tech.* **65**, 4925–4932 (2017).

[62] Kianinejad, A., Chen, Z. N. & Qiu, C. W. Design and modeling of spoof surface plasmon modes-based microwave slow-wave transmission line. *IEEE Trans. Microw. Theory Tech.* **63**, 1817–1825 (2015).

[63] Kianinejad, A., Chen, Z. N. & Qiu, C. W. Low-Loss Spoof Surface Plasmon Slow-Wave Transmission Lines with Compact Transition and High Isolation. *IEEE Trans. Microw. Theory Tech.* **64**, 3078–3086 (2016).

[64] Guan, D., You, P., Zhang, Q., Lu, Z., Yong, S. and Xiao, K. A Wide-Angle and Circularly Polarized Beam-Scanning Antenna Based on Microstrip Spoof Surface Plasmon Polariton Transmission Line. *IEEE Antennas Wirel. Propag. Lett.* **16**, 2538–2541 (2017).

[65] Liao, D., Zhang, Y. & Wang, H. Wide-Angle Frequency-Controlled Beam-Scanning Antenna Fed by Standing Wave Based on the Cutoff Characteristics of Spoof Surface Plasmon Polaritons. *IEEE Antennas Wirel. Propag. Lett.* **17**, 1238–1241 (2018).

[66] Zhang, Q., Zhang, Q. Le & Chen, Y. Spoof Surface Plasmon Polariton Leaky-Wave Antennas Using Periodically Loaded Patches above PEC and AMC Ground Planes. *IEEE Antennas Wirel. Propag. Lett.* **16**, 3014–3017 (2017).

[67] Pang, Y. *et al.* Spatial k-dispersion engineering of spoof surface plasmon polaritons for customized absorption. *Sci. Rep.* **6**, 1–9 (2016).

[68] Ren, J., and Yin, J. Y. Broadband Microwave Absorber. *Opt. Mater. Express* **9**, 2060–2071 (2018).

[69] Chen, X. & Fan, W. Ultrasensitive terahertz metamaterial sensor based on spoof surface plasmon. *Sci. Rep.* **7**, 1–8 (2017).

[70] Cheng, D. *et al.* Terahertz biosensing metamaterial absorber for virus detection based on spoof surface plasmon polaritons. *Int. J. RF Microw. Comput. Eng.* **28**, 1–7 (2018).

[71] Hu, X. *et al.* Metamaterial absorber integrated microfluidic terahertz sensors. *Laser Photonics Rev.* **10**, 962–969 (2016).

[72] Della Giovampaola, C. & Engheta, N. Plasmonics without negative dielectrics. *Phys. Rev. B* **93**, 1–8 (2016).

[73] Li, Z. *et al.* Effective Surface Plasmon Polaritons Induced by Modal Dispersion in a Waveguide. *Phys. Rev. Appl.* **7**, 1–9 (2017).

[74] Ge, L., Chong, Y. D. & Stone, A. D. Steady-state ab initio laser theory: Generalizations and analytic results. *Phys. Rev. A - At. Mol. Opt. Phys.* **82**, 063824 (2010).

[75] von Neumann, J. & Wigner, E. P. Über merkwürdige diskrete Eigenwerte. *Collect. Work. Eugene Paul Wigner* 291–293 (1993).

[76] Friedrich, H. & Wintgen, D. Interfering resonances and bound states in the continuum. *Phys. Rev. A* **32**, 3231–3242 (1985).

[77] Hsu, C. W., Zhen, B., Stone, A. D., Joannopoulos, J. D. & Soljacic, M. Bound states in the continuum. *Nature Reviews Materials* **1**, 1–13 (2016).

[78] Zhao, M. & Fang, K. Mechanical bound states in the continuum for macroscopic optomechanics. *Opt. Express, Vol. 27, Issue 7, pp. 10138-10151* **27**, 10138–10151 (2019).

[79] Lyapina, A. A., Maksimov, D. N., Pilipchuk, A. S. & Sadreev, A. F. Bound states in the continuum in open acoustic resonators. *J. Fluid Mech.* **780**, 370–387 (2015).

[80] Hsu, C. W. *et al.* Observation of trapped light within the radiation continuum. *Nature* **499**, 188–191 (2013).

[81] Azzam, S. I., Shalaev, V. M., Boltasseva, A. & Kildishev, A. V. Formation of Bound States in the Continuum in Hybrid Plasmonic-Photonic Systems. *Phys. Rev. Lett.* **121**, 253901 (2018).

[82] Leitis, A. *et al.* Angle-multiplexed all-dielectric metasurfaces for broadband molecular fingerprint retrieval. *Sci. Adv.* **5**, 1–9 (2019).

[83] Jacobsen, R. E., Krasnok, A., Arslanagic, S., Lavrinenko, A. V. & Alú, A. Embedded eigenstate in a single resonator for sensing. *Conf. Lasers Electro-Optics 2021* **2** (2021).

[84] Han, S. *et al.* All-Dielectric Active Terahertz Photonics Driven by Bound States in the Continuum. *Adv. Mater.* **31**, 1–9 (2019).

[85] Rybin, M. V. *et al.* High- Q Supercavity Modes in Subwavelength Dielectric Resonators. *Phys. Rev. Lett.* **119**, 243901 (2017).

[86] Koshelev, K., Lepeshov, S., Liu, M., Bogdanov, A. & Kivshar, Y. Asymmetric Metasurfaces with High- Q Resonances Governed by Bound States in the Continuum. *Phys. Rev. Lett.* **121**, 193903 (2018).

[87] Bogdanov, A., Koshelev, K., Kapitanova, P., Rybin, M., Gladyshev, S., Sadrieva, Z., Samusev, K., Kivshar, Y. and Limonov, M.. Bound states in the continuum and Fano resonances in the strong mode coupling regime. *Adv. Photonics* **1**, 1 (2019).

[88] Silveirinha, M. G. Trapping light in open plasmonic nanostructures. *Phys. Rev. A - At. Mol. Opt. Phys.* **89**, 023813 (2014).

[89] Monticone, F. & Alù, A. Embedded photonic eigenvalues in 3D nanostructures. *Phys. Rev. Lett.* **112**, 213903 (2014).

[90] Krasnok, A. *et al.* Anomalies in light scattering. *Adv. Opt. Photonics* **11**, 892 (2019).

[91] Monticone, F., Doeleman, H. M., Den Hollander, W., Koenderink, A. F. & Alù, A. Trapping Light in Plain Sight: Embedded Photonic Eigenstates in Zero-Index Metamaterials. *Laser Photonics Rev.* **12**, 1700220 (2018).

[92] Zhen, B., Hsu, C. W., Lu, L., Stone, A. D. & Soljačić, M. Topological nature of optical bound states in the continuum. *Phys. Rev. Lett.* **113**, 1–5 (2014).

[93] Doeleman, H. M., Monticone, F., Den Hollander, W., Alù, A. & Koenderink, A. F. Experimental observation of a polarization vortex at an optical bound state in the continuum. *Nat. Photonics* **12**, 397–401 (2018).

[94] Kuratowski, K. Topology (Academic Press, New York. 1966).

[95] M.Z. Hasan, and C.L. Kane, "Colloquium: Topological insulators," *Rev. Mod. Phys.* 82, 3045–3067 (2010).

[96] L. Lu, J.D. Joannopoulos, and M. Soljačić, "Topological photonics," *Nat. Photonics* **8**, 821–829 (2014).

[97] T. Ozawa, H.M. Price, A. Amo, N. Goldman, M. Hafezi, L. Lu, M.C. Rechtsman, D. Schuster, J. Simon, O. Zilberberg, and I. Carusotto. "Topological photonics," Rev. Mod. Phys. **91**, 15006 (2019).

[98] A.B. Khanikaev, S.H. Mousavi, W.K. Tse, M. Kargarian, A.H. MacDonald, and G. Shvets, "Photonic topological insulators," Nat. Mater. **12**, 233–239 (2013).

[99] Z. Wang, Y. Chong, J.D. Joannopoulos, and M. Soljačić, "Observation of unidirectional backscattering-immune topological electromagnetic states," Nature **461**, 772–775 (2009).

[100] X. Yin, J. Jin, M. Soljačić, C. Peng, and B. Zhen, "Observation of topologically enabled unidirectional guided resonances," Nature **580**, 467–471 (2020).

[101] J. Jin, X. Yin, L. Ni, M. Soljačić, B. Zhen, C. Peng. "Topologically enabled ultrahigh-Q guided resonances robust to out-of-plane scattering," Nature **574**, 501–504 (2019).

[102] Guo, Y., Xiao, M. & Fan, S. Topologically protected complete polarization conversion. *Phys. Rev. Lett.* **119**, 1–5 (2017).

[103] Liu, W. *et al.* Circularly polarized states spawning from bound states in the continuum. *Phys. Rev. Lett.* **123**, 116104 (2019).

[104] Ye, W., Gao, Y. & Liu, J. Singular points of polarizations in the momentum space of photonic crystal slabs. *Phys. Rev. Lett.* **124**, 153904 (2020).

[105] Yoda, T. & Notomi, M. Generation and annihilation of topologically protected bound states in the continuum and circularly polarized states by symmetry Breaking. *Phys. Rev. Lett.* **125**, 53902 (2020).

[106] Khurgin, J. B. How to deal with the loss in plasmonics and metamaterials. *Nat. Nanotechnol.* **10**, 2–6 (2015).

[107] Kronig, R. L. On the theory of dispersion of x-rays, *J. Opt. Soc. Am.* **12**, 547 (1926)

[108] Kramers, M. H. A. La diffusion de la lumiere par les atomes, *Atti Cong. Intern. Fisica* (Transactions of Volta Centenary Congress) Como, Vol. **2** (1927).

[109] Berini, P. & De Leon, I. Surface plasmon-polariton amplifiers and lasers. *Nat. Photonics* **6**, 16–24 (2012).

[110] Xiao, S. *et al.* Loss-free and active optical negative-index metamaterials. *Nature* **466**, 735–738 (2010).

[111] Estakhri, N. M. & Alù, A. Physics of unbounded, broadband absorption/gain efficiency in plasmonic nanoparticles. *Phys. Rev. B - Condens. Matter Mater. Phys.* **87**, 1–9 (2013).

[112] A. Krasnok and A. Alù. Active Nanophotonics. *Proceedings of the IEEE* **108**, 628 (2020).

[113] Kurokawa, K. Some Basic Characteristics of Broadband Negative Resistance Oscillator Circuits. *Bell Syst. Tech. J.* **48**, 1937–1955 (1969).

[114] Zhang, Y. *et al.* Toward Surface Plasmon-Enhanced Optical Parametric Amplification (SPOPA) with Engineered Nanoparticles: A Nanoscale Tunable Infrared Source. *Nano Lett.* **16**, 3373–3378 (2016).

[115] Gather, M. C., Meerholz, K., Danz, N. & Leosson, K. Net optical gain in a plasmonic waveguide embedded in a fluorescent polymer. *Nat. Photonics* **4**, 457–461 (2010).

[116] Sadatgol, M., Özdemir, Ş. K., Yang, L. & Güney, D. O. Plasmon Injection to Compensate and Control Losses in Negative Index Metamaterials. *Phys. Rev. Lett.* **115**, 1–6 (2015).

[117] Stockman, M. I. The spaser as a nanoscale quantum generator and ultrafast amplifier. *J. Opt. A Pure Appl. Opt.* **12**, (2010).

[118] El-Ganainy, R. *et al.* Non-Hermitian physics and PT symmetry. *Nat. Phys.* **14**, 11–19 (2018).

[119] Bender, C. M. & Boettcher, S. Real spectra in non-hermitian hamiltonians having PT symmetry. *Phys. Rev. Lett.* **80**, 5243–5246 (1998).

[120] Rüter, C., Makris, K., El-Ganainy, R., Christodoulides, D., Segev, M. and Kip, D.. Observation of parity-time symmetry in optics. *Nat. Phys.* **6**, 192–195 (2010).

[121] Zyablovsky, A. A., Vinogradov, A. P., Pukhov, A. A., Dorofeenko, A. V & Lisyansky, A. A. PT-symmetry in optics. *Physics-Uspekhi* **57**, 1063–1082 (2014).

[122] Miri, M. A. & Alù, A. Exceptional points in optics and photonics. *Science (80-.).* **363**, (2019).

[123] Lin, Z. *et al.* Unidirectional invisibility induced by PT-symmetric periodic structures. *Phys. Rev. Lett.* **106**, 1–4 (2011).

[124] Shen, Y., Deng, X. H. & Chen, L. Unidirectional invisibility in a two-layer non-PT-symmetric slab. *Opt. Express* **22**, 19440 (2014).

[125] Longhi, S. Invisibility in PT-symmetric complex crystals. *J. Phys. A Math. Theor.* **44**, (2011).

[126] Ge, L., Chong, Y. D. & Stone, A. D. Conservation relations and anisotropic transmission resonances in one-dimensional PT-symmetric photonic heterostructures. *Phys. Rev. A - At. Mol. Opt. Phys.* **85**, 1–10 (2012).

[127] Longhi, S. PT-symmetric laser absorber. *Phys. Rev. A - At. Mol. Opt. Phys.* **82**, 1–4 (2010).

[128] Wong, Z. J. *et al.* Lasing and anti-lasing in a single cavity. *Nat. Photonics* **10**, 796–801 (2016).

[129] Hodaei, H. *et al.* Enhanced sensitivity at higher-order exceptional points. *Nature* **548**, 187–191 (2017).

[130] Deslandes, D. & Wu, K. Integrated microstrip and rectangular waveguide in planar form. *IEEE Microw. Wirel. Components Lett.* **11**, 68–70 (2001).

[131] Xu, F. & Wu, K. Guided-wave and leakage characteristics of substrate integrated waveguide. *IEEE Trans. Microw. Theory Tech.* **53**, 66–72 (2005).

[132] Balanis, C. Advanced engineering electromagnetics, 2nd ed., J. Wiley & Sons, New York (2012).

[133] Collin, R. Foundations for microwave engineering, 2nd ed., Wiley-IEEE Press, New York, (2001).

[134] N. Cselyuszka, Z. Sakotic, G. Kitic, V. Crnojevic-Bengin, N. Jankovic, "Novel Dual-band Band-Pass Filters Based on Surface Plasmon Polariton-like Propagation Induced by Structural Dispersion of Substrate Integrated Waveguide", *Sci. Rep.* **8**, 8332 (2018).

[135] L. Su, J. Mata-Contreras, P. Vélez, F. Martín, "Configurations of Splitter/Combiner Microstrip Sections Loaded with Stepped Impedance Resonators (SIRs) for Sensing Applications", *Sensors* **16** (12) (2016).

[136] M. Memon, S. Lim, "Millimeter-Wave Chemical Sensor Using Substrate-Integrated-Waveguide Cavity", *Sensors* 16 (12) (2016)

[137] G. Galindo-Romera, F. J. Herraiz-Martinez, M. Gil, J. Martinez-Martinez, D. Segovia-Vargas, "Submersible Printed Split-Ring Resonator-Based Sensor for Thin-Film Detection and Permittivity Characterization", *IEEE Sensors Journal* 16 (10) (2016).

[138] S. Majidifar, G. Karimi, "New approach for dielectric constant detection using a microstrip sensor", *Measurement* 93 (2016).

[139] R. Ramzan, M. Omar, O. Siddiqui, "Energy-Tunneling Dielectric Sensor Based on Substrate Integrated Waveguides", *IEEE Sensors Journal* 17 (5) (2017).

[140] J. Leroy, C. Dalmay, A. Landoulsi, F. Hjeij, C. Mélin, B. Bessette, et al., "Microfluidic biosensors for microwave dielectric spectroscopy", *Sensors and Actuators A: Physical* 229 (2015).

[141] O. Siddiqui, M. Kashanianfard, O. Ramahi, "Dielectric Sensors Based on Electromagnetic Energy Tunneling", *Sensors* 15 (4) (2015).

[142] A. Chahadih, P. Cresson, Z. Hamouda, S. Gu, C. Mismer, T. Lasri, Microwave/microfluidic sensor fabricated on a flexible kapton substrate for complex permittivity characterization of liquids, Sensors and Actuators A: Physical 229 (2015).

[143] I. Rusni, A. Ismail, A. Alhawari, M. Hamidon, N. Yusof, An Aligned-Gap and Centered-Gap Rectangular Multiple Split Ring Resonator for Dielectric Sensing Applications, Sensors 14 (7) (2014).

[144] A. Ebrahimi, W. Withayachumnankul, S. Al-Sarawi, D. Abbott, High-Sensitivity Metamaterial-Inspired Sensor for Microfluidic Dielectric Characterization, IEEE Sensors Journal 14 (5) (2014).

[145] C. Mariotti, W. Su, B. Cook, L. Roselli, M. Tentzeris, Development of Low Cost, Wireless, Inkjet Printed Microfluidic RF Systems and Devices for Sensing or Tunable Electronics, *IEEE Sensors Journal* **15** (6) (2015).

[146] R. Blakey, A. Morales-Partera, "Microwave dielectric spectroscopy – A versatile methodology for online, non-destructive food analysis, monitoring and process control", *Engineering in Agriculture, Environment and Food* **9** (3) (2016).

[147] Khaled, D., N. Novas, N., Gazquez, J, Garcia, R., Manzano-Agugliaro, F. "Fruit and Vegetable Quality Assessment via Dielectric Sensing", Sensors **15** (7) (2015).

[148] G. Ayissi Eyebe, B. Bideau, N. Boubekeur, É. Loranger, F. Domingue, Environmentally-friendly cellulose nanofibre sheets for humidity sensing in microwave frequencies, *Sensors and Actuators B: Chemical* **245** (2017)

[149] W. Chen, K. Stewart, R. Mansour, A. Penlidis, "Novel undercoupled radio-frequency (RF) resonant sensor for gaseous ethanol and interferents detection", *Sensors and Actuators A: Physical* 230 (2015).

[150] A. Benleulmi, N. Sama, P. Ferrari F. Domingue, "Substrate Integrated Waveguide Phase Shifter for Hydrogen Sensing", *IEEE Microwave and Wireless Components Letters* **26** (9) (2016).

[151] T. Chretiennot, D. Dubuc, K. Grenier, "Microwave-Based Microfluidic Sensor for Non-Destructive and Quantitative Glucose Monitoring in Aqueous Solution", *Sensors* 16 (10) (2016).

[152] A. Ebrahimi, W. Withayachumnankul, S. Al-Sarawi, D. Abbott, "Microwave microfluidic sensor for determination of glucose concentration in water". *IEEE 15th Mediterranean Microwave Symposium* (2015).

[153] M. Islam, M. Islam, M. Samsuzzaman, M. Faruque, N. Misran, "A Negative Index Metamaterial-Inspired UWB Antenna with an Integration of Complementary SRR and CLS Unit Cells for Microwave Imaging Sensor Applications", *Sensors* 15 (5), (2015).

[154] G. Gennarelli, S. Romeo, M. Scarfi, F. Soldovieri, "A Microwave Resonant Sensor for Concentration Measurements of Liquid Solutions", *IEEE Sensors Journal* 13 (5), (2013)

[155] S. Deng, P. Wang, X. Yu, "Phase-Sensitive Surface Plasmon Resonance Sensors: Recent Progress and Future Prospects", Sensors 17 (12) (2017).

[156] J. Wang, W. Lin, E. Cao, X. Xu, W. Liang, X. Zhang, "Surface Plasmon Resonance Sensors on Raman and Fluorescence Spectroscopy", Sensors 17 (12) (2017).

[157] P. Singh, "SPR Biosensors: Historical Perspectives and Current Challenges", Sensors and Actuators B: Chemical 229 (2016).

[158] Špačková, B., Wrobel, P., Bocková, M. & Homola, J. Optical Biosensors Based on Plasmonic Nanostructures: A Review. *Proc. IEEE* **104**, 2380–2408 (2016).

[159] N. Cselyuszka, Z. Sakotic, V. Crnojevic-Bengin, V. Radonic and N. Jankovic, "Microwave Surface Plasmon Polariton-Like Sensor Based on Half-Mode Substrate Integrated Waveguide for Highly Sensitive Dielectric Constant Detection," *IEEE Sensor J.* **18** (2018).

[160] Pozar, D.M. *Microwave engineering, 4th Edition. John Wiley & Sons*, (2011).

[161] A. Kraszewski, "Prediction of the Dielectric Properties of Two-Phase Mixtures", Journal of Microwave Power 12 (3) (1977).

[162] Chong, Y. D., Ge, L., Cao, H. & Stone, A. D. Coherent perfect absorbers: Time-reversed lasers. *Phys. Rev. Lett.* **105**, 1–4 (2010).

[163] Chong, Y. D., Ge, L. & Stone, A. D. PT-symmetry breaking and laser-absorber modes in optical scattering systems. *Phys. Rev. Lett.* **106**, 1–4 (2011).

[164] Ruan, Z. & Fan, S. Superscattering of light from subwavelength nanostructures. *Phys. Rev. Lett.* **105**, 1–4 (2010).

[165] Baranov, D.G., Krasnok, A. and Alù, A. Coherent virtual absorption based on complex zero excitation for ideal light capturing. *Optica* **4**, 1457-1461 (2017).

[166] Grigoriev, V. *et al.* Optimization of resonant effects in nanostructures via Weierstrass factorization. *Phys. Rev. A - At. Mol. Opt. Phys.* **88**, 011803 (2013).

[167] Kurokawa, K. Power Waves and the Scattering Matrix. *IEEE Transactions on Microwave Theory and Techniques.* **13,** 194–202 (1964).

[168] Whittaker, D. M. & Culshaw, I. S. Scattering-matrix treatment of multilayer photonic structures. **60**, 9 (1999).

[169] Haus, H. *Waves and Fields in Optoelectronics* (Prentice-Hall, Englewood Cliffs, NJ, 1984).

[170] Fan, S., Suh, W. & Joannopoulos, J. D. Temporal coupled-mode theory for the Fano resonance in optical resonators. *J. Opt. Soc. Am. A* **20**, 569 (2003).

[171] Ge, L., Chong, Y. D. & Stone, A. D. Steady-state ab initio laser theory: Generalizations and analytic results. *Phys. Rev. A - At. Mol. Opt. Phys.* **82**, 063824 (2010).

[172] Bernardi, M., Palummo, M. & Grossman, J. C. Extraordinary sunlight absorption and one nanometer thick photovoltaics using two-dimensional monolayer materials. *Nano Lett.* **13**, 3664–3670 (2013).

[173] Bao, Q. *et al.* Broadband graphene polarizer. *Nat. Photonics* **5**, 411–415 (2011).

[174] Liu, N., Mesch, M., Weiss, T., Hentschel, M. & Giessen, H. Infrared perfect absorber and its application as plasmonic sensor. *Nano Lett.* **10**, 2342–2348 (2010).

[175] Dallenbach, W. and Kleinsteuber, W., Reflection and absorption of decimeter-waves by plane dielectric layers, *Hochfrequenztechnik und Elektroakustik* **51**, 152 (1938).

[176] Salisbury, W.W. Absorbent body of electromagnetic waves, U.S. Patent No. 2,599,944, **10** (1952).

[177] Krasnok, A., Baranov, D. G., Generalov, A., Li, S. & Alù, A. Coherently Enhanced Wireless Power Transfer. *Phys. Rev. Lett.* **120**, 143901 (2018).

[178] Li, H., Mekawy, A., Krasnok, A. & Alù, A. Virtual Parity-Time Symmetry. *Phys. Rev. Lett.* **124**, 193901 (2020).

[179] Ra'Di, Y., Krasnok, & Alù, A. Virtual Critical Coupling. *ACS Photonics* **7**, 1468–1475 (2020).

[180] Lepeshov, S. & Krasnok, A. Virtual Optical Pulling Force. *Optica* **7**, 7, 1024-1030 (2020).

[181] Bowden, C. M. & Dowling, J. P. Near-dipole-dipole effects in dense media: Generalized Maxwell-Bloch equations. *Phys. Rev. A* **47**, 1247–1251 (1993).

[182] Anemogiannis, E., Glytsis, E. N., and Gaylord, T. K. Determination of guided and leaky modes in lossless and lossy planar multilayer optical waveguides: reflection pole method and wavevector density method. *J. Lightwave Technol.* **17**, 929–940 (1999).

[183] Sweeney, W. R., Hsu, C. W. & Stone, A. D. Theory of reflectionless scattering modes. *Phys. Rev. A* **102**, 1–20 (2020).

[184] Vahala, K. J. Optical microcavities. *Nature* **424**, 839–846 (2003).

[185] Ilchenko, V. S. & Matsko, A. B. Optical resonators with whispering-gallery modes - Part II: Applications. *IEEE J. Sel. Top. Quantum Electron.* **12**, 15–32 (2006).

[186] Duggan, R., Ra'Di, Y. & Alù, A. Temporally and Spatially Coherent Emission from Thermal Embedded Eigenstates. *ACS Photonics* **6**, 2949–2956 (2019).

[187] Marcuvitz, N. On Field Representations in Terms of Leaky Modes or Eigenmodes. *IRE Trans. Antennas Propag.* **4**, 192–194 (1956).

[188] Monticone, F. & Alù, A. Leaky-wave theory, techniques, and applications: From microwaves to visible frequencies. *Proc. IEEE* **103**, 793–821 (2015).

[189] M. Y. Shalaginov *et al.*, "Enhancement of single-photon emission from nitrogen-vacancy centers with TiN/(Al,Sc)N hyperbolic metamaterial," *Laser Photonics Rev.*, vol. 9, no. 1, pp. 120–127, 2015.

[190] L. Li, W. Wang, T. S. Luk, X. Yang, and J. Gao, "Enhanced Quantum Dot Spontaneous Emission with Multilayer Metamaterial Nanostructures," *ACS Photonics*, vol. **4**, no. 3, pp. 501–508, 2017

[191] V. Caligiuri, M. Palei, G. Biffi, S. Artyukhin, and R. Krahne, "A Semi-Classical View on Epsilon-Near-Zero Resonant Tunneling Modes in Metal/Insulator/Metal Nanocavities," *Nano Lett.*, vol. **19**, no. 5, pp. 3151–3160, 2019.

[192] N. C. Passler *et al.*, "Strong Coupling of Epsilon-Near-Zero Phonon Polaritons in Polar Dielectric Heterostructures," *Nano Lett.*, vol. 18, no. 7, pp. 4285–4292, 2018.

[193] A. Paarmann, I. Razdolski, S. Gewinner, W. Schöllkopf, and M. Wolf, "Effects of crystal anisotropy on optical phonon resonances in midinfrared second harmonic response of SiC," *Phys. Rev. B*, vol. 94, no. 13, pp. 1–9, 2016.

[194] Y. Ra'di, C. R. Simovski, and S. A. Tretyakov, "Thin Perfect Absorbers for Electromagnetic Waves: Theory, Design, and Realizations," *Phys. Rev. Appl.*, vol. 3, no. 3, p. 037001, Mar. 2015.

[195] D. G. Baranov, Y. Xiao, I. A. Nechepurenko, A. Krasnok, A. Alù, and M. A. Kats, "Nanophotonic engineering of far-field thermal emitters," *Nat. Mater.*, vol. 18, no. 9, pp. 920–930, Sep. 2019.

[196] Bulgakov, E. N. & Maksimov, D. N. Topological bound states in the continuum in arrays of dielectric spheres. *Phys. Rev. Lett.* **118**, 1–5 (2017).

[197] Zhang, Y. *et al.* Observation of polarization vortices in momentum space. *Phys. Rev. Lett.* **120**, 186103 (2018).

[198] Wang, B. *et al.* Generating optical vortex beams by momentum-space polarization vortices centered at bound states in the continuum. *Nat. Photonics* **14**, 623–628 (2020).

[199] Huang, C. *et al.* Ultrafast control of vortex microlasers. *Science* **367**, 1018–1021 (2020).

[200] Li, M. et al. Higher-order topological states in photonic kagome crystals with long-range interactions. *Nat. Photonics* **14**, 89–94 (2020).

[201] Berkhout, A. & Koenderink, A. F. Perfect absorption and phase singularities in plasmon antenna array etalons. *ACS Photonics* **6**, 2917–2925 (2019).

[202] Berkhout, A. & Koenderink, A. F. A simple transfer-matrix model for metasurface multilayer systems. *Nanophotonics* **9**, 3985–4007 (2020).

[203] Balistreri, M. L. M., Korterik, J. P., Kuipers, L. & van Hulst, N. F. Local observations of phase singularities in optical fields in waveguide structures. *Phys. Rev. Lett.* **85**, 294–297 (2000).

[204] Dennis, M. R., O'Holleran, K. & Padgett, M. J. Chapter 5 Singular Optics: Optical vortices and polarization singularities. *Progress in Optics* **53**, (2009).

[205] Alaee, R., Albooyeh, M. & Rockstuhl, C. Theory of metasurface based perfect absorbers. *J. Phys. D. Appl. Phys.* **50**, (2017).

[206] Huang, S. *et al.* Extreme Sound Confinement from Quasibound States in the Continuum. *Phys. Rev. Appl.* **14**, 1 (2020).

[207] Foteinopoulou, S., Devarapu, G. C. R., Subramania, G. S., Krishna, S. & Wasserman, D. Phonon-polaritonics: Enabling powerful capabilities for infrared photonics. *Nanophotonics* **8**, (2019).

[208] Decker, M. et al. High-Efficiency Dielectric Huygens' Surfaces. *Adv. Opt. Mater.* **3**, 813–820 (2015).

[209] Molesky, S. & Jacob, Z. High temperature epsilon-near-zero and epsilon-near-pole metamaterial emitters for thermophotovoltaics. *Opt. Lett.* **21**, 96-110 (2013).

[210] Bykov, D. A., Bezus, E. A. & Doskolovich, L. L. Bound states in the continuum and strong phase resonances in integrated Gires-Tournois interferometer. *Nanophotonics* 9, 83–92 (2020).

[211] Amin, M., Farhat, M. & Bağcı, H. An ultra-broadband multilayered graphene absorber. *Opt. Express* **21**, 29938 (2013).

[212] Yariv, A. and Yeh, P. Optical waves in crystals. *John Wiley and Sons* (1984).

[213] Alvear-Cabezón, E. *et al.* Epsilon near-zero all-optical terahertz modulator. *Appl. Phys. Lett.* **117**, (2020).

[214] Abedini Dereshgi, S. et al. Lithography-free IR polarization converters via orthogonal in-plane phonons in α-MoO3 flakes. *Nat. Commun.* **11**, 1–9 (2020).

[215] Kravets, V. G. *et al.* Singular phase nano-optics in plasmonic metamaterials for label-free single-molecule detection. *Nat. Mater.* **12**, 304–309 (2013).

[216] Tsurimaki, Y. *et al.* Topological engineering of interfacial optical Tamm states for highly sensitive near-singular-phase optical detection. *ACS Photonics* **5**, 929–938 (2018).

[217] Sreekanth, K. V. *et al.* Brewster mode-enhanced sensing with hyperbolic metamaterial. *Adv. Opt. Mater.* **7**, 1–6 (2019).

[218] Ouyang, Q. *et al.* Two-dimensional transition metal dichalcogenide enhanced phase-sensitive plasmonic biosensors: Theoretical insight. *J. Phys. Chem. C* **121**, 6282–6289 (2017).

[219] Sreekanth, K. V. *et al.* Biosensing with the singular phase of an ultrathin metal-dielectric nanophotonic cavity. *Nat. Commun.* **9**, (2018).

[220] Barth, I., Conteduca, D., Reardon, C., Johnson, S. & Krauss, T. F. Common-path interferometric label-free protein sensing with resonant dielectric nanostructures. Light Sci. Appl. **9**, (2020).

[221] Armitage, N. P., Mele, E. J. & Vishwanath, A. Weyl and Dirac semimetals in three-dimensional solids. *Rev. Mod. Phys.* **90**, 15001 (2018).

[222] Cheng, H. et al. Vortical Reflection and Spiraling Fermi Arcs with Weyl Metamaterials. *Phys. Rev. Lett*. **125**, 93904 (2020).

[223] Shastri, K. & Monticone, F. Dissipation-induced topological transitions in continuous Weyl materials. *Phys. Rev. Res.* **2**, 33065 (2020).

[224] Gao, W. et al. Photonic Weyl degeneracies in magnetized plasma. *Nat. Commun*. **7**, 1–8 (2016).

[225] Longhi, S. Bound states in the continuum in PT -symmetric optical lattices, *Opt. Lett*. **39**, 1697 (2014).

[226] Kartashov, Y.V., Mili´an, C., Konotop, V. V., and Torner, L. Bound states in the continuum in a two-dimensional PT - symmetric system, *Opt. Lett*. **43**, 575 (2018).

[227] Song, Q. *et al.* Coexistence of a new type of bound state in the continuum and a lasing threshold mode induced by PT symmetry. *Sci. Adv.* **6**, 1–10 (2020).

[228] Novitsky, D., Shalin, A., Pavlov, A., Bobrovs, V. & Novitsky, A. Quasi-bound states in the continuum induced by *PT*-symmetry breaking. (2021).

[229] Baldacci, L., Zanotto, S., Biasiol, G., Sorba, L. & Tredicucci, A. Interferometric control of absorption in thin plasmonic metamaterials: general two port theory and broadband operation. *Opt. Express* **23**, 9202 (2015).

[230] Baranov, D. G., Krasnok, A., Shegai, T., Alù, A. & Chong, Y. Coherent perfect absorbers: Linear control of light with light. *Nat. Rev. Mater.* **2**, (2017).

[231] Sakotic, Z., Krasnok, A., Cselyuszka, N., Jankovic N., and Alú, A. Berreman embedded eigenstates for narrow-band absorption and thermal emission, *Phys. Rev. Appl.* **13**, 1 (2020).

[232] Sakotic, Z., Krasnok, A., Alú, A., and Jankovic N. Topological scattering singularities and embedded eigenstates for polarization control and sensing applications. *Photonics Res.* **9**, 6 (2021).

Published work

1. **Z. Sakotic**, A. Krasnok, A. Alú, and N. Jankovic. Topological scattering singularities and embedded eigenstates for polarization control and sensing applications. *Photonics Research* **9**, 7 (2021). **(M21)**

2. **Z. Sakotic**, A. Krasnok, N. Cselyuszka, N. Jankovic, and A. Alú. Berreman Embedded Eigenstates for Narrow-Band Absorption and Thermal Emission. *Physical Review Applied* **13**, 064073 (2020). **(M21)**

3. N. Cselyuszka, **Z. Sakotic**, V. Crnojevic-Bengin, V. Radonic, N. Jankovic. Microwave Surface Plasmon Polariton-Like Sensor Based on Half-Mode Substrate Integrated Waveguide for Highly Sensitive Dielectric Constant Detection. *IEEE Sensors Journal* **18** (24), 9984-9992. (2018) **(M21)**

4. N. Cselyuszka, **Z. Sakotic**, G. Kitic, V. Crnojevic-Bengin, N. Jankovic. Novel Dual-band Band-Pass Filters Based on Surface Plasmon Polariton-like Propagation Induced by Structural Dispersion of Substrate Integrated Waveguide. *Scientific reports* **8** (1), 8332. (2018). **(M21)**

5. **Z. Sakotic**, M. Drljaca, G. Kitic, N. Jankovic, N. Cselyuszka. LTCC Dual-band Bandpass Filter Based on SPP-like Propagation in Substrate Integrated Waveguide. *Proceedings of IEEE Eurocon*, Novi Sad, Serbia. (2019) **(M33)**

6. **Z. Sakotic**, A. Krasnok, N. Cselyuszka, N. Jankovic, A. Alú. Coherent Control of Scattering in Non-Hermitian PT-Symmetrical Systems. *Proceedings of Metamaterials Congress*, Rome, Italy. (2019) **(M34)**

7. **Z. Sakotic**, A. Krasnok, N. Cselyuszka, N. Jankovic, A. Alú. PT-Symmetric Cladding Layers for High-Q Brewster Modes and Embedded Eigenstates. *Proceedings of Metamaterials Congress*, Rome, Italy. (2019) **(M34)**

8. A. Krasnok, **Z. Sakotic**, N. Cselyuszka, N. Jankovic, A. Alú. Coherent Excitation of Embedded Eigenstates in non-Hermitian PT-Symmetrical Systems. *Proceedings of IEEE International Symposium on Antennas and Propagation and USNC-URSI Radio Science Meeting*, Paper: MO-UB.1P.5 Atlanta, USA. (2019) **(M34)**

9. **Z. Sakotic**, A. Krasnok, N. Cselyuszka, N. Jankovic, A. Alú. Coherent Virtual Absorption and Embedded Eigenstates in non-Hermitian PT-Symmetrical Systems.

Proceedings of Conference on Lasers and Electro-Optics, OSA Technical Digest, paper FW4D.5, San Jose, USA. (2019) **(M34)**

10.   A. Krasnok, **Z. Sakotic**, N. Cselyuszka, N. Jankovic, and A. Alú. Coherently Driven Embedded Eigenstates. *Frontiers in Optics + Laser Science APS/DLS*, OSA Technical Digest, paper FW1F.3, (2019) **(M34)**

11.   **Z. Sakotic**, A. Krasnok, N. Cselyuszka, N. Jankovic, A. Alú. Modes in Epsilon Near-Zero Structures – from Bulk Leaky Plasmons to Embedded Eigenstates. *Proceedings of the International conference of Quantum, Non-Linear and Nanophotonics*, Sofia, Bulgaria. (2019) **(M34)**

Prošireni izvod

Uvod

Elektromagnetski (EM) talasi su važan deo svakodnevnog života. Bilo da uzimamo u obzir vidljivu ili infracrvenu svetlost, ili radio talase - EM talasi podupiru mnoge aspekte života, nauke i tehnologije. Teorijski temelji elektromagnetike postavljeni su u 19. veku, kada je Džejms Maksvel objedinio tadašnje znanje u kompaktni skup jednačina 1865. godine [1]. Od tog trenutka nauka i tehnologija zasnovane na EM talasima doživele su ogroman napredak.

Generisanje, detekcija i kontrola učestanosti, amplitude, faze i polarizacije EM talasa danas je u središtu mnogih važnih tehnologija. Funkcionalnost komponenti i uređaja poput antena, lasera, solarnih ćelija, optičkih vlakana, mikroskopa, optičkih računara i biosenzora oslanja se na preciznu kontrolu svojstava EM talasa. Zadovoljavanje zahteva savremenih tehnologija zasnovanih na EM talasima zahteva multidisciplinarni pristup - inženjering novih materijala sa poboljšanim električnim i magnetskim svojstvima, korišćenje nanotehnologije za projektovanje nanostruktura koje interaguju sa vidljivom/infracrvenom svetlošću, a pre svega fundamentalno poznavanje i otkriće novih talasnih pojava koje omogućavaju prevazilaženje tehnoloških postojećih ograničenja.

Plazmonika i metamaterijali predstavljaju oblasti istraživanja koje mogu da odgovore na zahteve savremenih optičkih i mikrotalasnih tehnologija. Naime, plazmonika omogućava interakciju svetlosti sa materijalima na dimenzijama daleko manjim od svoje talasne dužine, što je omogućilo napredak biosenzorskih i spektroskopskih tehnologija koje zahtevaju interakciju na nanometarskim dimenzijama. Sa druge strane, metamaterijali podrazumevaju struktuiranje postojećih materijala kako bi se dobile proizvoljne EM osobine koje prirodni materijali ne poseduju. Na ovaj način moguće je prevazići ograničenja prirodnih materijala i postojećih tehnologija izrade, što ima veliki uticaj na savremene tehnologije zasnovane na EM talasima. Iako su ove oblasti sazrele i uspešno doprinele nauci i tehnologiji, još uvek nisu dovoljno istražene. Pored toga, nedostaci u vidu neizbežnih gubitaka i zahtevnih procesa izrade plazmoničnih metamaterijala ograničavaju mogućnosti njihove primene. Kako bi se ovi nedostaci prevazišli i njihov potencijal u potpunosti iskoristio, potrebna su dalja istraživanja i nova teorijska saznanja u vezi sa talasnim fenomenima prisutnim u plazmoničnim metamaterijalima.

U ovoj disertaciji, naš cilj je da proširimo mogućnosti kontrole talasa i poboljšamo interakciju svetlosti sa materijom istraživanjem novih talasnih fenomena u metamaterijalima i plazmonici. Koristeći funkcionalnosti različitih talasnih pojava, diskutujemo o njihovim posledicama na prostiranje i rasipanje talasa, i istražujemo različite strukture da bismo postigli kontrolu učestanosti, amplitude, faze i polarizacije EM talasa.

Metamaterijali i povšinski plazmonski polaritoni

Prostiranje elektromagnetskih talasa kroz sredinu, kao i njihova interakcija sa materijalom kroz koji se prostire, najviše zavise od dva parametra - dielektrične permitivnosti ε i magnetske permeabilnosti μ materijala. Kao što je opisano u konstitutivnim relacijama, oni diktiraju odziv materijala na pobudno električno i magnetnsko polje.

Potpuna kontrola dinamike talasa u medijumu zahtevala bi raspoloživost proizvoljnih vrednosti ε i μ u željenom opsegu učestanosti. Međutim, prirodni materijali ne mogu pružiti takvu fleksibilnost. Da bi se prevazišla ova ograničenja, uložen je veliki napor da se veštačkim putem dobiju proizvoljni električni i magnetski odzivi za kontrolu svojstava prostiranja talasa.

Metamaterijali nulte permitivnosti

Iako su prvi napori u istraživanju metamaterijala bili usredsređeni na postizanje dvostruko negativnog ponašanja (istovremeno negativni ε i μ) zbog neobičnih efekata poput negativnog prelamanja, zasebno su bili istraživani i realizovani metamaterijali nultog indeksa prelamanja (engl. *Near-zero-index – NZI*) [30-36]. Kako je indeks prelamanja definisan kao $n = \sqrt{\mu_r \varepsilon_r}$, nula indeksa prelamanja može se postići kada je permitivnost i(li) permeabilnost jednaka nuli. Međutim, budući da većina materijala u prirodi nema magnetske osobine, *epsilon-near-zero* (ENZ) režim je značajno lakše postići od *mu-near-zero* (MNZ) režima, stoga je ENZ režim dominantan pravac istraživanja u poslednjoj deceniji [9]. ENZ istraživanja se fokusiraju na dinamiku talasa u materijalima gde je stvarna ili efektivna permitivnost materijala blizu nule ili jednaka nuli. Materijali sa ovakim odzivima pokazali su izuzetne osobine u smislu kontrole amplitude, faze i polarizacije reflektovanih/transmitovanih EM talasa, međutim oni su još uvek u fazi istraživanja i imaju veliki potencijal za brojne primene. Značajan deo istraživanja u okviru ove disertacije usmeren je upravo na ENZ fenomen, uz pomoć kojeg će se realizovati različiti fenomeni i predložiti optičke komponente i senzori.

Površinski plazmonski polaritoni

Zbog ekstremne konfiniranosti površinskih plazmonskih polaritona (engl. *Surface-plasmon polariton - SPP*), oni su bili predmet istraživanja koja za cilj imaju da kontrolišu prostiranje talasa i da pojačaju interakciju svetlosti sa materijom na nanometarskim dimenzijama [5,6, 54-56]. Međutim, specifična priroda ovih modova zahteva negativnu permitivnost materijala koja uglavnom karakteriše metale, pa je takve talase moguće postići samo u optičkom delu spektra. Budući da njihove osobine mogu biti korisne za različite primene, uloženi su napori da se uz pomoć metamaterijala dobije plazmonični odziv u drugim delovima EM spektra. Konkretno, terahercna i mikrotalasna plazmonika su se posebno istakle poslednjih decenija [57-71]. Da bi se ovaj potencijal dalje iskoristio, biće istraženi SPP talasi zasnovani na talasovodu integrisanom u podlogu, kako bi se realizaovale mikrotalasne komponente visokih performansi.

Površinski plazmonski polaritoni zasnovani na talasovodu integrisanom u podlogu

Prvi fenomen koji istražujemo podrazumeva efektivne SPP talase realizovane uz pomoć strukturne disperzije talasovoda integrisanog u podlogu (engl. *Substrate-integrated waveguide – SIW*). Naime, na ovaj način je omogućeno dobijanje plazmoničnog odziva na mikrotalasnim učestanostima, iako je sa prirodnim materijalima to moguće postići samo u optičkom domenu EM spektra. Ovo čini SIW obećavajućim kandidatom za plazmonična integrisana kola, koja se mogu lako proizvesti u standardnoj tehnologiji štampanih ploča (engl. *Printed Circuit board - PCB*) ili LTCC (engl. *Low temperature co-fired ceramic*) tehnologijama. Data je teorijska osnova SPP modova u SIW-u na osnovu koje analiziramo, projektujemo i eksperimentalno validiramo dva dvopojasna mikrotalasna filtra i mikrotalasni senzor za detekciju tečnih analita.

Mikrotalasni filtri

Dobro je poznato da brzi razvoj komunikacionih sistema nameće zahteve za komponente visokih performansi, malih dimenzija, i niske cene izrade koje rade na dve ili više harmonijski nezavisnih učestanosti. Uzimajući u obzir te zahteve i potencijal SIW struktura, predlažemo dva nova dvopojasna filtra koja koriste efektivne SPP za postizanje rada na dve harmonijski nezavisne mikrotalasne učestanosti. Prostiranje efektivnih SPP obezbeđuje nulu transmisije u spektralnom odzivu, uz pomoć koje se propusni opsezi jasno razdvajaju u spektru, što je ujedno i osnovni princip predloženog filtriranja.

SIW predstavlja talasovod ispunjen dielektrikom koji je ograničen metalnim zidovima sa donje i gornje strane, dok nizovi vija koji povezuju gornju i donju graničnu površinu predstavljaju bočne zidove. Vije koje imitiraju bočne zidove dozvoljavaju prostiranje samo transverzalnih-električnih (TE) modova, dok su transverzalni-magnetski (TM) modovi zabranjeni [131]. TE modove karakteriše učestanost odsecanja, a svaki mod se može okarakterisati efektivnom permitivnošću koja zavisi od geometrije SIW-a. Ovo dovodi do strukturne disperzije tj. do toga da efektivna permitivnost koju talasi 'vide' zavisi od učestanosti:

$$\varepsilon_{eff} = \varepsilon_r - \left(\frac{c}{2af}\right)^2 \tag{A3.1}$$

Ukoliko se dva talasovoda koja imaju različite efektivne permitivnosti spregnu, moguće je naći opseg učestanosti gde jedan SIW ima negativnu, a drugi pozitivnu efektivnu permitivnost, što predstavlja jedan od potrebnih uslova za formiranje efektivnog površinskog SPP talasa. Da bi se dva SIW-a spregnula, potrebno je koristiti poprečne žice koje omogućavaju formiranje polaritona [73]. Takva dva spregnuta SIW-a predstavljaju osnovni gradivni blok koji omogućava prostiranje efektivnog SPP-a. Da bi se omogućilo dvopojasno filtriranje, potrebno je spregnuti tri različita SIW-a, kao što je prikazano na ponovljenoj slici 3.5, gde je skiciran izgled celopkupne trojslojne strukture. Budući da širina i dielektrična konstanta svakog
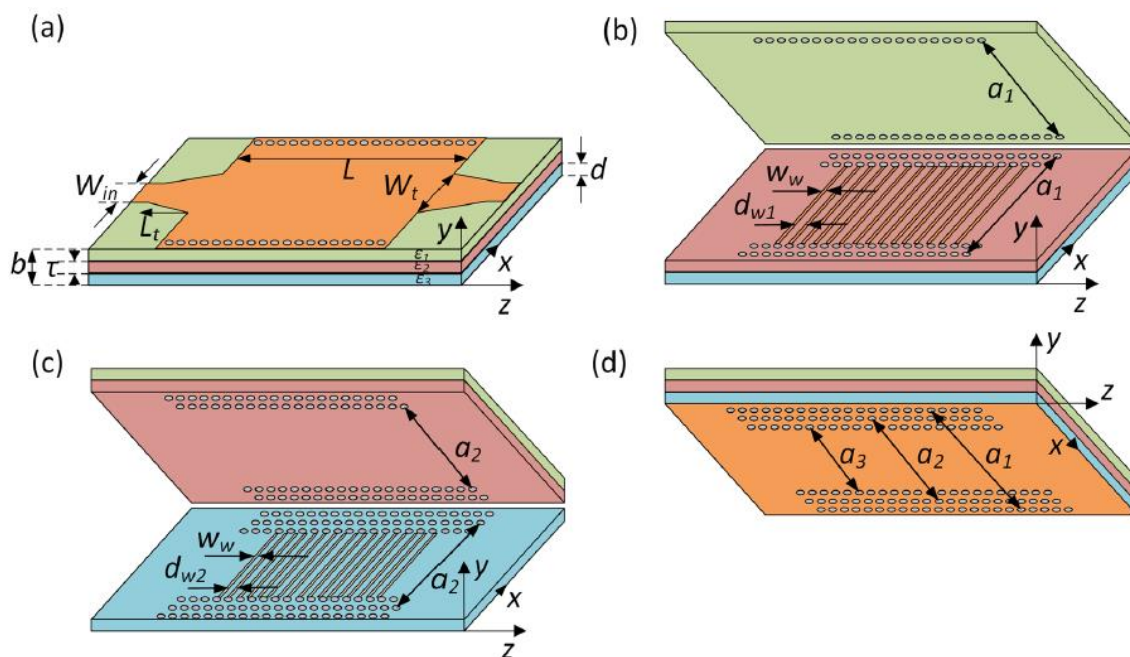

Ponovljena slika 3.5. Izgled predloženih filtara. (a) Cela struktura. (b) Razdelna površina gornjeg i srednjeg SIW-a. (c) Razdelna površina srednjeg i donjeg SIW-a. (d) Donja strana donjeg SIW-a.

zasebnog SIW-a predstavljaju mehanizam za nezavisnu kontrolu propusnih opsega, teoretski postoji šest stepeni slobode u projektovanju filtara.

Nakon što su tri SIW-a projektovana na osnovu teorijske analize, numeričke simulacije se koriste za fino podešavanje odziva strukture. Iako teorija može vrlo precizno odrediti položaje i karakteristike propusnih opsega, potrebno je numerički optimizovati filtar jer analitički model ne može predvideti međusobna sprezanja između slojeva koja utiču na odziv filtra. Takođe, za dobre performanse filtra potrebno je prilagoditi impedansu strukture na uvodnu mikrotalasnu liniju.

Filtri su fabrikovani korišćenjem standardne PCB tehnologije.Poređenje rezultata merenja i simulacija na ponovljenoj slici 3.12 pokazuje dobro slaganje, osim malih razlika u propusnim opsezima koje se mogu pripisati toleranciji proizvođača u vezi sa dielektričnom konstantom, kao i neznatnoj neusklađenosti vija u procesu izrade. Prvi filtar pokazuje dva propusna opsega na 2.65 i 3.75 GHz, sa unetim gubicima od 1.47 i 1.69 dB, a propusnost od 3 dB od 8.7% i 13.3%, respektivno. Centralne učestanosti drugog filtra su 4.8 i 5.7 GHz, njihovi uneti gubici su 2.22 i 2.17 dB, a širina propusnih 3-dB opsega su 5.2% i 8.2%, respektivno. Oba filtra su karakterisana dobrim performansama u opsegu i izvan opsega, kao i odličnom selektivnošću zahvaljujući nulama transmisije. Razlika u unesenim gubicima između prvog i drugog filtra može se pripisati činjenici da se prvi filtar sastoji od tri različite podloge čiji su ukupni dielektrični gubici manji nego kod drugog filtra. Stoga su gubici izraženiji u drugom predloženom filtru.

Predloženi filtri su prvi dvopojasni filtri zasnovani na konceptu efektivnih SPP talasa u SIW-u. Pored toga, odlikuju ih dobre performanse i mogućnost nezavisne kontrole propusnih
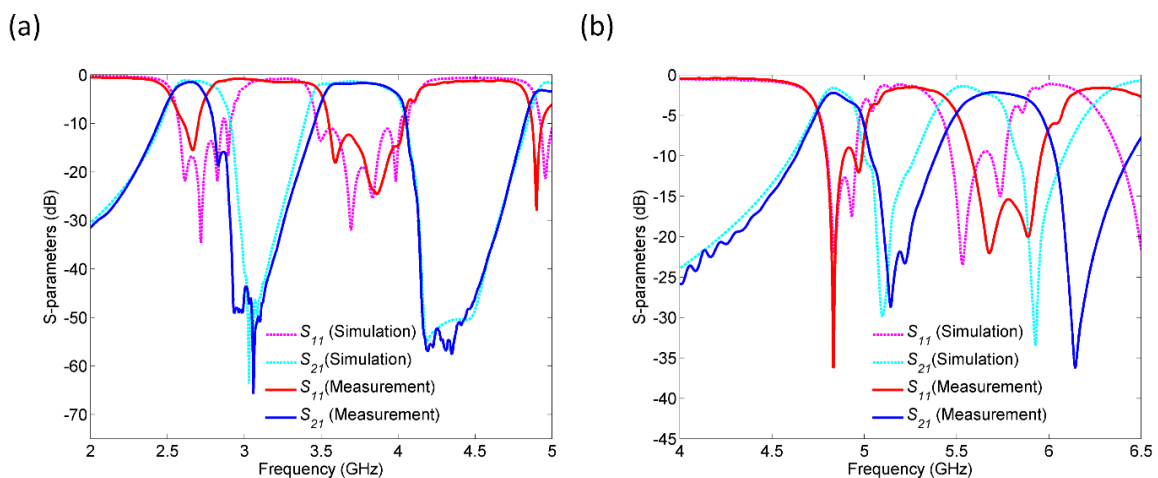

Ponovljena slika 3.12. Poređenje merenih i simuliranih rezultata: (a) Prvi predloženi filtar. (b) Drugi predloženi filtar.

opsega u smislu položaja i širine opsega. Štaviše, oni ispunjavaju uslove za jeftinu i niskoprofilnu konfiguraciju jer su realizovani kao SIW strukture. Kao takvi, oni se mogu smatrati veoma obećavajućim kandidatima za višepojasno filtriranje na mikrotalasnim učestanostima.

Mikrotalasni senzor

Poslednjih godina mikrotalasni senzori privukli su značajnu pažnju jer mogu da obezbede neinvazivnu detekciju analita. Štaviše, mikrotalasna kola mogu se lako proizvesti u PCB tehnologiji i lako ih je integrisati, što ih čini povoljnim kada su u pitanju zahtevi za kompaktnošću i jeftinom proizvodnjom. Ipak, mikrotalasni senzori vrlo često imaju nisku rezoluciju i osetljivost, npr. čak i značajna promena realnog dela dielektrične konstante obično izaziva vrlo mali relativni rezonantni pomak ili promenu amplitude signala na izlazu. Takav nedostatak ograničava primenljivost mikrotalasnih senzora. Kao što je ranije opisano, SPP talasi omogućavaju pojačanu interakciju svetlosti sa materijom na veličinama manjim od talasne dužine i odličan su kandidat za senzorske uređaje zbog njihove velike osetljivosti [153-155], pa bi primena prethodno opisanog koncepta efektivnih SPP modova mogla omogućiti mikrotalasne senzore visokih performansi.

U tom smislu je predložen mikrotalasni senzor zasnovan na *half-mode* SIW-u za vrlo osetljivu detekciju dielektrične konstante. Predlozena struktura se sastoji od dva dela ispunjena dielektričnim materijalom podloge, dok se na donjem delu nalazi i rezervoar u kome se nalazi tečni analit. Dva dela su spojena nizom žica, što omogućava prostiranje nalik na SPP na njihovoj razdvojnoj površini, kao što je objašnjeno ranije. Ovo podešavanje obezbeđuje oštru transmisionu nulu u odzivu strukture, čiji su položaj i izraženost veoma osetljivi na male promene realnog dela dielektrične konstante analita. Tečni analit koji se detektuje predstavlja
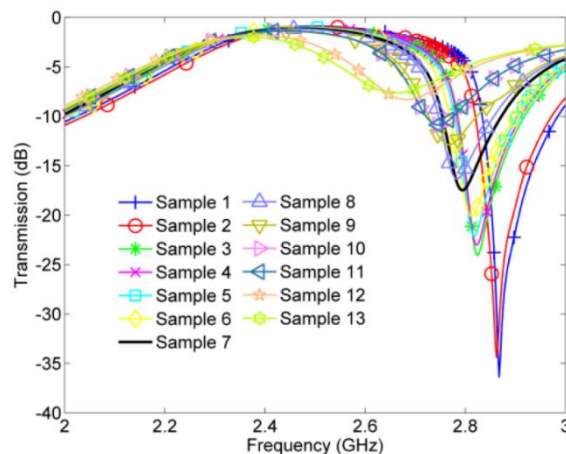
Ponovljena slika 3.19. Izmereni odziv senzora za različite analite.

mešavinu toluena i metanola, i tečni analiti pripremljeni su kao binarne smeše toluene i metanola. U čisti toluen čija je dielektrična konstanta jednaka 2.4-j0.11 dodavane su različite količine metanola pomoću mikropipete, sa ciljem da se dobiju realni delovi vrednosti dielektrične konstante u opsegu od 2.4 do 3.8. Mereni rezultati transmisije prikazani su na ponovljenoj slici 3.19, gde se uočava velika promena odziva tj. veliko pomeranje transmisione nule. Relativna osetljivost senzora dobijena uz pomoć formule $(f_{max}/f_{min}-1)*100/(\varepsilon_{max}-\varepsilon_{min})$ iznosi 6.62, što je uporedivo ili bolje od drugih mikrotalasnih senzora dielektrične konstante. Takođe, treba napomenuti da je posebna prednost predloženog senzora u tome što se vrši detekcija realnog dela dielektrične konstante u veoma malom opsegu, dok je većina mikrotalasnih senzora usmerena na detekciju širokog opsega dielektričnih konstanti.

Anomalije u rasipanju svetlosti sa planarnim strukturama

U analizi interakcije svetlosti sa makroskopskim strukturama, linearno rasipanje ima značajnu ulogu. Prilikom interakcije sa optičkim strukturama, EM talasi mogu proći kroz nekoliko jednostavnih procesa kao što su refleksija, transmisija, apsorpcija i difrakcija. Ovi procesi su predmet intenzivnih istraživanja u oblasti metamaterijala, gde talasi interaguju sa složenijim strukturama, i gde se može postići izuzetna kontrola nad svojstvima talasa prilikom procesa rasipanja. Nedavno je predstavljen niz neobičnih fenomena rasipanja u metamaterijalima i nanofotonici, kao što su koherentna savršena apsorpcija (engl. *Coherent perfect absorption - CPA*) [162], prostorno-vremensko-simetrični (engl. *Parity-time symmetric – PT-symmetric*) fazni prelazi [163], superrasipanje [164], vezana stanja u kontinuumu [89], i virtuelna apsorpcija [165]. Takve anomalije rasipanja mogu se opisati na intuitivan način kroz formalizam matrice rasipanja ili *S*-matrice (engl. *Scattering matrix*) [90,166], koji predstavlja koristan alat u analizi i projektovanju optičkih uređaja sa novim funkcionalnostima. Analizom ovih sistema u ravni kompleksne učestanosti mogu se uočiti singulariteti sopstvenih vrednosti *S*-matrice u obliku polova i nula što je veoma korisno jer se proces rasipanja može u potpunosti opisati položajem polova i nula [90]. Koristeći se pomenutom analizom, ispitujemo razne EM strukture i dolazimo do novih teorijskih saznanja. Na osnovu tih saznanja predloženo je nekoliko primena uključujući izvor uskopojasnog i usmerenog termalnog zračenja, infracrveni polarizator, fazni senzor, i laser-apsorber sa različitim funkcionalnostima.

Rezonance i vezana stanja u kontinuumu

Rezonance imaju veoma bitnu ulogu u EM uređajima, jer predstavljaju sveprisutnu pojavu u talasima. Uz pretpostavke vremenske zavisnosti $e^{-j\omega t}$ i odsustva izvora, rešenja

Makvelsovih jednačina sa isključivo izlaznim komponentama predstavljaju sopstvena stanja ili rezonancije sistema [74]. Rezonancije se obično odnose na stanja koja mogu da se pobude upadnim talasima iz slobodnog prostora, i koja se odlikuju sopstvenom učestanošću (rezonantna učestanost). Konvencionalno znanje o rezonancama nalaže da se one nalaze u kontinuumu zračećih modova, odnosno da se nalaze u svetlosnom konusu - mogu primati energiju spolja i zračiti energiju nazad u okolni medijum. To znači da je njihova sopstvena učestanost kompleksnog oblika, pri čemu je imaginarni deo sopstvene učestanosti inverzno proporcionalan životnom veku rezonance. Vreme relaksacije rezonance često se definiše kroz njegov Q-faktor odnosno faktor kvaliteta oscilacija $Q = -\omega_r/2\omega_i$.

Q-faktor rezonance je veoma važna karakteristika jer ona određuje vremenski odziv sistema na pobudu i ima velike posledice na interakciju svetlosti sa materijom. Rezonance visokog Q faktora poželjne su u svakom delu EM spektra, npr. uskopojasni filtri, laseri i senzori se zasnivaju na rezonatorima visokih Q-faktora. Stoga je potražnja za rezonatorima izuzetno visokog Q-faktora velika u savremenim komponentama i uređajima.

Ugrađena sopstvena stanja (engl. *Embedded eigenstate - EE*), poznata i kao vezana stanja u kontinuumu (engl. *Bound states in the continuum - BIC*), posebna su vrsta rezonancija. Iako se nalaze u kontinuumu zračećih stanja, ona ne zrače. Njihovo vreme relaksacije, a samim tim i Q-faktor je beskonačno veliko talasi su savršeno zarobljeni u rezonantnoj strukturi i osciluju bez prigušenja. O ovom kontraintuitivnom fenomenu prvi put su u kvantnoj mehanici raspravljali Vigner i Von Neumann 1929. godine [75]. Međutim, opšta talasna priroda EE-a shvaćena je tek u poslednjoj deceniji, nakon čega je ovaj fenomen ostvaren u različitim oblastima fizike sa mnogim primenama [77-93].

Vezana stanja u kontinuumu uz pomoć ENZ materijala za primenu u termalnom zračenju

Rasipanje talasa je veoma često korišćen proces u nauci i tehnologiji, a da bi došlo do procesa rasipanja, elektromagnetski talasi moraju da stupe u interakciju sa materijom. Ova interakcija leži u središtu današnje eksperimentalne fizike i tehnologije, kako u klasičnom tako i u kvantnom režimu. Fenomen blisko povezan sa interakcijom svetlosti i materije jeste konfiniranje talasa uz pomoć rezonanci sistema . Koncetrisanjem velikih količina elektromagnetske energije u malim zapreminama omogućila je napredak u oblastima optike i fotonike, gde su visoki Q-faktori i male zapremine modova realizovani različitim pristupima [90,184,185].
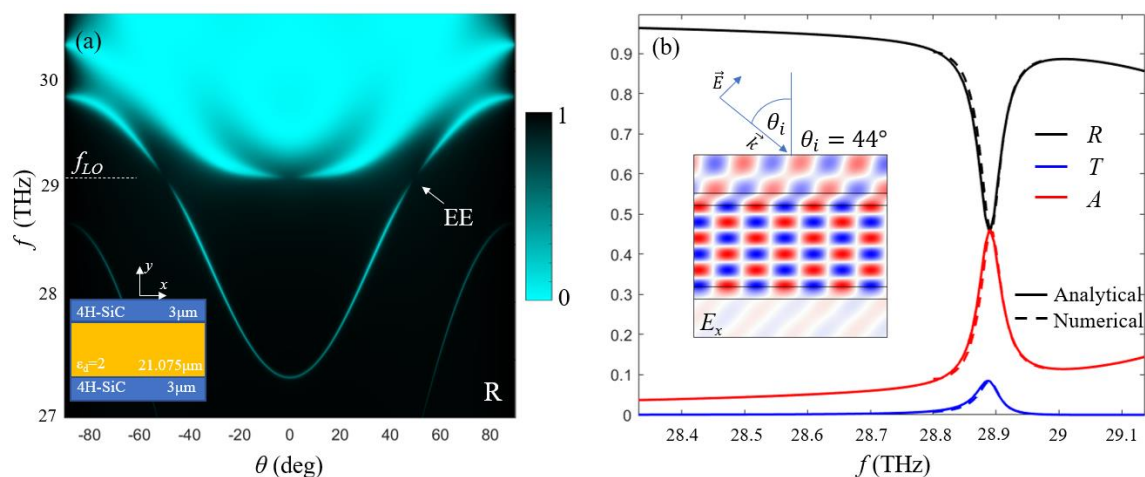
Ponovljena slika 5.11. Demonstracija kvazi-EE u SiC-u. (a) Spektar reflektance TM polarizovane svetlosti; na umetku je skica geometrije. (b) Reflektansa, transmitansa i apsorbanca za svetlost upadnog ugla od 44 °. Umetnuto: Distribucija električnog polja unutar strukture.

Za ekstremno konfiniranje svetlosti nedavno je predložen koncept ugrađenih sopstvenih stanja (EE) ili vezanih stanja u kontinuumu (BIC) [77-89]. Većina realizacija predložnih za dobijanje EE zasniva se korišćenju periodičnih struktura [77]. Međutim, nedavno je predložen i konceptualno drugačiji pristup za dobijanje EE koji se zasnivana korišćenju ENZ materijala [88,89,91].

Ovde istražujemo realističnu strukturu sa silicijum karbidom kao ENZ materijalom koji podržava EE velikog Q-faktora na projektovanom upadnom uglu od 50 stepeni, ponovljena slika 5.11. SiC je odličan kandidat za ovu svrhu jer ga karakterišu vrlo mali gubitci na rezonanci longitudinalnog fonona gde realni deo permitivnosti prolazi kroz nulu.

ENZ režim omogućuje pojačanu interakciju svetlosti i materije sa veoma uskopojasnim rezonantnim linijama. U slučaju realističnog ENZ materijala sa gubicima, ovo svojstvo rezultuje naglašenom apsorpcijom u blizini tačke ENZ-a. Ova karakteristika se može iskoristiti za projektovanje uskopojasnih apsorbera na osnovu vezanih stanja u kontinuumu [186]. Prateći konvencionalni pristup za postizanje savršene apsorpcije [194], smanjujemo transmisiju kroz strukturu povećavajući debljinu donjeg SiC sloja i razmatramo geometriju asimetrične strukture na ponovljenoj slici 5.13 (a). Reflektivnost ovog sistema tačno na EE je velika, što rezultira slabom apsorpcijom. Međutim, rezonance oko EE mogu prikazati apsorpcione vrhove sa izuzetno uskim linijama i po pitanju učestanosti i po pitanju uglova.

S obzirom na izuzetnu spektralnu i ugaonu selektivnost predložene apsorbujuće strukture, kao i na činjenicu da radna učestanost spada u dugotalasni infracrveni deo spektra
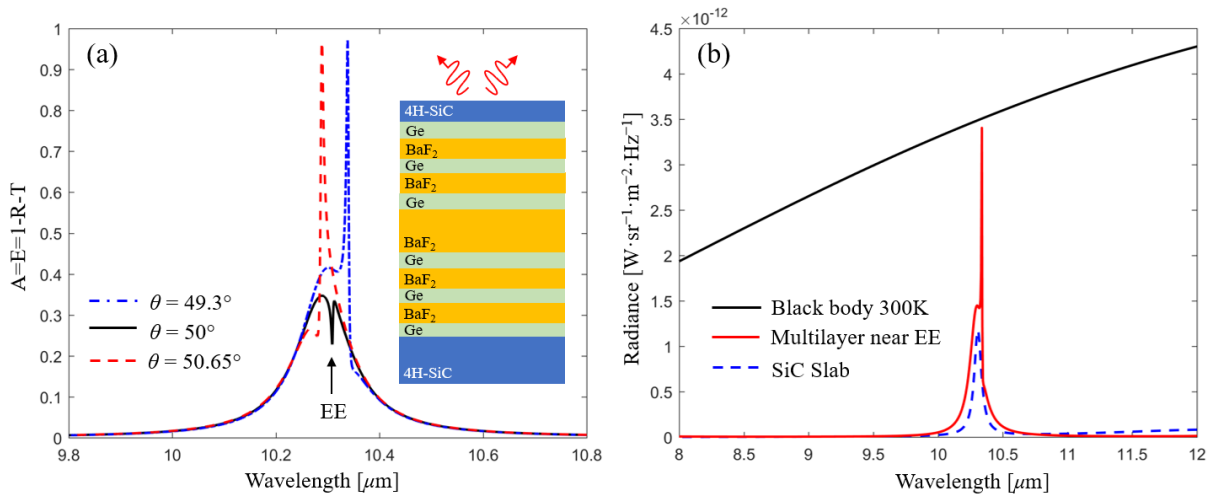
Ponovljena slika 5.13. Višeslojna struktura, ukupne debljine 19.35 μm. (a) Apsorpcija/toplotna emisija u okolini EE. (b) TM spektralna radijanca predložene strukture na uglu 49.3° u poređenju sa radijancama sloja SiC i crnog tela na 300K.

(8-12 μm), ona je odličan kandidat za projektovanje kvazi-koherentnih toplotnih emitera. Naime, Kirhofov zakon direktno povezuje optičku apsorpciju i toplotnu emisiju [195].

U tom smislu, proučavamo višeslojnu strukturu sa ponovljene slike 5.13 (a). Apsorpcione (emisione) linije za uglove u okolini vezanog stanja u kontinuumu prikazuju veoma uzak opseg, dok je tačno na uglu EE minimalna apsorpcija. Da bi se uporedile toplotne performanse predložene strukture sa slojem SiC, prikazana je spektralna radijanca u regionu 8-12 μm za istu strukturu, ponovljena slika 5.13 (b). Pik emisije u blizini EE pokazuje ekstremnu spektralnu selektivnost, sa širinom linije manjom od 10 nm na polu-maksimumu, a samim tim i superiornost u poređenju sa jednoslojnom SiC strukturom.

Topološki aspekti singulariteta *S*-matrice

Elektromagnetska vezana stanja u kontinuumu u periodičnim sistemima poseduju topološku karakteristiku u obliku singulariteta polarizacije u recipročnom prostoru. Njihova robusnost eksplicitno se pripisuje njihovoj topološkoj prirodi [92,93], zasnovanoj na činjenici da se ti singulariteti ponašaju u skladu sa očuvanjem topološkog "naelektrisanja", odnosno da mogu nestati samo ako se ponište sa singularitetom suprotnog "naelektrisanja" [196,197].

Iako je znanje o topološkim aspektima EE u periodičnim sistemima dobro utvrđeno, topološke karakteristike drugih sistema koji podržavaju EE nisu dovoljno istražene. Konkretno, EE koji nastaju u strukturama sa singularnim vrednostima permitivnosti, uglavnom koristeći ENZ materijale, proučavani su nedavno [38–41]. Međutim, njihovi topološki aspekti nisu utvrđeni, što bi moglo dodatno da poveća njihov potencijal za primenu u oblastima termalne fotonike, polarizacione optike i optičkih senzora.

146

Koncept topološke fotonike primenjujemo na planarne reflektujuće sisteme koji podržavaju EE. Koristeći formalizam matrice rasipanja i analizu kompleksne učestanosti, otkrivamo njihovu topološku prirodu i pojavu topološki zaštićenih singulariteta refleksije. Pokazujemo da su tačke savršene apsorpcije suštinski povezane sa EE. Predstavljene su metode formiranja, uništavanja i kontrole ovih topoloških singulariteta, pružajući svestran alat za manipulaciju amplitudom, fazom i polarizacijom reflektovanih talasa. Koristeći ove koncepte, demonstrirali smo nekoliko primena ovih pojava za kontrolu polarizacije i detekciju faze.

Ograničavamo diskusiju na reflektujuće strukture; takve strukture se mogu opisati *S*-matricom sa samo jednim elementom - koeficijentom refleksije. Singulariteti sopstvenih vrednosti *S*-matrice se u ovom slučaju potpuno poklapaju sa singularitetima koeficijenta refleksije što ima zanimljive posledice kada se uzmu u obzir jednopristupne strukture koje podržavaju EE.

Traženjem singulariteta koeficijenta refleksije u ravni kompleksne učestanosti, odnosno polova i nula koeficijenta refleksije, takođe određujemo singularitete *S*-matrice povezane sa sopstvenim modovima i savršeno apsorbujućim stanjima. Analizu započinjemo razmatranjem strukture na ponovljenoj slici 6.2 (a), gde materijal gornjeg sloja prati Drude disperziju permitivnosti $\varepsilon_1 = \varepsilon_0 \left[1 - \omega_p^2 / (\omega^2 + j\gamma\omega) \right]$. Analiziramo disperziju moda u blizini
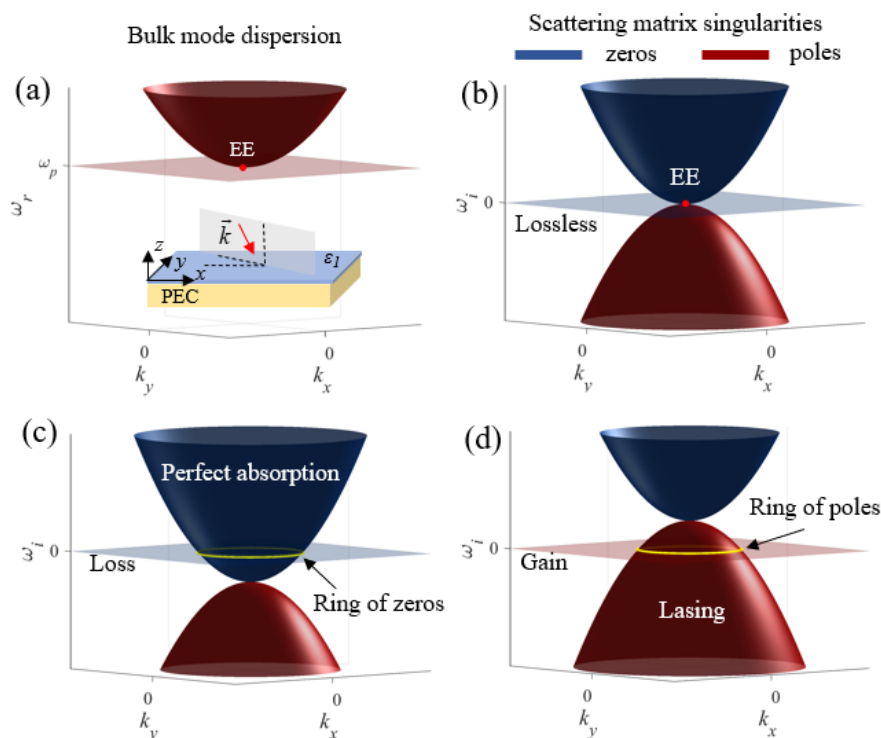
Ponovljena slika 6.2. (a) Disperzija TM moda. Disperzija polova i nula u prostoru imaginarne učestanosti za: (b) slučaj bez gubitaka, (c) slučaj sa gubicima, (d) slučaj sa pojačanjem.
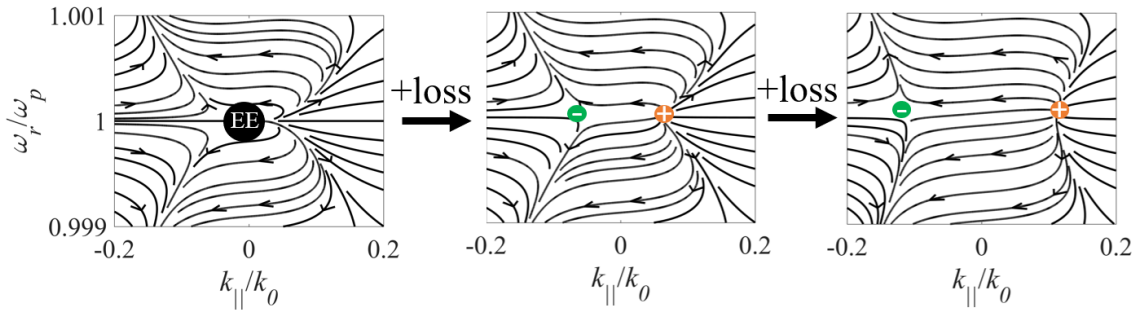
Ponovljena slika 6.3. Vektorski prikaz koeficijenta refleksije za jednu upadnu ravan u slučaju sa i bez gubitaka. Razdvajanje dva naelektrisanja suprotnog polariteta usled gubitaka.

plazmene učestanosti ω_p, ponovljena slika 6.2 (a), koja se dobija traženjem polova koeficijenta refleksije. Mod zrači sve manje kako se disperzija približava nultom transverzalnom talasnom vektoru, i na kraju se pretvara u EE na plazmenoj učestanosti i $k_\parallel = 0$.

Zbog postojanja samo jednog pristupa, nule i polovi koeficijenta refleksije identični su singularitetima S-matrice, što znači da oni u sistemu bez gubitaka predstavljaju kompleksno konjugovane parove. Dakle, disperzija nule refleksije (savršene apsorpcije) predstavlja sliku disperzija polova (moda) u ogledalu u prostoru imaginarne učestanosti, ponovljena slika 6.2 (b). Štaviše, nula refleksije u sistemu sa jednim portom podrazumeva savršenu apsorpciju, $A =$ 1- $|r|^2$, što je u suprotnosti sa slučajem bez gubitaka u dvopristupnom sistemu gde nula refleksije podrazumeva potpunu transmisiju.

Zbog postojanja EE, disperzija polova i nula se dodiruju na nultoj imaginarnoj učestanosti, odnosno tačno na plazmenoj učestanosti. Uvođenjem gubitaka (pojačanja) u materijal, disperzione površi se pomeraju ka dole (gore) duž ose imaginarne učestanosti, stvarajući prsten nula (polova) čisto realne učestanosti, ponovljena slika 6.2 (c, d). Presek singulariteta rasipanja sa osom realne učestanosti predstavlja topološki objekat – naelektrisanje sa brojem namotaja različitog od nule u datom parameterskom prostoru.

Topološki potpis ovih stanja može se posmatrati u prostoru vektorskog toka r, ponovljena slika 6.3. U ω_r-$k_\parallel$ dvodimenzionalnom prostoru, uzimajući u obzir jednu ravan incidencije, uočava se da se nakon dodavanja gubitka EE razdvaja na dva vrtloga, sedlastu tačku (zeleno) i izvornu tačku (narandžasto). Ove topološke tačke predstavljaju tačke savršene apsorpcije i moguće ih je uništiti samo ako se dovedu u kontakt sa topološkom tačkom suprotnog naelektrisanja. Ova veza između EE i topološki zaštićenih tačaka savršene apsorpcije prethodno nije utvrđena, a odnosi se na velik broj realnih materijala što ima velike posledice na kontrolu amplitude, faze i polarizacije talasa.

Kontrola polarizacije zasnovana na singularitetima koji proizilaze iz EE

Tradicionalno, manipulacija polarizacijskim stanjem svetlosti zasnovana je na talasnim kristalnim pločama [212]. Kada se svetlost prostire kroz birefrigentne kristale, njegove komponente ortogonalne linearne polarizacije (LP) imaju različite koeficijente apsorpcije i akumulacije faza, time omogućavajući stvaranje čisto horizontalne, vertikalne ili cirkularne polarizacije (CP) na izlazu. Prethodno pomenuti singulariteti savršene apsorpcije mogu da se iskoriste upravo u ovu svrhu. SiC u blizini svoje transverlzalne fononske rezonance podržava singularitete savršene apsorpcije i TE i TM polarizcije. Ovo svojstvo ima zanimljive posledice po pitanju kontrole polarizacije, jer dve ortogonalne komponente polarizacije imaju veoma različite koeficijente apsorpcije i akumulacije faza u području koje sadrži te tačke, omogućavajući različite linearne transformacije polarizacije prilikom refleksije. Da bismo testirali potencijal ovog svojstva, koristimo izotropni SiC. Ponovljena slika 6.11 prikazuje skicu razmatranog sistema i disperziju koeficijenta refleksije za dva različita upadna ugla i polarizacije. Nule koeficijenta refleksije TE i TM jasno su postignute za prikazane uglove.

Da bismo bolje ilustrovali ceo parametarski prostor i obuhvatili singularitete o kojima je diskutovano, prikazujemo elipsometrijski parametar $\tan^{-1}=(r_{TM}/r_{TE})$, ponovljena slika 6.12 (a), gde maksimalna vrednost na slici predstavlja TE nulu, dok minimalna predstavlja TM nulu. Jasno je da ove dve tačke u parametarskom prostoru funkcionišu kao polarizacioni filteri ili polarizatori - za mešoviti polarizacijski ulaz, samo TM ili TE polarizovano svetlo izlazi iz strukture. Osim toga što podržava nule obe polarizacije, fazna razlika između ortogonalnih
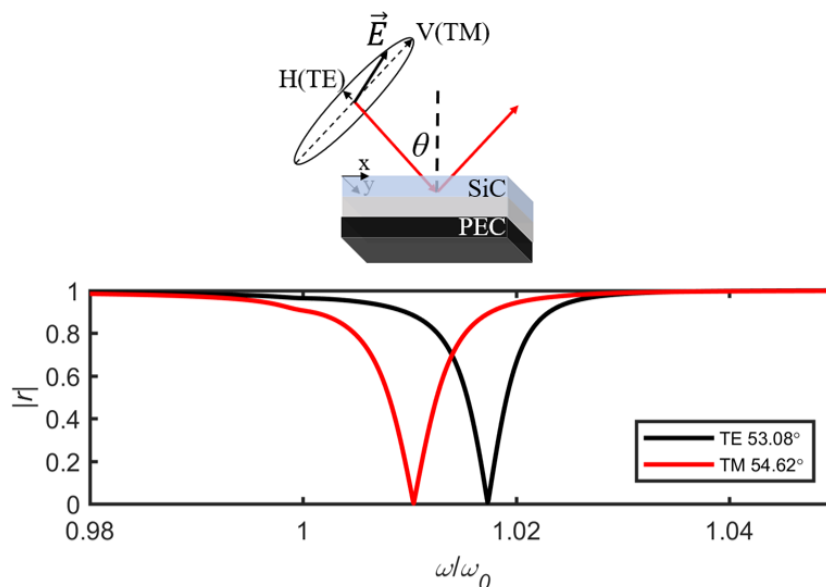
Ponovljena slika 6.11. Skica analizirane strukture sa nulama refleksije obe linearne polarizacije u blizini EE.
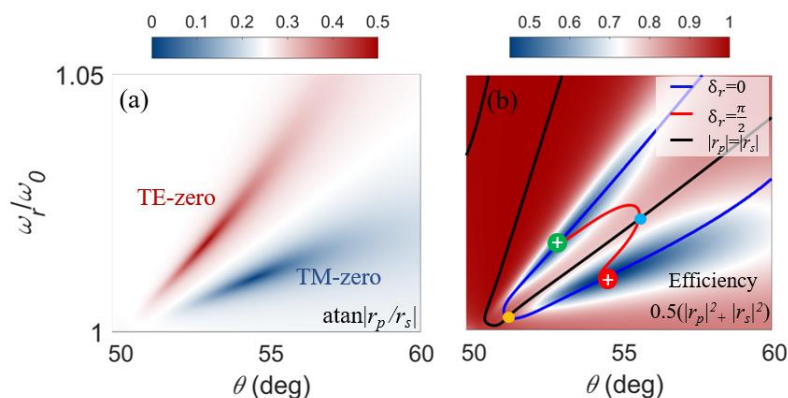
Ponovljena slika 6.12. (a) Elipsometrijski parametar gde se vide nule obe linearne polarizacije. (b) Ukupna refleksija kao indikator efikasnosti gde se vide specifične tačke polaziracije.

komponenti polarizacije koju unosi struktura takođe se dramatično menja u okolini singulariteta jer predstavljaju fazne vrtloge. Ovo svojstvo otvara mogućnosti za generisanje različitih stanja polarizacije na izlazu za mešoviti ulaz - na primer, pretvaranje LP u CP svetlost. Da bismo ilustrovali mogućnosti kontrole polarizacije, takođe iscrtavamo ukupnu refleksiju i konturne linije sa specifičnim vrednostima unete fazne razlike. Na ovaj način možemo pronaći tačke konverzije iz LP u CP i obrnuto, plava i žuta tačka na ponovljenoj slici 6.12 (b).

Kao što je rečeno, za manipulaciju polarizacijom talasa potrebni su birefringentni kristali, međutim te osobine materijala su retke u infracrvenom delu spektra. Stoga je doprinos predloženog koncepta to što je moguće manipulisati polarizacijom reflektovanog talasa sa postojećim materijalima u infracrvenom delu EM spektra.

Senzor singularne faze

Fazne vrtloge karakteriše tačka nedefinisane faze u njihovom centru oko koje se faza dramatično menja. Ova karakteristika, najčešće uočljiva u okolini nula refleksije, koristi se kao osnova za interferometrijsko merenje faze [215-220]. Naime, čak i male promene u okruženju mogu rezultirati ogromnim faznim promenama, stvarajući tako jedan od najosetljivijih sistema za detekciju faze.

Specifičnost ove metode je u tome što se približavanjem singularnoj tački vrtloga faza dramatičnije menja, povećavajući tako osetljivost sistema. Međutim, amplituda koeficijenta refleksije istovremeno pada. Osetljivost divergira kada se dostigne singularna tačka, ali refleksija koju treba meriti na detektoru više ne postoji. Ova inverzna veza između osetljivosti i koeficijenta refleksije ima važnu ulogu u takvim uređajima. Kritično pitanje u takvim uređajima je potreba za visoko preciznim upadnim uglom za dobijanje naglih faznih skokova. Zbog toga je osetljivost takvih uređaja teško predvideti i održavati stabilnom.
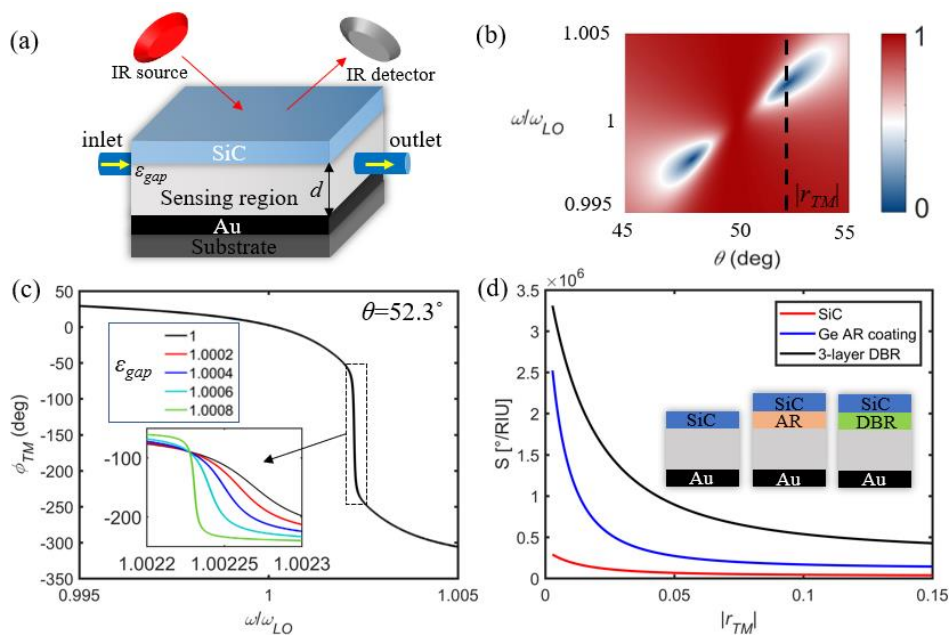
Ponovljena slika 6.14. Koncept detekcije faze zasnovan na faznim singularitetima. (b) Amplituda koeficijenta refleksije blizu EE za upadni ugao od 50 stepeni. (c) Faza koeficijenta refleksije u blizini vrtloga. Umetnuto: Fazna osetljivost na male promene permitivnosti šupljine. (c) Osetljivost za tri različite konfiguracije-poboljšanje zbog povećanog Q-faktora sa antirefleksnim staklom i DBR.

Da bismo rešili ova pitanja, koristimo neobičnu prirodu EE i povezanih topoloških singulariteta o kojima je bilo reči. Prvo, pokazujemo da upotreba EE u SiC obezbeđuje rezonance visokog faktora dobrote i omogućava izuzetno visoku osetljivost u okolini nula refleksije povezanih sa EE. Drugo, uvodimo koncept detekcije faze blizu tačke poništenja i pokazujemo da možemo eliminisati zahtev za izuzetno preciznim upadnim uglom koji ovakvi sistemi uglavnom imaju. Da bismo postigli ove ciljeve, predlažemo strukturu sa ponovljene slike 6.14 (a). Kao što je prikazano u prethodnoj raspravi, rezonator sa SiC-om može podržati EE na talasnoj dužini 10.3 μm (ENZ region) i prateće nule refleksije. Da bismo demonstrirali fazni skok, prikazujemo koeficijent refleksije ponovljenoj slici 6.14 (b-c). Pri konstantnoj frekvenciji i uglu, faza reflektovanih talasa dramatično se menja zbog promena permitivnosti reda 10^{-4}, omogućavajući vrlo visoku osetljivost, reda 10^5 stepeni/RIU. Međutim, kao što je ranije pomenuto, osetljivost u velikoj meri zavisi od amplitude koeficijenta refleksije, odnosno koliko je merenje blizu singularne tačke. Da bismo bolje shvatili ovu korelaciju, prikazujemo osetljivost izračunatu pri različitim vrednostima $|r|$ koja je data crvenom krivom na ponovljenoj slici 6.14 (d).

Kao što se i očekuje, vidi se povećanje osetljivosti kako se $|r|$ približava nuli. Međutim, umesto oslanjanja na izuzetno male vrednosti $|r|$ da bismo dobili veću osetljivost, , možemo povećati osetljivost povećanjem Q-faktora moda. To se može učiniti postavljanjem anti-

151
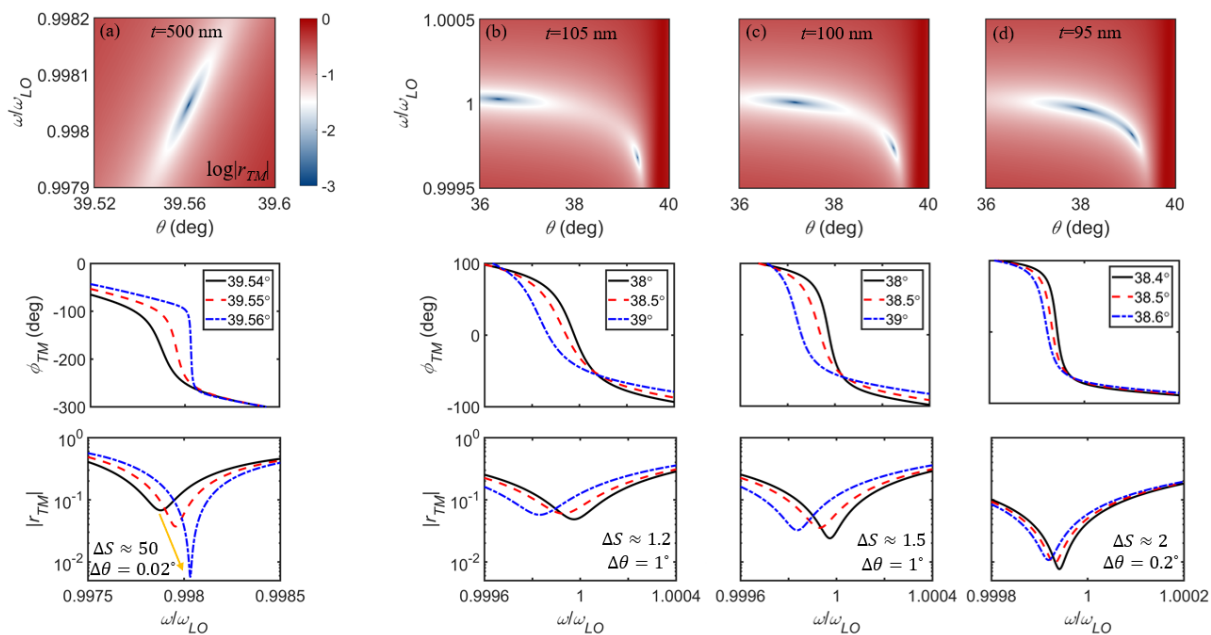
Ponovljena slika 6.15. Amplituda koeficijenta refleksije i osetljivost faze na promene upadnog ugla. (a) Koeficijent refleksije DBR strukture na slici 5 (c) je izuzetno osetljiv na male promene upadnog ugla, što rezultira promenom osetljivosti za jedan red veličine za veoma male promene ugla. (b)-(d) Senzor blizu tačke poništenja sa stabilizovanom osetljivošću. Amplituda koeficijenta refleksije je robusnija na varijacije upadnog ugla pri čemu se osetljivost ne menja mnogo za promenu ugla od 1 stepena za (b) i (c), i 0.2 stepena za (d)

refleksnog stakla visokog indeksa prelamanja ili distribuiranog Bragg-ovog reflektora (engl. *Distributed Bragg reflectot – DBR*) između šupljine i sloja SiC-a. U tu svrhu možemo koristiti dugotalasne IR materijale sa malim gubicima, na primer Ge i BaF$_2$. Kao što je prikazano na ponovljenoj slici 6.14 (d), ovo rezultira povećanjem osetljivosti za jedan red veličine.

Međutim, prikazano povećanje osetljivosti zahteva preciznost upadnog ugla reda veličine 0.01 stepeni. Za DBR strukturu prikazanu na ponovljenoj slici 6.14 (d), osetljivost opada za red veličine sa promenom ugla od samo 0.02 stepena, ponovljena slika 6.15 (a). Iako predstavljeni sistem ima superiornu osetljivost, on ima nedostatak jer osetljivost izuzetno zavisi od izabranog upadnog ugla. To može dovesti do nepouzdanih vrednosti osetljivosti, jer većina instrumenata nema toliko dobru rezoluciju.

Da bismo ublažili ovaj strogi zahtev, koristimo fenomen spajanja singulariteta. Približavanjem dva susedna singulariteta na blisko rastojanje u parametarskom prostoru, koeficijent refleksije između njih dobija skoro konstantnu vrednost, zadržavajući pritom snažan fazni skok, ponovljena slika 6.15 (b)-(d). Nadalje, finim podešavanjem debljine SiC-a pokazujemo da je |r| moguće kontrolisati i održavati konstantnim u proširenom ugaonom opsegu, čime se eliminišu strogi zahtevi za upadni ugao i obezbeđuje stabilna osetljivost. Međutim, ovo dolazi po cenu niže apsolutne osetljivosti, jer spajanje dva singulariteta zahteva

smanjenje ukupnog Q-faktora. Postoji kompromis između osetljivosti sistema i robusnosti na varijacije upadnog ugla. Na primer, struktura na ponovljenoj slici 6.15 (a) ima 3 puta veću apsolutnu osetljivost od strukture na ponovljenoj slici 6.15 (d) (izračunato za istu vrednost $|r|$). Međutim, u većini praktičnih slučajeva mnogo je lakše ostvariti potrebne uglove za drugu strukturu i dobiti predviđenu osetljivost. Ovi rezultati pokazaju da topološke karakteristike EE nude raznovrsne metode za projektovanje senzora i da mogu odgovoriti na različite izazove naprednih sistema detekcije faze.

Topološka priroda singulariteta *S*-matrice u dvoportnim sistemima sa gubicima i pojačanjem

Kao što ćemo dalje pokazati, stvaranje para singulariteta iz EE neophodna je posledica dodavanja gubitaka i pojačanja u razmatrane planarne strukture. Da bismo otkrili ovo fundamentalno svojstvo EE u dvopristupnim sistema, koristimo istu analizu kao i ranije.

Razmatramo singularitete sopstvenih vrednosti S-matrice u ravni kompleksne učestanosti. Ponovljena slika 7.3 prikazuje skicu razmatrane višeslojne strukture i dato je grafičko objašnjenje nastajućih singulariteta. Razmatramo tri slučaja, polazeći od višeslojne ENZ-dielektrik-ENZ konfiguracije bez gubitaka koja podržava EE, ponovljena slika 7.3 (a). Kao što je prethodno objašnjeno, EE predstavlja degeneraciju pola i nule S-matrice u sistemima
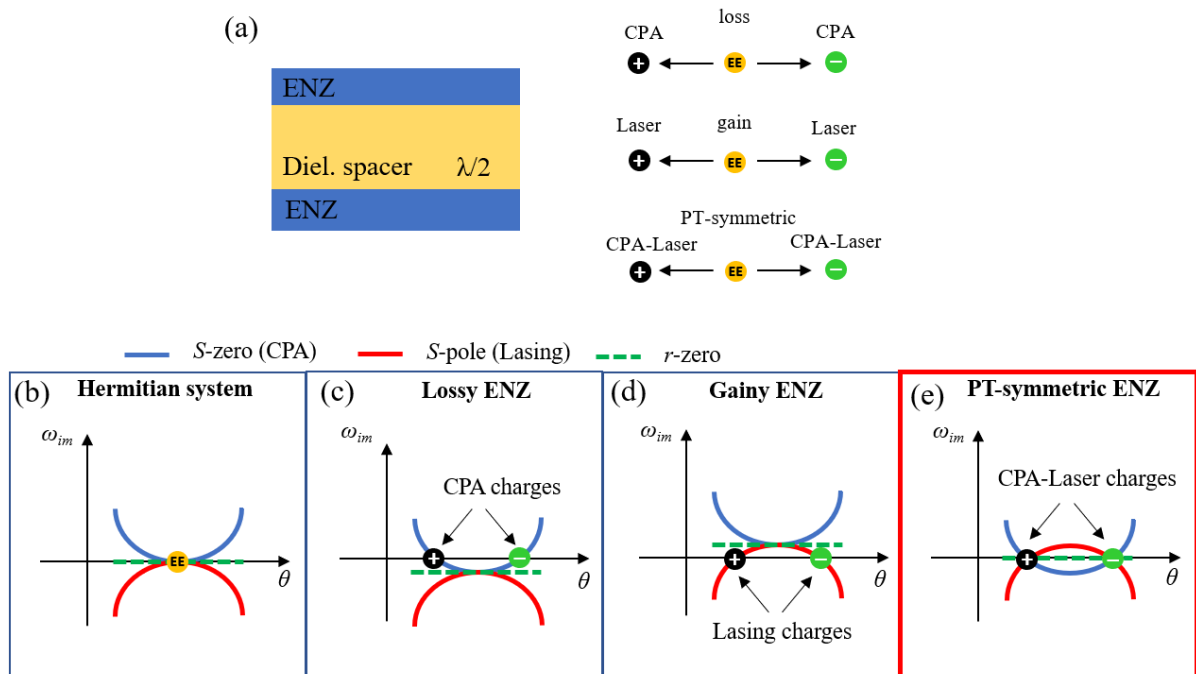
Ponovljena slika 7.8.1. (a) Razdvajanje EE u dva singulariteta suprotnih naelektrisanja. (b) U slučaju bez gubitaka, disperzija polova i nula se dodiruje na $\omega_{im} = 0$. (c) Gubici pomeraju polove i nule na dole, stvarajući dva CPA singulariteta koja se pojavljuju u okolini EE. (d) Pojačanje pomera singularitete ka gore stvarajući dva laserska stanja. (e) PT-simetrična struktura istovremeno gura nule ka dole, a polove ka gore, stvarajući dva laser-apsorber rešenja za realnu učestanost.

bez gubitaka. U okolini EE, disperzija polova i nula S-matrice ima paraboličan oblik, ponovljena slika 7.3 (b). Uvođenjem gubitaka disperzija singulariteta pomera se ka dole, stvarajući dva preseka sa osom d (ωim = 0, tj. čisto realna učestanost). Ove tačke predstavljaju dva rešenja koherentne savršene apsorpcije CPA, jer predstavljaju rešenja problema čisto upadnih talasa za realnu učestanost. Ponovljena slika 7.3 (d) prikazuje suprotan slučaj sa pojačanjem, gde se singulariteti pomeraju ka gore uz osu imaginarne učestanosti. Ovo rezultira sa dva laserska stanja, simetrično raspoređena oko EE. Konačno, kada se gubici i pojačanje uvedu na PT-simetričan način, nule se pomeraju nadole, a polovi se pomeraju nagore, stvarajući presek njihovih disperzionih linija tačno na osi realne učestanosti, ponovljena slika 7.3 (e). Ova degeneracija pola S-matrice i nule predstavlja rešenje CPA-lasera, odnosno tačke koja je istovremeno i laser i apsorber. Posebno treba istaći da ove tačke predstavljaju topološki zaštićene tačke. Veza između EE i singulariteta S-matrice, kao i topološka priroda ovih efekata prethodno nije ustanovljena i ima velike posledice za senzore, topološku fotoniku, i lasere niskog praga.

Zaključak

U okviru ove disertacije detaljno su analizirani talasni fenomeni u plazmoničnim metamaterijalima. Glavni fokus istraživanja bili su efektivni SPP talasi na mikrotalasnim učestanostima i vezana stanja u kontinuumu u planarnim optičkim strukturama.

Predstavljene su mikrotalasne komponente zasnovane na efektivnim površinskim plazmonima u talasovodima integrisanim u podlogu, koje predstavljaju prve realizovane komponente na ovom principu. Karakterisane su dobrim performansama, malom veličinom i jednostavnom tehnologije izrade, što ih čini dobrim kandidatima za komponente u savremenoj mikrotalasnoj tehnologiji.

Pojava i karakteristike vezanih stanja u kontinuumu u planarnim strukturama su sistematično i sveobuhvatno predstavljene. Posebno je značajno to što je utvrđena topološka priroda singulariteta koji nastaju iz vezanih stanja u kontinuumu. Predstavljeni teorijski okvir se odnosi na širok spektar realnih materijala, i ima širok spektar potencijalnih primena. Ovo je demonstrirano sa nekoliko primera primene, uključujući infracrveni polarizator, fazni senzor, izvor uskopojasnog i usmerenog termalnog zračenja, i laser-apsorber sa raznim funkcionalnostima.

Potrebno je dodati i da rezultati prikazani u poglavljima 5, 6 i 7 predstavljaju odličnu osnovu za dalja istraživanja. Iako je prikazan veći broj novih rezultata, predstavljeni teorijski

okvir i uspostavljena topološka priroda analiziranih efekata, kao i opšta priroda prikazanih rezultata ostavljaju prostor za nova istraživanja.

Short biography

Žarko Šakotić was born on December 2nd, 1989. in Doboj, Bosnia and Herzegovina. He finished primary and secondary school in Sombor, Serbia. Undergraduate and master's studies were completed at the Department of Computer Science and Electrical Engineering, at the Faculty of Technical Sciences, University of Novi Sad in 2015 and 2016, respectively.

Since 2016, Žarko Šakotić has been working at the BioSense Institute, University of Novi Sad, where he works as a research assistant in the Center for Sensor Technology.

As a part of the MCA-RISE H2020 project NOCTURNO, he was a visiting scholar at the University of Texas at Austin in the metamaterials and plasmonics group, and later at the Advanced Science Research Center CUNY, New York in the Photonics Initiative. He was also a visiting scholar at the Australian National University, in Canberra, Australia, in the nonlinear physics group.

His research interests are metamaterials, nanophotonics and plasmonics. In his research work so far, Žarko Šakotić has coauthored 6 papers in international journals and 10 papers at international conferences.

Kratka biografija

Žarko Šakotić rođen je 2. decembra 1989. godine u Doboju, Bosna i Hercegovina. Osnovnu i srednju školu pohađao je u Somboru. Osnovne i master studije završio je na Katedri za računarstvo i elektrotehniku na Fakulteta tehničkih nauka Univerziteta u Novom Sadu 2015., odnosno 2016. godine.

Od 2016. godine radi na Institutu BioSens, Univerzitet u Novom Sadu, gde radi kao istraživač saradnik u Centru za senzorsku tehnologiju.

Kao deo MCA-RISE H2020 projekta NOCTURNO, bio je gostujući istraživač na Univerzitetu u Teksasu u Ostinu, SAD u grupi za metamaterijale i plazmoniku, a kasnije i u Advanced Science Research Center u Njujorku, SAD u okviru grupe za fotoniku. Takođe je bio u istraživačkoj poseti na univerzitetu Australian National University u Kanberi, Australija, u grupi za nelinearnu fiziku.

Njegova istraživačka interesovanja su metamaterijali, nanofotonika i plazmonika. U dosadašnjem istraživačkom radu Žarko Šakotić je bio koautor 6 radova u međunarodnim časopisima i predstavio je 10 radova na međunarodnim konferencijama.

План третмана података

Назив пројекта/истраживања
Novel wave phenomena based on plasmonic metamaterials and their application in sensors and components/ Нови таласни феномени базирани на плазмоничним метаматеријалима и њихова примена у сензорима и комппонентама
Назив институције/институција у оквиру којих се спроводи истраживање
а) Природно-математички факултет, Универзитет у Новом Саду, Нови Сад б) Институт БиоСенс, Универзитет у Новом Саду, Нови Сад в)
Назив програма у оквиру ког се реализује истраживање
Физика плазме
1. Опис података
1.1 Врста студије *Укратко описати тип студије у оквиру које се подаци прикупљају* _____**У овој студији нису прикупљани подаци** _____
2. Прикупљање података
3. Третман података и пратећа документација
4. Безбедност података и заштита поверљивих информација
5. Доступност података
6. Улоге и одговорност